UNIVERSITY OF
PLYMOUTH

THE SENSITIVITY OF MARGINALLY STRATIFIED SHELF SEA FRONTS TO TURBULENT MIXING PROCESSES

BY

MARCUS MAXIMILIAN ZANACCHI

A THESIS SUBMITTED TO THE UNIVERSITY OF PLYMOUTH IN PARTIAL FULFILMENT FOR THE DEGREE OF

DOCTOR OF PHILOSOPHY

SCHOOL OF BIOLOGICAL & MARINE SCIENCES

August 2019

Copyright Statement

Abstract

Turbulent mixing plays an important role in controlling the vertical structure of temperature, salinity and density in shelf seas. It is crucial in controlling the seasonal stratification in temperate shelf seas, though our incomplete knowledge of the processes involved prevents an accurate representation in numerical shelf sea modelling. This study made use of both observational field work and numerical turbulence modelling to identify first- and second-order mixing mechanisms in weakly stratified waters in the Celtic Sea, U.K.

Field work was conducted both in spring (May, 2012) and summer (August, 2012). During the 11-day field work in spring, an overall warming of the well-mixed water column ($\triangle$0.7°C) was observed at a rate consistent with seasonal solar heat input at the sea surface. This was well-represented in numerical simulations for the same period, conducted using the two-equation $k - \varepsilon$ statistical turbulence closure model implemented in the General Ocean Turbulence Model (GOTM). Comparative observations conducted over a 12-day period in summer (August, 2012) identified significant advective control with warming (1.7°C) substantially outpacing the calculated solar heat input (0.5°C). Field work in summer presented vertical thermal gradients as a result of the seasonal stratification ($T_{top} - T_{bot} = 2.5$°C). The largest variability in stratification occurred over the neap-spring cycle; a breakdown in thermal stratification occurred during the transition to spring tides although the timing was controlled by strong surface forcing conditions which increased surface mixing and also advected well-mixed waters over the study site.

The passage of non-linear internal waves were observed along the seasonal thermocline during slack water, increasing shear and reducing the dynamic stability of the water column. These were likely to be generated by hydraulic control and released during the transition from sub-critical to super-critical

flow in the form of lee waves. Two packets of non-linear internal waves with a vertical displacement of the leading wave of 11 m and a period between successive troughs of approximately 23–36 minutes were recorded.

Microstructure profiles of derived turbulent dissipation sampled over 12.4 hour tidal cycles were conducted at both neap and spring tides in spring and summer. Results show bottom boundary layer mixing to be the primary control on the water column structure with a dominant M_2 tidal periodicity. The phase lag and tidal asymmetry observed was well reproduced by the 2-equation turbulence model. Phase lags were observed to increase with height above the bed with neap tides generating a larger phase lag at the top of the bottom boundary layer than at spring tides. The impact of a stratified water column was observed in the maximum height attained by the bottom boundary layer in summer although there was no observable increase in the phase lag in contrast to that reported in the literature. A lack of an internally stratified water column in the GOTM model meant that it did not reproduce the stratification effects on the growth of the bottom boundary layer. Turbulent dissipation levels in the numerical simulations also diverged from that observed in the interior supporting the notion of missing mixing mechanisms providing an additional source of turbulence to the shelf sea interior. The lack of interior mixing let to an over estimation in the strength of the thermocline in GOTM in comparison to the in-situ observations.

The findings of this study concludes that in weakly stratified shelf seas typical of the conditions presented at this study site, the primary mechanism controlling the vertical structure of the water column is the strength of the tidal mixing that varies significantly over the spring-neap cycle. Increased surface forcing from strong wind events potentially can tip the balance between a stratified and well-mixed water column through increased vertical mixing in the surface layer near the thermocline and by generating enhanced horizontal advection as well as baroclinic instabilities. This study reaffirms the necessity for shelf sea numerical models to correctly parametrise interior mixing under stratified conditions since the lack of mixing led to an over estimation in the strength of the thermocline. One candidate mechanism identified in this study with the potential to enhance interior mixing were non-linear internal lee waves generated by the topography in the vicinity of the study site.

Declaration

At no time during the registration for the degree of Doctor of Philosophy has the author been registered for any other University award without prior agreement of the Doctoral College Quality Sub-Commottee. Work submitted for this research degree at the Plymouth University has not formed part of any other degree either at Plymouth University or at another establishment.

Word count for the main body of this thesis: **49,600**

Signed: _____

Marcus Maximilian Zanacchi

Date: _____

Posters and conference presentations:

PRIMaRE 1st Annual Conference, 4–5th June 2014, *Plymouth, U.K.*, Poster Presentation: **Zanacchi, M.M.**, Hosegood, P., Schwarz, J., Torres, R., Cazenave, P., Cox, S., Does the Extraction of Energy from the Sea Surface Really Impact on Regional Physical and Biological Processes?

16th Biennial Challenger Society Marine Conference, 8–11th September 2014, *Plymouth, U.K.*, Poster Presentation: **Zanacchi, M.M.**, Hosegood, P., Schwarz, J., Torres, R., Cazenave, P., The Influence of Near-Surface Mixing on a Tidal Mixing Front in the Southern Celtic Sea.

PlyMSEF, 2nd February 2015, *Plymouth, U.K.*, Poster Presentation: **Zanacchi, M.M.**, Hosegood, P., Schwarz, J., Torres, R., The Tidal Mixing Front Off North Cornwall.

PlyMSEF, 11th February 2016, *Plymouth, U.K*, Poster Presentation: **Zanacchi, M.M.**, Hosegood, P., Torres, R., Investigating the Impact of Stratification on the Bottom Boundary Layer from In-Situ Observations.

A.G.U. Ocean Sciences, 28th February 2016, *New Orleans, U.S.A*, Poster Presentation: **Zanacchi, M.M.**, Hosegood, P., Torres, R., Investigating the Impact of Stratification on Turbulent Dissipation in a Marginally Stratified Shelf Sea.

Workshops Attended:

Coastal Ocean Processes Workshop, Chalenger Society for Marine Sciences, Liverpool, 25–26th March 2014.

This study was financed with the aid of a studentship from the Natural Environmental Research Council. Relevant scientific seminars and conferences were regularly attended at which work was often presented. Remotely sensed sea surface temperature data were provided by the NERC Earth Observation Data Acquisition and Analysis Service (NEODAAS). Sea surface radiative fluxes were obtained from the UK Meteorological Office Unified Model (v7.9) and reanalysis data were obtained from the European Centre for Medium Range Weather Forecasts (ECMWF).

Acknowledgements

I would like to firstly acknowledge the assistance and constructive guidance of my supervisory team; Dr Phil Hosegood, Dr Riccardo Torres, and Dr Jill Schwarz — thank you all for your patience and support. I am also deeply indebted to my colleagues, technical and marine staff whose time and effort were paramount to the collection of the observational data on which most of this work is based upon. To my friends and colleagues in the office, thank you for all the laughs, distractions, and moral support over the years. The enthusiasm and dedication to your work served as a daily reminder to why it is all so worth it in the end! Last, but by no means least, to my parents and all my family, I thank you from the bottom of my heart, for your encouragement and support in taking on this great endeavour.

Postscript

As I complete my PhD thesis, I look back at how far I have come in oceanography and recall the first time I sat down and seriously questioned the motion of the ocean. Well, in fact, I was lying down in our boat, so seasick that I never wanted to see the ocean again, ever! My thought was in that wretched moment; why was the sea surface constantly rolling towards me and why couldn't I make it stop.

Fast forward many years to my undergraduate degree and I vividly remember that moment of enlightenment when Dr Nimmo Smith described surface wave orbital motion and, furthermore, how it flattens near the seabed, resulting in a back-and-forth oscillatory motion. This was the link that transported me back to the time when Scuba diving, I wondered why the sea grasses only swayed back and forth with no apparent up and down motion (that I can still taste). In that moment, many years later, I realised that curiosity, observation and knowledge had come together to solve one of my life's greatest conundrums, and it was in that moment that I truly was content.

Now, I am grateful for the opportunity to dive deep into the enigmatic topic that is turbulence, observing the mysteries of the deep blue ocean and contributing in some small way to creating the linkages of knowledge that will benefit us all. As I once read in the vast array of literature out there, *"Turbulence is fluid motion unplugged!"*.

Contents

List of Figures

List of Tables

Nomenclature

Symbols

α	thermal expansion coefficient
β	haline contraction coefficient
c_p	Specific heat capacity of water
C_d	Surface drag coefficient
C_d	Bottom drag coefficient
ε	rate of dissipation of turbulent kinetic energy
ρ	density of seawater
g	acceleration due to gravity
h	water depth
j_b	Buoyancy flux
K_z	vertical eddy diffusivity
N	buoyancy frequency (Brunt-Väisälä)
Q	surface heat flux
R_ρ	density ratio
Re	Reynolds Number
Ri_g	gradient Richardson Number
S	vertical velocity shear
τ	wind stress
u, v, w	velocity components in x, y, z
U, V, W	mean current velocity components
W_{10}	wind speed at 10 m above sea surface

Abbreviations

ADCP	Acoustic Doppler Current Profiler
AVHRR	Advanced Very High Resolution Radiometer

BBL	Bottom Boundary Layer
BM-ADCP	Bed-moored ADCP
CTD	Conductivity, Temperature and Depth
DNS	Direct Numerical Simulations
FVCOM	Finite Volume Coastal Ocean Model
kHz	kilohertz
km	kilometres
LES	Large Eddy Simulations
MSS	Microstructure Sensor
NAO	North Atlantic Oscillation
nm	nautical miles
R.V.	Research Vessel
SST	Sea Surface Temperature
TKE	Turbulent Kinetic Energy
TW	terra watts

CHAPTER 1

INTRODUCTION

1.1 Background

The importance of turbulent mixing in shelf seas cannot be understated since it is the dominant mixing mechanism controlling the vertical structure of the water column. Turbulence is the energetic, vortical and eddying state of fluid motion, which promotes vigorous mixing and the transport of fluid properties (heat, salt and momentum) at rates far higher than that of molecular processes alone (Thorpe, 2005). Of particular interest to this study is the manner in which turbulence stirs shelf seas — the complexity of the various turbulent mixing processes, and their interactions, play an important role in controlling the vertical structure of the water column. This is particularly influential in temperate shelf seas where the seasonal changes in thermal stratification is primarily regulated by the competition between stabilising surface heat input and de-stabilising turbulent mixing processes (Simpson and Hunter, 1974; Garret et al., 1978; Loder and Greenberg, 1986; Simpson and Bowers, 1984).

In regions of dominant tidal stirring, such as the North-west European continental shelf (Simpson et al., 1978), the north-western Atlantic shelf (Loder and Greenberg, 1986), the Patagonian shelf (Glorioso and Simpson, 1994; Rivas and Pisoni, 2010), and East China Seas (Lee et al., 2015), tidal currents make up the largest proportion of kinetic energy input and generates significant turbulent mixing as it flows over the seabed (Simpson et al., 1981). To first order, it is the strength of the tidal current, in combination with the water depth, that determines the competition between the vertical extent of turbulent mixing and thermal stratification (Simpson and Hunter, 1974). Typically, stronger tidal currents are found with decreasing depth and hence, it is mostly the shallower waters that remain well-mixed whilst stratified regions lie further offshore. Additional turbulent mechanisms are situated near the surface, including: surface forcing arising from the wind and waves, Langmuir circulation and convection; and within the interior, by shear driven mixing, internal tides or hydraulic control near rough topography. Not only do these processes contribute to the competition for stratification but are also influential in controlling vertical fluxes, given their proximity to the surface boundary layer and thermocline region. As such, turbulent mixing is also largely responsible for producing the enhanced biological production found in shelf seas, primarily by driving vertical fluxes of nutrients, phytoplankton and oxygen across the seasonal thermocline (Sharples et al., 2001; Huisman et al.,

2004). Thus, turbulent mixing not only plays an important role in the physical regime but also in shelf sea biogeochemical processes too.

The boundary interface between the well-mixed and thermally stratified waters are known as shelf sea fronts. Frontal zones are usually distinguished by the large horizontal gradients in density as the thermocline isopycnals slope to the surface where there is an exact balance between surface heating and stirring. The sea surface gradients in temperature are clearly observed by satellite remote sensing which provides a convenient way of tracking fronts and following their evolution (Miller, 2011). Complex mixing processes are associated with shelf sea fronts which lead to increased turbulent mixing. For example, the influence of surface wind mixing and the spring-neap cycle have been observed to significantly control the position and intensity of fronts (Simpson and Bowers, 1981), as well as the effects of the Earth's rotation (Simpson and Sharples, 1994; Simpson and Tinker, 2009). Additional mixing along the thermocline, as a result of inertial stress or the internal tide, also contribute to mixing in shelf seas (Pingree and Griffiths, 1978; van Haren, 2000; Rippeth, 2005). Discontinuities in temperature and salinity set up density-driven baroclinic circulation with the most pronounced feature of the circulation being an along-front, near-geostrophic jets (Hill et al., 1993; Brown et al., 2003). Baroclinic instabilities in the frontal jet generate eddies that can pinch off and substantially contribute to the transfer of properties across fronts (Badin et al., 2009).

The physical dynamics driven by the balance between mixing and stratification is pivotal in determining the biological environment, especially for primary production in shelf seas (Huthnance et al., 2001; Sharples and Dye, 2008). Shelf sea fronts are associated with enhanced levels of primary productivity (Pingree et al., 1976; Tett, 1981). Known to be 'hotspots' for marine life, shelf sea fronts are spawning and feeding grounds for many species of fish, sea birds and marine mammals (Belkin et al., 2009; Cox et al., 2016b,a). Physical processes along the front including upwelling, surface convergence and cross-frontal exchanges promote the accumulation of nutrients, phytoplankton and zooplankton species (Bakun, 2006). Surface convergence along surface fronts can also lead to a concentration of pollutants and microplastics, thus endangering the marine organisms that preferentially feed there (Belkin et al., 2009; Thiel et al., 2011; Zhang et al., 2017). Furthermore, the onset of seasonal stratification in shelf seas triggers the annual spring bloom (Sverdrup, 1953).

The development of the thermocline restricts phytoplankton to the surface layer where they receive sufficient sunlight to multiply rapidly and provide the rest of the marine ecosystem the first significant supply of organic fuel following the winter months (Sharples and Dye, 2008). Following the spring bloom, productivity within the upper layer is maintained and redistributed by turbulent mixing processes supply and recycle nutrients up into the photic zone. New production over the summer is often observed to be highest in the thermocline region due to the flux of nutrients into the surface layer from below through diapycnal turbulent mixing; the result of which is commonly known as a subsurface chlorophyll maximum (Holligan, 1984; Sharples et al., 2001; Hickman et al., 2012). These mixing mechanisms are important for sustaining primary production throughout summer once the upper waters are depleted of nutrients during the spring bloom. Three candidate mechanisms for sustaining the diapycnal nutrient flux across the thermocline in shelf seas are internal waves, inertial motions and the spring-neap variability in tidal mixing (Sharples, 2008; Simpson and Sharples, 2012).

The impact of future changes in shelf sea stratification and turbulent mixing would be hugely consequential since, globally, shelf seas maintain a disproportionate significance on the ocean's biogeochemical cycles (Simpson and Sharples, 2012; Rippeth, 2005). Turbulence mixes cold, nutrient rich, waters upwards fertilizing the sunlit surface waters and enhances planktonic interactions, all the whilst promoting the high biological productivity observed in shelf seas (Ross and Sharples, 2008; Visser, 2011). Shelf seas are estimated to account for 15–30% of the total ocean biological primary production even though they make up only seven percent of the global ocean by area (Townsend et al., 1994; Muller-Karger et al., 2005). Furthermore, this disproportionately high productivity maintains over 90% of the global commercial fisheries (Pauly et al., 2002). The formation of seasonal thermal stratification, in conjunction with increasing sunlight and high nutrient concentrations, leads to the rapid growth of phytoplankton in the spring bloom (Sverdrup, 1953; Townsend et al., 1994). The high levels of primary production enable shelf seas to sequester 20–50% of atmospheric CO_2 through a mechanism referred to as the continental shelf pump (Tsunogai et al., 1999; Thomas et al., 2004). Temperate shelf seas are more efficient at sequestering carbon due to the formation of the seasonal thermocline which acts as a vertical transport barrier allowing the net export of CO_2 from the surface layer to the subsurface layers where it then may be transported on to the deep ocean (Wollast, 1998; De Haas et al., 2002; Thomas

et al., 2004). These processes are predominantly driven by vertical exchange across the seasonal thermocline and highlights the extensive impact turbulent mixing has on the global climatic significance and biological productivity of shelf seas (Howarth et al., 2002; Icarus Allen et al., 2004).

1.2 Motivation and Implications

In the past, attention has largely been focused on tidal mixing fronts, notably in the Irish Sea (Simpson and Hunter, 1974; Rippeth, 2005; Horsburgh et al., 1998, 2000). This has led to significant progress being made in understanding the turbulent dynamics that control stratification in shelf seas and has led to the development of the basic theory of the heating-stirring competition (Simpson and Hunter, 1974; Simpson et al., 1996; Scully and Friedrichs, 2007). The position of tidal mixing fronts can be adequately described by the ratio of the water depth to the cube of the tidal current strength ($SH = log_{10}h/u^3$), the Simpson and Hunter parameter (Simpson and Hunter, 1974; Simpson and Bowers, 1981). This is based on the simplest model in which only surface heating and tidal stirring is considered and has been validated for prominent tidal mixing fronts on the North-west European shelf (Pingree and Griffiths, 1978) and also in other temperate shelf seas (Garret et al., 1978; Bowman and Esaias, 1981; Bowman et al., 1983). Our good understanding of these regimes is reflected by our ability to accurately simulate their dynamics in numerical models (Holt et al., 2005; Burchard et al., 2008; Holt and Umlauf, 2008).

Yet observational and remote sensing efforts have since shown that, even in tidally-dominant temperate shelf seas, the existence of a 'web of ephemeral fronts' that exhibit non-tidal spatial and temporal variability suggests that a more complex and delicate balance exists between turbulent mixing and stratification (Figure 1.1). Such complex and variable behaviours are not confined to the North-west European shelf; high-resolution satellite oceanography and improvements in edge detection algorithms have allowed such patterns to be observed and recorded in shelf seas around the globe (Belkin et al., 2009; Lee et al., 2015; Belkin and Helber, 2015; Pisoni et al., 2015). These observations have led to the suggestion that, in regions where tidal mixing is comparatively weak, the relative importance of upper ocean mixing processes (e.g. wind stress and surface wave forcing), and other second-order turbulent mixing processes in the thermocline (e.g. internal waves and inertial motions) increase and in some case may even dominate (Simpson et al., 1978; Loder and

Greenberg, 1986; Castelao et al., 2010; Craig and Banner, 1994; Babanin and Haus, 2009).

The studies highlighted above suggest that a more detailed understanding of the key processes that govern turbulent mixing and restratification in marginally stratified shelf sea requires these second-order processes be recognised and developed upon. This notion is particularly relevant when considering state-of-the-art numerical models of continental shelf seas as was highlighted by Rippeth (2005) and Holt et al. (2005). A model study conducted by Holt et al. (2005) reported the over-estimation of autumn surface temperatures due to the late breakdown of seasonal stratification. The lack of inclusion of small-scale, non-local, mixing processes in this model study, especially in the upper mixed layer, were identified as possible reasons for the inaccuracies (Holt et al., 2005). These issues highlight the importance of the small-scale turbulent mixing mechanisms in providing an accurate representation of mixing in shelf seas. These short-comings have a consequential effect on biological modelling capabilities and climate research (Prestidge and Taylor, 1995; Sommer and Lengfellner, 2008; Sharples et al., 2010). So far, intensive observations have led to a better understanding of the role of small-scale processes in shelf seas (Moum et al., 2008). These observational efforts have led to improved quantitative assessments of turbulence closure models in such scenarios as the tidally mixed Celtic Sea (Simpson et al., 1996), the bottom boundary layer turbulence on the Oregon shelf (Kurapov et al., 2005), and have also contributed to the suggestion of alternate, improved, turbulence parameterizations (MacKinnon and Gregg, 2003a).

The physical, biological and economic well-being of shelf seas continues to be of significant importance in relation to possible future climate scenarios. Under a 'business as usual' medium future emissions scenario (A1B — IPCC-SRES, 2000), European shelf sea water temperatures are expected to rise by between 1.5 and 4°C, and develop stronger stratification ($\sim$20%), with substantial consequences for the physical and biological environment (Lowe et al., 2009; Holt et al., 2010). There is already substantial evidence for this observed warming over the past decades based on remote sensing (Gómez-Gesteira et al., 2008) and long-term monitoring (Dye et al., 2013). Strengthening stratification reduces the vertical mixing efficiency thereby inhibiting the flux of nutrients required to sustain the biological productivity in the upper layer photic zone. Sharples et al. (2006) and Young and Holt (2007) have also reported a trend

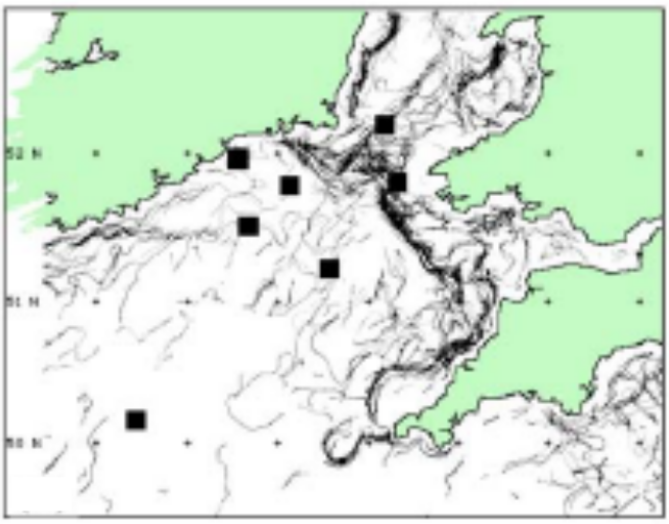

Figure 1.1: *A composite front map derived from AVHRR satellite estimates of temperature in the Celtic Sea (30 April–8 May 2000). Adapted from (Pemberton et al., 2004). The composite front map was derived from frontal metrics described in (Miller, 2009))*

towards an earlier onset of the spring bloom in European shelf seas mainly due to warming air temperatures increasing stratification early on in spring. Extended periods of stratification have been shown to have serious negative effects on shellfish populations below the thermocline, due to a reduction of food supply and in extreme cases oxygen depletion (Dolmer, 2000). Further evidence suggests that long-term changes in salinity are occurring, although the short-term, year to year, variability tends to dominate the signal (Holt et al., 2010). It is anticipated that this study will contribute towards our understanding of turbulent mixing processes in order to better model shelf sea systems in light of the predicted changes in shelf seas (Sharples et al., 2010).

1.3 Study Aims & Objectives

The aim of this study is to quantify the sensitivity of marginally stratified shelf seas to the key processes that govern turbulent mixing and contribute to the evolution of the water column in a manner not consistent with tidally-driven bottom boundary layer mixing alone. In order to accomplish this, the study primarily makes use of observational data, complemented with both modelled and remotely sensed data, collected in a marginally stratified shelf sea region off the north coast of Cornwall, UK.

The objectives of this study were to:

- collate and use in-situ observations to determine the hydrodynamics of the study site including: full water-column current field; turbulent dissipation rates, temperature, salinity and density structure; surface wave field; surface wind field.
- determine the spatio-temporal structure of the surface front at the study site using in-situ observations and satellite remote sensing.
- identify the vertical mixing regime arising from tidal friction and other second-order mechanisms.
- test the results from the observations in the 1-dimensional General Ocean Turbulence Model (GOTM) to detail the importance of each mechanism.

1.4 Study Location — the Celtic Sea

This research is primarily based in the southern Celtic Sea and upon observational data collected in the proximity of a shelf sea front (Figure 1.2). The chosen study site was relevant to the research as a transient front forms in spring and has been observed to persist through to autumn (Dietrich, 1951; Pingree and Griffiths, 1978; Miller, 2009).

The Celtic Sea is a dynamic, mid-latitude, shelf sea on the NW European Shelf that is controlled by a dominant seasonal heating cycle, tides, atmospheric fluxes, riverine inputs and cross-shelf exchanges with the open ocean. It is subjected to intense fishing activity as it contains many important commercial species of fish and crustaceans (Hardisty, 1990; Pemberton et al., 2004).

The study region was situated approximately 18 km offshore of St Ives, off the north coast of Cornwall. Within the study region, the presence of thermal and the associated chlorophyll fronts have been reported in both observations (Pingree and Griffiths, 1978) and model studies (Fearnhead, 1975; Holt and Umlauf, 2008). Advanced Very High Resolution Radiometer (AVHRR) sea surface temperature (SST) imagery, from the time of data collection (August, 2012), clearly show the presence of sharp horizontal gradients in temperature that align with those reported in the literature (Figure 1.2). The region has an average sea surface temperature (SST) of approximately 8-10 °C in February and 16-17 °C in August (Uncles, 2010). Figure 1.2 inset presents the SST from

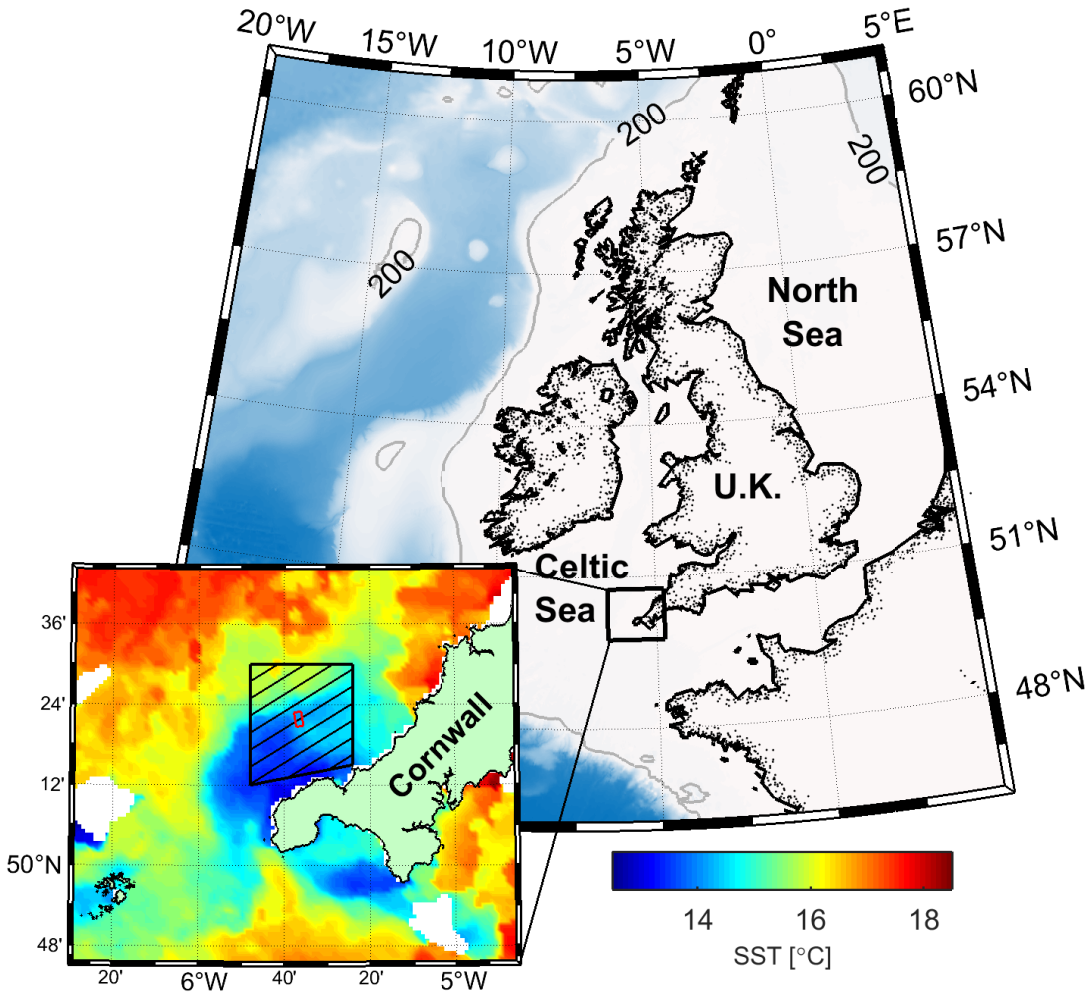

Figure 1.2: *The Northwest European shelf. Inset: seven day composite SST (03-09/08/2012) from AVHRR of the study region showing the area of study (hatched) and the location of the Wave Hub, a renewable wave energy generation site (red polygon).*

August, 2012, with offshore, warm waters reaching 18°C whereas inshore of the frontal region temperatures were 4 °C cooler. Recent observations, through in-situ measurements and satellite remote sensing, have identified spatio-temporal variability that is not consistent with tidal periodicity alone. The hypothesis is that the transient front responds readily to surface forcing due to its exposure to the Atlantic Ocean in a manner similar to that observed by Wang et al. (1990) in a model study of the Celtic front.

The Celtic Sea experiences the same regional atmospheric conditions as South-

ern England. Wind speed and direction generally depends on the positioning of the high and low pressure systems with the wind blowing parallel to the isobars in geostrophic balance. The pressure gradient is usually steeper in winter with a mean wind speed of 5 m s^{-1} from the west-south-west. Summer time atmospheric conditions are generally weaker and have a mean wind speed of 2.5 ms^{-1} from the west (Pingree, 1980). This region is exposed to the North Atlantic Ocean from a westerly and south-westerly direction. Consequently, the fetch[1] may be up to 6,000 km long and swell conditions are generally large in comparison to the southern coast of Cornwall. Southern Ireland provides the region protection from a north-westerly direction. In this instance the fetch is reduced to 200 km across the Celtic Sea (Hardisty, 1990).

The tidal range in this region of the Celtic Sea is 5.8 m (Ashton et al., 2013). Tidal flows in the vicinity of the study site have peak current speeds of 1.2 ms^{-1} and are predominantly orientated south-west — north-east during the flood tide and vice versa during the ebb (Ashton et al., 2013). The majority of the currents are tidally driven, although horizontal density gradients play an important role in residual flows that are particularly present during the summer and autumn (Holt and Proctor, 2008). The salinity in the study region remains relatively constant over the short-term, due to no significant sources of fresh water land drainage nearby. Considerable inter-annual variability due to increased rainfall in winter does also occur (Dye et al., 2013). The bathymetry at the study site is relatively smooth, gradually deepening to the north-west out towards the middle of the Celtic Sea.

The study site lies within the vicinity of a test site for marine renewable energy — the Wave Hub (Hub, 2006). Recently, governmental bodies, the scientific community and general public have become increasingly concerned with the state of shelf seas in a changing environment (Sommer and Lengfellner, 2008; Holt et al., 2010; Reeve et al., 2011; Frost et al., 2012). The potential for over-exploitation of the Celtic Sea, combined with an uncertain future climate, provide a strong motivation to fully understand the physical and biological shelf sea environment before irreversible changes occur. The growth of marine renewable energy extraction is largely based upon the energy extracted from shelf sea waters (Witt et al., 2012; Carpenter et al., 2016). Studies suggest that future large-scale developments of offshore wind farms could have significant impacts on the distribution of stratification by changing the vertical mixing

[1]The uninterrupted straight-line distance over which sea surface swell is generated.

regimes due to the installation of turbine structures in shelf seas (Carpenter et al., 2016). This argument may be extended to other forms of renewable energy extraction such as wave energy devices proposed for the Wave Hub site. It is hoped that the results of this study may consequently guide our actions when harnessing the natural resources of shelf seas.

1.5 Thesis Outline

This thesis incorporates the following chapters: Chapter 2 outlines the relevant background theory and reviews the literature in relation to this research; Chapter 3 describes the methods and instrumentation involved in the fieldwork and describes the numerical model used in this study. Chapter 4 investigates the seasonal and neap-spring variability observed during fieldwork while Chapter 5 investigates the vertical structure of the water column at the study site and identifies the turbulent mixing mechanisms present. The numerical modelling simulations are described in Chapter 6, and finally, the results are summarised, discussed and conclusions made in Chapter 7.

CHAPTER 2

The Turbulent Dynamics of Seasonally Stratified Shelf Sea Regions

This chapter reviews the physical dynamics that are intimately linked to marginally stratified shelf sea regions. The focus of this research is the influence of turbulent mixing and re-stratifying processes in marginally stratified shelf seas that have lately been identified to be of greater importance in determining the vertical water column structure, especially where the dynamics are not dominated by tidal mixing alone (Rippeth, 2005; Rippeth and Meier, 2005).

We firstly introduce the statistical approach to turbulence in context of reviewing mechanisms that bring about the production, mixing and dissipation of turbulent kinetic energy (TKE) in shelf seas. Secondly, the vertical mixing regimes that characterize both well-mixed and stratified regions are described along with conditions required for frontogenesis — fronts are conditioned by the physical dynamics and provides an identifiable delineation between different mixing regimes on either side of the boundary. Finally, focus is on the vertical structure of turbulent mixing in the water column. The water column is divided into three identifiable sections: tidally-generated frictional mixing originating in the bottom boundary layer (BBL), internal mixing along the pycnocline in stratified conditions and surface mixing generated by wind and wave forcing.

2.1 Turbulence in Shelf Seas

Turbulence is characteristically energetic and distinguished by chaotic, vortical, eddy-like structures, embedded in one another with different sizes and strengths that gives a highly irregular appearance to the background flow (Cushman-Roisin and Beckers, 2011). Turbulent flows are also incorporated over a wide range of scales; from the macro-scale that contains most of the energy for turbulence production, to the smallest micro-scales where turbulent energy is dissipated into heat through viscosity. The actual scales are relative and the upper limit is determined by the energy-containing eddies, $\mathcal{O}(m)$, whereas dissipation occurs by molecular friction at the smallest scales of $\mathcal{O}(\leq mm)$ in turbulent regions (Thorpe, 2005). The complex interactions across the large range of scales involved make the instantaneous turbulent fluctuations inherently difficult to measure and quantify except for in a highly idealised and statistical manner.

The underlying assumption in the statistical approach is that the random

turbulent fluctuations at the turbulence micro-scale are proportional to the non-random, larger scale gradients that can be measured or modelled. This allows the variance of a measured quantity, such as current velocity or the temperature field, to be related to the turbulent kinetic energy with a parameter of proportionality — the turbulent eddy viscosity — which is related to the strength of the stirring (Burchard et al., 2008). Since it is the resulting dynamical effect of turbulence that is of interest in shelf sea mixing, and not the individual turbulent motions themselves, we can afford to treat turbulent interactions in a statistical manner.

All Newtonian fluid motion, including turbulent flows, may be accurately described by the Navier-Stokes equations. The Navier-Stokes equations for an incompressible fluid with constant density, ρ, and constant kinematic viscosity, ν , in generalised form is:

$$\frac{\partial \mathbf{u}}{\partial t} + \mathbf{u} \cdot \nabla \mathbf{u} = -\frac{1}{\rho}\nabla P + \nu \nabla^2 \mathbf{u} \qquad \nabla \cdot u = 0 \tag{2.1}$$

with $\nabla \cdot u = 0$ being the continuity equation denoting incompressibility in the flow. Here, $u(x,t)$ is the fluid velocity field and $P(x,t)$ is pressure. The LHS of Equation 2.1 is the sum of the Eulerian and non-linear advective accelerations. The RHS is the sum of the pressure and viscous dissipative forces per unit mass per unit volume. The Navier-Stokes equations describe the rate of change in momentum and are fully deterministic; once the initial velocity field and boundary conditions are specified the evolution of the flow field is completely determined (for a fuller derivation, see Pope (2000)).

The transition of a fluid's motion from a linearly uniform laminar flow to an fully developed turbulent flow may be determined by comparing the turbulence-producing, non-linear inertial term ($u \cdot \nabla u$) to the turbulence-dampening, viscous dissipation term ($\nu \nabla^2 u$) in Equation 2.1, and relating them by the non-dimensional Reynolds number (after Simpson and Sharples (2012)):

$$Re = \frac{non-linear}{viscous} = \frac{u \cdot \nabla u}{\nu \nabla^2 u} \approx \frac{u^2/L}{\nu u/L^2} \approx \frac{UL}{\nu} \tag{2.2}$$

where U is the characteristic velocity scale, L, the characteristic length scale, and ν, is the characteristic viscosity (water: 1×10^{-6} m^{2}s^{-1}). For $Re << 1$, the non-linear terms in the Navier-Stokes equations may be neglected and

the fluid flow is laminar. However, when $Re >> 1$, the non-linear terms are responsible for the highly fluctuating turbulent flow field in space and time. However, the transition from laminar to turbulent flow depends on the particular geometry of the flow and the nature of the perturbations and as such may not be assigned a critical value. Typically, oceanic flows remain in a laminar state up to a Reynolds number of 1×10^4 due to density stratification (Thorpe, 2005). Nevertheless, the majority of current flows in shelf seas are turbulent since Reynolds numbers for the characteristic velocities (0.1–1 m s^{-1}) and length scales (10–100 m) exceed 1×10^4 (Thorpe, 2005).

Turbulence may be mathematically expressed by the Reynolds decomposition, $F = \langle F \rangle + F'$, whereby any time-dependent variable, F, is expressed as the sum of a mean quantity, $\langle F \rangle$, and a turbulent component, F' (Figure 2.1). The statistically coherent turbulent fluctuations can be quantified in the form of Reynold-averages — ensembles over a period longer than a singular random fluctuation but shorter than the time-scale of the mean flow. Thus, the energy contained in the turbulent fluctuations, the turbulent kinetic energy, k, is quantified as the variance of the velocity fluctuations:

$$k = \frac{1}{2}(\overline{u'^2} + \overline{v'^2} + \overline{w'^2}) \tag{2.3}$$

where $\overline{u'}$, $\overline{v'}$, $\overline{w'}$ are a statistically coherent Reynold-average of the orthogonal turbulent components of velocity in a Cartesian coordinate system.

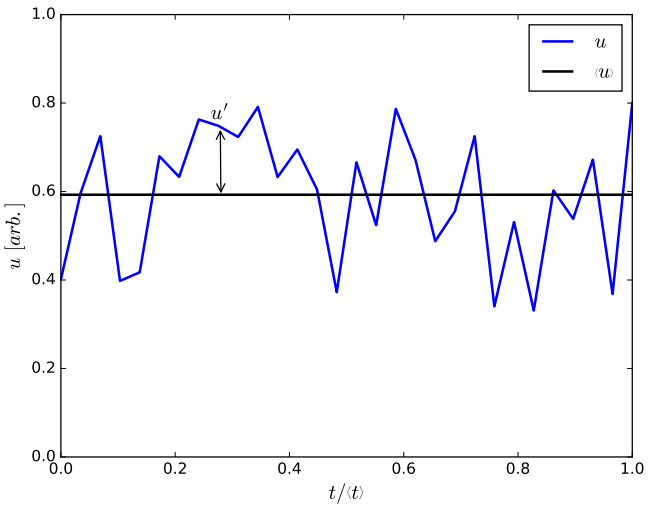

Figure 2.1: *Schematic describing the Reynold's decomposition of a velocity field, u, into its mean, $\langle u \rangle$, and fluctuating components, u'.*

Turbulent kinetic energy is extracted from the mean flow by turbulent shear production or convective instability and transferred down to smaller scales where energy is lost to mixing (buoyancy production) or dissipation. By considering a local equilibrium of turbulence in a steady state the time evolution of TKE consists of the following terms (after Simpson and Sharples (2012)):

$$\frac{\partial k}{\partial t} = \underbrace{\frac{1}{\rho_0}(\tau_{xz}\frac{\partial u}{\partial z} + \tau_{yz}\frac{\partial v}{\partial z})}_{shear\ production} - \underbrace{\frac{g\rho' w'}{\rho_0}}_{mixing} - \underbrace{\varepsilon}_{dissipation} \tag{2.4}$$

where t is time, z is depth, ρ_0 is the mean density, τ are the Reynolds shear stresses, and g acceleration due to gravity. The shear stresses in the TKE production term stem from the Reynold-averaged Navier-Stokes equations and describe the covariance of the turbulent fluctuations and are responsible for the vertical transport of turbulent momentum:

$$\begin{aligned} \tau_{xz} &= -\rho\overline{u'w'} \\ \tau_{yz} &= -\rho\overline{v'w'} \end{aligned} \tag{2.5}$$

These turbulent fluctuations are inherently difficult to solve and requires multiple undetermined coefficients for the higher-order moments which are too computationally expensive to solve except in Direct Numerical Simulations[1]. Hence, the common and long standing statistical method is to relate these non-linear turbulent fluxes to the small-scale gradients in fluid properties (i.e. momentum) with the use of an eddy viscosity (ν_t):

$$\begin{aligned} \tau_{xz} &= \rho\nu_t\frac{\partial u}{\partial z} \\ \tau_{yz} &= \rho\nu_t\frac{\partial v}{\partial z} \end{aligned} \tag{2.6}$$

Scalar quantities, such as temperature and salinity, are treated in a similar manner except though requiring a different parameterization coefficient, which is referred to as an eddy diffusion coefficient, ν_t'.

The second term in Equation 2.4 relates the rate at which turbulent motions increase the potential energy through vertical mixing. Mixing extracts energy

[1]DNS modelling solves the Navier-Stokes equations for all physically important scales; from the largest turbulent eddies to the dissipation scales. It is extremely computationally expensive and currently unfeasible for shelf sea scenarios.

from the turbulence since work is done in raising the potential energy of the system by conversion of the turbulent kinetic energy.

The third term in Equation 2.4 is the turbulent dissipation term, ε, which causes the irreversible transfer into heat energy by viscous dissipation at molecular levels (Equation 2.7).

$$\varepsilon = \nu \overline{\frac{\partial u_i'}{\partial x_j}\left(\frac{\partial u_i'}{\partial x_j} + \frac{\partial u_j'}{\partial x_i}\right)} \tag{2.7}$$

where ν is the kinematic viscosity of seawater (10^{-6} m^2 s^{-1}), and i, j are tensor notation used for brevity to sum the three components of velocity (u, v, w) over three spatial coordinates (x, y, z). The overbar denotes the ensemble average of velocity fluctuations.

Under the simplifying assumption that the turbulence is isotropic, i.e. the turbulence has no preferred orientation and is the same in all directions at the smallest scales, the dissipation term may be reduced from 12 terms (Equation 2.7) to one (Equation 2.8) (Batchelor, 1953):

$$\varepsilon = 7.5\nu(\overline{\frac{\partial u}{\partial z}})^2 \tag{2.8}$$

where ν is the kinematic viscosity of the water. The assumption of isotropic turbulence is a tentative subject especially under stratified conditions where the turbulent dynamics are modified. The effects of stratification can be parameterized by the non-dimensional ratio $\varepsilon(\nu N^2)^{-1}$, where N is the buoyancy frequency (Stillinger et al., 1983). Investigation by Yamazaki and Osborn (1990) found that for a value of $\varepsilon(\nu N^2)^{-1} > 20$, dissipation estimates obtained from the anisotropic formula compare favourably to that from the isotropic formula. For decreasing values of $\varepsilon(\nu N^2)^{-1}$, the errors increased but were limited to less than 35% in oceanic pycnoclines and hence it is concluded that ε is sufficiently well described by the isotropic formula (Stips, 2005).

Studies have shown that at sufficiently high Reynolds numbers, turbulence has a universal spectrum and the transfer of energy from production scales to dissipative scales was proposed by Kolmogorov (1991) to act as a series of interactions of turbulent eddies of decreasing size (Figure 2.2). The smallest scale at which viscous forces start to dissipate the turbulent energy is known as the Kolmogorov length scale and describes the size of the smallest possible

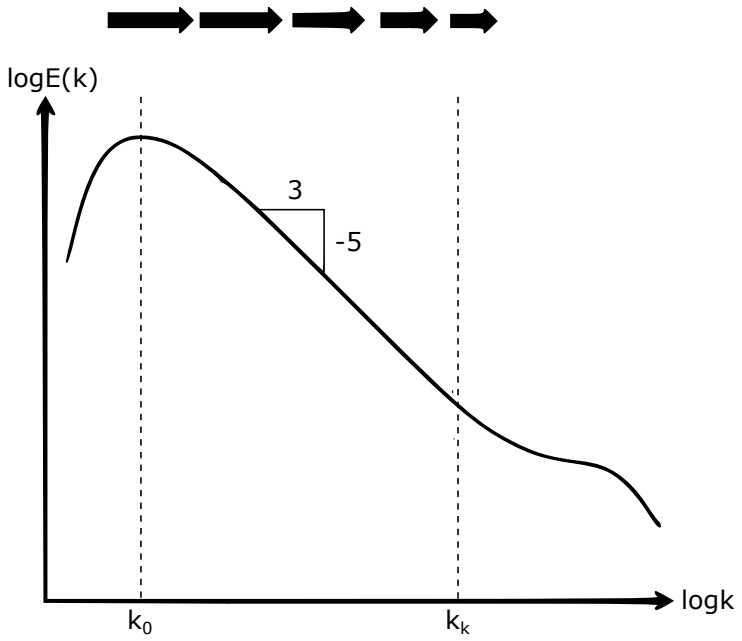

Figure 2.2: *Idealized energy spectra showing the cascade of energy in the direction of arrows from the large-scale turbulent eddies wavenumbers, k_0, to the dissipation wavenumber, k_k. The Kolmogorov $-5/3$ power law is annotated in the inertial sub-range ($k_0 << k << k_k$). Schematic adapted from Heinz and Roekaerts (2001).*

eddies in the flow (after Thorpe (2005)):

$$k_k = \left(\frac{\nu^3}{\varepsilon}\right)^{1/4} \tag{2.9}$$

The transfer of energy illustrated in Figure 2.2 is referred to as the 'energy cascade' and within the spectrum there is a viscosity independent, inertial subrange ($k_0 << k << k_k$) that takes the characteristic form:

$$\Phi_{(k)} = \alpha\varepsilon^{2/3}k^{-5/3} \tag{2.10}$$

where $\Phi(k)$ is the spectral kinetic energy density, $\alpha = 1.5$ is a universal constant, k is the wavenumber ($k = 2\pi/eddy\ diameter$).

An important implication of the universal spectrum and inertial subrange argument is the applicability of local isotropy, in which the small-scale turbulence structure is isotropic even when the large-scale structure is not (Luznik et al., 2007). This is an important concept that allows the turbulent kinetic energy to be derived from measurements in single directions, since simultaneous measurements in three dimensions are often impractical, and allows estimates

of ε to be obtained from observed velocity spectra from microstructure profilers (Thorpe, 2005). The measurement of isotropic turbulence from microstructure profilers is discussed in detail in Section 3.2.1.

2.1.1 The Boundary Region — Tidal Mixing Fronts

In shelf seas, the dominant forcing mechanism is the oscillatory flow driven by the barotropic tides. The strength of turbulent mixing generated by this oscillatory flow fluctuates in time, regulated by the periodicity of the tidal flow.

Tidal mixing fronts mark the boundary between well-mixed waters and the stratified waters (Figure 2.3). The frontal region is characterized by strong horizontal density gradients that may be observed in the sea surface temperature signature (Miller, 2009), or salinity in regions of fresh water influence (Simpson, 1997; Simpson et al., 2002).

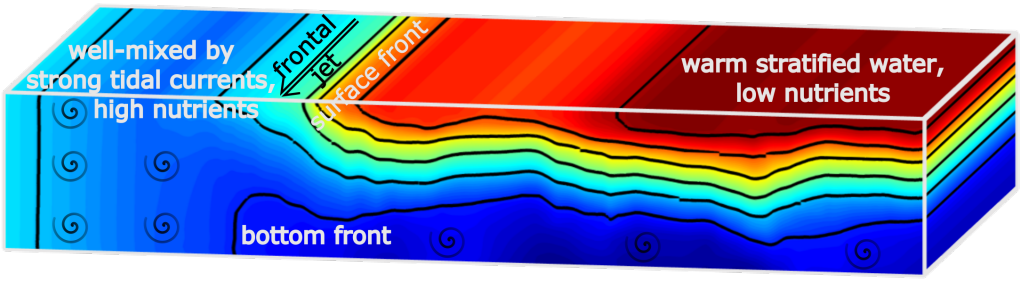

Figure 2.3: *Schematic of a shelf sea tidal-mixing front. The background cross-section is a temperature transect obtained at the study site. Annotations are overlaid describing the variation in physical dynamics and properties between well-mixed (LHS) and stratified (RHS) regions.*

Shelf sea fronts on the Northwest European continental shelf have been surveyed and documented since early on in the 20th century by Matthews (1911) who identified stratified and well-mixed regions in the Irish sea, and later on by Dietrich (1951), who suggested the importance of tidal currents in controlling mixing. It was not, however, until the use of numerical modelling (Pingree and Griffiths, 1978) and infrared satellite imagery (Simpson and Bowers, 1981) that tidal mixing fronts were identified as persistent features in summer on the Northwest European shelf. There have since been further studies on the Northwest European Shelf (van Aken et al., 1987; Hill et al., 1993; Horsburgh et al., 2000; Brown et al., 2003; Simpson et al., 2009; Le Boyer et al., 2009), and also in other shallow mid-latitude shelf seas, including, the Gulf of Maine and

Georges Bank (Loder and Greenberg, 1986), South China Sea (Shi et al., 2015), and in the southern hemisphere in the Tasman Sea (Badin et al., 2009), greater Cook Strait (Bradford et al., 1986) and on the Patagonian shelf (Glorioso and Simpson, 1994; Rivas and Pisoni, 2010).

The approximate location of these fronts were shown to be predicted quantitatively by Simpson and Hunter (1974), in the energy argument (Qh/u^3) that describes the competition between the buoyancy input from surface heating (Q) and water depth (h) versus tidal mixing (U). Within a regional context, the rate of heating may be taken as constant and therefore the argument is further simplified to (h/u^3), in which the water depth and strength of the tidal current determines the water column structure. This leads to the basic premise that inshore, shallower, regions with strong tidal currents are well-mixed since intense turbulent mixing is generated and overcomes the stratifying influence of surface heating in summer, while deeper, offshore, waters have weaker tidal currents and remain stratified due to surface heating in summer. The location of tidal mixing fronts are predicted to occur at a critical value of h/U^3 for each shelf sea region — these are often quoted as $log_{10}(h/U^3)$ due to the wide range of values for different shelf seas. In general, these values vary only slightly within a shelf sea and the critical value applicable to the Celtic Sea and the NW European shelf is $log_{10}(h/U^3) = 2.7 \pm 0.4$ (Simpson and Sharples, 1994). This parametrization has since been well-tested against observational data and found to be in good agreement in locations that have predominantly strong tidal currents on the European continental shelf (Hill et al., 2008; Holt and Proctor, 2008). It has also been successfully tested in the Gulf of Maine (Garret et al., 1978), the Bering Sea (Schumacher et al., 1979) and in Long Island Sound (Bowman and Esaias, 1981). The h/u^3 parameter forms the basis of the energy argument in tidal-mixing fronts.

There have since been a number of variations to the h/u^3 parameter put forward by various authors in recognition of the additional mixing mechanisms available, although their contribution to the vertical mixing in shelf seas is not fully understood. Simpson et al. (1978) suggested wind mixing as an extra stirring parameter to h/u^3. Subsequent results with the inclusion of the wind mixing parameter were positive with Bowers and Simpson (1987) reporting a better fit to observed frontal location in water depth of less that 50 m. The rate of mixing is quantified by the mixing efficiency which is the ratio of the buoyancy flux to the dissipation and estimated between 0–0.2 depending

on the mixing mechanism and its proximity to stable density stratification (Simpson and Sharples, 2012). Simpson et al. (1978) estimated the tidal mixing efficiency in shelf seas to be 0.0037, while wind mixing efficiency was estimated to be 0.023. The higher wind mixing efficiency is related to the proximity of the wind stirring power to the pycnocline in the upper water column. Empirical estimates of mixing efficiencies from internal wave mixing along the thermocline was 0.056 (Stigebrandt and Aure, 1989). The choice of mixing efficiency is somewhat arbitrary and based on empirical results (i.e. tidal mixing efficiency was calculated as 0.0028 in Simpson et al. (1977)). Simpson et al. (1981) modelled the seasonal cycle stirred by wind and tides with fixed mixing efficiencies. They found that the spring-neap adjustment was overestimated and that a feedback term that allowed for the effects of increased stratification at neap tides provided a better fit of the spring-neap adjustment. This highlights the influence of existing stratification on inhibiting vertical mixing and the overall buoyancy field dependence of mixing efficiencies (Holford and Linden, 1999).

An additional control to the heating-stirring competition first suggested by Garret et al. (1978) and Stigebrandt (1988) introduces the effect of rotation in limiting the vertical extent to which theboundary stresses penetrate the water column. They suggest that in addition to Qh/u^3 control, the height of the boundary layer depends on the Ekman layer depth and hence frontal position would follow a critical value of fh/u_*, where f is the Coriolis parameter, and $u*$ is the friction velocity. However, given the predominance of tidal currents in shelf seas, Soulsby (1983) showed how both the oscillatory nature and rotational aspects of the currents are important. Oscillatory tidal motions under the influence of the Earth's rotation cause tidal currents to trace out elliptical patterns that may be decomposed into clockwise and anti-clockwise circular components as is shown in Figure 2.4 following Prandle (1982). Both the phase and direction of the current vary with height, causing time dependent veering in the vertical current profiles.

For conditions typical of fronts in the European shelf seas, Simpson and Sharples (1994) conducted a series of numerical experiments of vertical mixing with a 1-D model that included the effects of rotation and concluded that for anticlockwise rotation (polarity (P) $>$ 0.3), the effects of rotation on the bottom boundary layer should reduce the level of mixing and move the front to lower h/u^3 (i.e. stronger tidal currents required). Their results also show

that for rectilinear tidal currents there is only a small displacement and for clockwise rotating currents, the frontal position is well described by the h/u^3 parameter. Further observations from two oppositely polarized locations in the Celtic Sea confirm the model results and describe a limited BBL in the case of anticlockwise rotation (P $\approx +0.6$) in clear contrast to the extended BBL observed at the clockwise rotating site, P ≈ -0.6, (Simpson and Tinker, 2009).

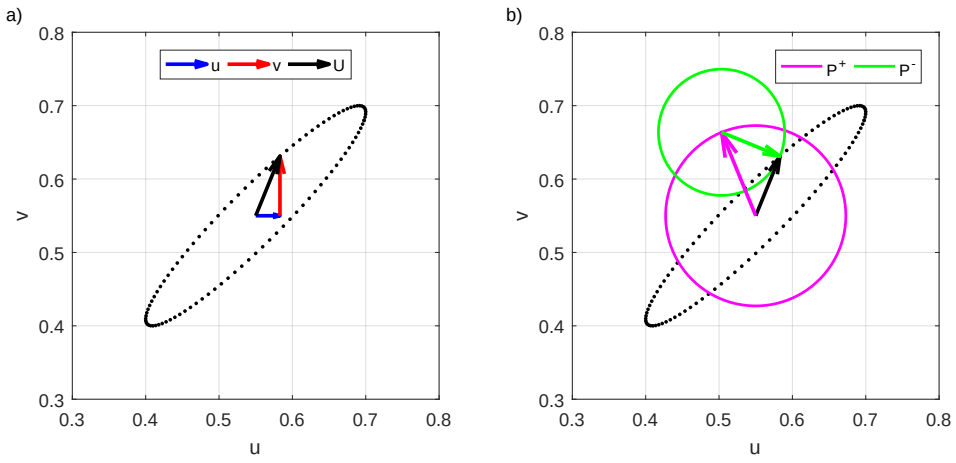

Figure 2.4: *Schematic showing the decomposition of velocity vector in $u - v$ plane (a) into cyclonic and anti-cyclonic components (b) following Prandle (1982). a) the elliptical path (black dotted) traced by the oscillatory tidal current,U, may be decomposed into u and v vectors. b) The same oscillatory tidal current, U, is shown in terms of cyclonic (P^+) and anti-cyclonic components (P^-).*

Tidal-mixing fronts have a typical horizontal cross-front length of $\leq$10 km and along-front length of $\geq$100 km (Badin et al., 2009). The horizontal cross-front density gradients associated with the front set up a quasi-geostrophic frontal jet that flows along the front. These jets are reported to have velocities in the order of 0.15 ms^{-1} (Hill et al., 1993). A study by Hill et al. (1997) identified a cyclonic gyre along a bottom front in the Celtic Sea with flow speeds of 0.09–0.2 ms^{-1}. Similarly, Horsburgh et al. (1998) identified a jet associated with the strongest density gradients at the bottom of the Celtic Sea tidal-mixing front. These residual circulation patterns have been identified in modelling studies of the Irish Sea (Horsburgh et al., 2000). A secondary circulation cell is also formed perpendicular to the front and frontal jet. This circulation generates upwelling on the mixed side and downwelling on the stratified side. This circulation pattern results in surface convergence which creates surface slicks and the accumulation of biomass on the sea surface. Additionally, baroclinic instabilities may form small mesoscale eddies of 2-4 km that last for between

1-6 days depending on frontal intensity (Badin et al., 2009). These eddies can favour biological production as they facilitate the lateral transfer of nutrients across the front. These eddies have been reported in the Ushant front in the southern Celtic Sea (Pingree and Griffiths, 1978).

2.1.2 The Well-mixed Regions

A comprehensive measurements of a well-mixed location in a well-mixed regime was made by Simpson et al. (1996) in the Irish Sea. The tidal currents were at maximum approximately 1 m s^{-1} at the time of measurements and the tidal ellipse was degenerate. The turbulent dissipation rates were measured over a 25 hour period using a microstructure profiler and presented a typical tidally driven BBL. Maximum values were 10^{-4} W m^{-3} within the BBL, close to the bed. Dissipation rates were closely related to the phase of the current and with maximum values occurring during maximum current velocities. A quarter-diurnal variation in dissipation rates was clearly distinguished. An increasing phase lag with height above the bed was reported and in the well-mixed site, the phase lag was 1.8 hours at a height of 30 m above the bed (HAB). Similar phase lags in maximum dissipation rates with height above the bed were reported by Burgett et al. (2001) on the Georges Bank.

2.1.3 The Stratified Regions

Similar tidal cycles of dissipation measurements were made in a stratified location in the Irish Sea by Simpson et al. (1996) and, in contrast to the well-mixed site, the height of elevated dissipation rates within the BBL were inhibited to 20-30 mab by a thermocline, above which dissipation rates were significantly reduced. Diapycnal mixing across the thermocline was highlighted by Sharples et al. (2001) to be an important mechanism for the transfer of nutrients into the euphotic zone, and is required to sustain the subsurface chlorophyl maximum which is observed to persist throughout the summer period. Thermocline mixing arises from shear instability in the currents, either by internal wave breaking (Sharples et al., 2001; Rippeth and Inall, 2002), or near-inertial oscillations from changes in wind direction or forcing (van Haren et al., 1999).

The water column stability may be quantified by the gradient Richardson Number:

$$Ri_g = \frac{N^2}{S^2} \tag{2.11}$$

where, N, is the buoyancy frequency, S shear frequency. which indicates the potential for shear instabilities to overcome the stabilizing influence of stratification. For values less than 0.25, shear instability and internal wave breaking results in turbulent mixing. Gradient Richardson numbers of $Ri < 1$ were found in shelf sea summer stratification by van Haren et al. (1999), suggesting that the shelf sea thermocline remains at marginal stability, and the inclusion of near-inertial current shear and internal wave breaking are important mixing mechanisms in shelf seas. Further evidence for thermocline mixing in the Celtic Sea was given by Rippeth et al. (2005), where enhanced turbulent dissipation within the thermocline corresponded to regions of low Ri_g.

Internal waves generated by flow instability and turbulence were found to be generated along the density interface and changed direction during the tidal cycle. van Haren et al. (1999) suggest that in the North Sea internal wave breaking to be responsible for the nutrient flux into the near-surface layer which is associated with a phytoplankton bloom 4-5 days later. The effects of stratification were also seen in observations from the western Irish Sea (Simpson et al., 1996). Here, the thermally stratified site had lower observed levels of dissipation in comparison to a similar well-mixed site. When compared to results obtained from a one-dimensional turbulence closure model (Mellor-Yamada 2.0) significant deviations of dissipation rates were found mid-water column. These were attributed to processes not included in the model, namely the effect of internal wave breaking. Burchard et al. (1998) compared two turbulence closure models (Mellor-Yamada 2.0 and $\kappa - \varepsilon$) and also concluded that for stratified conditions in the Irish Sea the models required internal wave parametrisation to correctly predict the observed levels of turbulent dissipation.

2.2 The Vertical Structure of Turbulent Mixing in Shelf Seas

Oceanic boundary layers describe a region in proximity to an interface, such as the sea surface or the seabed, in which the presence of the boundary directly influences fluxes of momentum and/or buoyancy (Thorpe, 2005). In the case of wall-bounded flows, such as that of the bottom boundary layer (BBL), frictional forces decrease the mean velocity from an uninhibited, free-stream velocity

away from the boundary to zero at the seabed. If the boundary layer is not solid, like that at the sea surface, the velocity rapidly changes from one side of the boundary to match that on the other side of the boundary. In both cases, the velocity shear within the boundary layer imparts a shear stress that, at the high Reynolds Numbers encountered in shelf seas, generate turbulent flows that typically characterise the shelf sea boundary layers. The height of the boundary layer may be defined in the idealised case by the point at which the velocity profile achieves 99% of that outside the influence of the boundary (free-stream velocity, U_∞). In shelf seas, boundary layers are further complicated by the influence of the Earth's rotation and the oscillatory nature of the dominant tidal forcing.

2.2.1 Mixing in the Bottom Boundary Layer

The bottom boundary layer is where frictional effects of the seabed is felt by the current flow. This causes a reduction in velocity inversely proportional with height above the seabed. The current profile within the unstratified wall layer is seen to approximate a logarithmic profile on a dimensional argument basis, and referred to as the log-layer (after Tennekes and Lumley (1972)

$$U = \frac{u_\star}{\kappa} ln \frac{z}{z_0} \tag{2.12}$$

where $u_\star$, is the friction velocity, z_0, boundary roughness length, z, height above the bed, and κ, is the dimensionless von Kármán constant with an empirically derived value of 0.4.

The friction velocity may be calculated from profiles of velocity within the constant stress layer, alternatively, it may be calculated directly from the turbulent Reynolds stress measurements via the so-called eddy-correlation method, or thirdly calculated from measurements of dissipation.

Figure 2.5 illustrates two scenarios that differentiate between a well-mixed and stratified water column. In shallow regions, with relatively strong tidal currents, the frictional stresses generated at the seabed can extend all the way to the surface arresting the currents throughout the water column (Figure 2.5a). If the water depth is relatively deep enough that the BBL does not extend to the surface, velocity approaches the free-stream velocity (U_∞), which describes the mean velocity of the water column not under the influence of the BBL nor any other frictional stresses (Figure 2.5b). The theoretical vertical

profile of velocity in the BBL increases from zero at the seabed to a maximum velocity at the uppermost part of the BBL. In this schematic the log-layer is divided into two further sublayers in which the outer sublayer is heavily dependent on the nature of the free-stream current (Soulsby, 1983). These are most likely to be the influence of surface waves and stratification in shelf seas.

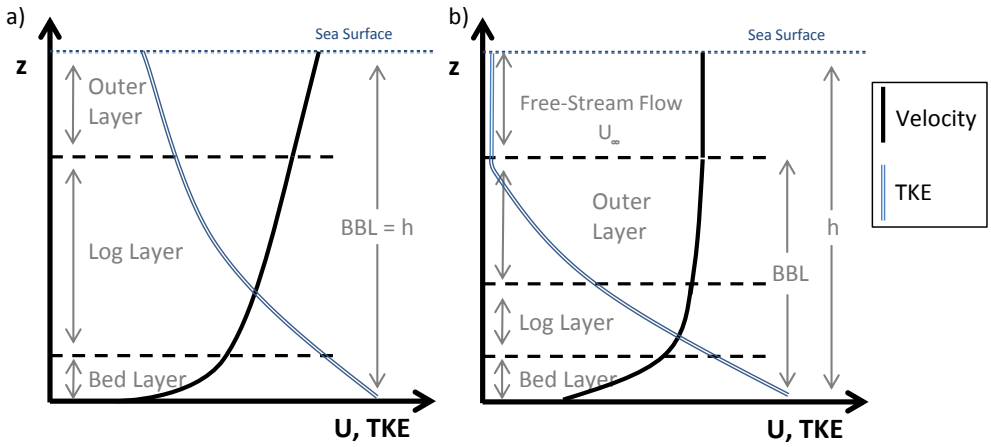

Figure 2.5: *Schematic of an idealised bottom boundary layer illustrating the logarithmic current velocity profile (U) in a) where the BBL reaches the surface and b) the BBL is limited to the depth of the free-stream velocity (after (Soulsby, 1983)).*

In shelf seas, the predominant source affecting the uppermost layer within the bottom boundary layer is the oscillatory currents caused by the tides. Therefore, the vertical profile of this part of the bottom boundary layer will evolve mainly in relation to the tidal periodicity, with the added influence of Earth's rotation on the oscillatory motion and other transient factors such as surface wave action and stratification.

The effects of stratification on the vertical profile of turbulence in the upper mixed layer is also of interest to this study, especially with the possibility of comparing stratified and well-mixed locations. Taylor and Sarkar (2008) investigated with the use of LES (Large Eddy Simulations) modelling the benthic Ekman layer formed with a uniformly stratified, steady geostrophic flow and in contact with the seabed. As the strength of the stratification exterior to the BBL increases, the boundary layer decreases significantly. They found that the structure of the boundary layer is confined by the stratification as the boundary layer properties of Reynolds stress, turbulent heat flux and Ekman veering were not evident above the pycnocline. In the outer layer, turbulence-

generated internal waves were observed radiating away from the boundary layer. In a similar manner, Gayen et al. (2010) investigated the effects of stratification on a boundary layer under an rectilinear, oscillatory current in a large eddy simulation (LES) modelling study. Results show stratification strongly affects vertical velocity profiles, boundary layer thickness and turbulence levels (Gayen et al., 2010). The influences of the oscillatory flow were seen in the asymmetric turbulent levels between the acceleration and deceleration stages, while the asymmetry increased with increasing stratification. A lag in maximum levels of turbulence was found with respect to maximum velocities. This lag was found to be dependent on the height above the wall and also with levels of stratification. Phase lags have been observed elsewhere in stratified and mixed conditions in both observations and modelling studies (Simpson et al., 1996; Burchard et al., 1998; Sharples et al., 2001).

2.2.2 The Impact of Surface Forcing and Restratification

Turbulent mixing in the surface boundary layer of the ocean plays an important role in the complex air-sea interactions that couples the ocean and atmosphere through fluxes of heat, momentum and mass (Thorpe, 2005; Simpson and Sharples, 2012). In an idealised case, the vertical profile of turbulence dissipation would be logarithmic, similar to that of a non-slip boundary such as the BBL (Paskyabi and Fer, 2010). However, the surface boundary layer is directly influenced by surface heat fluxes, wind stress and surface waves and hence is significantly different from an idealised non-slip boundary (Thorpe, 2005). Within the surface boundary layer, indications of enhanced levels of turbulent mixing are reported in comparison to the typical law-of-the-wall scaling (Anis and Moum, 1995).

In the case where the enhanced turbulent layer penetrates deeper than the surface mixed layer, turbulent motions work against the stratification and a part of the turbulent energy is used in mixing the water column and increasing the potential energy of the water column. By understanding how deep this turbulent mixing penetrates, we can identify the mechanisms responsible for deepening the surface mixed layer and potentially creating a well-mixed water column in marginally stratified shelf sea regions.

The resulting turbulent dissipation in the surface layer affected by the wind-driven wave breaking can be of orders of magnitude larger than that produced by shear mixing from wind stress alone (Soloviev and Lukas, 2003; Terray et al.,

1996). The depth to which dissipation rates are elevated due to wave breaking is of particular interest to this study yet remains elusive in the literature. Agrawal et al. (1992) reported enhanced dissipation rates due to wave breaking to a depth of $10^5 u_*^2 g^{-1}$; where u_* is the friction velocity ($u_* = (\tau_w/\rho_0)^{1/2}$), which is equivalent to the significant wave height ($H_{1/3}$). Furthermore Soloviev and Lukas (2003) concluded that the majority of the wave breaking energy was dissipated within an even shallower band equal to $0.25H_s$. Yet Stips et al. (2005) reports the wave affected layer reaching a depth of 2 to 3H$_s$.

Although breaking waves input the largest contribution of TKE, non-breaking waves do also contribute to the energy flux by wave stress and imparting an orbital motion to the fluid parcel which causes a net displacement termed Stokes drift (Thorpe, 2005). The combination of wind-driven Stokes drift and the current shear generates counter-rotating vortices aligned with the wind direction, setting up sub-surface circulation cells called Langmuir circulation that further enhance vertical mixing (Langmuir, 1938). This circulation forms the familiar narrow bands of foam and flotsam seen on the sea surface on a windy day. Langmuir circulation is now considered to be a principal surface layer mixing process, confirmed by both observational (D'Asaro and Dairiki, 1997; Farmer and Li, 1995; Plueddemann et al., 1996; Smith, 1992) and model studies (Li et al., 1995; Skyllingstad et al., 2000). Furthermore, strong interaction between turbulence and Langmuir circulation has been termed Langmuir turbulence and has been shown to contribute towards deepening the mixed layer (Kukulka et al., 2009).

CHAPTER 3

METHODS: INSTRUMENTATION, DEPLOYMENT STRATEGY & NUMERICAL MODELLING

In this chapter, the fieldwork instrumentation and deployment strategy is described, along with the numerical model setup. In-situ observations are a crucial component in capturing the processes occurring in the frontal system, yet represent a limited snapshot in space and time. In order to complement the observations, numerical simulations using a one-dimensional, vertically resolving, General Ocean Turbulence Model (GOTM) were conducted to firstly evaluate what is seen in the observations, and secondly, to fill in the gaps between the discreetly sampled observations. The chapter firstly describes the general sampling strategy before giving a brief overview of the instrumentation's theory, after which each instrument's deployment strategy is described in turn. Secondly, the chapter continues with a description of the numerical model setup, forcing fields, and validation of simulations. Lastly, an implementation of surface wave breaking parameterization is tested in GOTM.

3.1 Fieldwork Strategy

The data collected as part of this research were obtained over two periods in May and August, 2012. The sampling strategy was designed to capture the difference in turbulent mixing regimes during weakly stratified conditions in May for comparison with more strongly stratified conditions in August. In addition to the seasonality in stratification levels, the impact of the spring-neap tidal cycle on turbulent mixing — specifically in the BBL — was also investigated with the instruments deployed over a 12-day period covering the transition from neap to spring tides.

To achieve this goal, a combination of instruments were used in the fieldwork including the deployment of long-term moored instruments over the 12-day period, and short-term towed or profiled instruments sampling over individual 12.4-hour, semi-diurnal, tidal cycles. The long-term deployments included a bed-moored Acoustic Doppler Current Profiler (BM-ADCP), described in Section 3.2.2, and thermistor mooring (Section 3.2.3) to monitor, with high vertical and temporal resolution, the current and temperature fields at the frontal zone throughout the observation periods. The short-term deployments included turbulence microstructure profiles, (Section 3.2.1), deployed over individual tidal cycles with concurrent vessel-mounted ADCP (VM-ADCP) measurements. These were interspersed with towed Conductivity Temperature Depth (CTD) transects to establish the large-scale spatial pattern on either side of the front (Section 3.2.4). Supporting meteorological data were supplied from

a met-station mounted aboard the vessel and supplemented by the Sevenstones meteorological buoy. Additional wave data was supplied by a directional wave buoy deployed in the vicinity of the study site by Plymouth University. Details of the specific instrumentation and the associated data processing are provided in the following Sections.

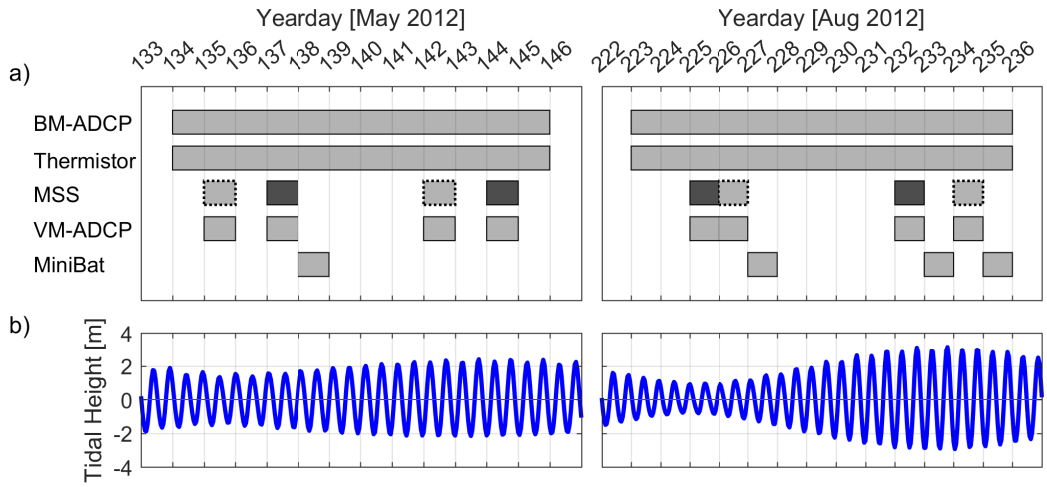

Figure 3.1: a) *Instrument deployment periods in May and August 2012. MSS sampling conducted at Station 1 is presented as dashed box while sampling at Station 2 is darker grey.* ***b)*** *Derived tidal heights from TPXO8.0 European Shelf solutions for the study location.*

Figure 3.1a shows the timing of the instrument deployments in relation to the spring-neap tidal cycle — Figure 3.1b. The tidal height was calculated for the study location using TPXO8.0 GLOBAL tidal solution with the European Shelf 1/30° solutions (Egbert and Erofeeva, 2002). The moored instruments were deployed prior to the turbulence microstructure tidal cycles and recorded continuously for the duration of each of the 12-day deployment periods. These captured the transition from neap tides to the more energetic spring tide conditions. The short-term turbulence microstructure tidal cycles and towed CTD transects were conducted on separate days, with the turbulence microstructure tidal cycles staggered over the neap and spring tides. The turbulence microstructure sampling locations were located on either side of the front with Station 1 (St1) situated offshore and Station 2 (St2) inshore. The BM-ADCP and thermistor mooring was situated in between the two turbulence microstructure profiling stations (Figure 3.2).

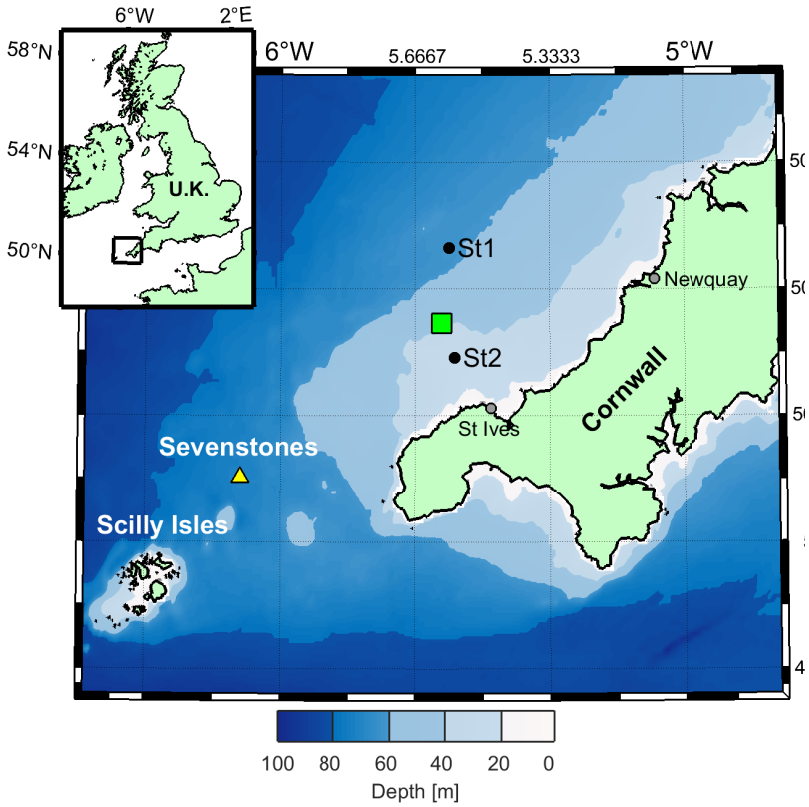

Figure 3.2: *The locations of the offshore (St1) and inshore MSS stations (St2) situated in mean depths of 65m and 35m, respectively. The green square symbol identifies the location of the BM-ADCP with the thermistor string and wave buoy located nearby.*

3.2 Instrumentation & Deployments

3.2.1 Turbulence Microstructure Profiler

Turbulence should ideally be measured in a statistically robust, four-dimensional domain (three space and one time). The measurements must also be conducted over a representative duration and cover the full range of turbulence spatial scales — from dissipative eddies (O 0.01 m) to the largest energy-containing eddies (O 1 m). Such highly resolved measurements are yet impractical using vertical profiling instruments in shelf seas since the spatial-scale limitations of the mechanical sensors inhibit measurements over the full turbulence spectrum. The use of microstructure profilers require a number of simplifying assumptions, including invoking turbulence isotropy and the universal turbu-

lence spectrum, which have been shown to adequately capture the physical dynamics to within an acceptable degree of accuracy (Moum et al., 1995; Prandke et al., 2000). In this section, we describe how vertical microstructure profilers are used to obtain turbulent dissipation rates from the measured small-scale vertical shear and explain the assumptions made. Much of the methodology is common to all microstructure profilers but many aspects, for example the data processing steps, described in this section are particular to the turbulence microstructure instrument used in this study.

Measuring Turbulence in Shelf Seas Using a Microstructure Profiler

Turbulent fluctuations occur at scales smaller that the fluctuations associated with the mean flow. Microstructure profilers use mechanical shear probes to measure these small-scale velocity fluctuations from which the shear variance is used to estimate the turbulent dissipation rate under the assumption of stationary, homogeneous, and isotropic turbulence (Osborn, 1974; Polzin and Montgomery, 1998). The shear probes measure the velocity fluctuations by utilizing a piezoceramic beam that senses the tangential shear force and produces a voltage output that is proportional to the instantaneous cross-stream (horizontal) component of the velocity field (Figure 3.3). The voltage output is converted to a velocity acceleration following Lueck (2005):

$$\frac{\partial u}{\partial t} = \frac{1}{2\sqrt{2}\rho G S V}\left(\frac{\partial E}{\partial t}\right) \tag{3.1}$$

where $2\sqrt{2}$ is a calibration constant, ρ is the density of seawater (kg m^{-3}), G is the gain of the electronic sensor, S is the shear probe sensitivity, V is the fall-velocity (m s^{-1}), and E is the sensor output voltage (volts). The assumption of a stationary turbulent field is invoked in order to obtain the vertical shear ($\partial u/\partial z$) from the velocity fluctuations ($\partial u/\partial t$). This is referred to as the Taylor's frozen-field assumption (Equation 3.2), and implies that the turbulent field evolves slowly relative to the time period of measurements. Hence, the time derivative can be converted into spatial derivative in the direction of profiling:

$$\frac{\partial u}{\partial z} = \frac{1}{V}\left(\frac{\partial u}{\partial t}\right) \tag{3.2}$$

This assumption was found to hold true for turbulence microstructure measurements although it does impart a lower limit on the instrument fall-velocity ($V \geq 0.5$ m s^{-1}) during profiling (Lueck, 2005). The vertical shear can hence be

computed:

$$\frac{\partial u}{\partial z} = \frac{1}{2\sqrt{2}\rho GSV^2}\left(\frac{\partial E}{\partial t}\right) \tag{3.3}$$

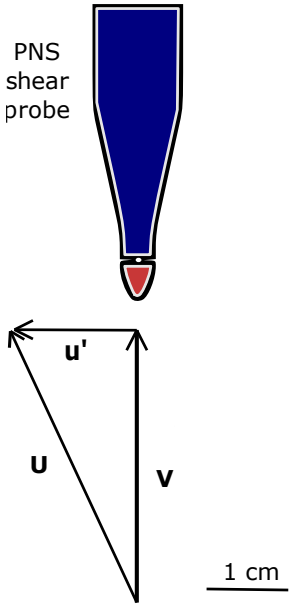

Figure 3.3: *Measurement geometry of the PNS shear probe used by the MSS to measure the small-scale turbulent velocity fluctuations. A piezoceramic beam, connected to the airfoil (red), senses the force generated by the cross-stream component of the flow (U) and produces a voltage output that is proportional to the instantaneous velocity fluctuations (u'). Diagram adapted from Prandke (2009a).*

In order to obtain accurate dissipation rate estimates from the measured vertical shear profile, the shear variance is subdivided into overlapping sections from which the power spectra is calculated and integrated over the full inertial subrange (Stips, 2005) — an example of which is presented in Figure 3.4. However, the spatial response of the shear probes is generally too large to resolve fluctuations down to the Kolmogorov microscale. In order to account for this deficit, the power spectrum is fitted to the universal Nasmyth spectrum and the higher wavenumbers are included by interpolation (Thorpe, 2005). The fitted shear spectrum can then be used in Equation 2.8 to obtain accurate dissipation rate estimates.

Sources of errors involved in the estimation of dissipation rates are summa-

rized by Stips (2005). These uncertainties are due to a combination of technical limitations of the shear probes and profiling instrument (electrical noise, profiler vibrations, limited spatial response of shear probes, calibration errors), bad profiling technique (mechanical induced turbulence, ships wake turbulence), and data processing (separating turbulent and non-turbulent velocities fluctuations). The cumulative uncertainties of these measurements have been determined to fall within a factor of two for the measurements of turbulent dissipation (Moum et al., 1995). Additionally, given the sensitivity of the shear probes to mechanical vibrations from the instrument and attachments, the noise threshold for the turbulence microstructure is 10^{-9} W kg^{-1} (Prandke et al., 2000). Stips (2005) concluded that given the natural variability in dissipation rates, as was also highlighted by Moum et al. (1995), obtaining representative and consistent (with small relative errors) data is more important than the accuracy of the dissipation rate itself.

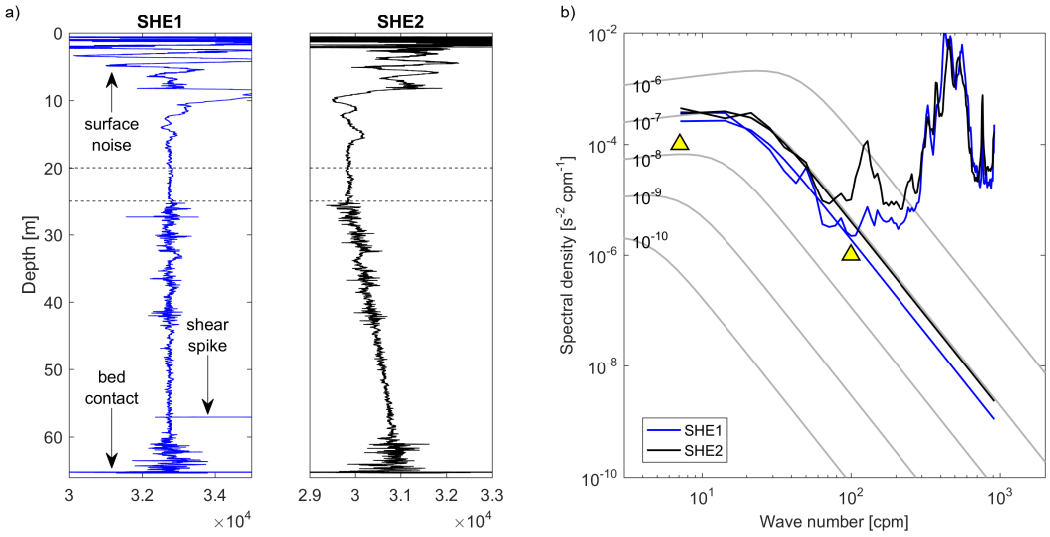

Figure 3.4: *a) An example of the MSS raw shear profiles from the two shear probes (SHE1 & SHE2) and b) the computed spectra from a subsection of the shear profiles (20–25 m) from which the dissipation rates are derived using the fitted universal Nasmyth spectrum for wavenumbers between the triangles (smoothed lines). The smooth grey lines are the Nasmyth universal shear spectrum for the denoted levels of dissipation. The high frequency peaks in the spectrum are caused by mechanical vibrations and excluded from the dissipation rate fitting.*

Instrument Practical Background

The ISW-Wassermesstechnik MSS90 microstructure profiler (MSS) was equipped with two radially symmetric airfoil shear probes, a fast temperature sensor (microthermistor), acceleration and tilt sensors, that sampled at a very high

sampling rate (1024 Hz) in order to obtain the high-resolution shear measurements at the required micro-scales for isotropic turbulence. In addition, the MSS included a standard CTD and additional optical sensors measuring temperature, conductivity, pressure and wavelength-specific light attenuation metre at a comparatively lower sampling rate of 24 Hz, making the MSS a versatile profiling instrument.

The instrument is constructed of a cylindrical pressure housing, containing the power supply and electronic circuitry, and the oceanographic sensors mounted externally to the leading face (Figure 3.5). Of primary importance to the design of the MSS is the prevention of the instrument's turbulent wake from contaminating the measurements of oceanic turbulence. To achieve this, the turbulence shear probes are mounted proud of the body and in front of the auxiliary sensors. These delicate shear probes and auxiliary sensors are protected from damage by a front guard which is specifically designed to shed its turbulent wake away from the shear probes. As is seen in Figure 3.5, the instrument is further designed to reduce vortex shedding by using a tasselled front guard and 'string fringes' to the rear. Laboratory tests have shown the remaining mechanical vibrations to be typically outside that of the spectral range of oceanic microstructure shear and therefore may be distinguished from the natural shear signal during data processing, resulting in an improved dissipation rate estimate (Stips, 2005).

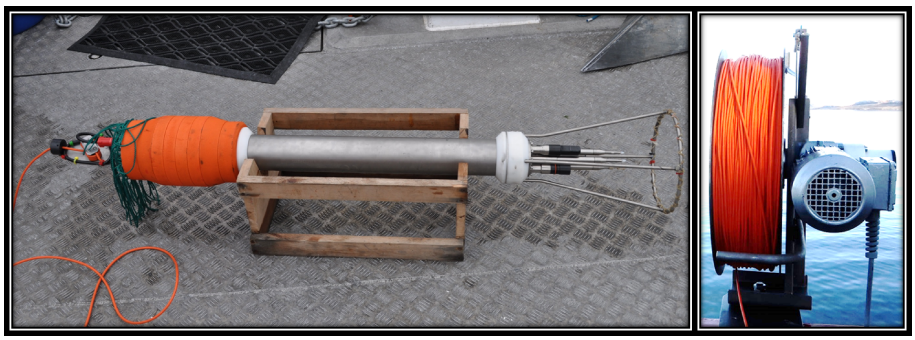

Figure 3.5: *Left: The MSS turbulence profiler on deck prior to deployment. The instrument is loosely tethered to the vessel by the orange cable seen in the left foreground. This cable is attached to the top of the pressure housing that consists of green 'fringes', to increase dynamic stability and reduce vibrations; orange buoyancy elements; metal casing, and sensors attached to leading end and probe guard. Image courtesy of Dr. S. Cox (Plymouth University). Right: The MSS is operated by electric winch and cable drum attached to the vessel's transom.*

In this fieldwork, the instrument was operated from a drifting vessel in descending mode which allowed for the safe and practical use given the water

depth and open ocean conditions at the study site. The instrument was released at the surface and allowed to free-fall. The instrument's righting moments and desired fall-velocity ($0.5 < V < 1.5$ m s^{-1}) were controlled by weights attached to the lower end and synthetic foam buoyancy rings attached to the upper end of the pressure housing (orange rings in Figure 3.5). The instrument was recovered after each profile by a loosely tethered, load-bearing, data cable attached to the trailing face of the pressure housing. The signal was initially filtered and amplified in the MSS90 before being transmitted in real-time to the vessel via the data cable. This allowed for real-time monitoring of the instrument's depth and fall-velocity during profiling which was required when operating near to the seabed.

MSS Deployment

The MSS was deployed from a drifting vessel and profiled at a nominal fall-velocity of 0.7 ms^{-1}. Approximately, every seven profiles (approx. 20-30 minutes) the instrument would be recovered onboard to allow the ship to reposition, thereby leading to quasi-continuous profiles over the tidal cycle. Standard operating procedure was to allow plenty of slack cable to be let out whilst the instrument was in free-fall in order to minimize any sources of drag or induced vibrations. The timing and location of MSS sampling is given in Table 3.1.

Table 3.1: *The dates, location and tidal information for MSS deployments in May & August, 2012.*

Station		**Latitude [DD]**	**Longitude [DD]**	**Depth [m]**
Station 1 (St1)		50.465°N	5.582°W	65
Station 2 (St2)		50.292°N	5.569°W	35
Date	**Yearday**	**Station**	**Tides**	**Tidal Range [m]**
14/05/2012	134	St1 (offshore)	neaps	2.6
16/05/2012	136	St2 (inshore)	neaps	3.2
21/05/2012	141	St1 (offshore)	springs	4.5
23/05/2012	143	St2 (inshore)	springs	4.3
12/08/2012	224	St2 (inshore)	neaps	2.0
13/08/2012	225	St1 (offshore)	neaps	3.0
19/08/2012	231	St2 (inshore)	springs	5.8
21/08/2012	233	St1 (offshore)	springs	5.5

Data Processing

Approximately 100–200 profiles were cast per 12.4 hour tidal cycle during this fieldwork. A number of post-processing steps were systematically applied to each shear profile to obtain estimates of turbulent dissipation and are listed in order of operation in the Appendix (Table A.1 & A.2). The post-processing was conducted using the proprietary software package *MSSPro* using the suite of 'modules' specifically designed for this purpose and detailed in Table A.1 & A.2. A modular format to the data processing gives the user the flexibility to select various filtering options by inputting or excluding certain modules. Implicit to the data processing was the extraction and smoothing of the CTD and auxiliary data. Here, we describe the post-processing of the raw shear data to produce estimates of turbulent dissipation rates conducted in *MSSPro*.

Profiles were recorded and stored as individual data files. For each profile, the following data processing steps were carried out:

1. The upper and lower vertical depth limits for each profile were identified and the profile cropped to the following specification — the upper limit was set at 6 m for all profiles and the lower limit was set at the seabed. The upper depth limit was set to reduce external contamination of mechanical shear spikes from the instrument's initial acceleration as well as the operating vessel's turbulent wake. The seabed was identified in each profile manually by the exceptionally large shear spike (see Figure 3.4a) caused by the instrument's rapid deceleration as it made contact with the seabed followed by a constant pressure reading and a zero fall-velocity (rate of change of pressure with time).

2. The cropped shear profiles were then despiked using a number of algorithms that, firstly, identified and removed non-coherent signals from the two shear sensors and, secondly, calculated the local variance of the signal and removed spikes that exceeded 2.7 times the standard deviation (Prandke, 2009b). These spikes, an example of which may be seen in Figure 3.4, are typically caused by contact with planktonic or other particulate matter that must be removed prior to further treatment. Previous studies have found that unless removed, these spikes caused the final dissipation rate to be over-estimated by up to 30% (Stips, 2005).

3. The physical shear was calculated from Equation 3.3. High frequency noise was then removed with the use of a Butterworth filter applied in both forward

and backward direction to prevent phase distortion. The CTD and auxiliary data were also filtered using a moving average smoothing function and is described in Table A.2 (Appendix A).

4. The ε rate was calculated by an iterative fitting of the measured shear spectrum to the universal Nasmyth spectrum as described in Section 3.2.1 (Figure 3.4).

3.2.2 Acoustic Doppler Current Profiler (ADCP)

Instrument Background

Measurements of 3-spatial and 1-temporal dimension current velocities were obtained using an Acoustic Doppler Current Profiler (ADCP) during the fieldwork. The ADCP calculates vertical profiles of current velocities by transmitting a series of acoustic 'pings' at set frequencies (broadband ADCPs), and receives the returned echoes from suspended particles in the water column. The particulate matter backscatter the transmitted acoustic pulse with a Doppler frequency shift that is dependant on their speed and direction relative to the ADCP (RDInstruments, 1996). An important assumption made is that the particulate matter is travelling at the same rate as the parcel of water it occupies (Nystrom and Oberg, 2002). With the use of the inbuilt compass and pitch/roll sensors these velocities are typically further processed to obtain the current velocities relative to geodetic Earth coordinates. ADCPs can be deployed moored to the seabed or mounted aboard a vessel or other autonomously operating platform.

Modern broadband ADCPs operate a series of multiple transmitted pulses that utilise the equivalent time dilation of the returning echoes to obtain more precise Doppler measurements. High frequency broadband ADCPs (i.e. 614 kHz) permit smaller bin sizes (approx. 0.5 m) but are limited in range (approx. 38 m) due to stronger signal attenuation at high frequencies. Lower frequencies (307 kHz) allow broadband ADCPs to profile to depths of approximately 83 m, although require larger bin sizes (approx. 1 m) and hence lower vertical resolution (RDInstruments, 2009). Therefore, the choice of operating frequency depends on the total water depth to be sampled and requires a trade-off between profile range and the vertical resolution (bin-size). The returned echoes from a series of pings are averaged to form an 'ensemble' record which improves the error estimate for the velocity as well

as reducing the amount of processing and memory storage space. ADCP's manufactured by RDI implement a variety of user-defined 'Modes' with varying ping characteristics, time lags between pings and wave pulse forms. The operating 'Mode' is selected for either its robustness to be used in turbulent environments, (e.g. Mode 1), or measurement precision that may only work in relatively limited quiescent conditions, (e.g. Mode 5). In this fieldwork, the bed-moored ADCP made use of Mode 12 processing. Mode 12 is a high frequency ping configuration that makes use of a sequence of 'sub-pings' per ping and an aggregated processing and averaging method. In Mode 12 the sub-pings are averaged before transforming the data to Earth-related coordinates, in a Cartesian coordinate system, using the ADCP instrument's pitch/roll and compass data. However, in order to achieve high-frequency sampling, the auxiliary data is only sampled once per ping and it is assumed that the instrument does not change in orientation during the sub-pings making Mode 12 only suitable for static, bed-moored, deployments. The advantage of Mode 12 is the high frequency, high volume, sub-ping sampling reduces the standard deviation thereby improving the signal-to-noise ratio of the signal. Further details on the specific configurations of the bed-moored and vessel-mounted ADCPs are described below.

Bed-moored ADCP Deployment

A broadband 614.4 kHz RDI Workhorse ADCP was deployed on the seabed at a depth of 55 m in a trawl-resistant housing for two extended periods. The deployment was co-located with the thermistor mooring allowing the velocity structure to be related to the temporal evolution of the temperature structure.

An operating frequency of 614.4 kHz provided full water column coverage, however, the blanking distance, side-lobe reflection and surface waves impeded measurements from the near-seabed and near-surface. Blanking distance is caused by the acoustic energy lingering after the transmitted pulse is finished, which means the receiver cannot receive echoes immediately after transmitting. This translates into a blanking distance immediately out from the face of the instrument from which no measurements can be obtained. Side-lobe reflection originates from the echo of a hard surface (sea surface or sea bed) which can overwhelm the echo of the scatterers in the water. Given the beam spread of the acoustic signal, the side lobes facing the hard surface may return to the ADCP at the same time as the main lobe signal. This stems from the orientation of

the beams of between 20-30° from normal. The blanking distance for the BM-ADCP was 1.6 m of the instrument and side-lobe reflection reduced coverage by 10% of the water column depth at the surface (approx. 5.5 m) (RDInstruments, 1996). The ADCP was configured to 1 m vertical bin resolution and in Mode 12 for both deployments. The ensemble time period differed between deployments; on yearday 133-144 it was 1 second and yearday 223-234 it was 2 seconds.

Figure 3.6: *Left: Bed-mounted ADCP in a trawl-resistant housing on deck (red circular acoustic transducers in blue casing mounted to the upper face of the yellow housing). Right: Instrument deployed on the seabed at the study site in May 2012. The ADCP was recovered using a positively buoyant recovery line stored within the housing and released via an acoustic release mechanism.*

Vessel-mounted ADCP Deployment

A 307.2 kHz RDI Workhorse Broadband ADCP was mounted to the vessel and recorded velocity measurements from underneath the vessel whilst MSS profiling and towed CTD transects were undertaken. The operating frequency provided a deeper profiling range but at the cost of vertical resolution — the depth bins was set to two metres. The ADCP was set to a standard configuration for all fieldwork, recording at 1 ping per ensemble at a rate of one ensemble every 3 s. In a similar manner to the BM-ADCP, the inherent blanking distance and sidelobe reflection caused a diminished velocity reading near the sea surface and seabed.

3.2.3 Thermistor Mooring

Instrument Background

The temporal variability in vertical temperature structure was recorded by thermistors attached to a mooring chain at 2 m intervals, weighted at the

bottom and attached to a sub-surface float for buoyancy. The thermistors were Star-Oddi DST Centi-T temperature loggers and DST Centi-TD temperature and pressure loggers. The instruments were accurate to ± 0.1°C, ± 0.3 dBar and were set to take one measurement every 2 minutes.

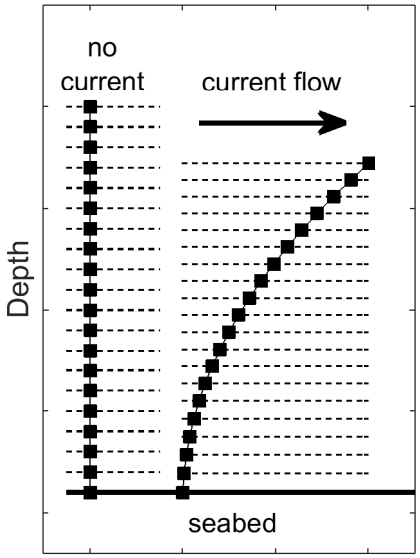

Figure 3.7: *Schematic showing the effect of the tidal currents causing 'mooring knock-down' whereby the current induced tangential drag causes the mooring line to bend downwards. This causes the thermistor instruments to divert from the vertical and equally spaced setup desired.*

In order to obtain a time-invariant vertical grid during post-processing, the instrument depth readings obtained from the pressure sensors were converted to a height above bed (HAB). In order to achieve this, two factors were considered. Firstly, the change in depth due to the change in tidal elevation that varies over time. In order to remove the tidal signal, the tidal elevation signal, obtained from the bottom-most pressure sensor fixed to the mooring block on the seabed, was removed from each instrument's pressure reading. Note, that the instruments with no pressure sensors were spaced at known intervals between the pressure sensors and hence their instantaneous depths were obtained from interpolating between the pressure sensors. Secondly, since the top of the mooring was not fixed, the mooring line experienced 'knock-down' whereby the frictional drag imposed by the current flow causes a horizontal and vertical displacement of the mooring line (Figure 3.7). This varied the depth of each sensor in a non-linear manner depending on the current speed and the instrument's distance from the seabed. The effect of this may be seen

in the de-tided pressure timeseries in Figure 3.8. This was removed through the interpolation onto a linear vertical grid with a uniform vertical spacing of 1 m.

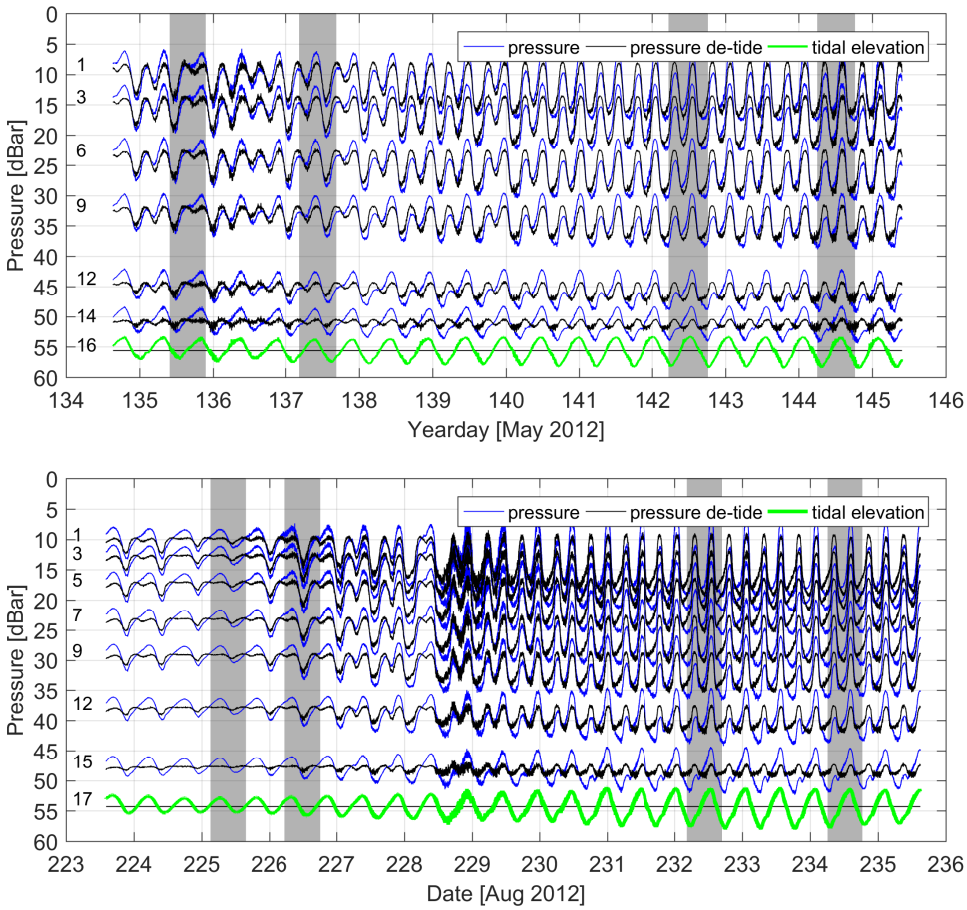

Figure 3.8: *The pressure readings for the thermistors showing the pressure readings (blue), de-tided pressure (black) obtained from subtracting the tidal signature (green) from each sensor. The remaining variability in the de-tided signal was due to current flow causing instrument knock-down. Grey vertical bars denote period of MSS tidal-cycles at both sampling stations.*

In addition to the thermistors, two Star-Oddi DST CTDs were attached at the top and bottom of the mooring providing low-resolution salinity readings (accuracy: 0.1 salinity units). Salinity was observed to vary less than 1 unit ($34.85 < S < 35.8$) over the sampling period and its influence on density is assessed below (Section 3.2.3).

Thermistor Deployment

The Star Oddi thermistors were spaced approximately 2–3 m apart, from 1 m above the seabed to approximately 10 m below the surface in 56 m of water.

The mooring did not extend to the surface due to the navigational risk caused by an unmarked mooring buoy. The thermistors were set to record every 1 minute for the duration of the deployment. Calibration of the pressure and temperature sensors were performed during post processing by calculating the bias in in each sensors' readings prior to initial deployment and applying the offset to the recorded data.

Assessing the Influence of Salinity on Density

The density structure, and associated gradients, were calculated using the temperature data from the thermistor mooring under the assumption of a constant salinity of 35.34. The validity of this assumption was based on assessing the relative influence of temperature and salinity on density which may be expressed by the density ratio, R_ρ:

$$R_\rho = \frac{\alpha(\Delta T)}{\beta(\Delta S)} \tag{3.4}$$

where, α and β are the thermal expansion and haline contraction coefficients. The density ratio was computed from vertical profiles of mean temperature and mean salinity available from the MSS tidal cycles at both Station 1 and 2. The inverse density ratios presented in Figure 3.9 show that temperature had a dominant influence on density ($R_\rho^{-1} < |1|$). For the depths in which $R_\rho^{-1} > |1|$, N^2 was minimal, indicating a well mixed water column in which the density gradients were very small and, as a result, the influence of the small salinity fluctuations were deemed insignificant on the vertical turbulent mixing processes.

3.2.4 Towed CTD Platform — the MiniBat

Instrument Background

The OSIL Minibat is a towed instrument platform upon which instrument packages can be attached and towed in an undulating pattern to obtain a 2D vertical slice of the water column. The MiniBat was operated in semi-autonomous mode in which the vertical dive pattern was controlled by the deck controller using real-time telemetry provided by the on-board pressure and attitude sensors. The deck control unit also allowed the data to be recorded on a laptop in real-time. The instruments attached to the MiniBat was an AML 'Standard MiniCTD' instrument package with an additional AML 'chlorophyll-

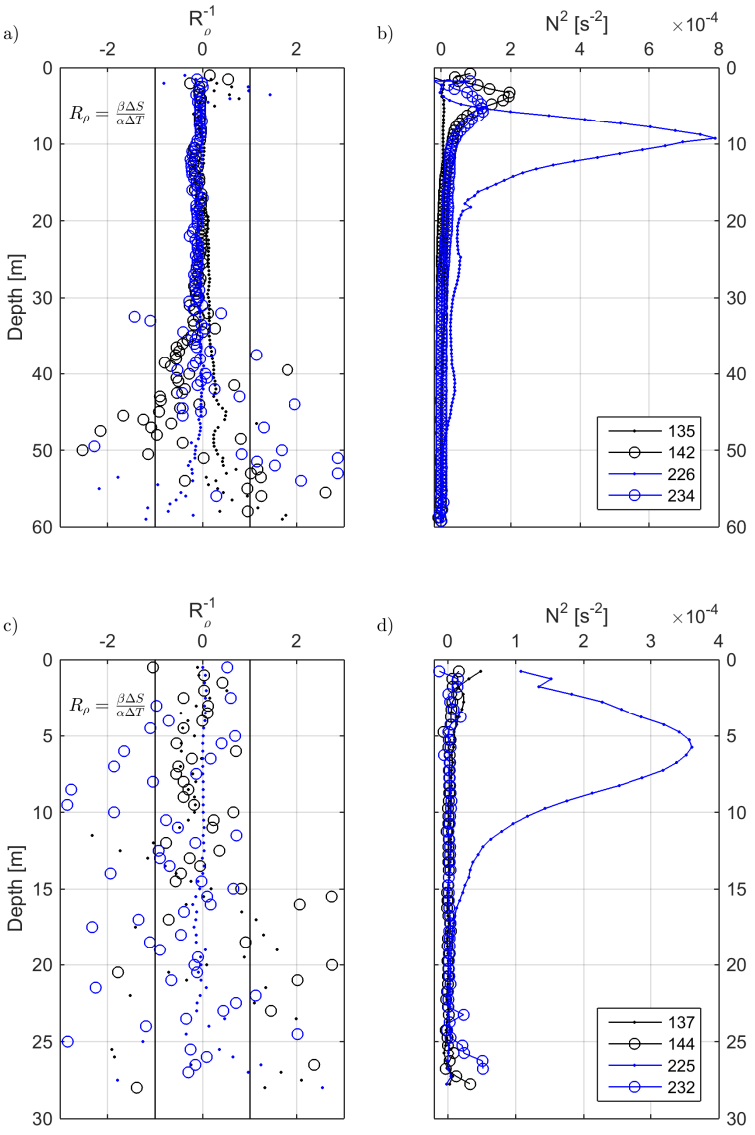

Figure 3.9: *LHS: The inverse density ratio calculated from profiles of mean temperature and salinity for each MSS tidal cycle for Station 1 (a) and Station 2 (c). Absolute values of less than unity signify a dominant temperature influence on density. RHS: Buoyancy frequency squared (N^2) showing the level of stratification and hence gradients in water properties for Station 1 (b) and Station 2 (d). Sections of R_ρ^{-1} values of greater than unity (salinity dominant) had very low N^2 and hence small gradients in density in a well-mixed water column. MSS tidal cycle identified by the yearday in the Figure legend.*

A fluorometer' and an AML 'optical back scatter' sensor.

Minibat Deployment

The purpose of the MiniBat surveys was to map the frontal structure by running multiple transects in a grid pattern. The MiniBat was towed at 4-

6 knots (2-3 m s^{-1}) and had a theoretical dive depth of 30 m. However, in practice, maximum dive depth obtained during transects was approximately 22 m due to the excess drag on the MiniBat cable prohibiting deeper dives. The horizontal resolution obtained during fieldwork was approximately 300 m per undulation whilst profile data was available at a resolution of less than a metre after post-processing. Calibration of the sensors were performed prior to the cruise by the manufacturer – AML Oceanographic. Figure 3.10 shows the location of the transects conducted in May (Yearday 138: green) and August (Yearday 227: blue & 233: cyan).

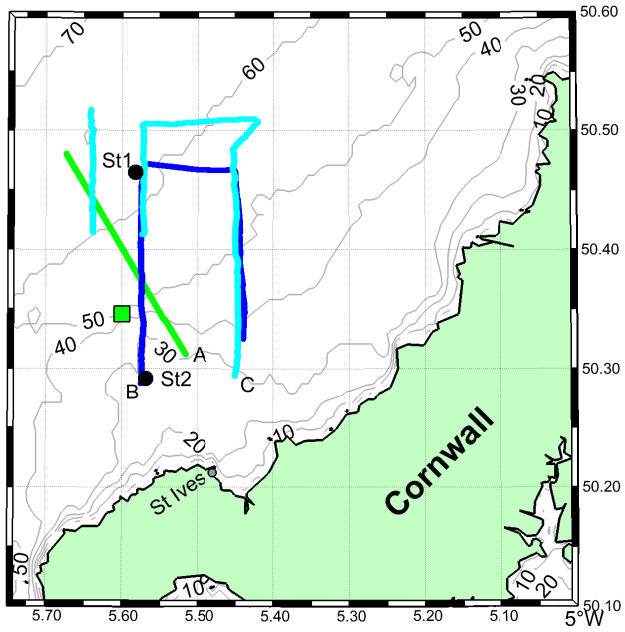

Figure 3.10: *Minibat transects conducted on Yearday 138 (A: green) and Yearday 227 (B: blue) & Yearday 233 (C: cyan). Bathymetric contours shown in metres. The location of the two MSS sampling stations, St1 & St2 are indicated as well as the BM-ADCP and thermistor mooring (green square).*

3.2.5 Meteorological and Wave Data

Meteorological data was made available from the Sevenstones meteorological-buoy (50° 6.15' N, 6° 6.0' W), situated 25 nm west of the study site (Figure 3.2). This data was used to provide measurements of wind speed and direction from which the surface wind stress was calculated. The wind stress acts to accelerate the ocean surface, thereby creating an unstable sheared flow from which instabilities in the flow produce turbulence in the surface boundary

layer (D'Asaro, 2001).

Both wind speed and direction was measured in ten-minute averages from which the dataset was post-processed to provide quality controlled data at hourly intervals (pers. comms. Met Office). This dataset is publicly available from the EMODnet portal (www.emodnet.eu/data). Throughout this thesis, wind speed is adjusted to 10 m above sea level and wind stress calculated with the parameterizations of Large and Pond (1981).

The applicability of Sevenstones data for use at the study site was confirmed by comparing it to data obtained aboard the vessel during MSS sampling. A comparison of hourly-averaged wind speed data showed good agreement between the two datsets, $R^2 = 0.73$, presented in Figure 3.11. Figure 3.12 presents the wind direction and is referred to 'direction from' throughout this thesis in standard meteorological format. Wind direction showed a weaker correlation between the two sources with the Sevenstones data giving a more consistent long-term direction indicator.

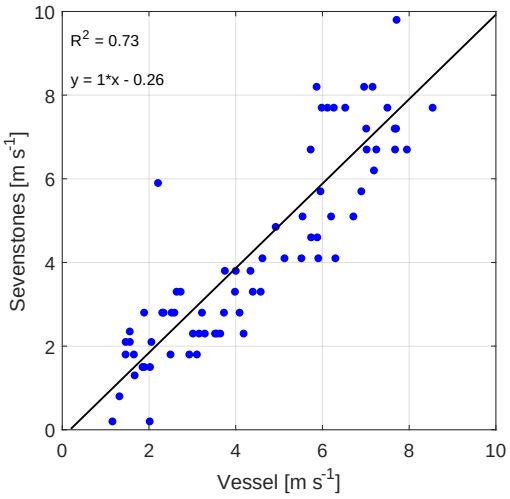

Figure 3.11: *Windspeed comparison between the Sevenstones meteorological buoy (SS) versus the vessel-mounted meteorological station (FS) during MSS sampling. Sevenstones Met shows good agreement ($R^2 = 0.73$) and provides a long-term, temporally consistent, meteorological dataset.*

In addition to wind stress, surface gravity waves generates boundary layer turbulence in both breaking and non-breaking cases. Wave data for this study was made available from a Seawatch Mini II directional wave buoy deployed at the study site in the vicinity of the thermistor mooring (50° 21.0' N, 6° 37.2' W). The wave buoy provided raw roll, pitch and heave data at 2 Hz, from which

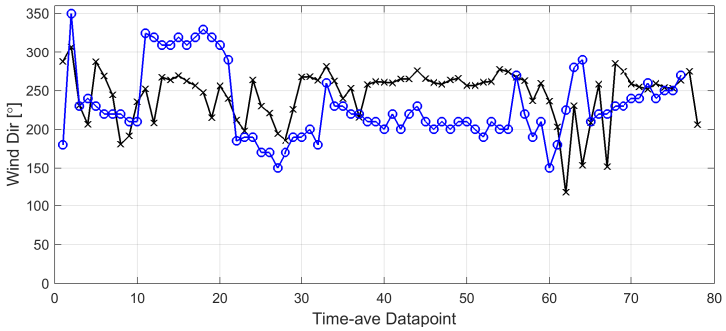

Figure 3.12: *Comparison wind direction between the vessel-mounted met-station (black, x) and Sevenstones met buoy (blue, o). Data points are hourly averaged.*

significant wave height, period, and directional measurements were obtained at 3 minute intervals after quality control (Lopez, 2017).

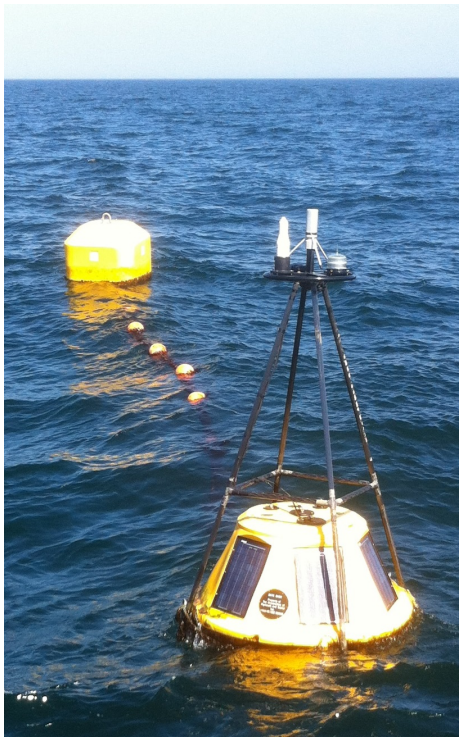

Figure 3.13: *Wave buoy deployed at the study site measuring directional wave spectra. Image courtesy of Phil Hosegood (Plymouth University)*

3.3 The General Ocean Turbulence Model

The General Ocean Turbulence Model (GOTM) is a one-dimensional water column model developed to simulate hydrodynamic and biogeochemical processes in marine and limnic waters (Burchard et al., 1999). A key component of GOTM is its ability to simulate the vertical turbulent fluxes using a choice of well-tested statistical turbulence 'closure' models (Burchard and Bolding, 2001). In such models, the random character of turbulence is statistically represented in the mean flow properties on scales larger than that occupied by the micro-scale turbulence (Burchard et al., 2008). A major advantage of one-dimensional statistical turbulence models is that it is much less numerically complex and therefore consumes much less computational effort than either three-dimensional scales or Large Eddy Simulation (LES) and Direct Numerical Simulations (DNS) turbulence models. Hence, GOTM allows us to simulate the impact of turbulence and small-scale vertical mixing in shelf seas scenarios using affordable computational effort for multiple simulations.

GOTM primarily solves the one-dimensional versions of the transport equations of momentum, salt and heat. The transport equations are derived from the incompressible Reynolds-averaged Navier-Stokes (RANS) equations of motion, with the hydrostatic ($p \sim \rho g h$) and Boussinesq approximations ($\Delta\rho << \rho_0$) applied. These approximations aid in simplifying the numerical treatment of the transport equations, yet retain an acceptable degree of accuracy for statistical turbulence modelling (Burchard et al., 1999). The RANS equations are derived by substitution of the Reynolds decomposition ($F = \overline{F} + F'$), into the equations of motion and ensemble-averaging the result. The new set of equations for the averaged quantities are formally equivalent to the Navier-Stokes equations, but now contain several new, unkown, second moments such as the Reynolds stresses ($\overline{u'_i u'_j}$), and turbulent heat and salt fluxes ($\overline{u'_i T'}$, $\overline{u'_i s'}$). Further transport equations may be derived for these second moments, but third moments appear in the equations (and so on...). Hence, the so-called 'closure' is required to truncate this series and relate the unsolved quantities to the gradients in fluid properties by means of the eddy viscosity, ν_t, and diffusivity, ν'_t (see Equation 2.6 in Section 2.1).

The eddy viscosity and diffusivity are a product of the TKE, k, a characteristic length scale representing the energy containing turbulent motions (macro length scale), L, and dimensionless proportionality terms known as stability

functions, c_μ and c'_μ;

$$\begin{aligned} \nu_t &= c_\mu k^{1/2} L \\ \nu'_t &= c'_\mu k^{1/2} L, \end{aligned} \tag{3.5}$$

Much of the unresolved physics is parametrized in the stability function. These are a function of the shear- and buoyancy-related gradient Richardson number under the local equilibrium assumption and characterises the inhibiting effect of stratification on mixing (Galperin et al., 1988; Kantha and Clayson, 1994; Burchard et al., 2008).

Many implementations of Equation 3.5 have been successfully derived for turbulence closure model and comprehensive reviews may be found in Burchard and Bolding (2001) and Burchard et al. (2008). Closure schemes range from constant values for ν_t and ν'_t, to more complex formulations based upon the gradient Richardson number stability function, and one- or two- equation models for the turbulent quantities. Of these, the two-equation models more accurate and numerical stable (Burchard et al., 2008). The most popular two-equation transport equations are the kL equation in the Mellor-Yamada model (Mellor and Yamada, 1982), and the k-ε model (Rodi, 1980, 1987). Comparison studies on the performance of these two-equation turbulence closures have shown they perform equivalently in most idealized and realistic cases (Burchard et al., 1998; Burchard and Petersen, 1999). In this research, the k-ε model combined with the algebraic second-moment stability functions, as proposed by Canuto et al. (2001), were implemented due to its accuracy, numerical stability, and extensive investigations demonstrating is suitability in similar shelf sea settings (Burchard and Bolding, 2001; Burchard et al., 2005a; Umlauf and Burchard, 2005). In addition, the model skill may be assessed by direct comparison between the modelled ε and the observed ε sampled using the MSS. The aim of the numerical experiments is to investigate how well a 1-D vertical mixing model can simulate water column adjustments in a marginally stratified location under weakly and strongly stratified conditions.

Table 3.2: *The k-ε model constants used in these simulations.*

c_1	c_2	c_3(-)	c_3(+)	σ_k	σ_ε
1.44	1.92	-0.4	1.0	1.0	1.3

3.3.1 Model Setup

GOTM may be obtained from the online GIT repository (https://github.com/gotm-model/code) and run on most popular operating systems using:

1. an executable programme with a graphical user interface (GUI) for the Windows operating system,

2. installed and run using a pre-compiled executable file

3. compiled from source code

Using the GUI executable programme offers the user the simplest manner to run GOTM whereby the model may be run without adjusting any of the parameters in the namelist files. However, this severely restricts the user's ability to adapt the model to a user-specific shelf sea scenario. Furthermore, at the time of writing, the GUI version was not updated on the website as regularly as the source code version. Running the model using the pre-compiled executable file allows the user more flexibility in adjusting the parameters in the namelist files. The disadvantage of this method is that a pre-compiled executable may not be compatible with the computer hardware, nor operating system, and in some cases may cause floating-point bit errors in the numerical calculations. The recommended method is to run GOTM by compiling the up-to-date source code available online for your specific machine to ensure a smooth operation in which the user has full control over the setup and subsequent namelist parameters for each simulation. In this study, source code for GOTM version 4.1.0 was compiled using the Intel Fortran compiler for all simulations on a Windows 7 64-bit operating system. Model setup was completed in the Fortran namelist files. Each model simulation was undertaken in 2 minutes (wall clock) and the output data stored in NetCDF and post-processed in Matlab.

The model domain was set up to simulate the vertical water column at both MSS Stations 1 & 2, as well as the thermistor mooring location. The model domain was generated with 100 vertical grid layers for water depths of 65, 55 and 35 m — corresponding to Station 1, thermistor mooring and Station 2. A non-uniform vertical grid was employed with smaller grid spacing towards the boundaries in order to improve the boundary dynamics (Burchard et al., 2005b). This prescribed a vertical grid resolution of approximately 0.2–0.4 m near the boundaries and 0.5–0.9 m in the interior, depending on the total

water depth, H (Figure 3.14).

Two simulation periods were run that encompassed the corresponding May and August fieldwork periods. For each simulation period, the model was initialized with observational data and allowed to spin-up for three days. The model timestep was set to 1 second and the model output was averaged over ten minute intervals. Initial model simulation parameters were set to standard k-ε values (Table 3.2) obtained from the Fladenground testcase scenario (www.gotm.net).

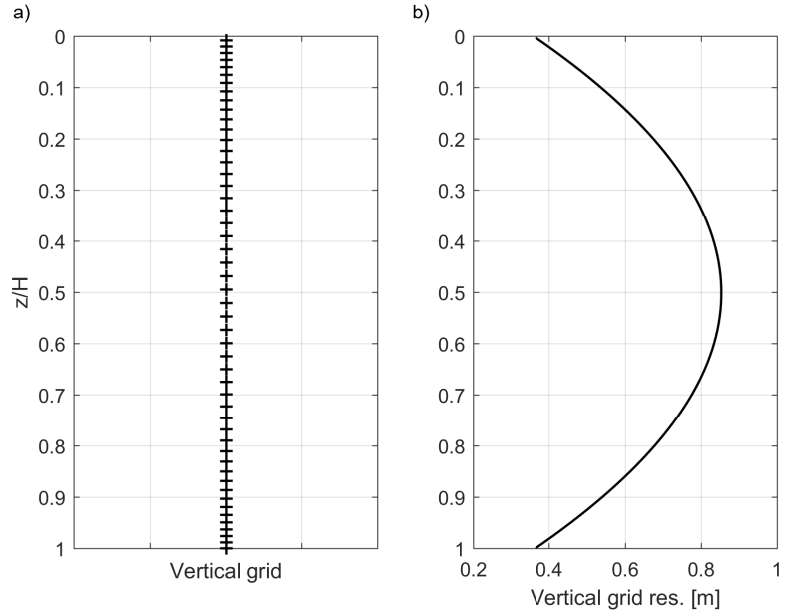

Figure 3.14: *Schematic detailing the vertical grid in the 1-D numerical model — GOTM.* ***a)*** *Here every third grid point is drawn to illustrate the increase in grid resolution employed near the boundaries.* ***b)*** *The vertical grid resolution set in the simulations was 0.38 m near the boundaries and decreased to 0.85 in the interior. The increase in grid resolution aids in resolving the boundary layer dynamics.*

3.3.2 Model Input Forcing

Pressure Forcing

Horizontal currents in GOTM are forced by both external and internal pressure forces, while explicit horizontal advection is excluded due to the horizontal constraints of vertical 1-D models. GOTM derives the external pressure forces from gradients of free surface elevation which in shelf seas are mainly driven by the barotropic tide with contributions from geostrophic and atmospheric components. The internal pressure forces are derived from horizontal density

gradients in the water although these were not explicitly prescribed in these simulations. The pressure forces may be inputted into the model by either prescribing a surface slope directly; u and v velocities from a fixed depth above the seabed from either observations, a barotropic tidal fit, or prescribing constant values; or a timeseries of full-water column u and v velocities from a 3-D model. In these simulations, ten-minute average timeseries of u- and v- velocities from the bed-moored ADCP at a single depth of 2 m above the bed were used to force the model. The advantage of forcing the model with an observed current field is that the vertical mean effects of advection and internal pressure gradients are implicitly included, whereas no effect would be included if prescribing a barotropic tidal fit or constant velocity field (Burchard et al., 1999). The assumption of zero convergence in the horizontal currents mean that the vertical velocities are set to zero to satisfy the continuity equation.

Surface Forcing

GOTM requires surface forcing in the form of heat flux, incoming solar radiation, wind stress and precipitation (Figure 3.15). The heat flux in GOTM, Q_{tot} ($>$0 into the ocean), is prescribed as:

$$Q_{tot} = Q_E + Q_H - Q_B \tag{3.6}$$

where, Q_E, is the latent heat flux, Q_H, is the sensible heat flux, and Q_B is the downward longwave back radiation at the surface. Incoming shortwave radiation is not included in Equation 3.6, since it is treated separately as a source of heat and included as its own input variable in the model. The heat fluxes were obtained from the Met Office Unified Model (v7.9) via the British Atmospheric Data Centre. Additional input surface forcing data for precipitation was also obtained from the Met Office Unified Model (v7.9). Hourly values of wind stress calculated using the Large and Pond (1981) bulk formulae were obtained from the Sevenstones wind data.

Internal Buoyancy Forcing

Prescribed temperature and salinity may either be in the form of an initial profile from which the simulation is initiated, or as a timeseries of profiles by which the model is 'nudged' towards observations. Nudging can be used in instances where the evolution of turbulent mixing is of primary importance and the simulation benefits from an accurate representation of the vertical

water structure with correct levels of buoyancy and density stratification. Both the initial profile method and nudging was carried out for temperature (Figure 3.15 g&h) in the simulations. Salinity was set to a constant value of 35.34 for all simulations since measurements showed minimal variation in salinity given the lack of freshwater sources nearby and minimal precipitation (Section 3.2.3). For each model domain, the initial temperature profile was obtained from observations. In the case of the MSS locations, the mean temperature profile over the first sampling tidal cycle was used. For the thermistor location, an average over the first day of observations were used to exclude the effect of tidal advection.

3.3.3 Model Spin-up and Validation

A model spin up period was included at the beginning to allow the initial conditions to settle to equilibrium. This was required to allow the model to adjust from initial conditions to a state of dynamic equilibrium in which the prognostic variables are numerically stable under the applied forcing. In order to reduce numerical instability during the spin up period, realistic initial conditions from observations were used. In addition, GOTM initializes many of the undiagnosed variables, such as the turbulent fields, at unrealistically low default values from which realistic values are calculated once the simulation begins. It is usually the case that achieving realistic values will take multiple time steps and while this occurs the model generates unrealistic mixing and diffusion with implications on the prognostic variables (e.g. the turbulent kinetic energy was initialized at constant values of 10^{-10} m^2 s^{-2} throughout the water column). Given an average turbulent viscosity at peak tide of 0.07 m^2 s^{-1} and a water depth of 55 m, we expect turbulence levels in the water column to equilibriate on time scales of approximately 12 hours (Equation 3.7).

$$t = \frac{H^2}{\nu} \tag{3.7}$$

where H is the water depth, and ν, is turbulent viscosity. As is shown in Figure 3.16, the elevated levels of TKE generated at the boundaries occupied the full water column in approximately 20 time steps (3.3 hours). This was faster than predicted using Equation 3.7 since levels of turbulent viscosity were larger than average in the boundary mixing layers. However, this does confirm that the model achieved turbulence equilibrium within the allocated spin-up period of three days. The corresponding effect on the temperature structure may be

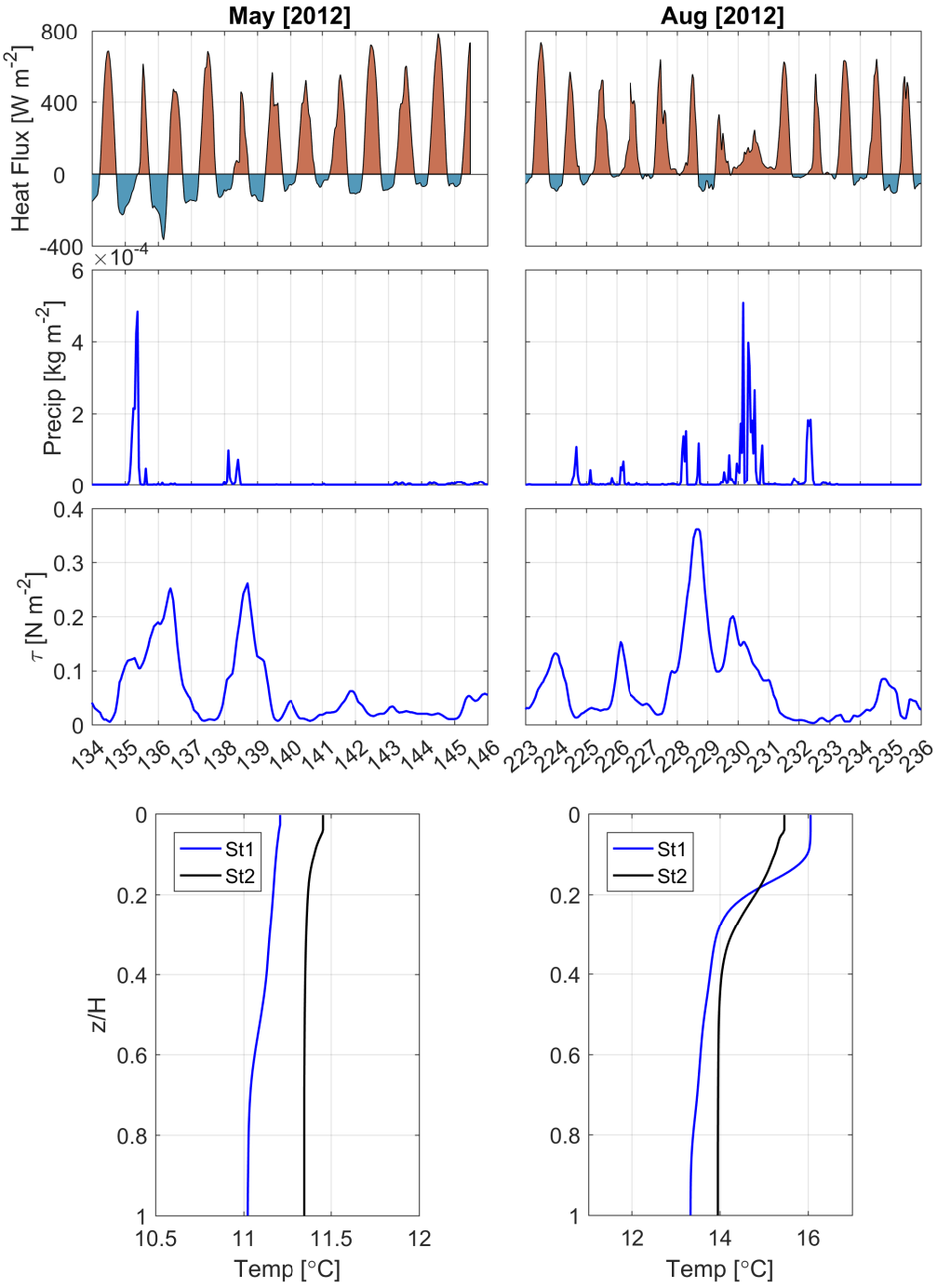

Figure 3.15: *The input data used to force GOTM in the simulations: shortwave and longwave heat flux (positive values into the ocean), precipitation (precip), surface wind stress (τ) and initial temperature profiles normalized by water depth.*

seen in Figure 3.16b.

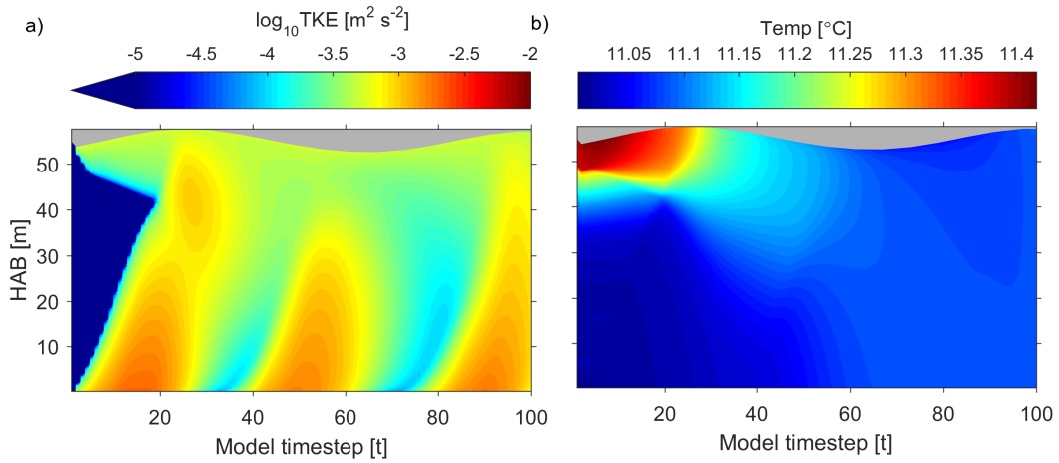

Figure 3.16: *Model spin-up showing the evolution of turbulent kinetic energy (TKE) and temperature over the first 100 time steps in simulations ($\Delta t = 10$ minutes).* ***a)*** *Levels of TKE initialized at constant background values of 10^{-10} m^2 s^{-2} over the whole water column and evolved to realistic values over 20 model time steps.* ***b)*** *The evolution of the temperature field in response to increasing levels of TKE.*

Once realistic values of turbulent mixing were achieved through the water column, the model was required to equilibriate to the diurnal heat flux cycle. In order to account for this, the model was allowed to spin-up for a period of three days prior to the start of the fieldwork for each simulation. This was deemed a suitable period by comparing the temperature and velocity structure to the thermistor timeseries and BM-ADCP. Further to choosing an adequate spin-up period, model simulations were started at slack tide in order to reduce the pressure gradients upon initialization. Realistic wind stress and net surface heat flux were initialized at the beginning of the spin-up period allowing for a smooth transition into the observation period.

The model's forcing is validated against the observed barotropic velocities from the bed-moored ADCP (Figure 3.17). Overall, the variability in the simulated velocities was well-represented by the observed velocities (Table 3.3). Greater than 94% of the variance in most of the simulated velocity components were explained by the observed velocities, except for the v-component in August which was slightly lower at 88%. The root-mean square error velocities were < 10 cm s^{-1} and slightly larger in August than in May with a maximum residual of 9 cm s^{-1}. The vertical profile of modelled velocities were in good agreement with that observed from the bed-moored ADCP. Figure 3.18 shows an example of 10-minute averaged u-velocity profile that shows good agreement

throughout the profile, including in the log-layer bottom boundary layer. Small scale variability observed in the bed-moored ADCP velocity profile were not captured by the model since current velocities were prognostic variables used as input forcing. As described in Section 3.3.2, the model was prescribed a velocity near to the bed and the velocity profile was subsequently calculated following a boundary log-layer profile.

Table 3.3: *The model's barotropic forcing validated against the observed barotropic velocities. The majority of the simulated variability in velocity may be explained by the variability in observed velocity as is shown in the high R^2 coefficients. The root-mean square error (RMSE) in the velocity components are low confirming a good fit to the observed data.*

	May [2012]		**Aug [2012]**	
	u-vel	v-vel	u-vel	v-vel
R^2	0.97	0.95	0.94	0.88
RMSE [m s^{-1}]	0.06	0.04	0.09	0.06

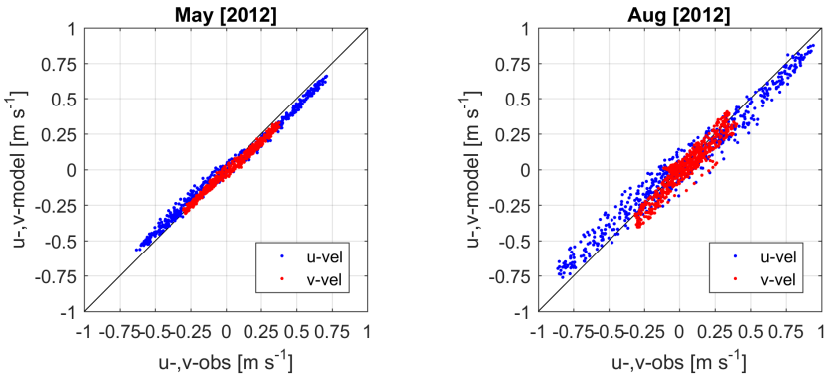

Figure 3.17: *The depth-mean u- and v-components of modelled current velocity validated versus the bed-moored ADCP components for the simulation period in May and August.*

3.3.4 Surface Wave Breaking Parameterization

The ocean's surface boundary is often assumed to behave as a classical wall layer, in which turbulent shear production is balanced by its dissipation and the velocity profile exhibits the classical logarithmic shape. Recent observations have revealed a near surface sub-layer with enhanced dissipation rates due to the diffusion of TKE generated by breaking surface waves (Agrawal et al., 1992; Anis and Moum, 1995). The implications of enhanced turbulence in the

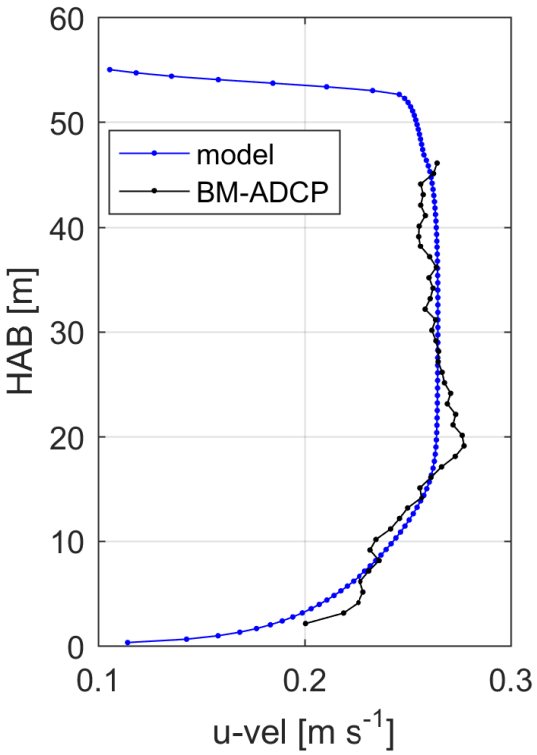

Figure 3.18: *Modelled velocities were in agreement with observed from bed-moored ADCP. Here an example profile of 10-minute averaged u-velocity show the good agreement.*

surface boundary layer is seen in the increased air-sea fluxes and the diffusion of heat from the surface (D'Asaro et al., 2014).

Surface breaking waves enhance turbulence in the surface layer by acting as a source of TKE. The effect of surface wave breaking was initially implemented in 1-D vertical turbulence models by Craig and Banner (1994) by injecting TKE at the surface at a rate, F_k, proportional to the surface friction velocity cubed (Umlauf et al., 2005):

$$F_k = \frac{\nu_t}{\sigma_k}\frac{\partial k}{\partial z} = \mu {u_\star}^3 \tag{3.8}$$

where ν_t, turbulent viscosity, σ_k, the turbulent Schmidt number, and μ is an empirically derived parameter representing the wave age and was set to 100 for fully developed waves as suggested by Craig and Banner (1994). This was implemented in the k—ε turbulence model following the modification of Burchard (2001). In the wave-enhanced layer, the effects of the increased turbulence should be detected in mixing the properties of the water column.

In this layer, a balance between the downward diffusion of the dissipated energy and turbulent dissipation is assumed, below which turbulent dissipation merges with the near-surface logarithmic layer in which shear-production balances dissipation (Umlauf et al., 2003).

Comparing the results between simulations with and without the parameterization for wave breaking show a slight increase in the turbulent viscosity profile in the upper two metres, with an associated reduction in turbulent production and increased rate of turbulent dissipation as was expected following the previous observations described above (Figure 3.19) — the viscosity and TKE production profiles were clipped in the Figure due to their zero values at the boundary. The parametrized effect of wave breaking was proportional to the wind stress magnitude with larger values during peak wind stress on Yearday 136 in comparison to low wind stress on Yearday 144. No significant changes to the temperature profiles resulted from the inclusion of surface wave breaking in the simulations. Nevertheless, the parameterization for surface wave breaking was included in all further simulations.

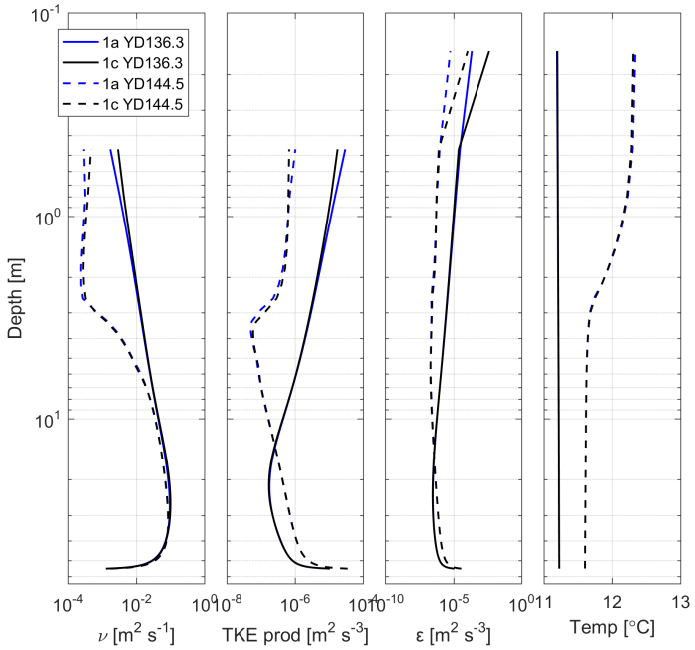

Figure 3.19: *Two simulations: 1a — no wave breaking (blue lines); 1c — wave breaking (black lines); comparing the effect of parameterised surface wave breaking on the turbulent viscosity (ν), TKE production, turbulent dissipation (ε), and temperature parameters. A further comparison between strong wind stress conditions (solid lines) on yearday (YD) 136 and weak wind stress conditions (dashed lines) on yearday 144 is included.*

CHAPTER 4

THE SEASONAL VARIABILITY OF A MARGINALLY STRATIFIED SHELF SEA FRONTAL SYSTEM

This Chapter introduces the physical dynamics within the study region and provides a seasonal comparison between spring and summer, 2012. Monthly composites of satellite-derived sea surface temperature (SST) and a simplified 1-D heating-stirring model, driven by realistic values representing the local meteorological conditions, are first presented to examine the seasonal evolution of thermal stratification in the Celtic Sea. The Chapter continues with analysis of the observational data collected at the study site in the Celtic Sea. Here, we start by describing the barotropic tidal currents, followed by the vertical water column structure and horizontal structure captured during fieldwork in both May (spring) and August (summer), 2012. The fieldwork set out to capture the early stages of the seasonal stratification in spring as well as the more strongly stratified conditions in summer and provides the basis for a seasonal comparison. During the fieldwork, a number of synoptic (strong wind and waves) and transient events (non-linear internal waves) were captured which influenced the mixing regime at the study site. Emphasis on describing the influence of these mechanisms on the horizontal and vertical structure of the water column in this marginally-stratified shelf sea setting concludes this Chapter.

4.1 The Seasonal Evolution of Temperature and Stratification in the Celtic Sea

In this Section, we examine whether a tidal mixing front is expected to occur in the vicinity of the study region due to surface heating and tidal stirring (Simpson and Bowers, 1981). Firstly, the seasonal evolution of temperature in the Celtic Sea for 2012 is investigated using monthly-mean SST values from satellite imagery. Secondly, a constant efficiency, vertical-mixing model relates the heating-stirring energy balance in the water column and is used to determine the formation of a front as described by Simpson and Bowers (1984); Simpson and Sharples (2012). Using the energy balance argument, it has been demonstrated that the position of tidal mixing fronts in the Celtic Sea are likely to occur in locations where the Simpson and Hunter criterion is $SH = 2.7 \pm 0.4$ (Simpson and Sharples, 1994).

4.1.1 Composite Monthly Sea Surface Temperatures in the Celtic Sea in 2012

Monthly-mean composites of SST were calculated using daily Level-3 Advanced Very High Resolution Radiometer (AVHRR) imagery and presented in Figure 4.1. The evolution of summertime temperatures in the Celtic Sea may be seen from the sequence of images, including the formation of a frontal boundary region within the vicinity of the study site (indicated by the white star) — the offshore waters warm and a patch of cooler inshore water remains off north Cornwall with strengthening horizontal thermal gradients into July and August.

The imagery confirmed that fieldwork conducted in May occurred during the onset of summer warming. A rapid increase in SST was observed between May and June (Figure 4.1a-b), in which temperatures increased from approximately 11°C to 13.5°C by June. The SST continues to warm into July and August, reaching a maximum of 17.5°C, before starting to cool again through September and October. The fieldwork conducted in August coincides with the period of warmest SST in offshore waters with sharp horizontal temperature gradients in the frontal region off north Cornwall.

4.1.2 1-D Heating-Stirring Model

The increase in SST observed in summer is indicative of the development of thermal stratification since the downward diffusion of heat is inhibited by the strengthening thermocline under an increasingly positive heat flux. To the contrary, the cooler SST signal observed inshore of the study site is indicative of a well-mixed water column since the lack of a thermocline allows the accumulating surface heat to be transferred down to the interior. Hence, the lack of thermal stratification allows water to be vertically mixed, bringing cooler bottom waters to the surface and thereby maintaining a cooler SST surface signature.

To test whether the observed thermal signatures within the vicinity of the study site relate to the development of stratification, a basic 1-D heating-stirring model[1] as described by Simpson and Bowers (1984) was employed to determine the monthly evolution of the water column's potential energy

[1] available online at www.cambridge.org/shelfseas

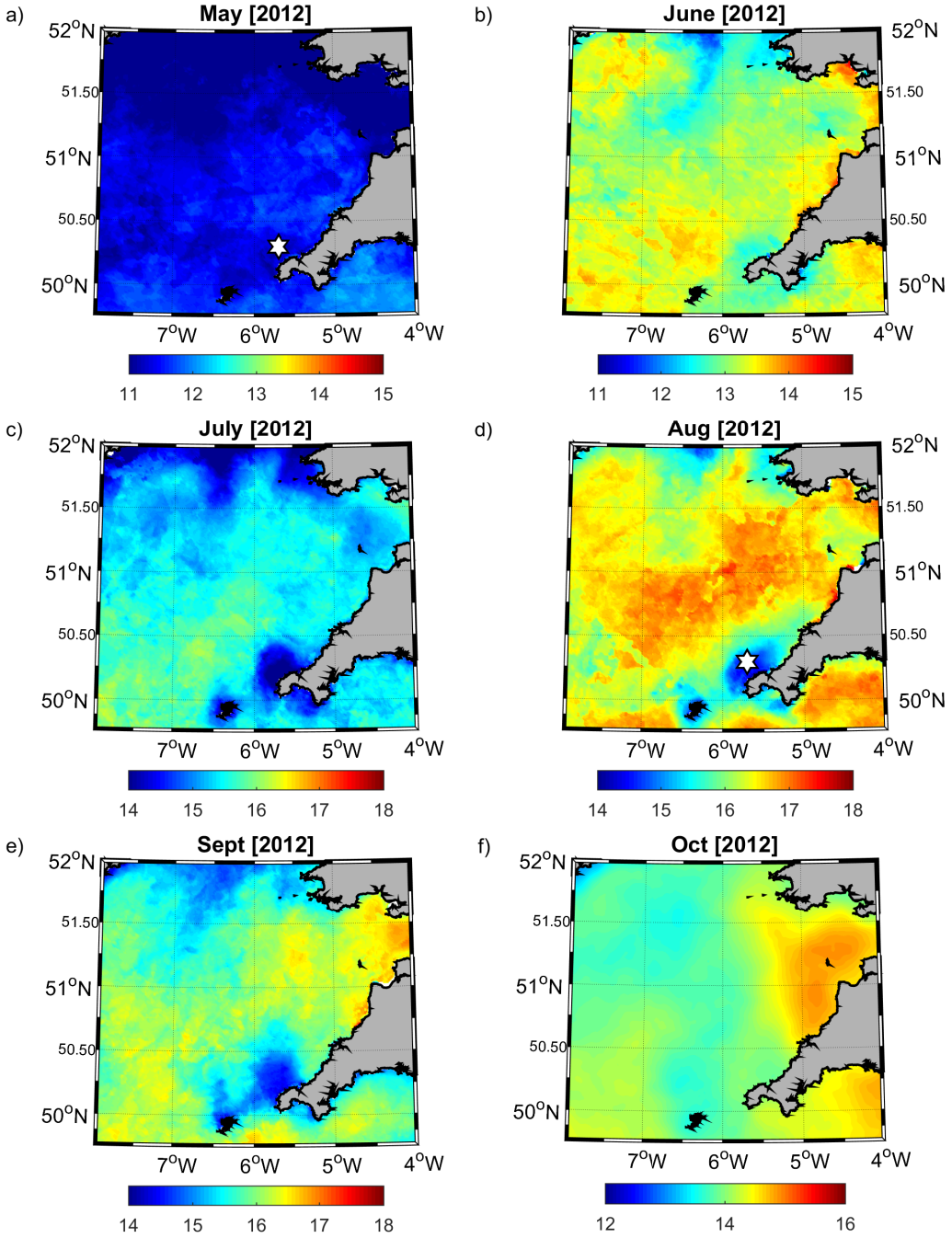

Figure 4.1: *Monthly composite SST in the Celtic Sea for summer 2012 (May–October). The observed increase in surface temperature is related to the seasonal increase in solar insolation and the subsequent onset of thermal stratification. The development of cooler inshore waters were observed off the north Cornwall coast within the vicinity of the study site (denoted at the star). Note the variable colour bars. SST measurements courtesy of NEODAAS, via Plymouth Marine Laboratory.*

anomaly, Φ:

$$\Phi = \frac{1}{H}\int_{-H}^{0}(\widehat{\rho} - \rho_{(z)})gzdz \tag{4.1}$$

where; H is the total water depth, $\widehat{\rho}$, depth-mean density, $\rho_{(z)}$, density profile, g, acceleration due to gravity, and dz is the sampling depth interval. A reference salinity of (35.34) in line with Section 3.1 was used to calculate the density. The potential energy anomaly is a quantitative measure of stratification and represents the work required per unit volume to bring about complete mixing of the water column (Simpson and Sharples, 2012). With the use of this model, the basic evolution of the vertical temperature profile may be determined, describing the influence of heating and stirring at a given location in the study region. In this instance, only variability on a seasonal scale was considered and hence may be used here to describe the warming pattern observed in the monthly SST composites in Figure 4.1. This also allowed the observations recorded in May and August to be put into a seasonal context.

The model describes a simplified two-layered water column in which buoyancy is input at the surface by solar radiation and the water column is mixed by wind and tidal forcing (Simpson and Sharples, 2012). The net heat flux (Q_n), responsible for the temperature change of the water column, is defined as the difference between the incoming solar radiation at the surface, Q_s, and the surface heat loss, Q_u, (Simpson and Sharples, 2012):

$$\begin{aligned} Q_n &= Q_s - Q_u \\ Q_u &= k(T_d - T_s) \end{aligned} \tag{4.2}$$

where; k, is a wind factor coefficient, T_d is dew-point temperature, and T_s is the sea surface temperature.

Q_s was determined from realistic values representing the local meteorological forcing and was simply defined as a sinusoidal curve fitted to ECMWF ERA-Interim synoptic reanalysis for the year 2012 (Figure 4.3a) in the form:

$$Q_s = \alpha + \beta cos(\omega t - \phi) \tag{4.3}$$

where α is the annual latitudinal mean, β, the amplitude of the seasonal cycle, ω, the frequency in radians, t, daily time step, and ϕ is the phase shift of the cycle relative to the beginning of the annum (Table 4.1).

The surface heat loss, Q_u, was calculated within the model and represents the

Table 4.1: *The variables used to fit sinusoidal curves to the meteorological parameters used in the 1D heating-stirring model.*

	Mean (α)	**Amplitude** (β)	**Phase Shift** (ω)	**Day of Max**
Solar radiation (Q_s)	119.63	109.26	-2.75	160
Wind speed (W)	8.19	2.24	0.15	356
Dew Point Temp (T_d)	9.00	4.03	2.6	209

outgoing longwave, sensible and latent heat fluxes following the equilibrium-temperature in Edinger et al. (1968). This method has the advantage that the heat loss terms are parameterised by only three terms; the dew-point temperature, sea surface temperature and wind speed (incorporated in k). The water column was initiated at the beginning of the year with a vertically homogeneous temperature profile representing the local mean winter conditions (10.7°C) after which it evolves in response to the heating and mixing terms. The surface temperature was used at each time step to calculate the heat loss term and hence a feedback between the sea temperature and net heat flux was included.

The resulting change in temperature due to the net heat flux is:

$$\Delta T = \frac{\Delta Q_i}{c_p \rho_0 h} \tag{4.4}$$

where; c_p, is the specific heat capacity of seawater (4000 J kg^{-1} C^{-1}), ρ_0, the reference density of water (1026 kg m^{-3}), and h, is the layer thickness. In the model, the heat input is distributed exponentially through the water column with 55% absorbed in the uppermost layer (Simpson and Sharples, 2012).

The kinetic stirring occurs by converting kinetic energy from the wind into potential energy. The penetration of mixing into the water column interior is limited by the available kinetic energy input and levels of stratification. The wind and tidal mixing (total power input $\times$ mixing efficiency, e) may be expressed as (after Simpson and Bowers (1981)):

$$\begin{aligned} e_s P_W &= e_s k_s \rho_a W^3 \\ e P_T &= e k_b \rho_0 \left| \hat{U}^3 \right| \end{aligned} \tag{4.5}$$

where; e_s is the mixing efficiency of the wind (0.023), e, mixing efficiency of the tide (0.004), P_W, wind power, P_T, tidal power, k_b, bottom drag coefficient,

k_s, surface drag coefficient and ρ_a, is the density of air (Simpson and Sharples, 2012). The temporal evolution of the water column thermal structure is hence a balance between the heating and stirring terms and may be formulated as:

$$\frac{\partial \Phi}{\partial t} = \underbrace{\frac{\alpha g Q_i}{2 c_p}}_{surface\ heating} - \underbrace{\frac{e k_b \rho_0 \left|\widehat{u}^3\right|}{h}}_{tidal\ stirring} - \underbrace{\frac{e_s k_s \rho_a W^3}{h}}_{wind\ stirring} \tag{4.6}$$

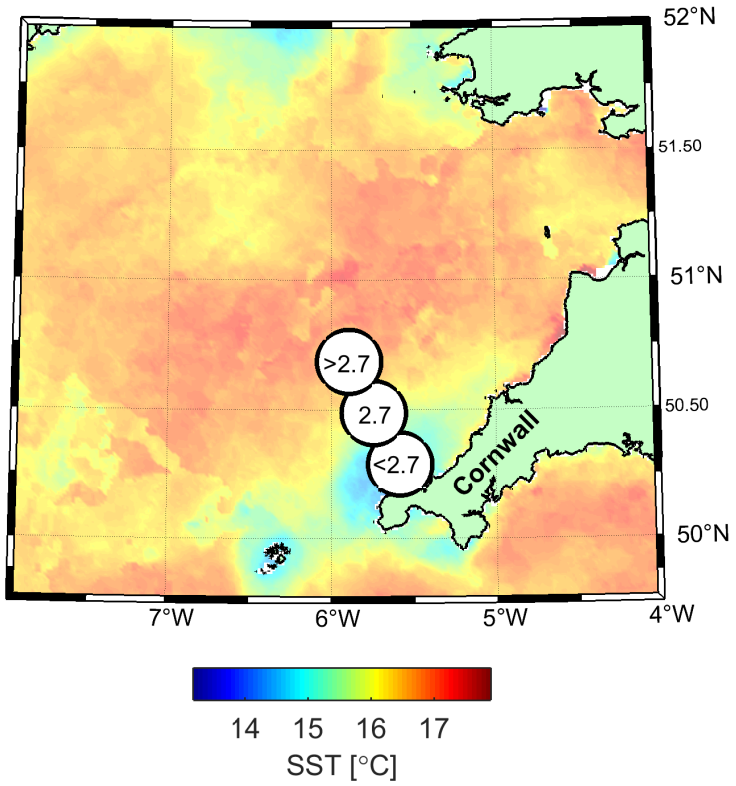

Figure 4.2: *The distribution of the Simpson-Hunter criterion ($SH = log_{10}(h/\widehat{u}^3)$) given the background monthly-composite SST values for August 2012. Warmer SST values is indicative of stratification and a SH value >2.7 since fronts in this region are likely to occur at SH = 2.7 (Simpson et al., 1982). In well-mixed conditions, the SH value would be <2.7 inshore of the frontal region.*

The model's geometry is determined analytically in terms of the Simpson-Hunter criterion, $SH = log_{10}(h/\widehat{u}^3)$, (Simpson and Hunter, 1974). The water depth and level of stratification required is provided from which the model derives the mean current speed required to satisfy the Simpson-Hunter criterion. This allows such an analytical model to be used without the current speed known a priori. Simpson et al. (1982) determined the critical value at which fronts are likely to occur in the Celtic Sea to be 2.7. SH values >2.7 are likely

to be stratified whilst <2.7 will be well-mixed conditions. In this investigation, the model compared three different shelf sea scenarios based upon this criteria, which represented a well-mixed site, $SH = 1.5$, a frontal region, $SH = 2.7$, and a strongly stratified site, $SH = 3.5$, in a manner analogous to that shown in Figure 4.2.

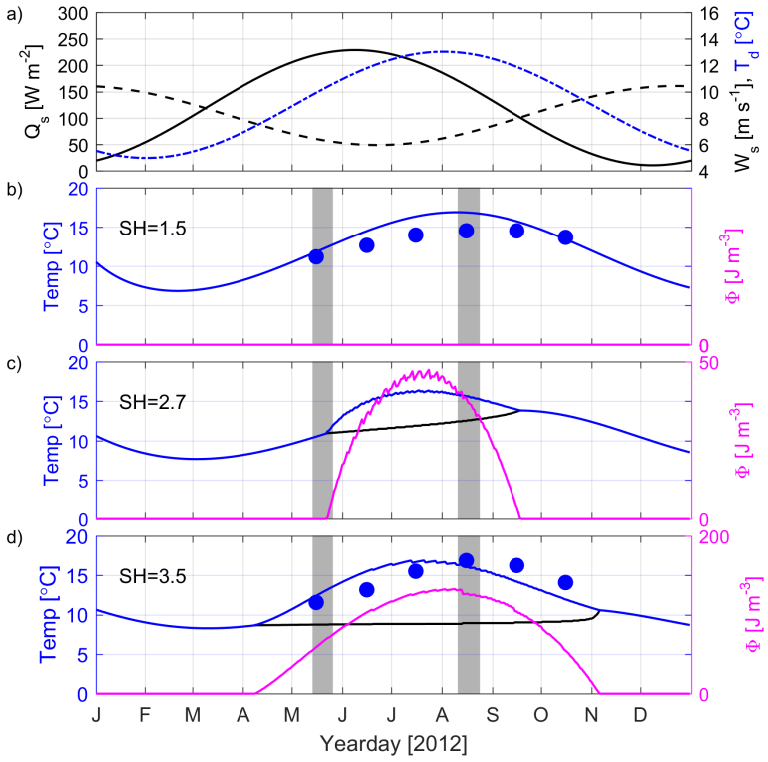

Figure 4.3: *The annual cycle of temperature and stratification (Φ) from the 1-D heating-stirring model. The meteorological parameters used to force the model is included at the top.* ***a)*** *Incoming solar radiation (Q_s; black line), wind speed (W_s; dashed black line) and dew-point temperature (T_d; blue dot-dashed line).* ***b)*** *top-bottom temperature for $SH = 1.5$, representing a well-mixed water column in the Celtic Sea. Blue line is surface temperature and black line is bottom temperature. The equivalent SST from the monthly mean AVHRR SST (above) for the well-mixed study location, off north Cornwall, is displayed as blue markers.* ***b)*** *top-bottom temperature for $SH = 2.7$, representing a tidal mixing frontal region.* ***c)*** *top-bottom temperature for $SH = 3.5$, representing an offshore stratified location. Similarly, the equivalent monthly mean AVHRR SST for a strongly stratified offshore location in the Celtic Sea is displayed as blue markers. The modelled potential energy anomaly (Φ) is presented in pink on the RHS.*

The seasonal cycle of temperature in three different shelf sea scenarios based on the Simpson-Hunter criterion, $SH = log_{10}(h/\widehat{u}^3)$, are presented in Figure 4.3b-d, showing the evolution of bottom and surface temperatures as well as

the potential energy anomaly. At $SH = 1.5$, the water was well-mixed ($\Phi = 0$ J m^{-3}) throughout the year whilst the top and bottom temperatures remained equal and varied sinusoidally in response to the input meteorological forcing. Monthly-averaged SST from Figure 4.1 (well-mixed region) are presented in blue markers for the months of May—October. The timing of maximum temperatures occurred in August (16.9°C) in the model and also in the SST (14.5°C). The simplified model overestimated the water column temperature by up to 2.4°C. This excess of heat storage may be due to the lack of advective fluxes (neaps-springs adjustment), the use of a constant efficiency model that doesn't account for stratification (Section 2.1), or alternate mixing mechanisms not included in Equation 4.6. Such shortcomings are inherent in simplified analytical models though, as argued in Simpson and Bowers (1981), the discrepancy lends itself to the notion that frontal formation in such marginally stratified conditions is a more complex process than may be predicted by the simple heating-stirring balance.

Within the frontal zone $SH = 2.7$, the model predicts weak stratification peaking in July at $\Phi = 48$ J m^{-3}. The onset of stratification occurred just after the middle of May, during the period of fieldwork (denoted by grey vertical bars), and reducing to well-mixed conditions by mid-September. Maximum top-bottom temperature difference was approximately 4°C. Maximum surface temperature in July was 16.0°C which was comparatively lower than that in $SH = 1.5$ due to the feedback in the surface heat loss term, Q_u, which increases with an increasing sea surface temperature (Simpson and Sharples, 2012). Bottom temperatures increased from 11°C at the point of separation in May to 14°C in September.

In more stratified conditions represented by $SH = 3.5$, the onset of stratification occurred earlier in the year near the beginning of April and continued through to November signifying a larger period of stratification than recorded in the other scenarios. Maximum $\Phi = 140$ J m^{-3} and a top-bottom temperature difference of 8.1°C, occurred in mid-July. Here, surface temperature was 16.8°C and bottom temperature was 8.8°C. As opposed to that observed in $SH = 2.7$, the bottom temperature did not increase steadily, instead remained relatively constant until near the end at which point a small though marked increase was observed. This is related to the relative strengths of tidal mixing and stratification inhibiting the downward flux of heat, and is discussed in further detail below in relation to the vertical temperature profiles in Figure 4.4.

The temperature profiles presented in Figure 4.4 exclude the winter months and are subdivided into two colour groups with red profiles denoting the period of increasing net heat flux (i.e. May, June, July), and blue for reducing heat flux, (i.e. August, September, October) — in order to ease the user's interpretation. For $SH = 1.5$, the water column remains vertically homogeneous with temperatures increasing from 11.9°C to 16.75°C before reducing again. At $SH = 2.7$, the water column was initially weakly stratified ($Delta$0.5°C) in May before increasing rapidly in June-July ($\sim \Delta$ 4°C). The increasing bottom temperatures observed in Figure 4.3 may also be seen here. The weaker stratification in conjunction with stronger $\widehat{u}^3$ derived in the SH parameter generates increased turbulent mixing and allows for an increased heat flux into the lower layer (Simpson and Sharples, 2012). This results in the increase in bottom temperatures that continued to warm even after the surface layer starts cooling. In the most stratified conditions at $SH = 3.5$, the water column was initially stratified ($\sim \Delta$ 3.5°C) and increased further in June-July ($\sim \Delta$ 7.5°C). As opposed to $SH = 2.7$, the bottom waters remained relatively constant and only started to increase in conjunction with a deepening thermocline, once the temperature difference reduced to $\Delta = 3.0$°C, similar to ΔT°C conditions at $SH = 2.7$. With a weakening thermocline and reduced surface heat input, higher levels of mixing was able to transfer heat into the bottom waters.

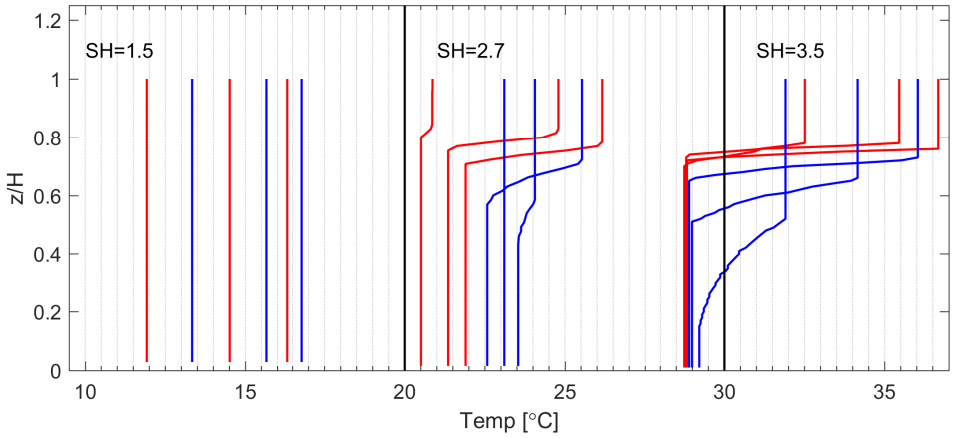

Figure 4.4: *Monthly mean temperature profiles from the 1-D heating-stirring model for the months of May through to October 2012. The depth is normalized by the water depth (H).* $SH = 2.7$ *&* $SH = 3.5$ *are offset by 10 degrees from each other.*

The monthly-composite SST imagery and 1-D heating-stirring model have combined to present an overview of the seasonal evolution of water column temperature structure in the southern Celtic Sea. The SST imagery showed that fieldwork conducted in May and August 2012 was successful in capturing

the weakly stratified conditions in Spring and the more strongly stratified conditions in Summer. The 1-D mixing model showed the evolution of the water column stratification of which the results compared favourably to model results presented in Simpson et al. (1982) for the Scilly Isles. For strongly stratified conditions off the Scilly Isles in July they recorded a maximum of $\Phi => 160$ J m^{-3} while in low stability regions $\Phi = 20$ J m^{-3}. These values were reported to be qualitatively consistent with the SH parameters.

Two processes not considered in this simple 1-D heating-stirring mixing model though have been reported to be influential in this region of the Celtic Sea are the spring-neap cycle and residual current flows (Simpson and Bowers, 1981; Simpson et al., 1982; Young et al., 2004). Simpson et al. (1982) reported significant displacement of the Φ contours in relation to SH off the Isles of Scilly. It was suggested that the influence of a northward residual current was the cause of the displacement. This residual current forms part of the overall cyclonic residual circulation pattern around the Celtic Sea region which has been successfully modelled (Young et al., 2004; Holt and Proctor, 2008) and observed in Lagrangian drifter experiments (Brown et al., 2003). Such residual currents have been found to be largely density-driven, however a significant influence from tidal residuals and wind forcing have also been reported (Brown et al., 2003).

The spring-neap tidal cycle has also been reported to influence levels of stratification through regulating the stirring power and mixing efficiencies over the fortnightly period (Simpson and Bowers, 1981). In this setup, no spring-neap variability is considered in the model since the objective was to explain the evolution of SST observed in the Celtic Sea on seasonal timescales only (Figure 4.1). The model obtains the tidal amplitude (stirring power) from the user defined SH parameter and water depth (i.e. $\widehat{u}^3 = SH/h$) and hence remains a constant.

In addition to the variation in stirring power, the spring-neap cycle introduces an additional source of stored buoyancy that is accumulated during reduced stirring at neap tides. One method of introducing the spring-neap cycle dependence on stratification is to include a variable mixing efficiency through a stability dependent term that is related to the level of background stratification as described in Section 2.1. Results from such variable mixing efficiency models show improved fit to frontal position and levels of potential energy anomalies (Simpson and Bowers, 1981; Bowers and Simpson, 1987).

This would be useful for studies focusing on shorter timescales in which the spring-neap variability would be influential on the outcomes and may form part of a further study. However, in this execution of the model, a constant mixing efficiency was used as it adequately described the seasonal evolution in water column structure.

4.2 The Barotropic Tidal Dynamics

The rest of this Chapter focuses on the data obtained from the fieldwork in May and August 2012.

4.2.1 Spectral Analysis

Barotropic tides typically constitute the primary forcing mechanism on continental shelves and play a key role in controlling the seasonal cycle and spatial distribution of stratification in the water column a has been shown in the Section above. The relative strength of the constituents regulate the magnitude and periodicity of the oscillatory motion over the tidal cycle, as well as influencing the lower harmonics such as the spring-neap cycle. In addition, the influence of a positively polarized rotation on the oscillatory motion limits the thickness of the turbulent BBL (Simpson and Tinker, 2009). Here we explore the barotropic tidal currents recorded by the long-term BM-ADCP to identify the tidal forcing periodicities that would drive the oscillatory motions experienced at the study site.

Spectral analysis, including both Fourier analysis and least-squares fitting, were performed on the 72-day, depth-mean, ADCP current record to distinguish the primary tidal forcing frequencies at the study site (Figure 4.5). The long-term ADCP data was used since it offered better spectral resolution making it possible to distinguish the semi-diurnal constituents following the Rayleigh criterion. The Rayleigh criterion states two tidal constituents of frequencies, f_j (s^{-1}), and, f_k (s^{-1}), can be separated if the record length, N (s), satisfies $N(f_j - f_k) \geq 1$. For the separation of the semi-diurnal constituents, this requires a record length of approximately greater than 15-days.

The depth-mean kinetic energy spectra is presented in Figure 4.5. The maximum peak in energy was observed at the principal semi-diurnal frequencies, M_2 & S_2, with a dominant principal lunar M_2 constituent. These results were consistent with tidal charts and numerical models for the Celtic Sea (Pingree,

1980; Kwong et al., 1997). Successive peaks in kinetic energy were observed at the principal diurnal (O_1, K_1) and the shallow-water higher harmonics, M_3, M_4, M_6.

Large amplitude shallow water constituents are known to occur in most places on the northwest European shelf, including the Celtic Sea, due to its shallow bathymetry, wide shelf, and regional tidal regime (Andersen, 1999). At the study site, the kinetic energy contained in the shallow water constituents were of the same order of magnitude as the diurnal frequencies observed in Figure 4.5. The largest amplitude shallow water constituent was contained in the M_4 overtide, generated by the non-linear interaction of the dominant M_2 constituent with itself.

No significant peak in energy was observed at the local inertial frequency. Further analysis conducted by decomposing the depth dependent baroclinic motions into the rotary components did not yield significant inertial components either.

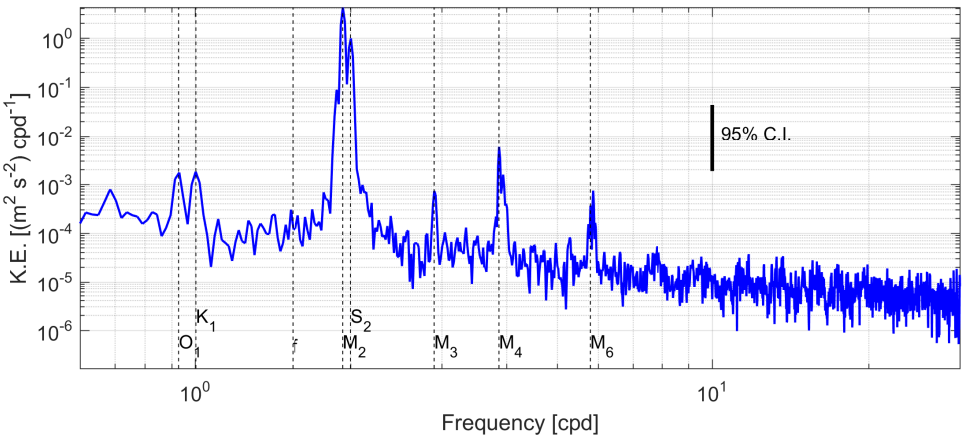

Figure 4.5: *The depth-mean kinetic energy spectra from the long term, bed-moored ADCP record (yearday 236–307). The diurnal, semi-diurnal and primary higher harmonic tidal constituents that have significant energy peaks are labelled. The local inertial frequency (f) is also displayed.*

4.2.2 Tidal Ellipse

The tidal constituents labelled in Figure 4.5, namely O_1, K_1, M_2, S_2, M_3, M_4, M_6, contained 96.4% of the total energy available in the barotropic currents. Of these, a significant proportion of the energy was contained in the M_2 and S_2 constituents (91% & of the total). Figure 4.6 presents the dominant M_2 and S_2 constituent tidal ellipses plotted on a bathymetric map at the location of the

bed-moored ADCP. The M_2 maximum current velocity amplitude was u = 0.58 m s^{-1} and v = 0.25 m s^{-1} as shown in the Figure inset. In comparison, the S_2 semi-major magnitude was approximately 47% of the M_2 magnitude with u = 0.27 m s^{-1} and v = 0.12 m s^{-1}. Both tidal ellipses exhibited a highly rectilinear semi-major axis, orientated alongshore and in parallel with the offshore depth contours.

The polarity, also known as ellipticity, is the ratio between the semi-minor and semi-major axis current velocities (L_{minor}/L_{major}), with positive values indicating rotation in a cyclonic direction (anticlockwise in the Northern Hemisphere). The polarity for the depth-mean M_2 constituent in this study was -0.06, indicating a clockwise rotating degenerate ellipse (Figure 4.6). The principal solar semi-diurnal (S_2) traces a similarly highly-rectilinear ellipse (P = -0.07), and was orientated in line with the M_2 ellipse. The polarity values and tidal ellipse parameters for these and other harmonics are presented in Table 4.2. Previous studies in the Celtic Sea have shown the tidal ellipses along the north Cornwall coast to be almost rectilinear due to the lateral constriction of the coastline (Carrillo et al., 2005). A chart of M_2 polarity presented in Simpson and Tinker (2009) shows a negatively polarised region to the southwest near the shelf break (P = -0.6) and a positively polarised region close to the mouth of the Bristol Channel (P = +0.6). The 0-polarity contour passes close to the east of the study site and confirms the minimal polarity seen in these results. Such low polarity values suggest minimal influence of the Earth's rotation in limiting mixing and instead a kinetic energy constraint exerts the dominant control at this site (Equation 4.6).

Table 4.2: *Tidal ellipse parameters in order of descending amplitude from the 72-day BM-ADCP as calculated from the least-squares fit to the harmonic constituents.*

Constituent	**Semi-major Axis [m s^{-1}]**	**Semi-minor Axis [m s^{-1}]**	**Polarity**	**Orientation [°]**	**Phase [°]**
M_2	0.615	-0.0355	-0.06	23.3	81.3
S_2	0.288	-0.0193	-0.07	22.4	112.0
M_4	0.0206	0.0087	0.42	19.9	186.0
O_1	0.0147	-0.002	-0.14	18.1	5.5
K_1	0.0132	0.000248	0.019	10.6	51.3
M_3	0.00703	-0.000495	-0.07	24.8	31.0
M_6	0.00577	-0.00097	-0.17	47.2	92.4

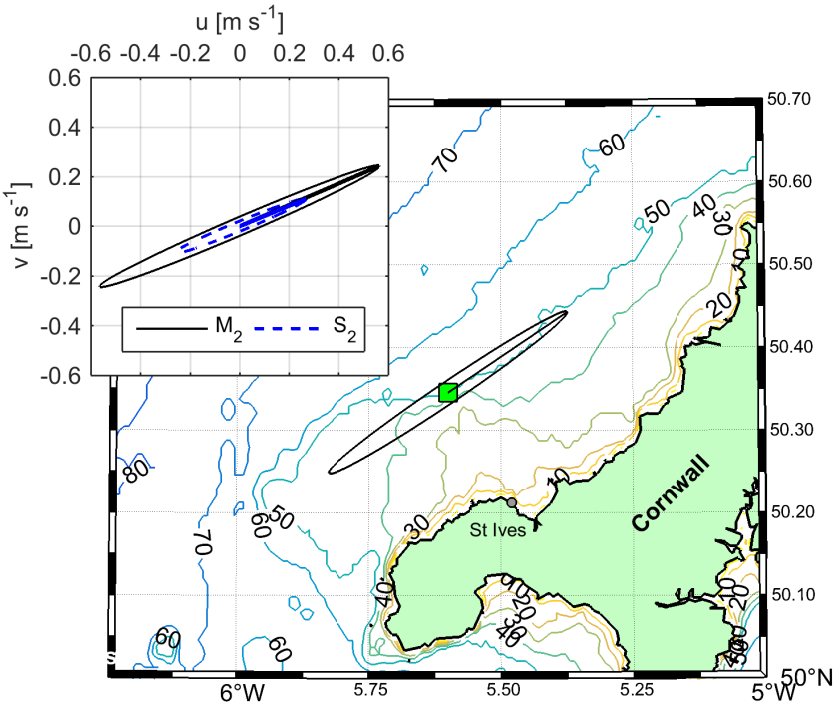

Figure 4.6: *The depth-mean M_2 tidal ellipse measured by the bed-moored ADCP (green square). The orientation of the major axis was alongshore and in parallel with the 60 m bathymetric contour.* ***Inset:*** *Scaled M_2 & S_2 ellipses. Maximum M_2 current velocities were 0.62 ms^{-1} and maximum S_2 current velocities were 0.29 m s^{-1}.*

4.3 The Weakly Stratified Regime in Spring

In this Section, the results from the 11-day deployment of the thermistor mooring and BM-ADCP, as well as the Minibat transects are presented for May, 2012. The conditions encountered in spring represented the onset of thermal stratification and conditions were generally weakly stratified as shown by the 1-D model in Figure 4.3.

4.3.1 Background Meteorological and Surface Wave Conditions

The recorded wind directions in May were spread over the NE, SE, and SW compass quadrants (Figure 4.7a). Much of the variability was at lower wind speeds, between 0–10 m s^{-1}, and are typical wind patterns for the British Isles

in Spring (Lapworth and McGregor, 2008). Stronger wind speeds (10–15 m s^{-1}) were more commonly directed from the northeast or southwest direction and associated with blocking anti-cyclones. Given the orientation of the north Cornish coastline, these winds potentially favour upwelling or downwelling conditions due to Ekman transport. A small fraction of predominantly stronger winds (10–15 m s^{-1}) were directed from the northwest quadrant. These were related to the passage of a number of low pressure systems, which are associated with stronger wind speeds though over short durations.

The wave field was predominantly directed between the west–northwest at an oblique angle to the coastline. The prevailing westerly wave direction is typical for the north Cornish coast and highlights the exposed nature of the study site to the North Atlantic Ocean to the west (Masselink et al., 2014). Significant wave heights were predominantly between 0–2 m with a small fraction between 2–3 m.

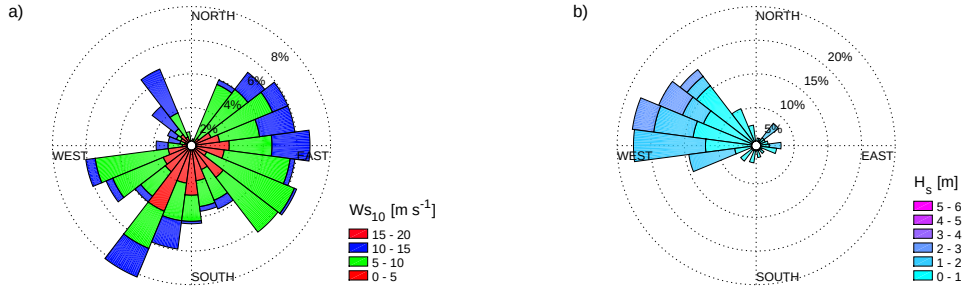

Figure 4.7: a) *Wind and* ***(b)*** *wave rose plots over the month of May 2012 (direction 'from').*

Given the strong influence of surface forcing on turbulent mixing in the upper water column, a more detailed timeseries of the wind and wave parameters is presented in Figure 4.8 and is referred to in context of the BM-ADCP and thermistor deployment between yearday 134 and 145.

Of particular interest to this study is the impact of wind and wave events on the establishment of stratification. Two strong wind events occurred towards the start of sampling on yearday 135–136 and 138 associated with the passage of

storms over the study site (Figure 4.8a). Wind speeds in excess of 10 m s^{-1} were recorded for more than 24 hours with peaks at 14.5 m s^{-1}. For the purpose of this study, we define a strong wind event to be a sustained duration of increased wind speed with maximum speeds over 10 m s^{-1}, following Korotenko et al. (2013). The first strong wind event starting on yearday 135 lasted for a duration of 38 hours (excluding the brief dip at yearday 135.25), with the wind direction veering from 270° to 350° over the course of the event (Figure 4.8b). Note the first MSS tidal cycle sampling occurred during this strong wind event. The second wind event on yearday 138 was of similar wind magnitude but slightly shorter in duration. However, the wind direction during this event was different, beginning in the east (90°) and backing north-northeast during the event. The remainder of the sampling period saw relatively consistent wind speeds with a mean magnitude of approximately 6.4 m s^{-1} with generally variable direction with a backing trend.

The first strong wind event saw a marked response in significant wave height, H_s, (Figure 4.8c). The initial increase in wind speed saw a corresponding increase in H_s to a maximum H_s of 2.8 m reached during peak wind speed on yearday 136. In contrast to the first wind event, the second wind event saw a small increase in wave height to a local maxima of 1.3 m. This may be explained by difference in direction of wind forcing for the two events. The first event was directed from the northwest, allowing for the fetch to build up the significant wave height over the open water. The second event was directed from the northeast where the build up of the significant wave height was prevented by the presence of landmass. Following these two strong wind events, the general conditions were calm with H_s <1 m to yearday 144 where an increase in H_s to 2 m was observed although no corresponding increase in local wind speeds were present. During this period, yearday 144–146, the waves were directed from 270°signifying the impact of a large fetch originating from the offshore shelf and Atlantic Ocean.

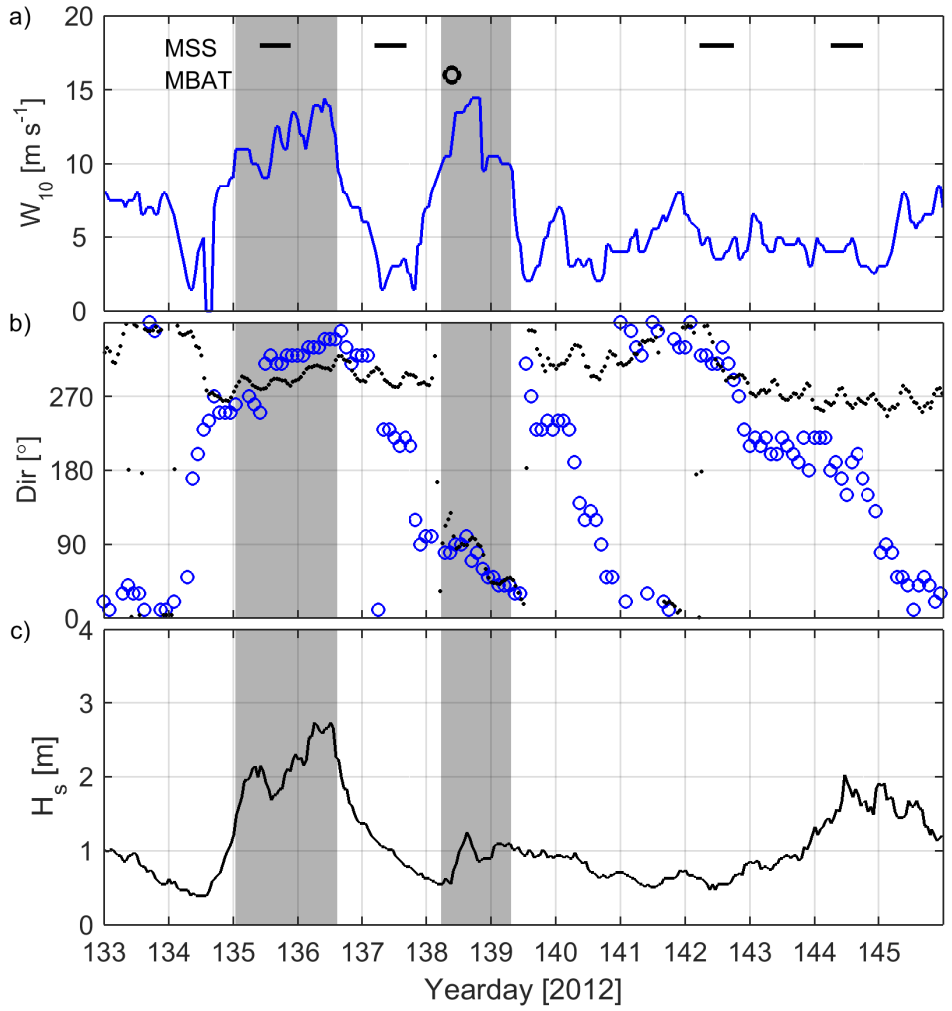

Figure 4.8: *Meteorological and wave conditions during fieldwork in spring 2012.* ***a)*** *hourly mean wind speed. Sustained winds >10 m s^{-1} are denoted in grey shade;* ***b)*** *wind (blue) & wave (black) direction (directions 'from');* ***c)*** *hourly mean significant wave height. The timing of MSS sampling and Minibat transects are presented in (a).*

4.3.2 The Sub-tidal Residual Currents in Spring

The requirement to remove the tidal signal in order to investigate the sub-tidal signal is justified by the dominant tidal signal on the North-west European shelf that typically exceed 90% of the total current variance (Carrillo et al., 2005; Brown et al., 2012). The tidal analysis conducted here and described in Section 4.2.1 are in agreement with these studies and showed $> 90\%$ of the current variability to be at tidal frequencies. Given the predominance of the oscillatory tidal signal in shelf seas, the background low-frequency currents

can be difficult to distinguish due to their relatively small amplitudes. These low-frequency currents may be referred to as residual currents and extracted by low-pass filtering the data with a carefully selected cut-off frequency that excludes the diurnal tidal signal and higher harmonics (Emery and Thomson, 2001).

A rudimentary method for removing the tidal signal is to implement a running-mean filter with a smoothing window greater than the diurnal frequency period. However, this method does not adequately suppress the tidal signal and leads to contamination of the low-frequency, sub-tidal, signal. In order to further reduce contamination from the tidal frequencies, Godin (1972) devised a 'tidal-elimination', cascading running-mean filter in which the hourly current observations are smoothed twice using a 24-point average and once using a 25-point average ($(A_{24}^2 A_{25})(24_{25}^2)$). Although this filter is an improvement on the prior method, spectral leakage from the diurnal frequency band is known to still occur in addition to significant attenuation in the 2–3 day weather window (Emery and Thomson, 2001; Shirahata et al., 2016). This attenuation may be particularly problematic for this study given the 1–3 day duration of the significant wind events. As has been previously described, the shelf sea response to external forcing is of particular interest to this study and therefore the residual currents in response to the wind forcing required particular attention. Hence, the Godin filter was deemed unsuitable and an alternate filter with a sharper cut-off frequency chosen. The filter eventually selected was the Chebyshev Type II low-pass cosine filter, selected due to its sharper cut-off frequency characteristics (Figure 4.9).

The choice of cosine filter parameters were carefully selected in order to reduce the leakage of unwanted diurnal tidal energy into the low frequency signal and its maximally flat passband window that would allow most of the sub-tidal energy to be retained. The filter response properties were determined by the cut-off frequency, 0.75 cycles per day, and an 8^{th} order transfer function, which minimized the spectral width of the transition band (effectively the width of the cut-off frequency between the passband and stopband). The magnitude of the stopband attenuation was set to -40 dB, which corresponds to an attenuation factor of 100 applied to the high-frequency component (Emery and Thomson, 2001). In addition to the sharp cut-off frequency, the phase properties of the signal were preserved by operating the filter in both the forward and backward direction over the timeseries. The filter response for

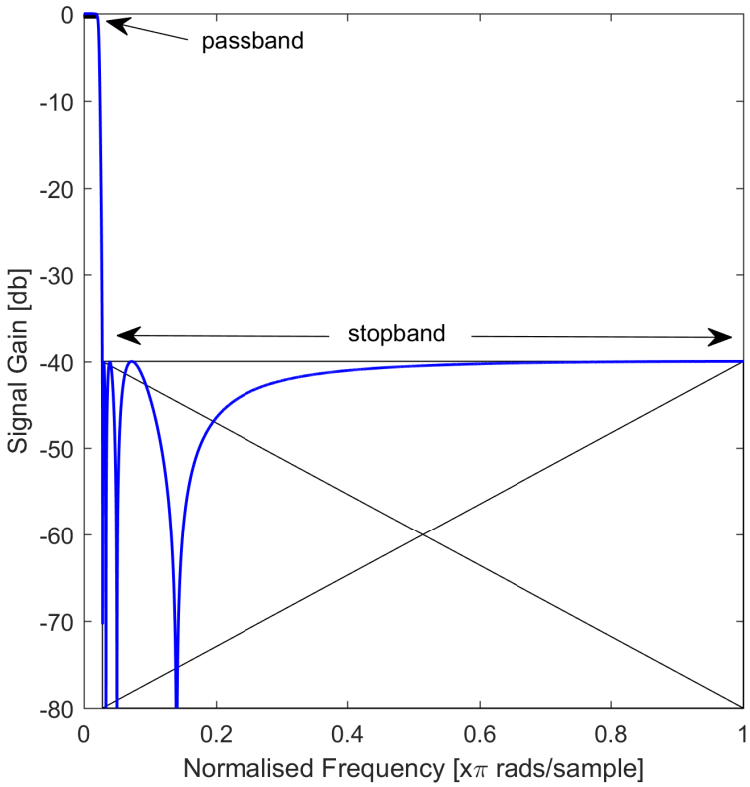

Figure 4.9: *The magnitude response for a Chebyshev Type II filter design used to detide the bed-moored ADCP data. An 8th-order low pass filter with a passband frequency limit of 0.75 cpd and a stopband attenuation of 40 dB was selected. The frequency is normalized by the Nyquist frequency and the negative signal gain denotes an attenuation of the signal in the stopband frequencies (-40 dB equates to a signal attenuation factor of 100).*

the selected Chebyshev Type II filter is shown in Figure 4.9 and highlights the flat passband and the narrow transition band which adequately filters out the diurnal tidal component (0.9–1 cpd). However, such a narrow transition band induced overshoot ripples and end-point 'ringing' (instability) that was observed at the beginning of the filtered timeseries. This required the first and last 24 hour portion of the filtered signal to be discarded. The resultant kinetic energy spectra for the sub-tidal signal is shown in Figure 4.10 and confirms that the low-pass filter successfully retained the sub-tidal signal whilst filtering out the diurnal and higher-frequency tidal signal. The results of the sub-tidal analysis showed the average residual current magnitude was 0.04 m s^{-1}, whereas the dominant tidal signal was an order of magnitude larger; 0.4 m s^{-1} (Figure 4.11). The $u-$component of the residual signal tended to be larger than the $v-$component, describing a predominantly easterly flow

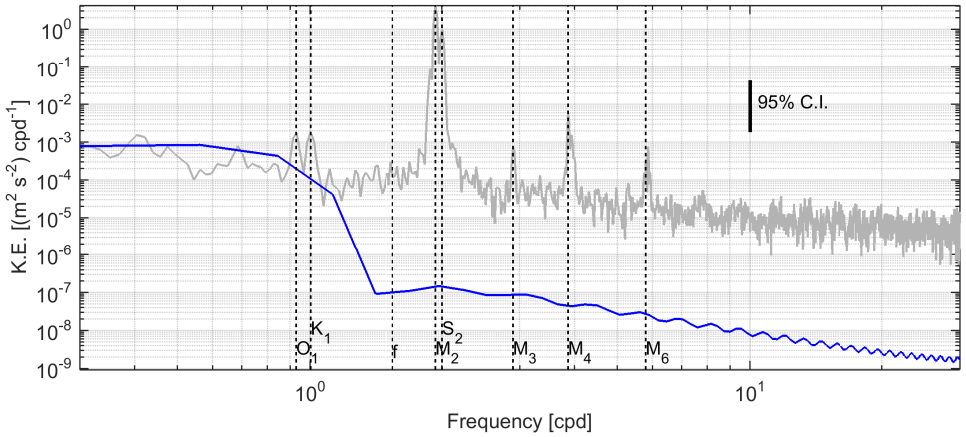

Figure 4.10: *The kinetic energy spectra for the sub-tidal residual signal in May. The background kinetic energy spectra is provided for comparison in grey.*

with a maximum $u-$component velocity of 9.5 cm s^{-1} attained on yearday 139. Sustained periods of strong winds caused pronounced variability in the sub-tidal residuals with the current responding to the wind direction in a manner resembling classical surface layer Ekman dynamics; a thin surface boundary Ekman layer forms under a wind-driven frictional stress and the integrated transport within this layer is directed to the right in the northern hemisphere and perpendicular to the wind (Ekman, 1905). The reversal of the residual current (Figure 4.11b) on yearday 136 during strong northwesterly winds (14 m s^{-1}) supports this notion, given that the wind direction would drive an Ekman transport to the southwest (negative $u-$ & $v-$ components).

The above dynamics best describes a simple case of unstratified, deep-water, conditions forced by a steady wind stress in which the Ekman transport would be; $\tau_s/rho_{ref}f$, and the surface Ekman boundary layer depth; $D = \sqrt{2\nu_t/f}$, is relatively thin in comparison to the water depth (where τ_s, is the surface wind stress; rho_{ref}, reference density, f, Coriolis parameter, and ν_t, the vertical eddy viscosity). The actual situation was complicated by shallow waters and the presence of the coastal boundary. In the case of shallow water depths, the frictional influence of the seabed prevents the development of the surface Ekman boundary layer and causes the momentum from the wind to be mixed to the bottom faster than the Coriolis acceleration can turn it; in this instance, the residual transport runs parallel with the wind (Ekman, 1905). This may be particularly important towards the inshore station (St2) but also during weakly-stratified conditions in May or even during spring tides when enhanced mixing extends the region of well-mixed waters thereby eliminating the slab-

like surface layer formed by the presence of stratification (Lentz, 2001).

Given the proximity to the coast in this study, the wind-driven component of the residual current is further influenced by the set up of pressure gradients. In this case, the northwesterly winds experienced on yearday 136 would act to pile up water against the coast and produce an opposing pressure gradient to balance the wind stress that would drive an offshore return flow (Tilburg, 2003). The downslope transport of less dense water within the BBL has been observed to generate enhanced turbulent mixing and cause an increase in BBL height (Trowbridge and Lentz, 1991; Hosegood and van Haren, 2003). During the second strong wind event (yearday 138), the wind was directed from the east and a subsequent reduction in eastward velocity was observed though the northward component persisted indicating an offshore flow again in line with Ekman dynamics. These surface offshore flow conditions suit the formation of upwelling along the coast since an bottom return flow is typically generated. In such conditions, strengthening of the vertical water column stability is predicted due to the denser bottom waters being forced up the slope (Lentz and Trowbridge, 1991). A wind stress that causes strong upwelling therefore has the potential to create a strongly stratified inshore region (Horwitz and Lentz, 2016). Following the passage of the second wind event, wind speeds rapidly decreased and veered round to the southwest. The residual currents were observed to increase with a strongest gain in the easterly component. A further veering in wind direction to the northwest on yearday 142 resulted in a similar reduction in the easterly current component as was observed on yearday 136.

The progressive vector diagram presented in Figure 4.12 shows the advection of bottom and surface water parcels to the northeast as a result of the computed residual currents under the assumption of a spatially uniform current field. This assumption is especially limited in coastal shelf seas due to the significant variability in currents from the effects of bottom topography and coastline geometry (Carlson et al., 2010). Nevertheless, in this instance, it provides a synoptic overview of the computed tidal excursion as well as the direction and distance of the background low frequency component. The average tidal excursion over a single spring tide, semi-diurnal, oscillation was 9 km with larger excursions occurring with the stronger current magnitudes at spring tides. The sub-tidal residual signal generated an average velocity of 3 km day^{-1} (3.5 cm s^{-1}).

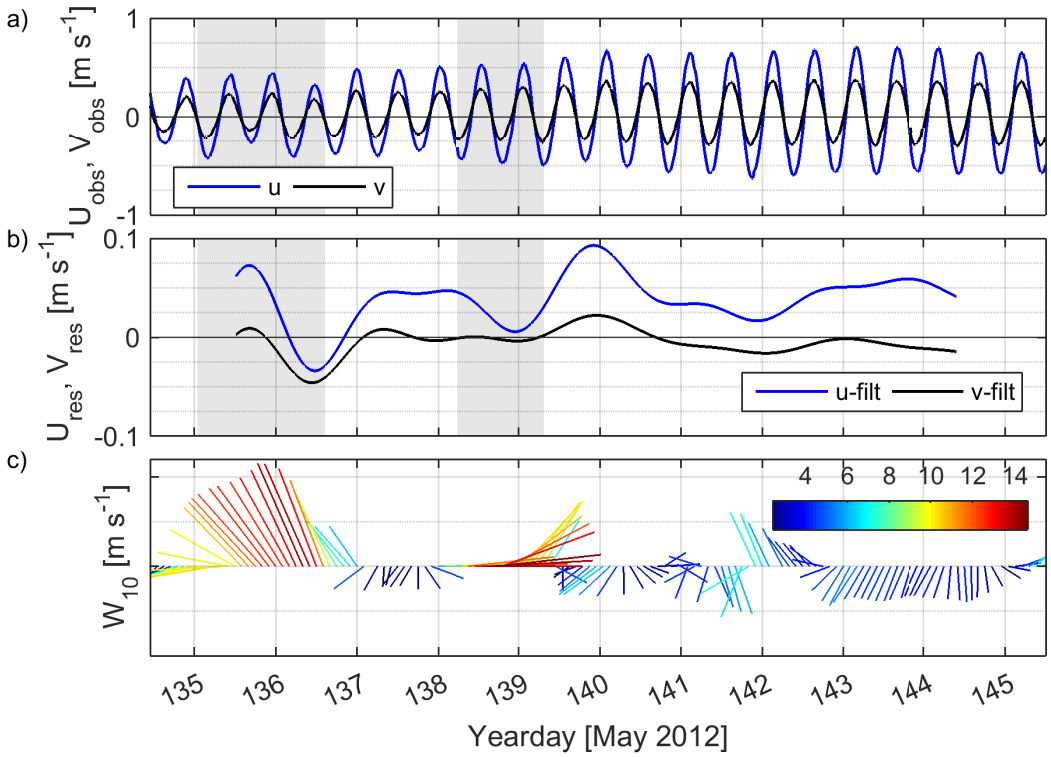

Figure 4.11: *The low frequency currents from the bed-moored ADCP during Spring fieldwork deployment.* ***a)*** *smoothed, depth-mean velocity components;* ***b)*** *residual current as calculated by an 8-th order Chebyshev Type II low-pass filter (0.75 cpd) to exclude the tidal signal;* ***c)*** *wind vector diagram showing velocity magnitude in colour (m s^{-1}) and vector direction 'from' (north up). Sustained winds >10 m s^{-1} are denoted in grey shade.*

The residual current flow differed between the surface and the near-bed with a stronger flow near the surface. As predicted, the surface flow was also influenced to a greater degree by wind stress as may be seen in the directional variability matching that described in Figure 4.11c. The result of the south-easterly wind stress on yearday 135–137 is observed in the Figure inset and describes an anti-cyclonic oscillation which was much more pronounced in the surface current; the bottom current merely reversed direction although in a cyclonic sense. Following the abatement of the significant wind event on yearday 136, and change in direction to the southwest, the residual currents continued to flow to the northeast. The resultant northerly shift during the second strong wind event was also identifiable on yearday 139. The near-bed signal again showed a subdued response to the apparent wind forcing with only a small northward shift on yearday 139. Following these two significant wind events, the direction of the sub-tidal flow continued to the northeast with the surface current orientated more to the north and with a greater daily excursion. By

the end of measurements on yearday 145, the surface and near-bed flows were separated by 15.9 km.

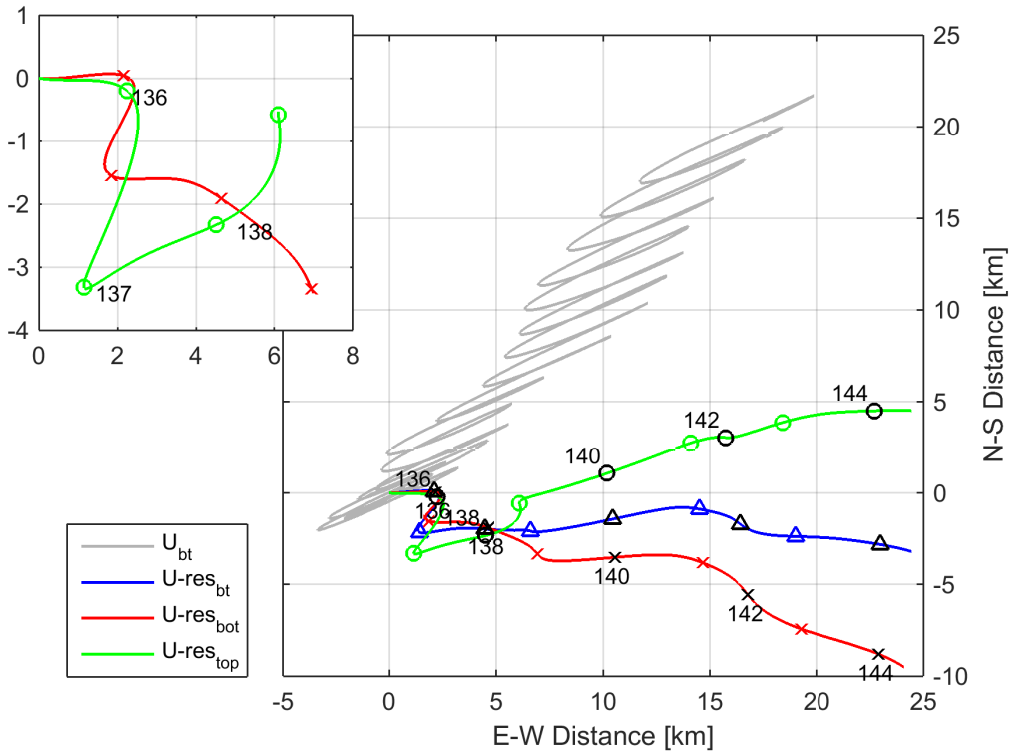

Figure 4.12: *The progressive vector diagram for currents measured by the BM-ADCP in Spring describing the water movement in a Lagrangian frame. The observed barotropic tidal currents are presented in grey and shows the tidal excursion limits over each tidal cycle. Computed surface- (green), depth-mean (blue), and near-bed- (red) residual currents are presented with the daily excursion indicated by yearday number.* ***Inset:*** *A low frequency oscillation in the surface current was observed between Yearday 135–137 with a less pronounced current reversal seen in the near-bed ADCP record.*

The results of this analysis indicated that wind-driven Ekman dynamics plays an important role in controlling the residual currents in the region. These results were in agreement with previous studies conducted in the Celtic Sea and Irish Sea. Howarth (1975) reported mean currents of 10 cm s^{-1} in response to significant wind events of 10 m s^{-1} and maximum velocities of 30 cm s^{-1} in unstratified conditions in St George's Channel. Further studies in this region found similar residual velocities from drifter tracks of 11 km day^{-1} (13 cm s^{-1}) along a thermal front, and 3 km day^{-1} (4 cm s^{-1}) away from the frontal feature (Horsburgh et al., 1998). Brown and Gmitrowicz (1995) reported that wind forcing was a primary driver of the low-frequency, along-axis variability in flow — through the generation of along-channel pressure gradients and direct wind

forcing — in the narrow North Channel of the Irish Sea, with the wind-driven component contributing between 2.5–11 cm s^{-1} of a mean flow of 20 cm s^{-1}. It was noted that cross-channel pressure gradients and tidal residuals also contributed to the flow.

4.3.3 The Vertical Water Column Structure in Spring

A more detailed timeseries of the meteorological parameters and the vertical water column structure are presented in Figure 4.13 for the period of the thermistor and BM-ADCP deployment in May. The wind speed was presented in terms of wind stress (τ) upon the sea surface, along with significant wave height (H_s) due to their potential to induce a downward momentum flux and the associated turbulent mixing (Figure 4.13a). During the strong wind events on yearday 135–137 and 138 peak wind stresses of 0.36 N m^{-2} were recorded on both occasions. Apart from these two events, the wind stress remained below 0.1 N m^{-2} for the rest of the deployment. The vertical temperature difference (ΔT) measured between the upper-most and bottom-most thermistor sensor on the mooring is also included in grey shade on the tertiary axis. Figure 4.13b presents the calculated surface buoyancy flux, J_b, (Equation 4.7) and provided a measure of buoyancy input at the surface from both thermal heating and freshwater input.

$$J_b = \frac{\alpha g Q_i}{c_p \rho} + \frac{g\beta}{\rho}(E - P)S_{surf} \tag{4.7}$$

where, α, is the thermal expansion coefficient; g, gravity; Q_i, surface heat input; c_p, specific heat capacity of water; ρ, density of seawater; β, haline contraction coefficient; E, surface evaporation; P, surface precipitation; and S_{surf}, surface salinity. Negative values of J_b indicate stabilizing conditions of heat input or precipitation into the ocean. In this case, the main buoyancy input was due to the seasonal heat input since there was negligible precipitation recorded and no significant sources of land drainage are known to occur within the vicinity of the study site.

The temperature timeseries, buoyancy frequency squared and vertical shear-squared are also presented in Figure 4.13c,d,e, respectively. The temperature timeseries was smoothed using a moving-average boxcar filter over a period of 1-hour and 15 m in the horizontal and vertical dimensions, respectively. Further bin-averaging to 10 minute and 2 m intervals were conducted for calculations of N^2 and S^2. The surface buoyancy flux (W kg^{-1}) was measured using a constant surface salinity of 35.34 as discussed in Section 3.2.3.

The vertical temperature structure contained a short period of near-surface thermal stratification ($N^2 = \log_{10}$-4.2) at the beginning of sampling with a calculated ΔT of 0.4°C. The warm surface water temperature decreased at the beginning of yearday 135 with a downward mixing of warm surface waters observed throughout the recorded water column. The subsequent breakdown of stratification (decrease in N^2 and a rapid decrease in ΔT) and rapid deepening of isotherms was associated with high S^2 ($\log_{10}$-4) in the mid-water column indicating the potential for shear-induced turbulent mixing.

The water column remained generally well-mixed for the remainder of the deployment apart from periods of near-surface warming that caused episodic increases in ΔT of approximately 0.1°C. The well-mixed structure was also seen in the contoured temperature structure (Figure 4.13c), in addition to the minimal N^2 levels in Figure 4.13d (10^{-6}–10^{-5}). Further periodic episodes of very weak stratification was measured in the ΔT that were typically $\leq$ 0.1°C. These episodes generally coincided with a positive buoyancy flux that was strongly regulated by the daily heat flux cycle.

An overall small warming trend over the deployment period was observed which extended throughout the water column in the well-mixed conditions. The temperature at the beginning of observations was approximately 11.0 °C and warmed by 0.7 °C over the 12-days. The increase in temperature was interspersed with periods of cooling ($\sim$ 0.1°C), creating a vertical banding pattern in the water column. This pattern was observed to occur at a semi-diurnal periodicity indicating it was most likely due to tidal advection (Figure 4.13).

Values of N^2 were generally low due to the lack of stratification observed in the temperature field. Short periods of elevated $N^2 = 10^{-5}$ s^{-2} were observed in the upper half of the water column whilst values remained low within the BBL (10^{-6} s^{-2}). In contrast, increased levels of shear were evident within the BBL occurring at semi-diurnal tidal periodicity, with maximum shear (10^{-4} s^{-2}) extending 10–30 m above the bed over the neap-spring tidal cycle. In general, elevated shear levels within the BBL were diminished at neap tides and conversely extended higher up in the water column during spring tides. Away from the bottom boundary, shear levels generally reduced with minimum $S^2 = 10^{-6}$ (s^{-2}) in the upper water column.

Periods of enhanced shear in the upper water column were generally associated

with elevated shear throughout the water column. These generally lasted the duration of a semi-diurnal tidal cycle although did not occur regularly. However, it was noticed that enhanced levels of upper water column shear generally caused a deepening of isotherms and a subsequent warming of the water column was observed. Whether this indicates active shear-induced turbulent mixing as the cause of the deepening was not immediately discernible and there seemed to be no direct link with the prevailing meteorological conditions nor heat input. A mechanism able to create unstable stratification at tidal periodicities is shear-induced convection where a horizontal density gradient is associated with vertical shear. In this instance, heavy water may be advected over lighter water and has been observed to occur on the continental shelf especially in regions of freshwater input and tidal mixing fronts (Allen et al., 1980; Sharples and Simpson, 1993; Rippeth et al., 2002). Model studies by Holt and Umlauf (2008) also have confirmed the occurrence of shear-induced convection in stratified shelf seas. This elevated levels of shear observed in the upper water column warranted further investigation that was taken up in Chapter 6

To investigate the vertical banding observed in the temperature timeseries, Fourier analysis was performed on the the top-most and bottom temperature records from the thermistor mooring to investigate the periodicity of the observed fluctuations (Figure 4.14). Also included was the calculated temperature timeseries (T_Q) from the surface net heat input (Equation 4.4). T_Q was calculated from yearday 136 since the initial period of stratification, on yearday 134–135, was poorly represented by the calculated net heat flux. The observed warming trend in the thermistor timeseries over the period of deployment was in good agreement with the predicted temperature increase from surface heating alone (T_Q).

The thermistor timeseries presented short-term, higher frequency variability that was not contained in T_Q. The temperature difference ($T_{detrend}$) between the observed and that calculated from the net heat input (T_Q) is presented in Figure 4.14b, from which the frequency spectra for both top and bottom timeseries were calculated in order to identify the periodicity of the high frequency variability (Figure 4.14c). The vertical banding observed in Figure 4.14c was clearly seen in the residuals in both the upper and bottom temperature timeseries. The Fourier analysis of the de-trended temperature timeseries indicated a strong semi-diurnal and diurnal periodicity associated with the

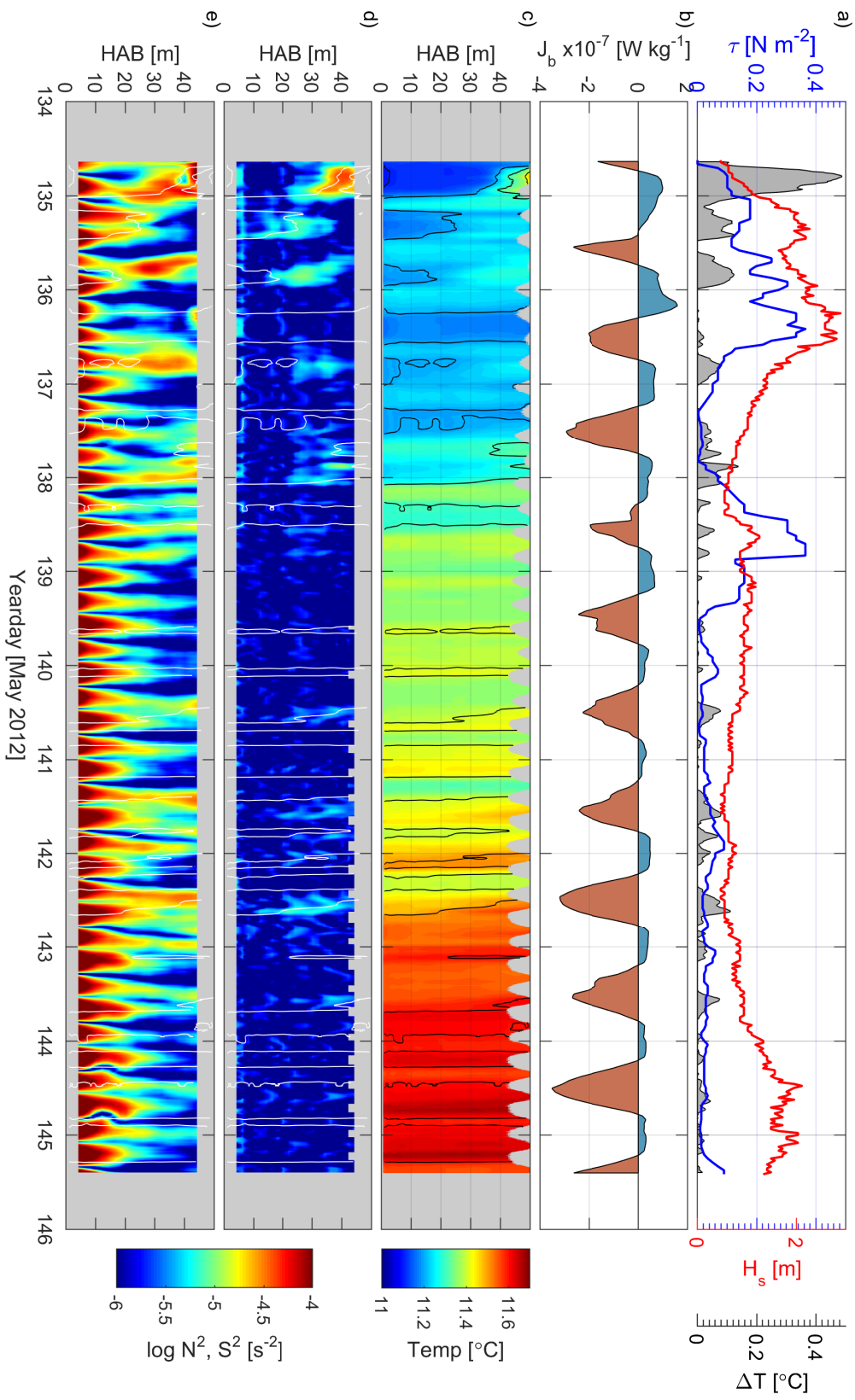

Figure 4.13: *Input forcing and vertical water column structure during the spring thermistor and BM-ADCP deployment.* ***a)*** *Observed wind stress from Sevenstones met buoy (τ), significant wave height from the Wave Hub wave buoy (H_s), and top-bottom thermistor temperature difference (ΔT) denoted in grey shade;* ***b)*** *buoyancy flux with negative values indicating a heat input into the ocean (J_b);* ***c)*** *thermistor mooring temperature (°C);* ***d)*** *buoyancy frequency squared (N^2);* ***e)*** *vertical shear squared (S^2). Temperature contours at 0.1°C intervals are overlaid on* ***c,d,e****.*

observed vertical banding (Figure 4.14). This is indicative of horizontal advection caused by the barotropic tides which were predominantly semi-diurnal at the study site.

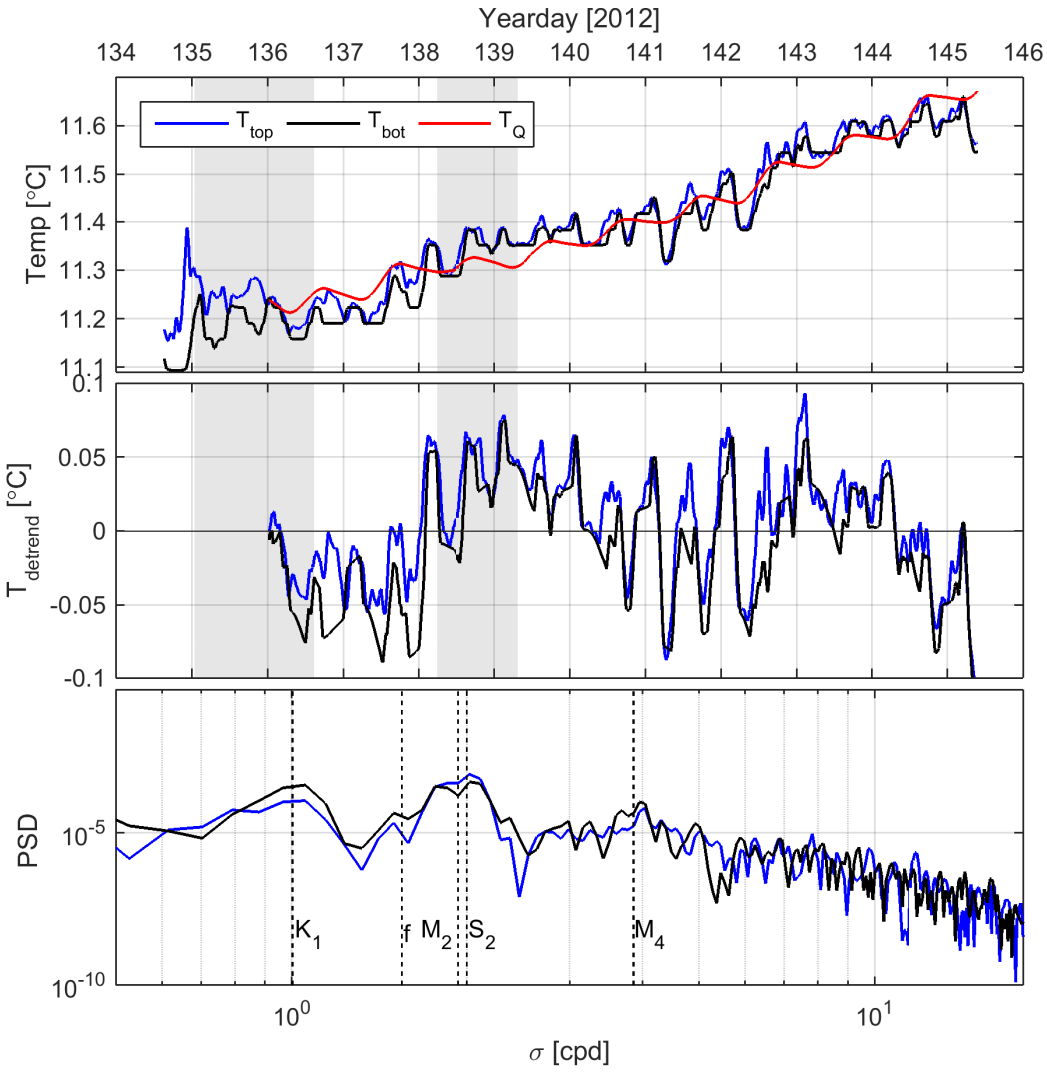

Figure 4.14: *Spectral analysis conducted on the thermistor temperature timeseries presenting the dominant signals observed.* ***a)*** *Temperature timeseries over the period of deployment in May from the top-most (blue) and bottom-most (black) thermistor sensor timeseries. The calculated surface net heat input (T_Q) is also presented. This was subtracted from the thermistor temperature to obtain residuals with the diurnal and lower-frequency variability excluded in order to investigate the high-frequency signal observed in the timeseries.* ***b)*** *The resulting de-trended and de-meaned residual temperature signal for the timeseries in (a).* ***c)*** *Power spectral density of the de-trended signal (b) with a hanning window applied. Primary tidal constituents and the local inertial frequency are labelled accordingly.*

4.3.4 The Spatial Water Column Structure in Spring

The thermal structure of the water column in the vicinity of the study site was surveyed between the inshore and offshore MSS sampling sites (Figure 4.15a). The transect was conducted on yearday 138 following the strong wind event on yearday 135–136 (Figure 4.15b). At the beginning of the transect, the inshore waters were vertically well-mixed and approximately 11.45°C. Contrary to what was expected, the inshore waters were approximately 0.2°C warmer than those observed further offshore. The SST in Figure 4.15a showed the inshore waters near St2 to be warmer than those offshore near St1 by approximately 1.5°C. This was suggested to be caused by the strong wind event which pushed the warmer offshore surface waters onshore since the winds were directed from the northwest. Further evidence for this was observed off the southern coast of Cornwall where, conversely, upwelled cooler waters due to the offshore winds were observed. Further offshore the water column was weakly stratified with much of the stratification in the upper 15 m. The largest vertical $Delta$T was present at 13.5 km (from the start of the leg) and associated with the presence of cool waters at 19 m.

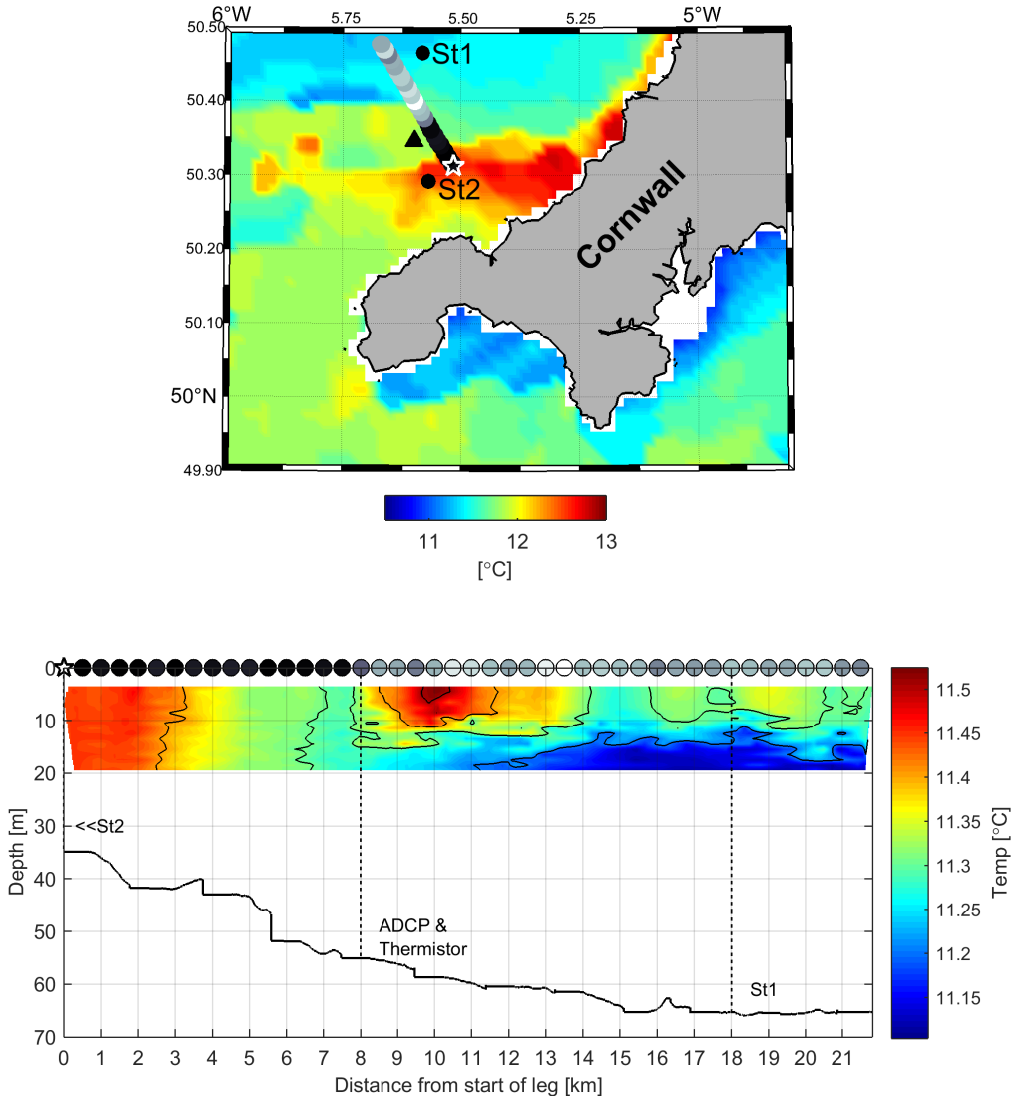

Figure 4.15: Top: *SST imagery from yearday 138 with the vertical temperature difference from a Minibat transect overlaid. Darker colours indicate a smaller ΔT and well-mixed waters whereas lighter colours indicate a larger ΔT and stratified waters. The pentagram indicates the start point of the transect shown in the bottom panel.* ***Bottom:*** *Vertical temperature structure from the MiniBat transect on yearday 138. Temperature contoured every 0.1°C. The position of the two MSS stations (St1 & St2) and the BM-ADCP and thermistor mooring (triangle) are indicated in both panels.*

4.4 The Strongly Stratified Regime in Summer

In this Section, the results from the 12-day deployment of the thermistor mooring, BM-ADCP and MiniBat transects are presented for strongly stratified conditions in August, 2012.

4.4.1 Background Meteorological and Surface Wave Conditions

Figure 4.16 presents the wind and wave field for the month of August. The wind was predominantly directed from the southwest at 5–10 m s^{-1} with the majority higher wind speeds (10–15 m s^{-1} & 15–20 m s^{-1}) directed between south–southwest. Much less variability was observed in the direction of the wind in comparison to May with very few easterlies recorded. The wave field was directed mainly from between the west and southwest with maximum recorded significant wave height of 5–6 m. Similarly, the wave field presented less variability than in May and the maximum significant wave height was greater.

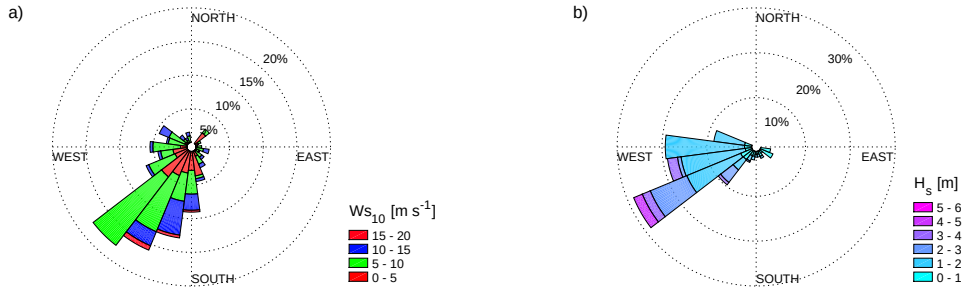

Figure 4.16: a) *Wind and* ***(b)*** *wave rose plots over the month of August 2012 (direction 'from').*

The mean wind speed over the 13-day deployment in August was 6.9 m s^{-1} (Figure 4.17). In total, four significant wind events, with wind speeds greater than 10 m s^{-1}, were recorded and identified in grey shade in the Figure. During the first event on yearday 223–224, wind speeds peaked at 10.8 m s^{-1} and

were directed from the east. No substantial increase in significant wave height was recorded during this event due to the wind directed from the east and the landmass causing a lack of fetch. The wave direction prior to the event was from the west but realigned itself to the local wind direction during the event — highlighting the influence of local wind events on the surface wave field. The following strong wind events were directed from the south and the waves from the southwest. Consequently, an increase of significant wave height was observed due to the longer fetch from directions unconstrained by land. The wind speeds peaked at 13 m s^{-1} on yearday 226 and significant wave height at 2.2 m immediately following the event. The largest wind speeds were recorded on yearday 228 at a peak of 17 m s^{-1}. As wind speeds peaked, the wind veered round from the east to the southwest which caused a subsequent rapid increase in significant wave height to 4.8 m before reducing in line with the decreasing wind speed. The last strong wind event peaked at 14 m s^{-1} and was directed from the south. Significant wave height remained above 2 m for the duration of this event. The wind speed and wave height decreased for the remainder of the deployment with a significantly variable wind direction occurring between the southeast and southwest. Significant wave height remained between 1–2 m with a slight increase occurring from 1 m to 1.8 m on yearday 234–235 due to an associated increase in wind speeds peaking at 9 m s^{-1}.

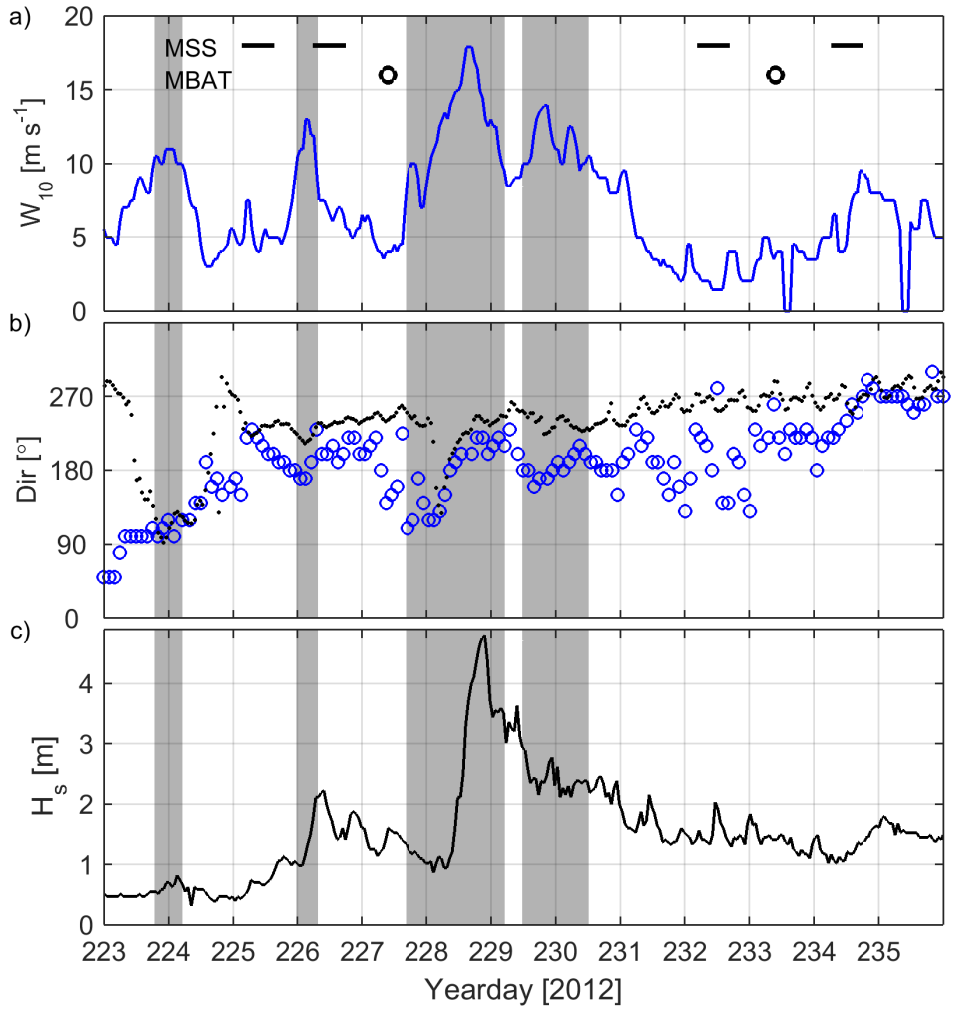

Figure 4.17: *Meteorological parameters for the fieldwork period in August, 2012.* ***a)*** *hourly mean wind speed with the significant wind events (> 10 m s^{-1}) denoted in grey shade; b) wind (blue) & wave (black) direction; c) hourly mean significant wave height. The MSS profiling periods conducted at Station 1 & 2 are indicated in (a) as well as the timing of the MiniBat surveys.*

4.4.2 The Sub-tidal Residual Currents in Summer

Figure 4.18 presents the barotropic currents recorded by the BM-ADCP over the fieldwork period in Summer. Fieldwork commenced during neap tides and continued through to spring tides. In comparison to the tide range during fieldwork in May (Section 4.3.2), this period presented a larger neap-spring inequality with weaker neap tides and stronger spring tide magnitudes (Figure 4.18a). The maximum velocity magnitudes recorded in August were 1.05 m s^{-1} in comparison to those recorded in May, 0.8 m s^{-1}, during spring tides.

In comparison, minimum velocity magnitudes recorded during neap tides in August were 0.1 m s^{-1} whereas in May it was 0.3 m s^{-1} during the neap tides.

As in the previous case in May, the residual currents in August generated a residual current to the northeast and was observed to respond readily to the local wind stress, although some inconsistencies were observed in the first half of the record (Figure 4.18b). The residual currents towards the beginning of the record were unusual in the sense that they were inconsistent with wind speed and direction. On yearday 225, a relatively light southerly wind set up a large Ekman flow with a strong u velocity component (9 cm s^{-1}). This decreased over the day, along with a slight reduction in the v component, although no decrease in wind speed was observed consistent with the strength and duration of the residual current. The strong wind wind event that followed on yearday 226 was directed from the south, although in this instance, did not have a large impact on the u-component unlike that of the previous day. However, the v-component increased slightly in response to this wind event. The strong wind event on yearday 228 did cause a large response in the residual currents with both the u- and v-components reaching their local maximums ($u = 11$ cm s^{-1}, $v = 7$ cm s^{-1}) before decreasing again on yearday 229. The final strong wind event again increased residual velocities in line with the southerly wind event after which the v-component remained around 5 cm s^{-1} while the u-component decreased to between 0–0.2 cm s^{-1} for the remainder of the record.

The barotropic currents and sub-tidal residuals are presented in a Lagrangian framework in the progressive vector diagram for the depth-mean current (grey) along with surface (blue) and near-bed (black) currents in Figure 4.19. The initial depth-mean tidal excursions were small (2–6 km) and their trajectories strongly influenced by the sub-tidal residual current. Following yearday 228, with the increase in current magnitude approaching spring tides, the oscillatory trajectories were steadier and the semi-diurnal tidal excursion increased to $\sim$11 km. The sub-tidal residual signal generated an average velocity of 4 km day^{-1} (5 cm s^{-1}).

The near-bed residual velocities and surface velocities traced considerably different paths right from the beginning of the record. The near-bed trajectory was mainly to the northeast except for on yearday 226 where the trajectory backed to a north-northwest direction and reduced in magnitude. The trajectory returned to the northeast on yearday 228 which corresponds to the

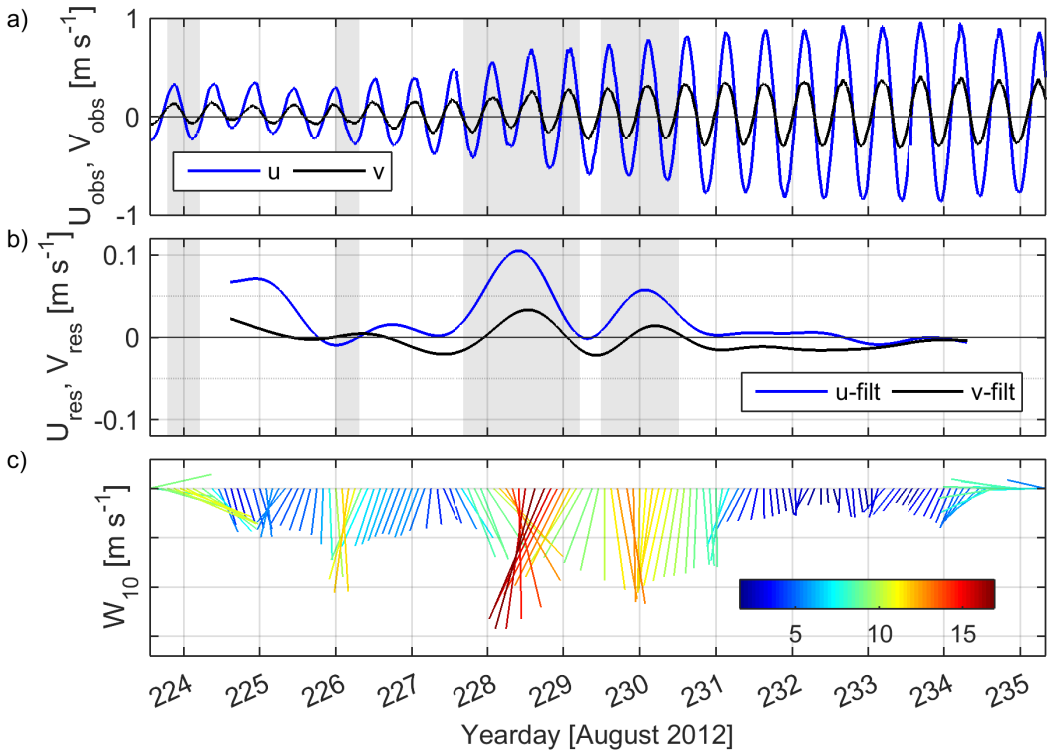

Figure 4.18: *The low frequency currents from the depth-mean, BM-ADCP during the Summer fieldwork deployment period.* ***a)*** *smoothed, depth-mean current velocity components;* ***b)*** *residual current as calculated by an 8-th order Chebyshev Type II low-pass filter (0.75 cpd) to exclude tidal frequency components;* ***c)*** *wind vector diagram showing velocity magnitude in colour (m s^{-1}) and vector direction 'from' (north up). Sustained winds >10 m s^{-1} are denoted in grey shade.*

increase in u- and v-velocity magnitudes observed in Figure 4.18b. In comparison, the surface trajectory maintained a more easterly trajectory with a greater trajectory magnitude. There was no significant deviation to the northwest on yearday 226 as opposed to that observed in the near-bed trajectory. Instead the surface trajectory remained to the east. Following the strong wind event on yearday 228, the surface trajectory increased significantly and included an increased northerly component to the flow. This was reflected in Figure fig:rescurrents08b towards the end of the record where the u-componenet reduced in comaprison to the v-component.

Figure 4.18 & 4.19 present the tidal and sub-tidal residual velocities in Summer which, in comparison to May, show a degree of inconsistency to a wind-driven flow. A primary candidate mechanism for this difference is the baroclinic component of the flow set up by density differences in the Summer stratified

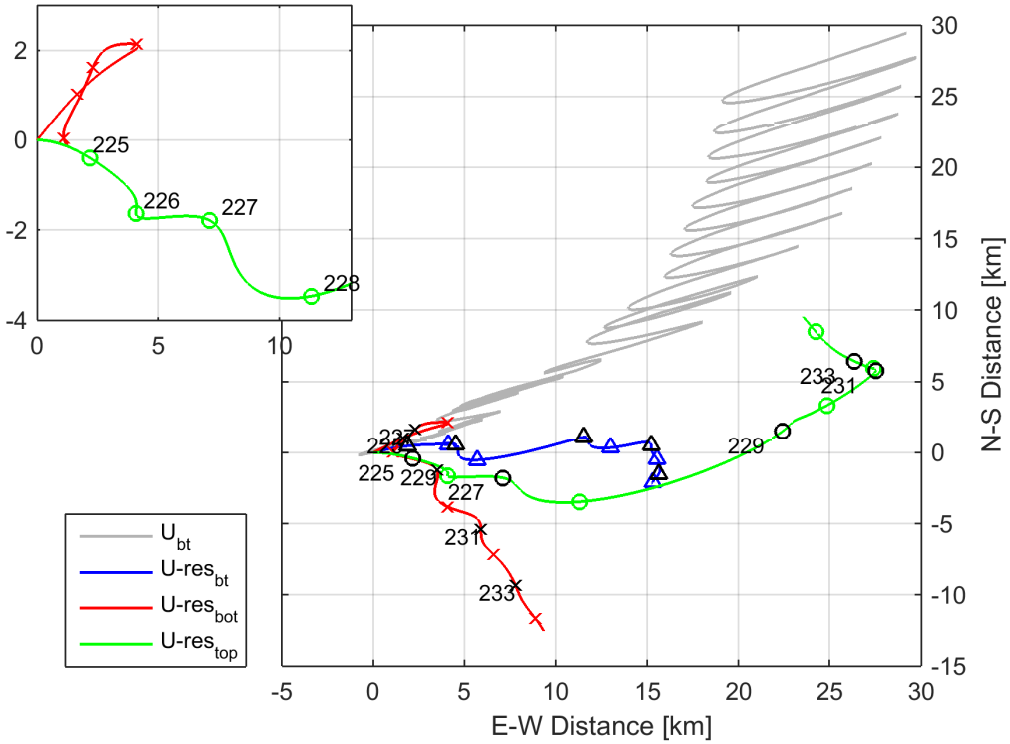

Figure 4.19: *The progressive vector diagram for currents measured by the BM-ADCP in summer describing the water movement in a Lagrangian frame. The observed barotropic tidal currents are presented in grey and shows the tidal excursion limits over each tidal cycle. Computed surface- (green), depth-mean (blue), and near-bed- (red) residual currents are presented with the daily excursion indicated by yearday number.*

waters (Horsburgh et al., 1998). As will be presented in the next Section, prior to yearday 228 the water column was stratified. Evidence for slab like motion and a decoupling between the surface and bottom layer may be seen in the near-bed and surface residual trajectories in Figure 4.19. Prior to yearday 228, the bottom layer exhibits a different trajectory in relation to the surface layer with a significant northward shift on yearday 226 that was not observed in the surface layer.

Episodic wind forcing may be expected to play a more significant role in the near-surface layer above the thermocline with the potential to increase the vertical mixing power and hence relocate the position of the front as described in Section 4.1.2 (Brown et al., 2003). The de-coupling of the surface layer causes differential advection of the surface and bottom fronts as was reported by Wang et al. (1990) in numerical simulations of a 1-D mixed-layer model embedded into a 3-D tidal model in which the position of the surface front

was significantly influenced by wind forcing while the position of the bottom front remained invariant. Furthermore, convective instability was reported in instances where the surface wind-stress drives more dense (mixed) water over lighter stratified water.

4.4.3 The Vertical Water Column Structure in Summer

Figure 4.20 presents a synthesis of data from the thermistor mooring and BM-ADCP. Figure 4.20a reflects the meteorological parameters shown in Figure 4.17 except in this instance the wind speed was given in terms of wind stress upon the sea surface — a parameter more in line with water column structure. Also included was a simple measure of stratification, ΔT, the vertical temperature difference between the top-most and bottom-most thermistor sensor. The timeseries of ΔT indicated a significant change in water column structure occurred during the strong wind event (0.65 N m^{-2}) on yearday 228. Prior to this, values of ΔT ranged between 0.1–1.6°C, with the maximum occurring on yearday 228. The majority of the stratification was observed between yearday 225–228 with ΔT values approximately 0.3–0.5°C over the period. Following the wind event of yearday 228, the ΔT significantly reduced for the remainder of the sampling period. It is useful to note that the thermistor mooring did not extend up to the sea surface and there was approximately a 10–15 m layer residing above the top-most thermistor sensor. As will be shown in the next Section with the MiniBat transects, a large proportion of the warm surface layer resided in the top-most 10 m in August. It is envisaged that the upper sensors of the thermistor mooring was sampling the lower section of the thermocline and hence the ΔT values did not reflect the total vertical temperature difference that is indicated in the MiniBat transects later on.

The buoyancy flux presented in Figure 4.20b was mainly positive with a strong diurnal signal. Daily maximum heat flux frequently surpassed -3×10^{-7} (W kg^{-1}) with negative values indicating a heat input into the ocean. Heat losses during the night were minimal (0–0.5×10^{-7} W kg^{-1}).

Given the significant change in water column structure on yearday 228, the following results and discussion refers to the pre-storm (yearday 223–228) and post-storm (yearday 228–236) periods. The vertical temperature structure shown in Figure 4.20c was fairly homogeneous at the start of sampling ($\sim$13°C). The contoured isotherms show a gradual deepening of the upper layer over the pre-storm period. The first significant downward intrusion of warm surface waters occurred on yearday 225 (ΔT= 0.6°C) which caused an associated increase in mid-column N^2 ($1 \times 10^{-4.25}$s^{-2}) and S^2 (1×10^{-4}s^{-2}) as shown in Figure 4.20d&e, respectively. The downward mixing of warm waters continued in this manner between yearday 225–228 further deepening the isotherms. In three noticeable instances on yearday 226–227, the deepening isotherms

extended to the bottom causing significant decreases in ΔT for a short period. The pre-storm period was typified by increased N^2 & S^2 values in the upper water column whilst the BBL was relatively thin ($\sim$14 HAB) with low N^2 and increased S^2 at a quarter-diurnal periodicity.

The breakdown in stratification occurred on yearday 228 coincident with the passage of the storm. During the initial increase in wind stress, a significant deepening of the upper water column isotherms occurred with a increase in upper water temperature. This caused the observed peak in ΔT. The initial deepening was associated with high shear throughout the water column and increased N^2. The peak wind stress on yearday 228 brought about a rapid change in water column structure with a complete reduction of stratification and an overall warming the the water column. N^2 and S^2 decreased rapidly with a mid-column patch of enhanced N^2 and elevated levels of S^2 only in the bottom frictional layer evident. Two potential mechanisms are suggested to have caused such a significant change in water structure. Firstly, with the significant increase in wind stress and significant wave height there is the likely possibility that surface forcing was the main contributor to the mixing. However, the second mechanism that can not yet be discounted is horizontal advection generated by tidal or Ekman transport. The post-storm period contained a well-mixed water column with warmer water temperatures ($\geq$15°C). An increasing frictional BBL was evident in S^2, in response to the stronger current magnitudes at spring tides. On intermittent occasions the enhanced S^2 from the BBL extended upwards though the water column for short durations at tidal periodicities. This became more regular following yearday 232, which was accompanied by vertically homogeneous cooler water temperatures being advected through at tidal periodicities. Increased levels of N^2 were associated with these cooler waters ($1 \times 10^{-4.5} s^{-2}$).

The top and bottom temperature timeseries recorded by the thermistor mooring is presented in Figure 4.21 for the August fieldwork period. The surface heat input (T_Q) is also shown in Figure 4.21a. The heat input was a poor match for the recorded temperature indicating advective sources of heat were present. The timeseries between yearday 224–226 presented a slight increase in temperature that was inline with the surface heat input. However, the recorded temperature increase following yearday 226 deviated significantly from that calculated in T_Q. The maximum temperature increase predicted by T_Q was $\sim$0.7°C whereas the actual recorded temperature increase at the

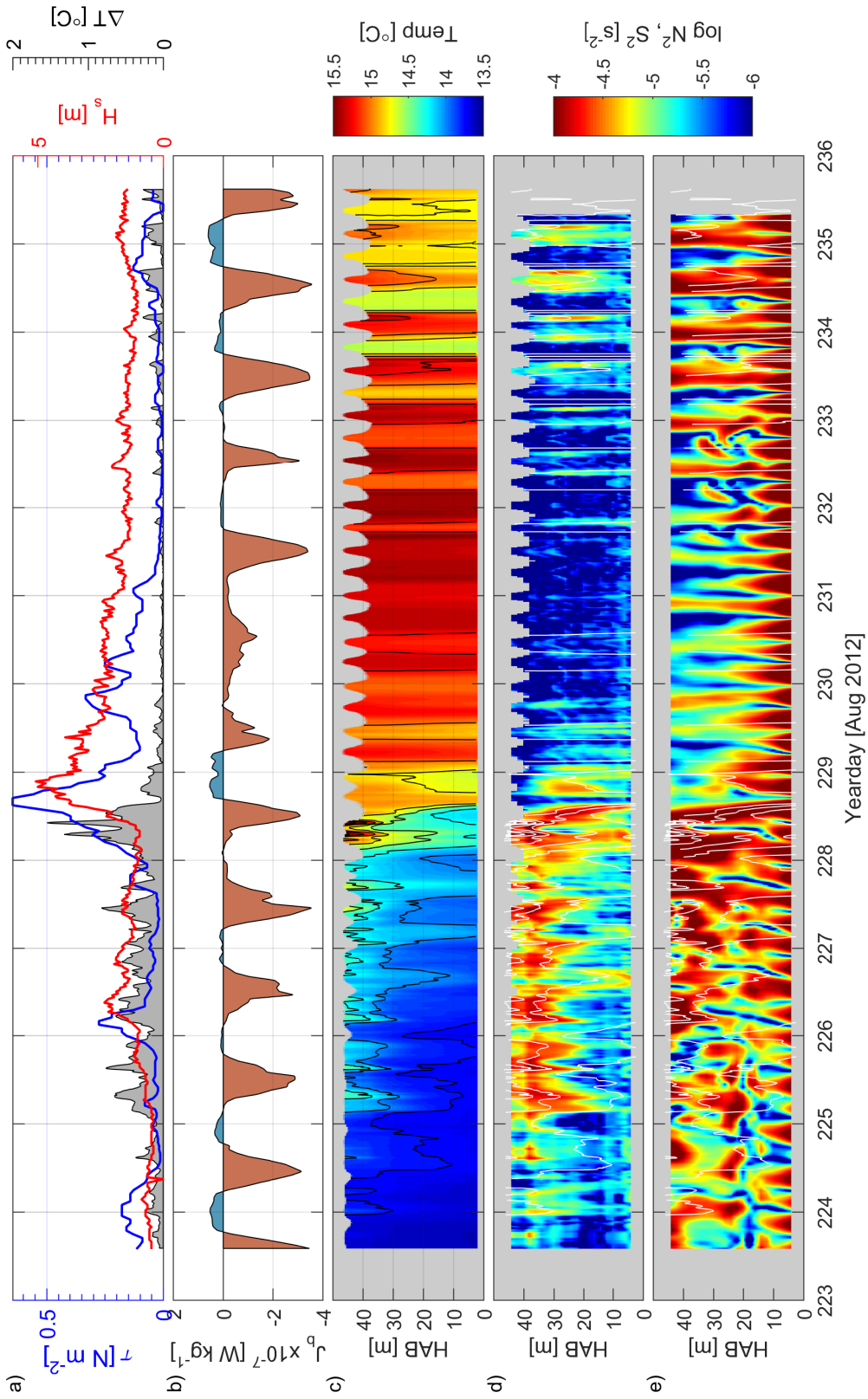

Figure 4.20: *Input forcing and vertical water column structure during the spring thermistor and BM-ADCP deployment.* ***a)*** *Observed wind stress from Sevenstones met buoy (τ), significant wave height from the Wave Hub wave buoy (H_s), and top-bottom thermistor temperature difference (ΔT) denoted in grey shade;* ***b)*** *buoyancy flux — negative values indicating a heat input into the ocean (J_b);* ***c)*** *thermistor mooring temperature (°C);* ***d)*** *buoyancy frequency squared (N^2);* ***e)*** *vertical shear squared (S^2). Temperature contours at 0.25°C intervals are overlaid on* ***c***,***d***,***e***.

study site was $\sim$2°C peaking on yearday 231. Large short-term variability was observed in the signals, especially in the upper thermistor. This variability may be seen in the de-trended timeseries in Figure 4.21b.

The de-trended temperature was obtained by calculating the difference between itself and a 6-point polynomial fit, from which spectral analysis (Figure 4.21c) described the forcing mechanisms. The upper water column presented larger variability ($\geq$0.2°C) in the pre-storm duration. These peaks were increases in temperature in comparison to the mean and were not confined to the strong wind events shown in grey shade (although a peak did occur during the event on yearday 226). The response in the bottom thermistor was variable with some upper thermistor peaks showing a corresponding increase in temperature at the bottom. During the strong wind event on yearday 228, the temperature variability increased in magnitude with the upper and bottom thermistors in phase with each other. This may be explained by the well-mixed water column. Following the strong wind event, the variability decreased up to yearday 231 after which the temperature fluctuations increased significantly again. Spectral analysis showed the main forcing periodicities in this instance to be at tidal frequencies with similar magnitudes in both the upper and bottom thermistors except for at the K_1 frequency, where more energy was contained in the upper thermistor signal.

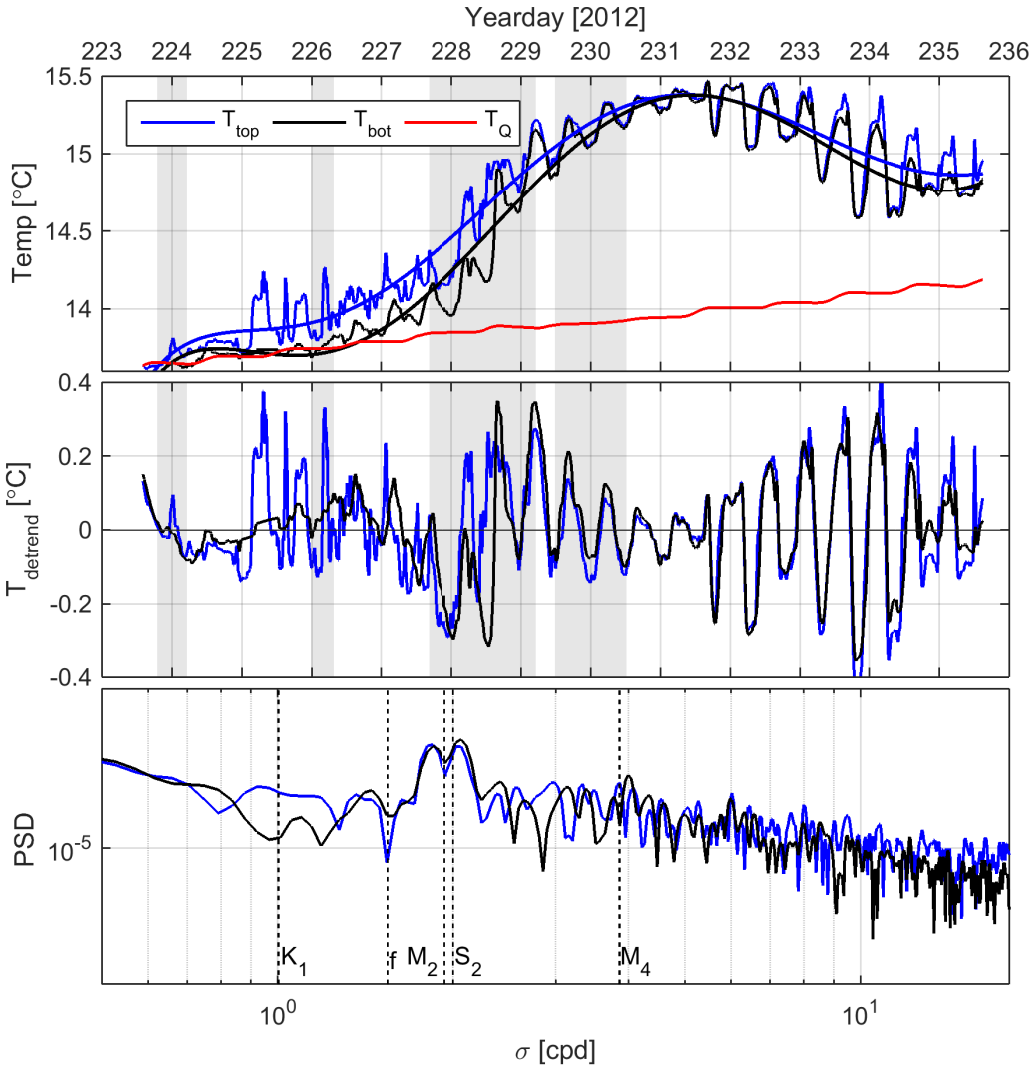

Figure 4.21: *Spectral analysis conducted on the top-most (top) and bottom-most (bottom) thermistor sensor presenting the dominant signals observed.* ***a)*** *Top (blue) and bottom (black) temperature timeseries over the period of deployment in August. A 6-point polynomial fit (smoothed line) was used to remove the low frequency variability presented in (b). The calculated surface heat flux is included for comparison (red).* ***b)*** *the resulting de-trended and de-meaned temperature signal for the timeseries in (a).* ***c)*** *Power spectral density of the de-trended signal (b) with Hanning window applied. Sustained winds >10 m s^{-1} are denoted in grey shade. Primary tidal constituents and the local inertial frequency are labelled accordingly.*

4.4.4 Non-Linear Internal Waves

Vertical velocities measured 40 mab and band-pass filtered between 15-60 minutes show two distinct packets of elevated velocities during yearday 225 (Figure 4.22). The corresponding temperature structure show these enhanced vertical velocities coincided with the vertical displacement of the isotherms in the upper water column that on closer inspection were non-linear internal waves (NLIW).

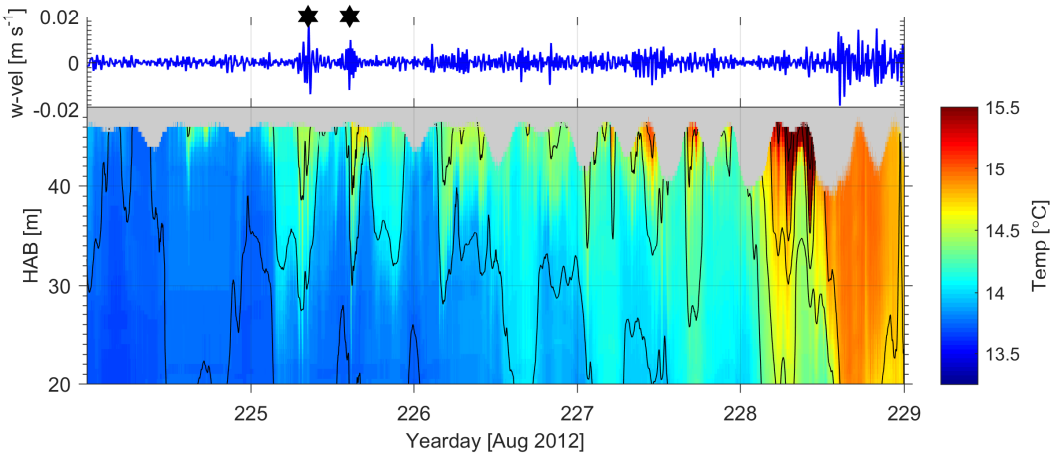

Figure 4.22: *Above: Depth-mean vertical velocities (w) measured by the BM-ADCP. The velocities were band pass filtered $15 \leq T_{pass} \leq 60$ mins. Below: The upper water column temperature structure in August. The presence of non-linear internal waves were observed during the two periods marked by stars.*

Packet 1

Figure 4.23 shows the observed vertical displacements in the isotherms occurring at the first star at yearday 225.3 overlaid on the alongshore current. The waves displaced warm water residing in the upper layer downwards for the duration of the wave packet. A packet of 5 individual NLIW were observed with a time period between successive troughs of 23–36 minutes and a maximum vertical displacement of 11 m in the leading waves. The NLIW occurred during slack tides while the current underwent the change from ebb to flood.

The generation of internal waves in shelf seas often occur as the barotropic tide interacts with topography at the shelf break. This was observed at the Celtic Sea shelf break by Vlasenko et al. (2014). However, in this case, the shelf break was too far away from the study site and instead the generation of NLIW by the barotropic tide flowing over a topographic ridge or bank was deemed the

most likely generation mechanism (Green et al., 2010). Here, the most likely location was the shallow bank situated off Lands End to the immediate west of the observation site. The proximity of the front was observed by the passage of the front at yearday 225.15 where the isotherms were observed to deepen rapidly as the front was advected through. Following the passage of the front and reduction of the tidal current the NLIW were potentially released from the generation location at the front and propagated away from the front. The vertical current structure in Figure 4.23 shows a phase reversal within the thermocline that occurred during the passage of the wave packet (yearday 225.3). The u_θ-component in the surface layer was positive while below the surface the currents were negative and at the bottom the currents were again positive.

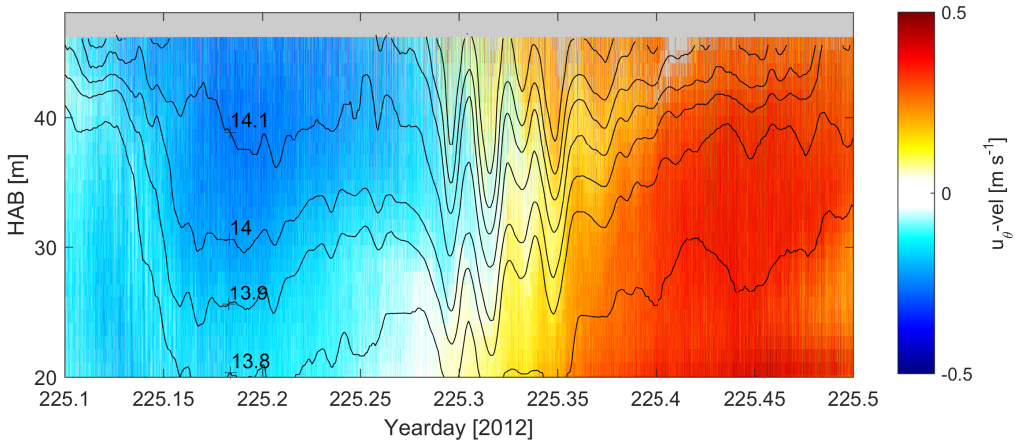

Figure 4.23: *High resolution observations of a NLIW packet observed in the temperature contours during the stratified period at neap tides (Yearday 225.3). The rotated-u component of velocity is plotted with temperature contours every 0.1°C overlaid.*

Enhanced S^2 was measured in the thermocline during the passage of the NLIW (Figure 4.24). Background levels of shear were $\leq 1 \times 10^{-5}$ s^{-2}, though during the passage of the waves, the shear rose up two orders of magnitude to $\sim \times 10^{-3}$ s^{-2}.

The stability of the thermocline during the passage of the NLIW was calculated with the Richardson Number (Ri). During the lead up to the NLIW strong evidence for marginal stability in the thermocline with the potential for shear instability to generate thermocline turbulence was observed with $0.25 < Ri < 1$ (Figure 4.25). The Ri intermittently reduced to less than 0.25 at the base of the thermocline and also in the near-surface region during the passage of the

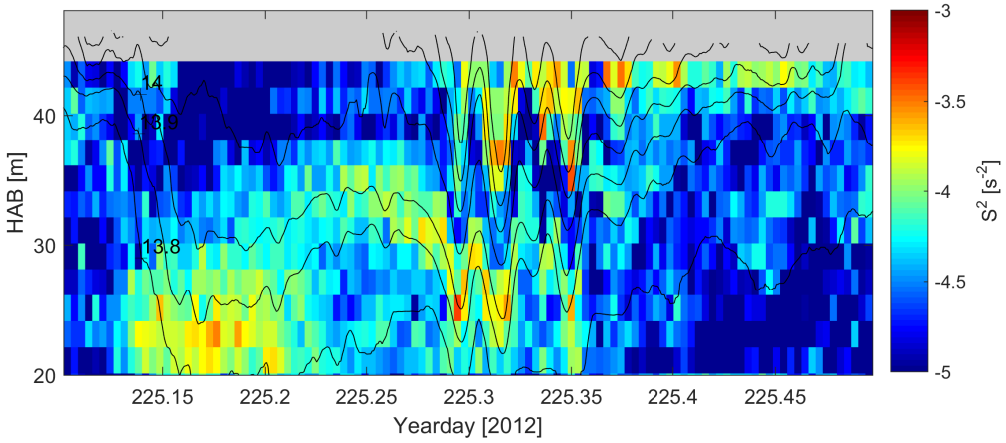

Figure 4.24: *Observations of NLIW with enhanced shear in the thermocline. (Yearday 225.3). The shear-frequency squared with temperature contours every 0.1°C overlaid.*

NLIW. This indicates the strong potential for shear-induced turbulent mixing with the potential to erode the thermocline and change levels of stratification.

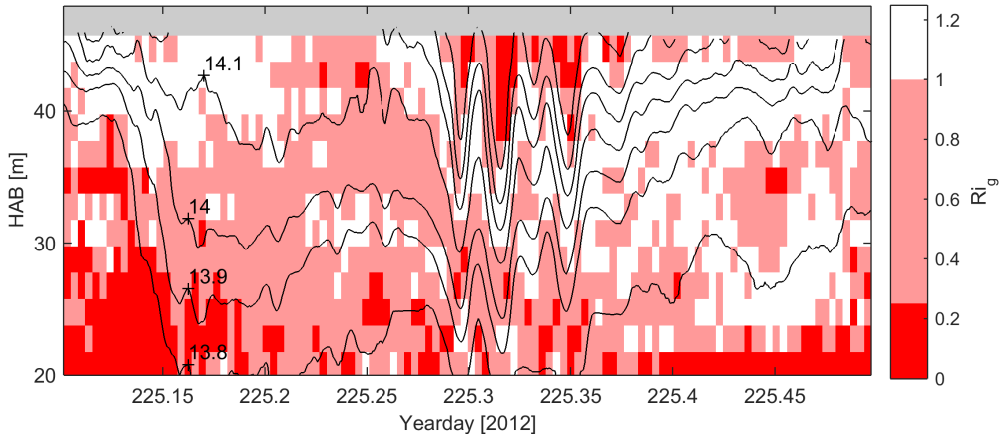

Figure 4.25: *Calculated Richardson numbers indicated instability in the thermocline as a result of the NLIW (Yearday 225.3). The Richardson number with temperature contours every 0.1°C overlaid.*

Given the proximity of the bank, we discuss the possibility of a topographically controlled hydraulic jump and generation of lee waves being formed near to the mooring site. Previous studies over isolated sills and ledges have demonstrated the generation of lee waves under hydraulically super-critical conditions (Klymak and Gregg, 2004). The composite internal Froude number was estimated as:

$$G^2 = F_1^2 + F_2^2 \tag{4.8}$$

where $F_i^2 = u_i^2/g'h_i$ are the internal Froude numbers for each layer, $i = 1, 2$, corresponding to the upper and lower layer, respectively, and g' is the reduced gravitational acceleration (Jones et al., 2014). The interface between the two layers was defined by the 13.9°C isotherm.

In super-critical conditions ($G^2 > 1$) the flow is dominated by kinetic energy and NLIW cannot propagate, whereas in sub-critical conditions ($G^2 < 1$), potential energy dominates and waves can propagate in any direction. Super-critical flows are fast and shallow, while sub-critical flows tend to be slower and deeper. A hydraulic jump occurs during the transition between super-critical and sub-critical flows. This may occur when the tidal current changes direction or the flow interacts with local topography (Farmer and Armi, 1999). Hydraulic jumps are usually accompanied by shear instability (Lawrence, 1990) and turbulent mixing (Moum and Nash, 2000). Figure 4.26 shows the NLIW packet was associated with a transition between super-critical to sub-critical flow which returned to super-critical flow following the passage of the NLIW packet.

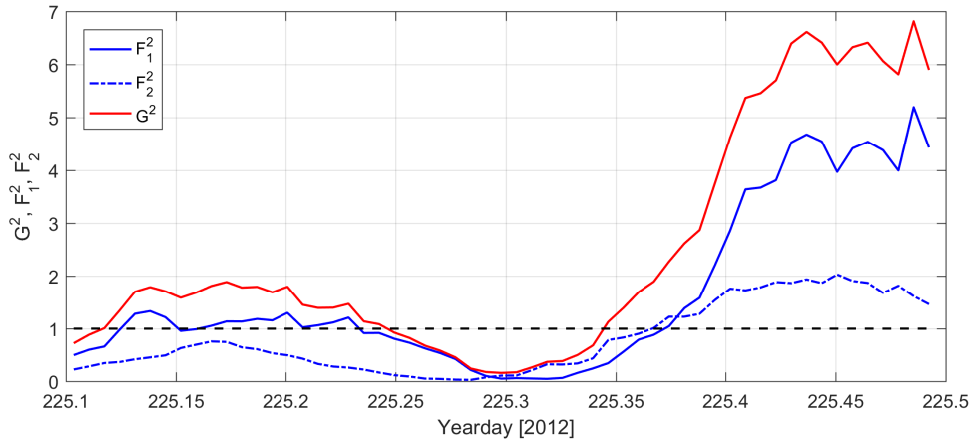

Figure 4.26: *The calculated Froude number associated with the passage of the NLIW during yearday 225.3. F_1^2, F_2^2, G^2 are the internal Froude numbers for the upper layer, lower layer and the composite Froude Number, respectively. The transition between sub-critical and super-critical flows occur at 1 and denoted by the dashed line.*

Packet 2

The second packet of NLIW were observed during yearday 225.6 and occurred during the tidal reversal (Figure 4.27). The amplitude of the largest leading wave was 11 m with a period of 23 minutes.

Enhanced S^2 was measured in the thermocline during the passage of the NLIW

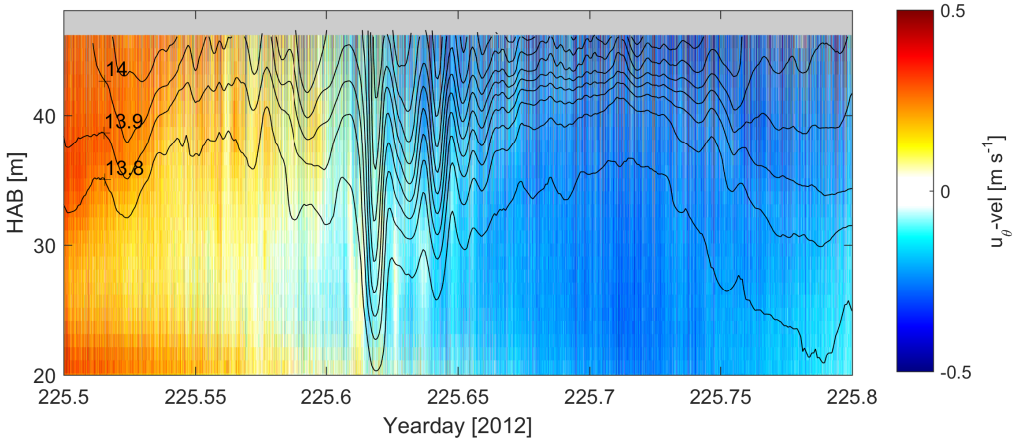

Figure 4.27: *High resolution observations of a NLIW packet observed in the temperature contours during the stratified period at neap tides (Yearday 225.6). The rotated-u component of velocity is plotted with temperature contours every 0.1°C overlaid.*

(Figure 4.28).

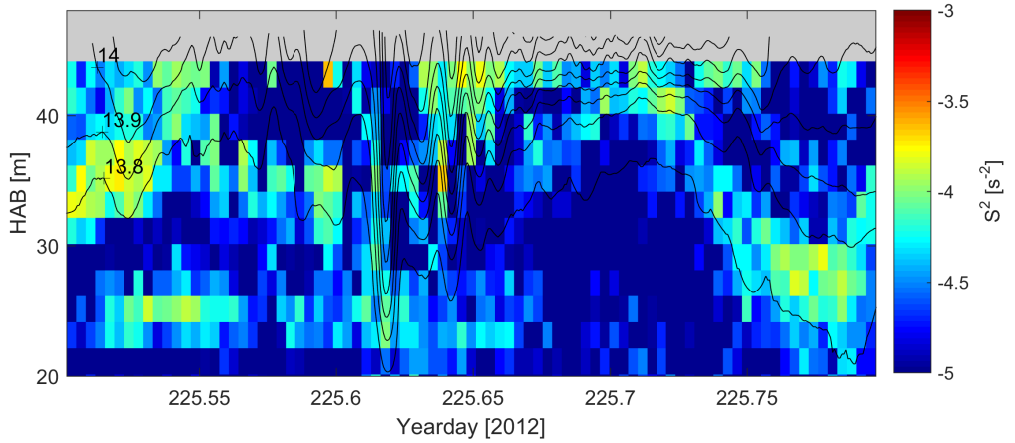

Figure 4.28: *Observations of NLIW with enhanced shear in the thermocline. (Yearday 225.6). The shear-frequency squared with temperature contours every 0.1°C overlaid.*

Water column stability was reduced with the potential of shear instability at the base of the thermocline since Ri were < 0.25 during the passage of the NLIW. Reduced stability within the thermocline was observed during the passage of the waves.

In a similar situation to the first packet, the passage of the NLIW coincided with a transition between super-critical and sub-critical flow. Following the passage of the NLIW, the Froude numbers returned to super-critical flow

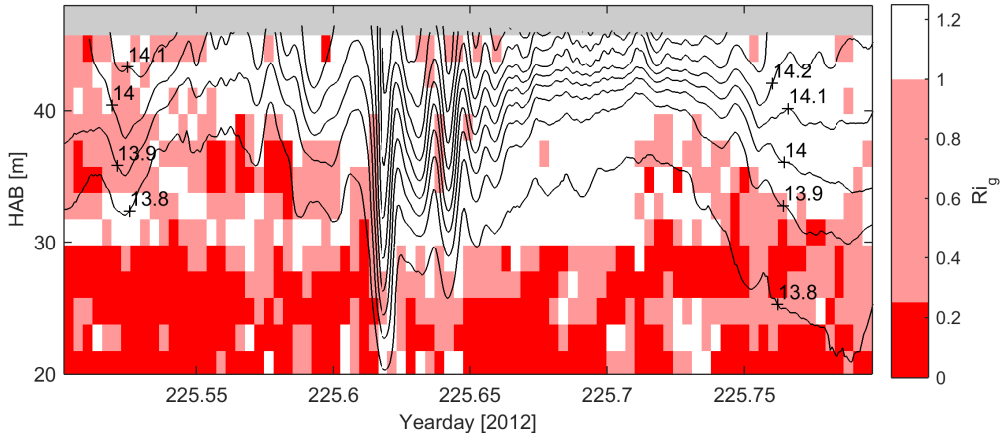

Figure 4.29: *Calculated Richardson numbers indicated instability in the thermocline as a result of the NLIW (Yearday 225.6). The Richardson number with temperature contours every 0.1°C overlaid.*

(Figure 4.30).

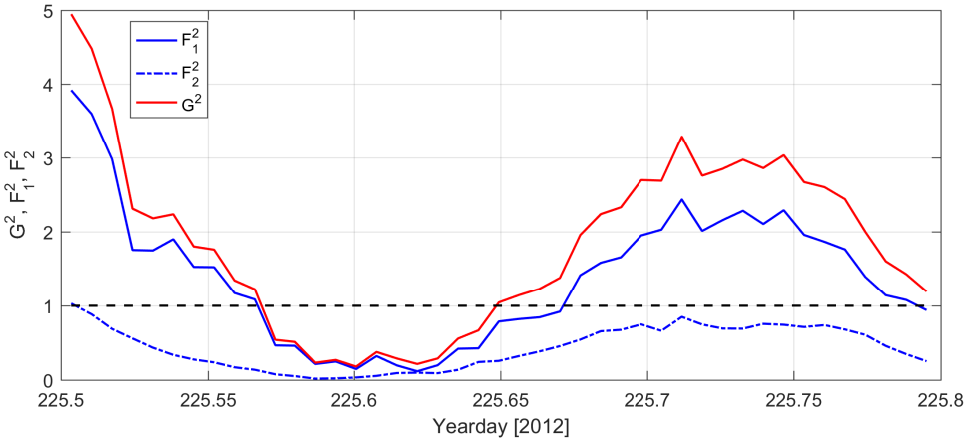

Figure 4.30: *The calculated Froude number associated with the passage of the NLIW during yearday 225.6. F_1^2, F_2^2, G^2 are the internal Froude numbers for the upper layer, lower layer and the composite Froude Number, respectively. The transition between sub-critical and super-critical flows occur at 1 and denoted by the dashed line.*

Figure 4.31 presents the echo intensity from the BM-ADCP on yearday 225, where higher echo intensities are indicative of stronger turbulence and/or resuspended material (Jones et al., 2014). In this instance, the increase in the echo intensities were situated in the mid water column and clearly related to the vertical displacement of the isotherms within the base of the thermocline and suggestive of turbulence in a stratified environment. Increased echo intensity was present at the base of the thermocline and during the vertical

displacements of the isotherms, including during the passage of the second NLIW packet.

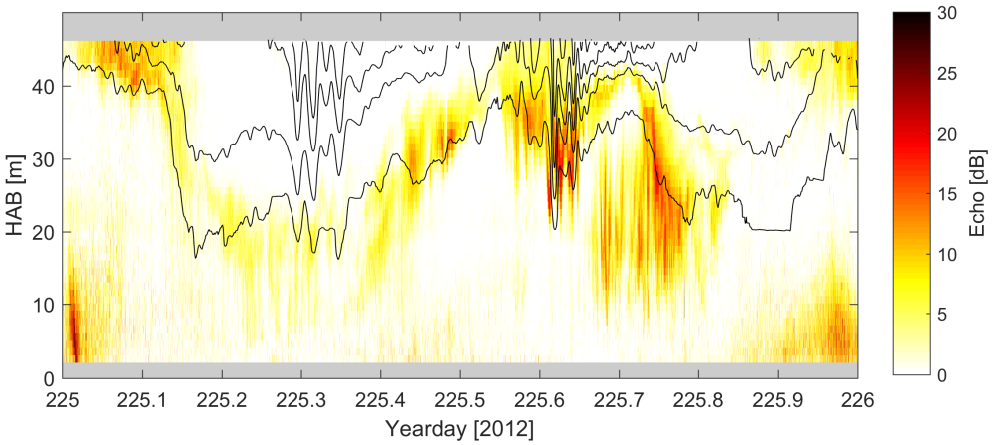

Figure 4.31: *BM-ADCP echo intensity for yearday 225 and for the duration of NLIW packet 1 & 2. Higher values of echo intensity indicate stronger turbulence and/or resuspended material. Since the increase in echo intensity is clearly related to surface and interior processes rather than near-bed processes, we consider that in this location echo intensity to be a proxy for stratified turbulence in the thermocline.*

4.4.5 The Spatial Water Column Structure in Summer

The passage of the storm on yearday 228 caused a rapid change in water column structure as discussed above. An understanding of the spatial response of the water column over this period was obtained from daily-averaged SST imagery and Minibat transects conducted prior to the storm on yearday 227 (Figure 4.32), and following the storm on yearday 233 (Figure 4.34).

The SST map in Figure 4.32 showed the presence of a thermal front at the study site on yearday 227. Cooler, inshore, waters (14.5°C) were separated by a sharp temperature gradient from a tongue of warm, offshore, water located in the proximity of St1 (∼16.3°C). The cooler water was constrained to a narrow band with temperatures increasing again close to the shoreline. The outermost part of this region was just captured at the start of the first Minibat transect and was observed to be well-mixed.

Overlaid onto the SST imagery were the top-bottom temperature difference as recorded along the Minibat transects. Dark circles indicated more well-mixed waters whilst a lighter shade indicated more-stratified conditions. The northward and southward legs of the Minibat transect (T1 & T3) crossed

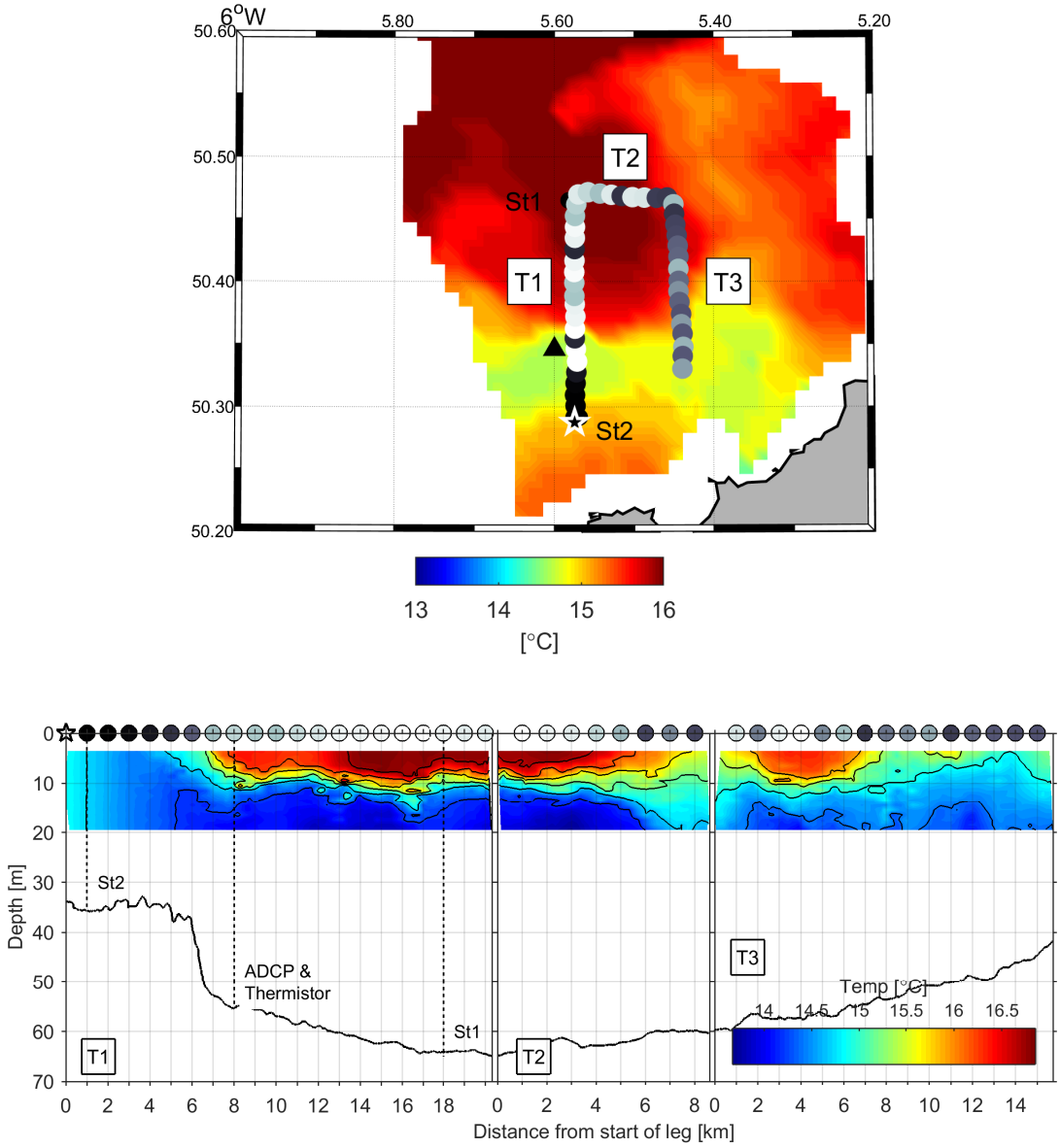

Figure 4.32: Top: *SST on yearday 227 with the Minibat transects overlaid showing the top-bottom difference in temperature (top: 2 m; bottom: 20 m). The temperature difference is denoted by the colour gradient with a dark colours representing well-mixed conditions and lighter colours indicating more stratification. The transect's start position is denoted by the white pentagram.* ***Below:*** *Temperature transect conducted on yearday 227 prior to the storm. Contours of temperature are overlaid at 0.5°C intervals.*

the front, although the vertical temperature difference as calculated from the Minibat transect did not fully align with the SST imagery. This was most likely due to the temporal scales of the datasets, with the Minibat transect offering a

snapshot in time whereas the daily-composite SST image would have smoothed out the effect of horizontal advection over the course of the semi-diurnal tidal cycle. This premise was supported by the smaller cross-frontal temperature gradient ($\Delta T/\Delta y$) calculated by the SST (0.1°C km^{-1}) in comparison to the Minibat transect (0.22°C km^{-1}). Transect T2 initiated near St1 and proceeded east crossing into cooler SST (15.5°C) on the eastern edge of the warm tongue. The third transect, T3, headed south, skirting the edge of the warm tongue before crossing the front into the cooler inshore waters.

As may be seen from the Minibat temperature transect in Figure 4.32, the warm SST near St1 was associated with a thermally stratified surface layer approximately 10 m thick. The Minibat transect captured the surface warm layer (1–10 m), thermocline (10–20 m) and cooler waters below ($\geq$20 m). The strongest stratification in the thermocline was on the western side of the tongue and captured in T1. The position of the front coincided with the steep topography at x =6 km indicating an influence of topographic control over the frontal position in shallow shelf seas. Evidence of transverse circulation generating upwelling of cold, bottom water on the mixed side may be observed in the upward-doming of the bottom front isotherm at x =5–7 km. This secondary circulation acts in a plane perpendicular to the front and is caused by the frictional effect on the geostrophic balance along the front (Hill et al., 1993). The narrow band of coolest waters along the front observed in the SST could also be identified at the surface between x =3–5 km and further suggests the presence of upwelling as was also reported in Simpson and Pingree (1978). The upward-doming of the bottom front may also be observed further along in T3 although the thermocline became more diffuse to the east as the transect manoeuvred along the edge of the front in T3.

Another dynamic phenomenon associated with the strong horizontal density gradients at the front are quasi-geostrophic along-front flows which are commonly referred to as frontal jets (Hill et al., 1993). An estimation of such flows may be calculated from the thermal wind shear using the density observations from the Minibat transects (Equation 4.9).

$$\begin{aligned} \frac{\partial u_g}{\partial z} &= \frac{g}{\rho_0 f}\frac{\partial \rho}{\partial y} \\ \frac{\partial v_g}{\partial z} &= -\frac{g}{\rho_0 f}\frac{\partial \rho}{\partial x} \end{aligned} \tag{4.9}$$

In order to deduce the velocity profiles, the thermal wind shear may be inte-

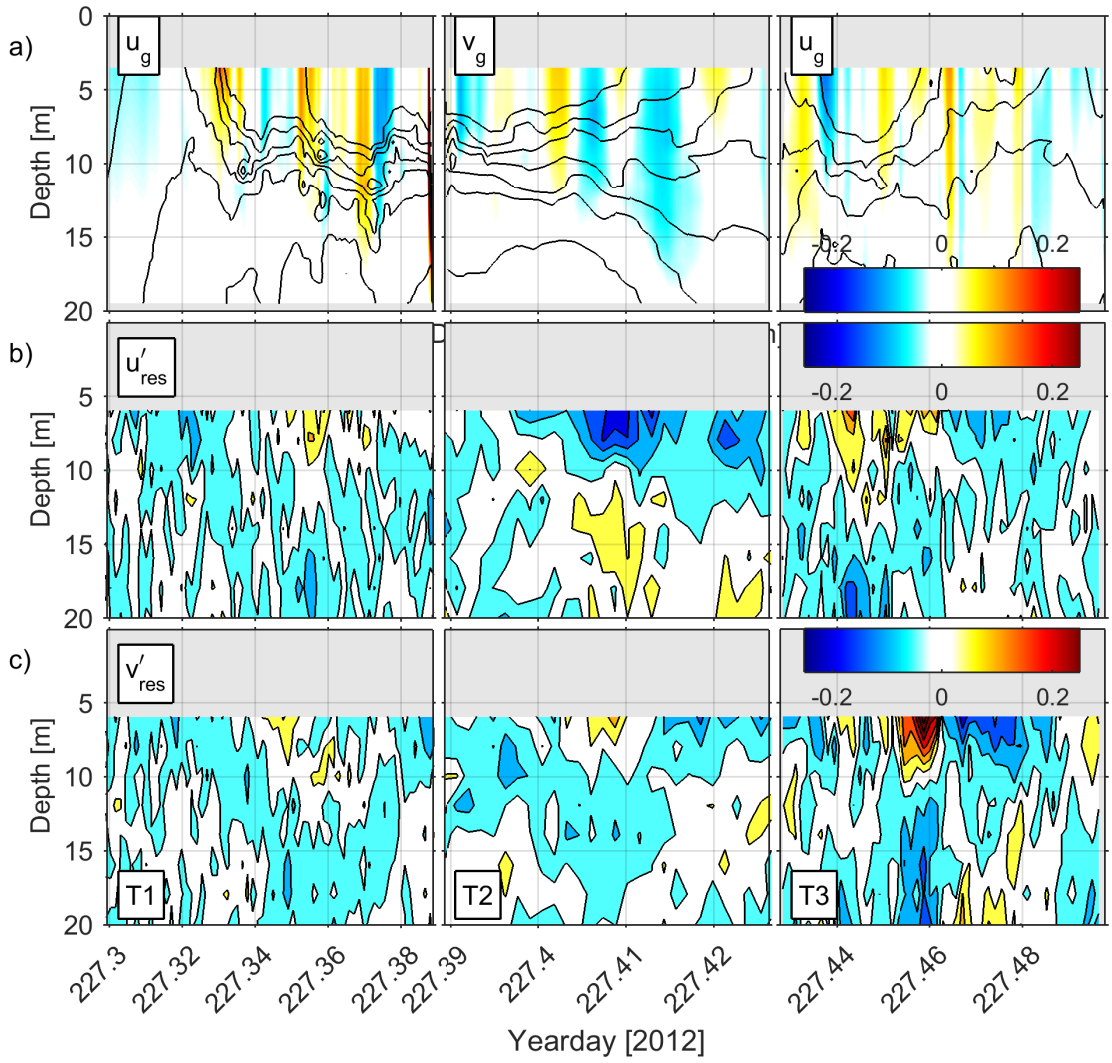

Figure 4.33: *The computed geostrophic velocities and in-situ ADCP residuals recorded during the Minibat transects, T1, T2, T3, on yearday 227.* ***a)*** *The geostrophic flow as estimated from the thermal wind shear with isopycnals overlaid in $\Delta 0.1$ kg m^{-3}.* ***b)*** *de-tided $u-$residual velocity;* ***c)*** *de-tided $v-$ residual velocity. Velocities are shown in m s^{-1}.*

grated upwards from a level of no motion which is usually assumed to be at the seabed (Simpson and Sharples, 2012). However, given the limitation of the Minibat depth to 20 m, we make the assumption that the level of no motion was at 20 m. This would introduce errors in the absolute magnitudes of the geostrophic velocities as well as potentially overlook the important horizontal density gradients in the bottom front. Nevertheless, this assumption allowed for quasi-geostrophic jets associated with the surface front to be distinguished, if not accurately quantified, and the resulting velocity field compared to the

de-tided signal as is presented in Figure 4.33.

The computed geostrophic velocities indicated velocities of up to 0.2 m s^{-1} were expected along the frontal interfaces. In T1, geostrophic velocities with both u_g and $-u_g$ components were estimated due to the complex density field with undulations along the thermocline and contributions made by the bottom front. The surface fronts observed between yearday 227.32–227.36 generated a predominantly easterly geostrophic flow at the outcropping isopycnals. Following this, the bottom front and undulations estimated both potential u_g and $-u_g$ velocities (yearday 227.36–227.38). In T2 (west-east transect), there was a predominantly southerly geostrophic current as estimated by the v_g component ($\partial\rho/\partial x$) although this was mainly generated by the bottom fronts and further undulations in the thermocline. Outcropping isopycnals indicated northerly v_g although to a lesser degree due to the weaker surface frontal gradients. T3 consisted of two primary surface outcropping isopycnals either side of the warm stratified water observed in the temperature transect with the associated easterly u_g. Undulations in the thermocline and upward doming of the isopycnals generated a complex velocity structure with estimated $-u_g$.

Figure 4.33b,c presents the de-tided vessel-mounted ADCP velocities recorded during the Minibat transects. No offset was applied to account for the spatial distance between the two instruments, however it is noted that the Minibat was towed $\sim$50 m behind the vessel and the ADCP data was binned into 2 minute ensembles for this analysis, equating to a horizontal distance of 370 m (ave. Minibat tow speed =6 kts), and therefore the Minibat was deemed to be within the ensemble limits. The methodology employed to extract the residual velocities was loosely-based upon that used by Lwiza et al. (1991) & Hill et al. (1993), whereby the vessel-mounted, geo-located, ADCP data was; cleaned to remove obvious errors; temporally bin-averaged; rotated to two orthogonal directions parallel and perpendicular to the front; and the tidal component removed by a least-squares fitting technique to the semi-diurnal and diurnal constituents (Lwiza et al., 1991). In this analysis, the data was cleaned; temporally bin-averaged (2 mins); and the ADCP velocities were de-tided by fitting a 4-th order polynomial trend line in a least-squares sense to the timeseries at each vertical bin-depth (dz =2 m). A least-squares fit to the tidal constituent frequencies was unsuitable since the timeseries was too short to perform a satisfactory fit and large errors were introduced when attempted — the total deployment took 5 hours on yearday 227 and 7 hours on yearday

233. Furthermore, no rotation of the currents to align them with the front was attempted due to the complex meandering structure of the front (observed in the SST) rendered a primary orientation difficult to distinguish.

The residual velocity structure as measured by the VM-ADCP presented a mixed result in comparison to the estimated geostrophic velocities. Furthermore it is noted that the residual velocities were not rotated to be orientated perpendicular to the front and hence the geostrophic component may be dispersed in both residual velocity components. The first frontal structure encountered in T1 (yearday 227.32–227.34) did not possess the u_{res} in the upper 10 m as was estimated in the geostrophic currents. However, there was a narrow band of increased $-u_{res}$ evident at the front which extended to 20 m. The second frontal structure (yearday 227.34–227.36) did contain u_{res} in the upper 10 m as estimated by u_g with velocities of $\sim$0.15 m s^{-1}. The third set of u_g was not evident in u_{res}. T2 contained an evident peak in near-surface velocity associated with the outcropping isopycnals in the middle of the transect. The velocities pertained to a north-northwesterly residual flow with u_{res} =-0.25 m s^{-1} and v_{res} =0.15 m s^{-1}; a potential baroclinic instability in the tongue of warm water. However, these velocities did not conform with those estimated by u_g although the influence of the the bottom density gradients were particularly strong. On closer inspection of $\partial\rho/\partial x$ there was evidence (+ve gradients) to suggest that the upper-most 7 m did support a northerly v_g which was, however, overwhelmed by the density gradients in the deeper layers. The T3 transect was directed to the south and manoeuvred along the edge of the warm tongue as was seen in the SST. Unlike the previous two transects, which were orientated relatively perpendicular to the front, T3 crossed the front obliquely on a number of occasions and therefore it is prudent to consider both u and v in this case. In fact, the most evident case for geostrophic flow occurred on the southern side of the warm water along the front orientated southwest—northeast (yearday 227.44–227.46); the residual velocities supported this with $+u > 0.1$ m s^{-1} and $+v > 0.2$ m s^{-1} components near the surface.

A second Minibat transect was conducted during spring tides on yearday 233 which was after the passage of the strong wind event (Figure 4.34). The SST presented a more defined patch of cooler inshore water with a sharp frontal region located in the vicinity of St1. This was further offshore in comparison to the transect conducted on yearday 227 though the frontal gradients remained similar; SST$\sim$0.15 °C km^{-1} and Minibat $\sim$0.14 °C km^{-1}. The inshore SST

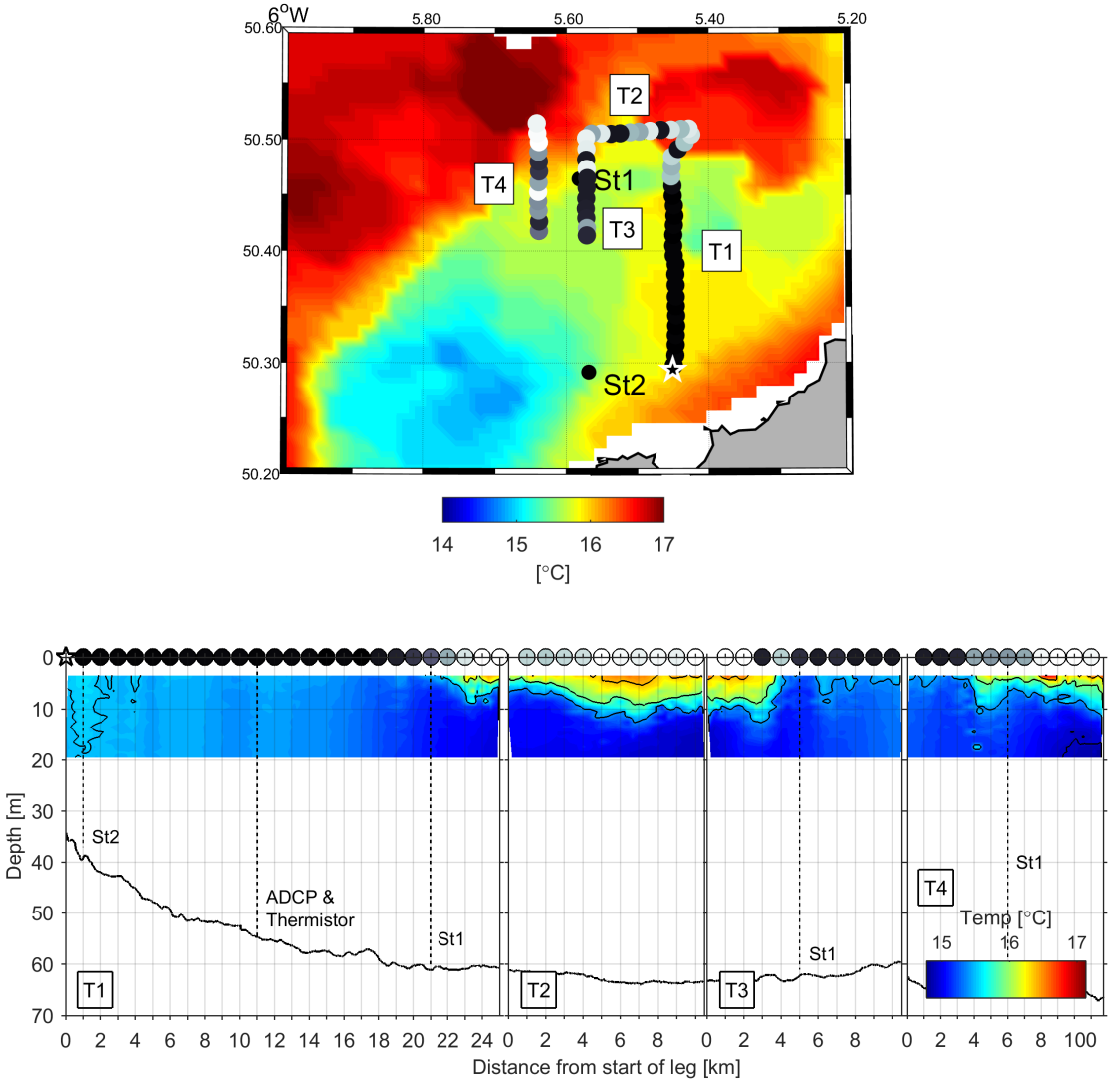

Figure 4.34: *Temperature transect conducted on yearday 233 following the storm. Contours of temperature are overlaid at 0.5°C intervals.*

was ∼15.0°C to the southwest of the study site which was warmer than on yearday 227 (+0.5°C). Offshore SST reached a maximum of ∼17.0°C which was also approximately 1°C warmer than observed on yearday 227. In between St1 & St2 the SST was ∼15.4°C which was in line with that recorded by the thermistor and similarly represented a ∼1°C increase in comparison to yearday 227. The vertical temperature difference as measured by the Minibat transects roughly aligned with the SST gradients. Some small scale lateral variability in the front was evident close the transect lines T1 & T2.

The Minibat temperature transect presented well-mixed inshore waters with

the thermally stratified offshore waters residing in the surface 10 m. The frontal structure was well defined with outcropping isotherms separating the well-mixed and stratified waters at the surface. Unlike that observed on the previous transect, there was much less temperature variability below the thermocline with no evident diffusion of the thermocline in the deeper waters unlike that seen in T2 & T3 in the previous transect. This was contrary to what would be expected of the stronger tidal currents during spring tides on yearday 233. Erosion of the thermocline base would be more likely during spring tides where the stronger tidal mixing power would be able to impinge on the thermocline in deeper waters. The sharp frontal gradient observed in the SST was replicated in the Minibat transect with the three frontal crossings easily identified with sharp horizontal gradients in temperature. A typical frontal structure was observed with a depression of the thermocline followed by coolest waters immediately on the other side of the front, suggesting a secondary transverse frontal circulation leading to convergence at the surface.

The geostrophic currents as estimated from the thermal wind shear indicated the potential for along-front jets during sampling (Figure 4.35). An easterly flow was estimated for all three crossings at the observed front. Maximum geostrophic currents were estimated at 0.23 m s^{-1} during T3 though the level of no motion was once again assumed at 20 m given the restriction of the in-situ density measurements. The majority of the residual currents were barotropic in structure across the surface 20 m and it was difficult to discern any surface jet intensification, especially looking at the residual velocities associated with frontal crossings. A seemingly clearer example of the increased u_{res} associated with a front was observed in T3 at yearday 233.505 where a indication of narrow band of u_{res} with the correct magnitude and direction ($+u_{res}$ =0.15) was associated with the maximum u_g at that frontal crossing.

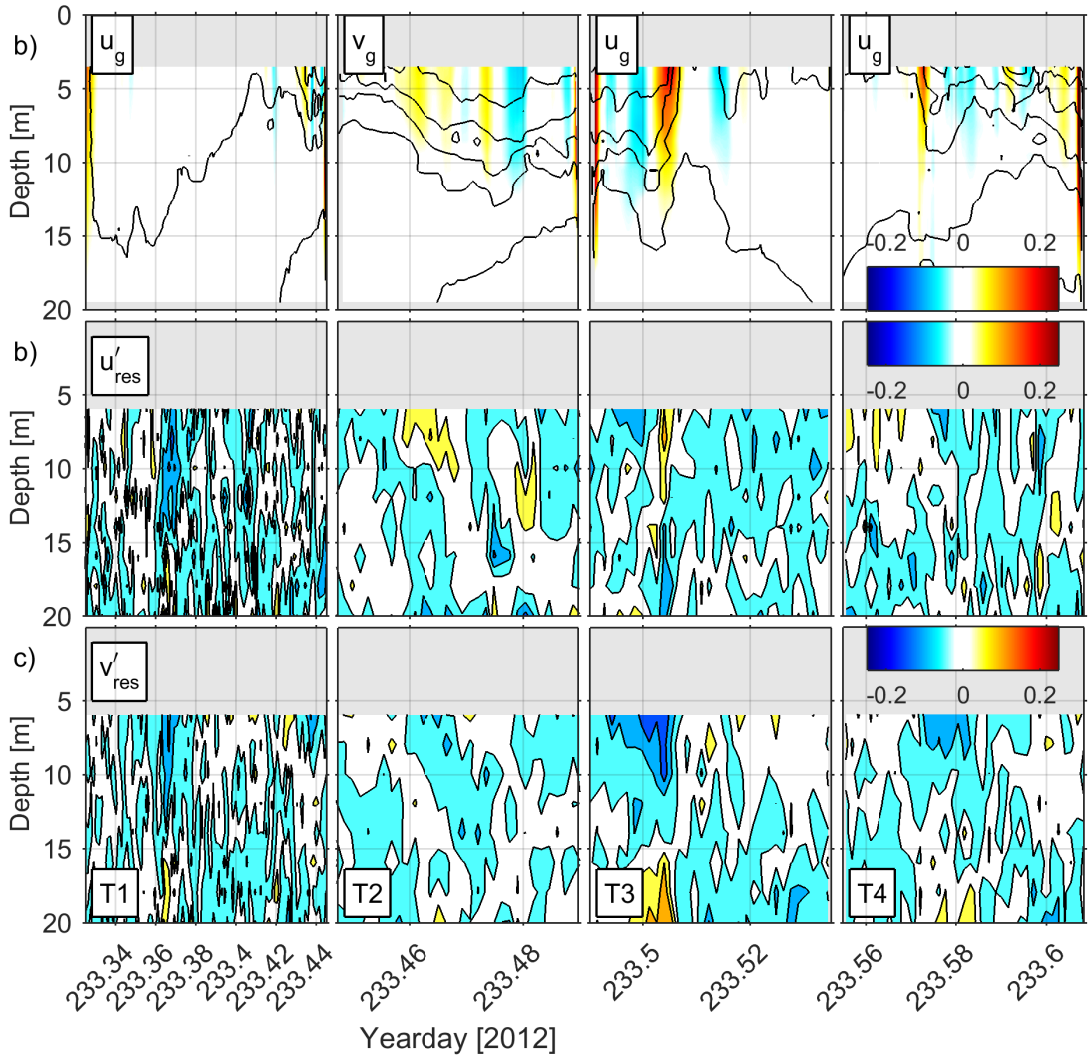

Figure 4.35: *The computed thermal wind and hydrodynamics of the frontal system on Yearday 227.* ***a)*** *The geostrophic flow as calculated by the thermal wind equation and associated with the horizontal density gradients.* ***b)*** *de-tided $u-$component of velocity;* ***c)*** *de-tided $v-$component of velocity. Velocity is in m s^{-1}.*

4.5 Summary

This Chapter set out to identify whether the formation of a shelf sea front within the vicinity of the study site was controlled by the seasonal heating-stirring balance and how susceptible it was to external forcing mechanisms. The identification of the mechanisms responsible for turbulent mixing and restratification requires knowledge of the background oceanographic environment. We describe the internal flow and water column structure during weakly-stratified spring time and strongly-stratified summer time conditions. Finally, the influence of interior mixing during strongly-stratified conditions on the vertical water column structure and turbulent mixing regime was investigated through the identification of non-linear internal waves (NLIW). The key findings of this Chapter are summarised as follows:

1. **Seasonal Cycles —** SST from monthly composite imagery showed the seasonal cycle of summer time warmin in the Celtic Sea. Average temperatures were approximately 11.5 °C in May which increased to a maximum 16.8 °C in August before cooling again. The formation of cool, inshore, water separated by sharp horizontal density gradients were indicative of the presence of a tidal mixing front off the north coast of Cornwall, in the vicinity of the study site. Cross frontal temperature difference averaged 2.4 °C in August between the inshore and offshore waters. The formation of such frontal signature initiated in June and broke down in October.

Having established the presence of a thermal front in the vicinity of the study site, a simple energy-based, heating-stirring model was used to establish analytically the vertical density profile, and hence formation of stratification, under the influence of local meteorological and bathymetric conditions. The temporal evolution of the water column structure shows how the inshore site ($SH = 1.5$) remains well-mixed throughout the year whereas the development of thermal stratification occurred within the theoretical frontal region ($SH = 2.7$), and further offshore ($SH = 3.5$). The results confirmed that a frontal zone based on the surface heating and tidal mixing was expected in the vicinity of the study site.

2. **Tidal Character —** Given the influence of the tides on the formation of stratification and driving shelf sea mixing, we determine the tidal characteristics for the study site. The results of spectral analysis presented a semi-diurnal regime with $>$90% of the tidal energy in the M_2 and S_2 constituents. Resolving

the tidal ellipses for these two constituents showed that the semi-diurnal currents were orientated parallel to the coastline and bathymetric contours. The tidal ellipses were highly rectilinear with small polarity of -0.06, indicating a slightly clockwise rotating component. The conclusion was made that the influence of rotation on the BBL dissipation height was minimal given such a small polarity. Progressive vector diagrams showed the trajectory of these tidally-driven oscillations which were between 9–11 km long along their major axis. Their overall position were influenced by the northeastward flow of the sub-tidal residual current.

3. **Synoptic Events —** Further decomposition of the ADCP data was able to determine a low-frequency, sub-tidal residual current. A consistent northeastward residual flow was present in both spring and summer, maintaining an average velocity of 3 km day^{-1} in spring and 4 km day^{-1} in Summer(3.5 cm s^{-1}, 4.5 cm s^{-1}). Between yearday 135–137, a low-frequency oscillation was observed that was a result of strong clockwise rotating wind event. The results show the influence of wind-forced Ekman dynamics in either imparting a direct push on the surface layer or setting up flow normal to the wind direction both with the potential for upwelling and downwelling occurring along the coastline (e.g. Figure 4.15). With the formation of density stratification the sub-tidal residual velocities presented a degree of inconsistency to a wind-driven flow and a primary candidate mechanism was a baroclinic flow set up by the horizontal density differences present in the stratified waters in Summer.

4. **Spring-neap variability —** The vertical temperature structure of the water column at the thermistor mooring was generally well-mixed in spring. The gradual warming observed in the timeseries over the period of deployment was in line with the positive solar heat flux into the ocean. Vertical banding in temperature observed in the timeseries was primarily due to advection at tidal frequencies with larger variability in temperature observed at spring tides. The lack of stratification in the water meant that buoyancy frequencies remained relatively low ($<10^{-5}$ s^{-2}), apart from an isolated period of weak near-surface stratification on yearday 134 and further weak enhancements related to the semi-diurnal advective temperature variations. The shear-squared timeseries presented a classic enhanced bottom-boundary layer shear profile ($>10^{-4.5}$ s^{-2}), extending up between 10–30 m above the bed over the neap-spring tidal cycle. Periodic extensions of elevated shear-squared BBL into the upper water column ($>10^{-5}$ s^{-2}) were observed along with further

near-surface sources of enhanced shear-squared. The enhanced upper water column shear was associated with periods of elevated ΔT, suggesting shear induced vertical mixing during these periods causing the downward mixing of warm surface waters.

The thermistor timeseries in August presented a stratified environment during neap tides and before the passage of a storm on yearday 228. This storm event completely altered the vertical structure of the water column, breaking down stratification and deepening the isotherms expounded by the high shear-squared values that accompanied the high wind stresses (≥ 0.5 N m^{-2}) and large significant waves ($\sim$5 m). The temperature change associated with the change in water mass pre- and post-storm was not associated with the increase in heat from the positive heatflux unlike that observed in spring. It was concluded that the strong northerly winds caused a large advective surge that brought warmer waters inshore, a conclusion supported by observations of the spatial structure from SST and Minibat surveys.

5. **Non-linear Internal Waves —** Two packets of NLIW were observed at the study site during the summer stratified period. The presence of the NLIW occurred at slack water during the change in tide. Such conditions are indicative of a hydraulic jump where the NLIW packet releases from the generation site during a transition from super-critical to sub-critical conditions and travel along the thermocline in stratified waters.

The passage of the NLIW were associated with increased levels of shear and turbulent mixing as demonstrated by the shear plots and Richardson numbers. The echo intensity recorded by the BM-ADCP showed increased turbulence during the passage of the NLIW. The presence of NLIW strongly suggests that alternate, interior, mixing processes are active in such marginally stratified shelf seas and the increased levels of turbulence strongly indicates that such processes play an important role in vertical mixing across thermocline.

CHAPTER 5

THE MIXING PROCESSES AT A SHELF FRONT

This Chapter investigates turbulent mixing in the vicinity of a tidal-mixing front which separated the, well-mixed, inshore waters from the seasonally stratified offshore regime. In-situ turbulence measurements were recorded at two stations, where the turbulence microstructure sensor (MSS) was repeatedly profiled over the semi-diurnal tidal cycle. Station 1 (St1) was located offshore (65 m) of the frontal zone in weakly-stratified waters, whilst Station 2 (St2) was located further inshore (35 m), in well-mixed conditions.

The aim of this study was to quantify the relative impact of turbulent processes arising from tidal friction at the seabed to the additional turbulent mixing processes that occur due to internal mixing and surface forcing. This Chapter firstly considers the evolution of turbulent mixing during the, weakly-stratified, spring season conditions, before investigating the role of stratification on the turbulent mixing processes in more strongly-stratified conditions present in late summer (Figure 5.1).

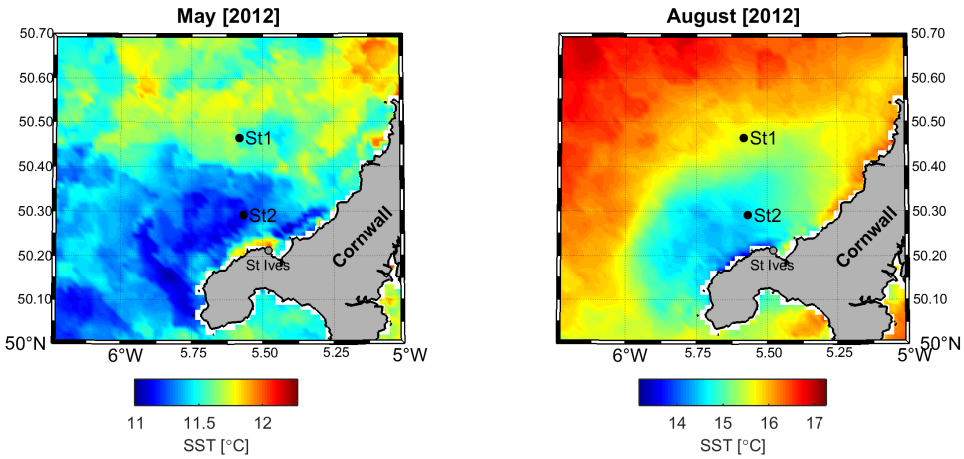

Figure 5.1: *Monthly-composite SST showing the formation of seasonal stratification at the study site with the offshore MSS sampling station (St1) representing weakly stratified waters whilst the inshore station was typically well-mixed (St2).*

5.1 The Weakly Stratified Conditions in Spring

In total, four complete (12.42 hour) tidal cycles were sampled during weakly stratified conditions in spring. Sampling was alternated between Station 1 and 2 conducted over a single tidal-cycle at both neap and spring tides. We firstly describe the background conditions during sampling before delving into the turbulent dissipation and associated datasets in detail while discussing

the proposed mechanisms recognised to bring about the observed turbulent mixing profiles in the data.

5.1.1 Background Conditions during Turbulence Profiling

As will be shown in this Chapter, many processes — both spatially and temporally — exist that cause variability in the water column structure seen here. As has been eluded to in the previous Chapter, and highlighted in Figure 5.1, the vertical structure of the water column varies spatially between Station 1 and 2 due to the levels of turbulent mixing and stratification. Significant temporal variability was also recorded between neap and spring tides, observed in the levels of tidal stirring and frontal advection over the excursion of the tide. Figure 5.2a presents the wind stress, significant wave height and barotropic current magnitude over the period of deployment in May.

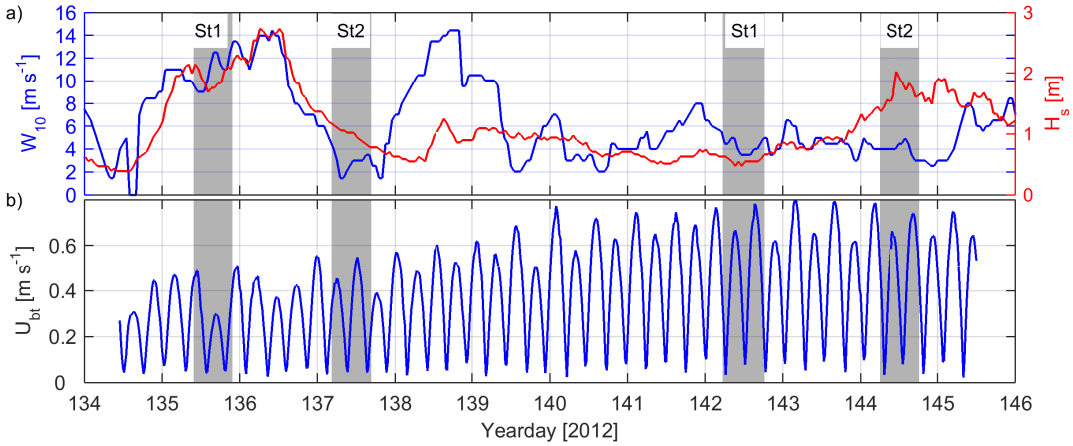

Figure 5.2: *Meteorological conditions during MSS sampling in May (grey shade).* ***a)*** *Wind speed (W_{10}) calculated for 10 m above the boundary and significant wave height (H_s).* ***b)*** *Depth-mean, barotropic tidal magnitudes as measured by the BM-ADCP situated approximately mid-way between St1 and St2.*

The conditions met sampling at St1 on yearday 135 was rough due to a significant wind event ($\geq$10 m s^{-1}) with large significant waves height, H_s $\sim$2 m, (Figure 5.2). Such conditions are conducive to inducing large mixing into the surface layer. In contrast, sampling on yearday 137 at St 2 was relatively calm, with wind speeds $\leq$4 m s^{-1} between the two storm events. The significant wave height was 1 m, having decreased from a peak of 2.8 m on yearday 136. Sampling on these two days occurred during neap tides; maximum barotropic tidal currents were $\sim$0.5 m s^{-1}. Figure 5.2b illustrates the unequal

semi-diurnal tidal regime recorded by the BM-ADCP with successive velocity maxima achieving asymmetrical current magnitudes. It is interesting to note that the particularly depressed ebb barotropic current recorded on yearday 135.7 was entirely tidal as was discovered when compared to a reconstituted tidal series from harmonic analysis.

The second group of sampling occurred during spring tides with the maximum barotropic tidal current was approximately 0.75 m s^{-1}. Meteorological conditions were calmer with winds of < 5 m s^{-1} during sampling on both days. Significant wave height was initially between 0.5–0.6 m on yearday 142 which increased to a maximum of 2 m during sampling on yearday 144.

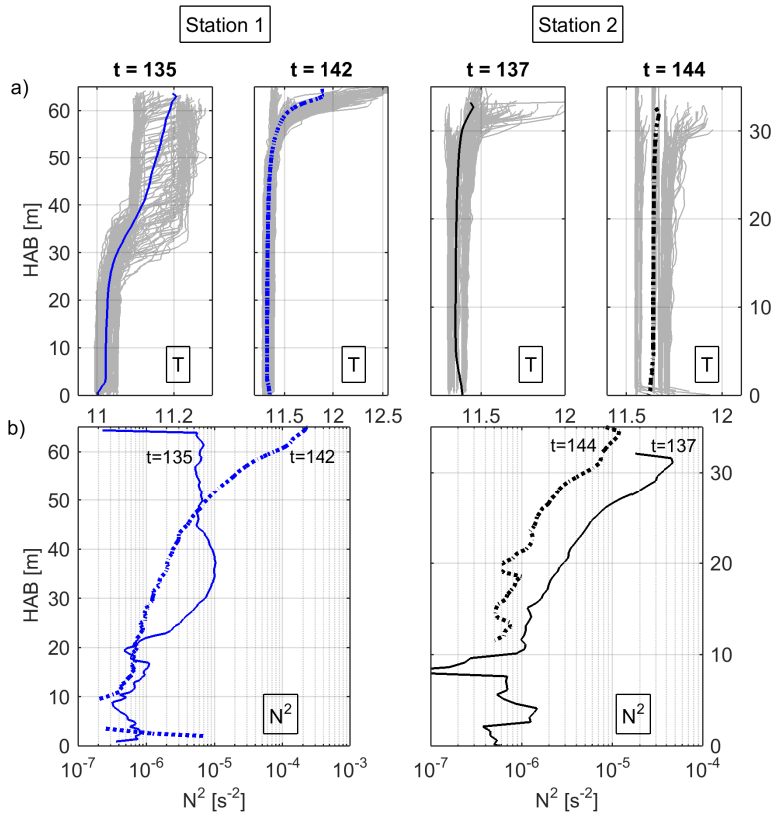

Figure 5.3: *The vertical temperature structure and squared buoyancy frequency for each 12.42 hour, MSS tidal cycle in spring.* ***a)*** *Individual MSS profiles of temperature (grey) and the tidal-cycle mean (blue).* ***b)*** *The moderately-smoothed buoyancy frequency squared (N^2), indicating the level of vertical stratification present.*

The vertical structure of temperature (T) and buoyancy frequency squared (N^2) are presented in Figure 5.3 to describe the water column structure during MSS profiling to put these results into context of the background stratification. Figure 5.3a presents individual profiles of temperature from the MSS in grey,

overlaid with the tidal-cycle average in blue. Each 12.4-hour tidal cycle is presented for both the offshore (St1) and inshore station (St2). Figure 5.3b presents the tidal cycle average buoyancy frequency squared (N^2) profiles that indicate the level of vertical stratification present.

Sampling on yearday 135 occurred during neap tides and the mean temperature was 11.1 $\pm$0.14°C (2 std.). A distinct homogeneous BBL was present in the bottom 25 mab. The temperature then increased above the BBL where the profiles exhibited a rise in temperature of between 0.1–0.2°C, with two distinct groups seen in the grey profiles. The warmer group of profiles (11.2°C) created a distinct two-layer vertical structure that deepened over the tidal-cycle whilst maintaining sharp gradients in temperature at the base. The downward transition of the thermocline suggested significant surface mixing occurred during the strong wind event recorded on yearday 135. The levels of stratification associated with the tidal-mean temperature profile ranged between a minima of 3×10^{-7} s^{-2} in the BBL to a maxima of 10^{-5} s^{-2} immediately above the BBL in the mid-water column at 35 mab. Above this mid-water column maxima, N^2 remained relatively constant at 6×10^{-6} s^{-2} up to the surface.

The following tidal cycle sampled at Station 1 was during spring tides on yearday 142. The mean temperature over the tidal cycle was 11.4 $\pm$0.28 °C, approximately 0.3°C warmer than on yearday 135. The water column was well-mixed between 0–50 mab, above which a relatively thin warm ($+$0.5°C) surface layer occupied the top 15 m. Maximum temperatures within the surface layer reached 12.5°C. Again, the surface layer exhibited two groupings indicating that the surface layer temperature conditions varied significantly over the course of sampling. The lack of vertical stratification below the surface layer was observed in the buoyancy frequency profile with N^2 values in the interior presenting a gradual increase up to a maximum of 2×10^{-4} s^{-2} in the near surface layer associated with the large vertical gradients in temperature.

In comparison to St1, minimal stratification was expected at St2 since it was inshore of the front predicted and observed in the previous Chapter. Sampling during neap tides on yearday 137, and also at spring tides on yearday 144, presented vertically homogeneous mean temperature profiles as would be expected due to the increase in tidally-driven turbulent mixing, with temperatures of approximately 11.35°C and 11.6°C, respectively. In a similar manner to that observed at St1, St2 exhibited near-surface warming in some of the grey profiles, again indicating warming at the surface over the tidal cycle. Sampling

during spring tides on yearday 144 showed the water column to be distinctly separated into two groups throughout the whole water column instead of just the surface layer as seen on the other sampling days.

The well-mixed water column at St2 was illustrated in the calculated low N^2 values for the majority of the water column. However, the strongest stratification in the near-surface layer was of an equivalent magnitude to that in the interior at St1 ($\sim 10^{-5}$ s^{-2}). Both yearday 137 and 144 were more strongly stratified in the surface layer than at neap tides at St1 (yearday 135).

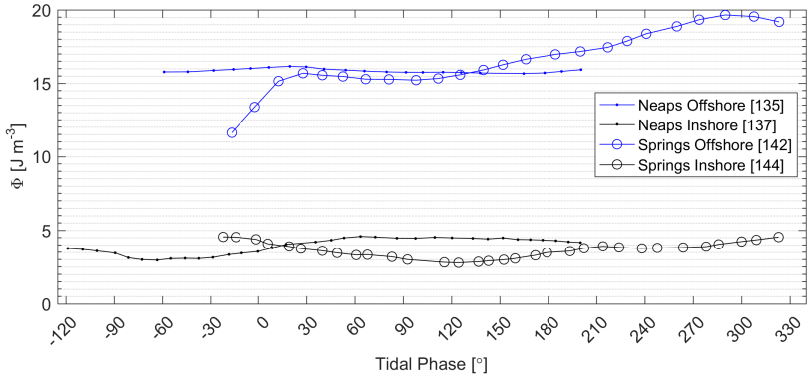

Figure 5.4: *The potential energy anomaly of the water column as calculated by the MSS density profiles during sampling at Station 1 & 2 in spring. The potential energy anomaly is a quantitative measure of stratification and represents the work required per unit volume to bring about the complete mixing of the water column.*

Figure 5.4 presents the potential energy anomaly (Equation 4.1) giving an indication of the variation in stratification levels over the MSS sampling tidal cycle. The offshore station retained a greater degree of stratification over the tidal cycle at both neap and spring tides, with a neap tide average of 16 J m^{-3} and a spring tide average of 16.5 J m^{-3}. The spring tide values increased from 11.5 J m^{-3} to a maximum of 19.5 J m^{-3} towards the end of sampling. The potential energy anomalies observed here were consistent with observations made in other parts of the Celtic Sea by Cross et al. (2015), at Station L4 (50° 15′N 4° 13′W). As was previously identified in the temperature profiles above, the vertical structure at the inshore station (St2) was fairly homogeneous and this was reflected in the low potential energy anomaly. The potential energy anomaly were relatively constant, between 3–5 J m^{-3} throughout both tidal cycles.

In summary, the background conditions during sampling in spring were vari-

able. The first tidal cycle on yearday 135 was conducted in strong winds with a relatively large significant wave height. The water column responded to the stormy conditions with a deepening of the surface mixed layer to a depth of 30 mab as was seen in the temperature profiles. The wind and waves then decreased for sampling on yearday 137 and the second sampling at St1 on yearday 142 was also under calm meteorological conditions though at spring tides. The final tidal cycle at St2 on yearday 144 occurred with relatively low wind speeds though the significant wave height had increased to 2 m. The temperature of the average profiles saw a gradual increase from 11.1 to 11.6°C over the course of the 9-day period. This was in line with that observed at the thermistor mooring due to the positive solar heatflux. In general, levels of N^2 were highest in the thermocline ($> 10^{-5}$ s^{-2}) and decreased to minima in the BBL ($< 10^{-6}$ s^{-2}). There was a distinct difference in potential energy anomaly between the inshore and offshore stations with the offshore station containing a larger anomaly denoting stronger stratification was present offshore.

5.2 Spring — the Turbulent Structure at the Offshore Station (St1)

5.2.1 Yearday 135 — Neap Tides

The evolution of turbulent dissipation and the vertical temperature structure is examined over the tidal cycle at neap tides (Figure 5.5). Here we examine the evolution of the tidally-driven bottom boundary layer (BBL) in response to the oscillatory tidal forcing, as well as the impact of significant wind and wave forcing at the surface on the vertical structure. Sampling on yearday 135 was conducted during a period of strong winds ($\geq$10 m s^{-1}) and an increasing significant wave height to a maximum of 2 m at the start and end of sampling; the sampling was conducted during rough sea conditions.

Profiles of turbulent dissipation rates as measured by the MSS are presented in Figure 5.5a. A tidally-driven turbulent BBL was evident by the enhanced turbulent dissipation rates and homogeneous temperature within the near-bed region (Figure 5.5a,b). Two periods of enhanced dissipation were observed at a quarter-diurnal (M_4) tidal periodicity induced by the accelerating tidal currents. Peak dissipation rates exceeding 10^{-6} W kg^{-1} were measured near the seabed that decreased by two to three orders of magnitude to 10^{-9} W kg^{-1} above

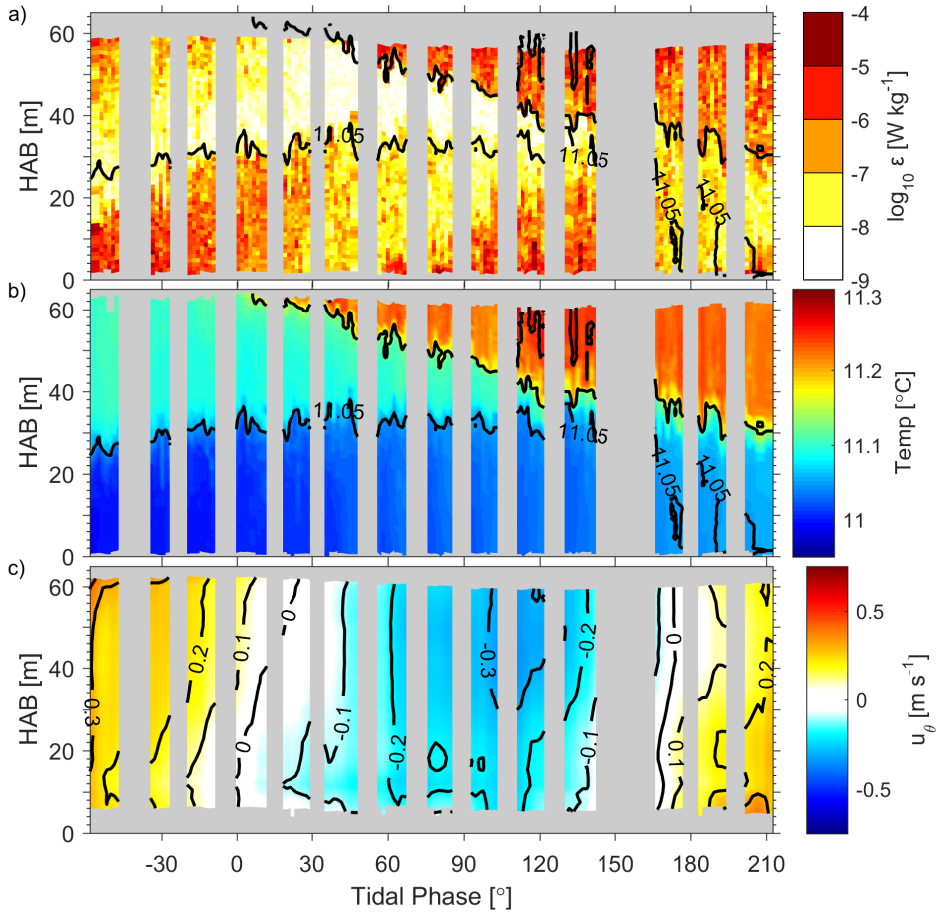

Figure 5.5: *MSS observations from Station 1 (offshore) on yearday 135 at neap tides.* ***a)*** *log base-10 turbulent dissipation rate with temperature contours overlaid,* ***b)*** *MSS temperature profiles,* ***c)*** *u-velocity rotated alongshore with velocity contours overlaid. The x-axis corresponds to the dominant M_2 tidal phase, whereby 0° refers to the minimum u-velocity near to the bed following the flood tide. Note the dissipation profiles were cropped near the surface to due to the more stringent data processing required to remove spurious shear measurements caused by the instrument's initial acceleration.*

the BBL. The cycle of dissipation approximately in phase with the velocity magnitudes, though a lag between the quarter-diurnal velocity signal and that of the turbulent dissipation was observed. This is most easily illustrated with the minimum dissipation rates succeeding the current velocity minima by approximately 20–50° near the bed. Similarly, the velocity minima during the second stage of the tidal cycle occurred between 140–160° while the dissipation minima was observed at 180–190° near to the bed. This phase lag between the dissipation rates and current velocity was observed to increase with height above the bed and is investigated further later in this Chapter.

The BBL was also evident in the temperature structure (Figure 5.5b). A cooler, well-mixed, bottom layer was observed to evolve through the tidal cycle. This temperature boundary layer was 24 mab at the beginning of sampling and was observed to increase in height to a maximum of 38 mab with the growth of the turbulent BBL. The 11.05°C temperature contour shows the enhanced dissipation rates during the fully developed stage of the BBL matched the height of the temperature contour with sharp gradients at the BBL interface in temperature and turbulent dissipation occurring concurrently. Towards the end of sampling (150–215°), a rise in temperature in the BBL was observed, most likely caused by weak vertical mixing from the deepening surface warm layer in contact with the BBL.

Figure 5.5c presents the measured ADCP current velocities with positive values indicating an alongshore flow in an easterly direction. Sampling commenced towards the end of a flood tide and captured the complete cycle of the subsequent ebb tide. The velocity magnitude attained a maximum of 0.45 m s^{-1} in the upper water column during the ebb tide between 100–130°. A phase lag in the vertical current profile was observed with the near-bed flow leading the upper water column.

Surface Forcing — storm conditions

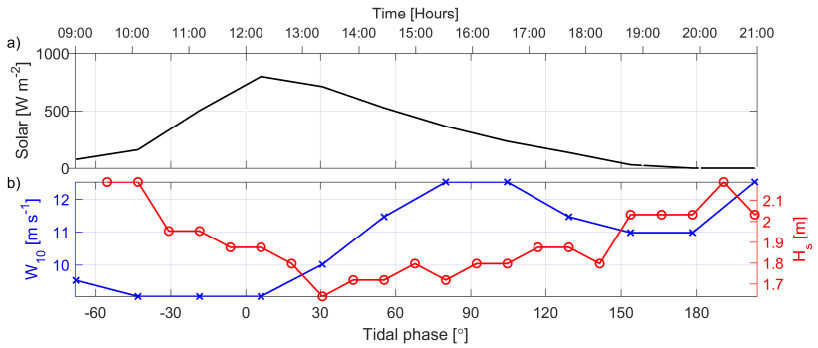

Figure 5.6: *Meteorological parameters for MSS tidal cycle on yearday 135.* ***a)*** *Solar short wave heat flux;* ***b)*** *wind speed measured at 10 m above the ground (blue,x) and significant wave height (red, o)*

The impact of the significant wind event was evident in the turbulent mixing and associated thermal structure. Figure 5.6 presents the meteorological conditions during sampling. The sampling began at 09:00 with an increasing solar heat flux that reached maximum at approximately mid-day and at high tide (0°), as presented in Figure 5.6. The wind speed also increased over the course of sampling, from 9 m s^{-1} to a maximum of 12.5 m s^{-1} around 16:00

(90°). The significant wave height decreased from 2.2 m to 1.65 m over the first half of the tidal cycle and then increased back to 2.2 m by the end of the tidal cycle.

The near-surface turbulent dissipation in Figure 5.5a indicated a deepening of the surface mixed layer (SML) between 40–210°, following the increase in wind speed and the short wave heat flux maxima. Dissipation rates in this layer were of the same magnitude as in the turbulent BBL (10^{-6} W kg^{-1}), providing a significant contribution to the overall turbulent dissipation. At the base of the deepening mixed layer, a distinct boundary with a sharp dissipation gradient separated it from the low background interior dissipation (10^{-9} W kg^{-1}) up to the point in the tidal cycle at which the depth of the SML matched the turbulent BBL. This occurred at 140° in the tidal cycle and elevated dissipation rates throughout the water column were observed with turbulent dissipation in the SML greater than below in the BBL during the decelerating stages of the tide.

The temperature in the surface mixed layer was relatively uniform, approximately 11.2°C, and was 0.1°C warmer than the interior and 0.2°C than the temperature within the BBL. The deepening SML maintained a sharp gradient in temperature that matched the depth of the enhanced dissipation throughout the tidal cycle. Hourly temperature profiles and N^2 presented in Figure 5.7 shows the evolution of temperature over the tidal cycle and the influence of the deepening SML on strengthening the thermocline, even under enhanced dissipation conditions. The buoyancy frequency squared (N^2) provides an indication of the strength of stratification and during the first half of the tidal cycle, maximum N^2 was associated with the temperature gradients at the top of the BBL (N$^2 = 1.5 \times 10^{-5}$ s^{-2}). Following the deepening of the SML, the increase in temperature gradients increased the N^2 associated with the temperature gradients in the upper water column (N$^2 = 5 \times 10^{-5}$ s^{-2}). The continual deepening of the SML created a well-mixed upper water column that was separated from the BBL by a temperature gradient that started broad and consolidated over the course of sampling, Towards the end of sampling, the strongest gradients were located at 30 mab with N$^2 = 3.5 \times 10^{-5}$ s^{-2} at 180°. Over the course of sampling, only a slight increase in BBL temperature (0.05°C) was recorded, indicative of the thermocline above the BBL from inhibiting the mixing of the warm surface water into the BBL.

The minimal increase in temperature in the BBL under enhanced turbulent

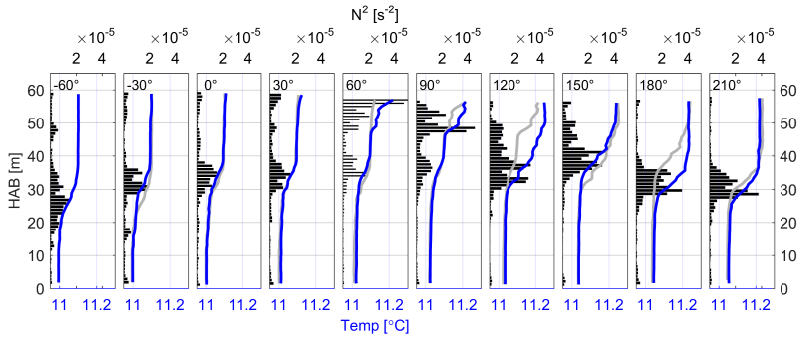

Figure 5.7: *MSS temperature profiles at 30° (1 hour) intervals over the tidal cycle on yearday 135. The present time profiles are denoted in blue and the grey profiles are the previous profile thereby illustrating the change over the interval. N^2 is presented by the horizontal bars and denotes stratification levels. The height of the BBL, as denoted by the homogeneous section of the temperature profile, was observed to evolve over the course of the semi-diurnal tidal cycle.*

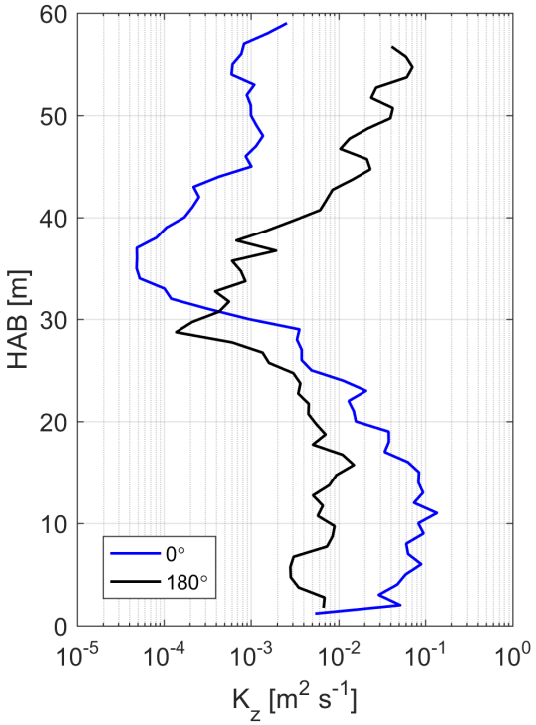

Figure 5.8: *Vertical eddy diffusivity from yearday 135 at 0°and 180°.*

dissipation and the increase in N^2 suggests a lack of vertical mixing across the thermocline. Analytical models and experiments suggest irreversible diapycnal mixing depends on the time evolution of turbulence, the stratification and the molecular diffusivity (Bouffard and Boegman, 2013). The amount of mixing as a result of the increased turbulent dissipation in the boundary layers may be given by the vertical eddy diffusivity;

$$K_z = \Gamma \frac{\varepsilon}{N^2} \tag{5.1}$$

where a mixing efficiency, Γ, of 0.2 was set (Osborn, 1980).

Figure 5.8 presents the vertical eddy diffusivity profiles for two stages of the tidal cycle on yearday 135 to illustrate the impact of the surface turbulent layer on mixing. During the first half of the tidal cycle (0°), eddy diffusivities (k_z) reached a maximum of 10^{-1} m^2 s^{-1} within the turbulent BBL and dropped to a minimum of 5×10^{-5} m^2 s^{-1} in the interior, above the BBL. Above the mid-column minima, diffusivities increased to 10^{-3} m^2 s^{-1} within the upper layer and reached a local maximum close to the surface of 3×10^{-3} m^2 s^{-1}. The increase in surface forcing and the deepening of the SML was reflected in the180°profile. Mixing rates in the SML were increased in comparison to previously and reached a maximum of 7×10^{-1} m^2 s^{-1} at the near-surface. Even during the latter stages of sampling in which the BBL growth had increased dissipation rates throughout the water column, there was still this significant decrease in the mid-water column. A mid-column minimum was present at 29 m, 10^{-4} m^2 s^{-1}. The lack of significant warming in the BBL, seen in Figure 5.3 & 5.5, can be related to this minima in K_z.

5.2.2 Yearday 142 — Spring Tides

The results of sampling at spring tides on yearday 142 are presented in Figure 5.10. The formation of the tidally-driven BBL was evident in Figure 5.10a and occurred at a quarter-diurnal periodicity in response to the M_4 tidal signal. During the peak of the BBL growth at 180° & 330° the BBL reached the near-surface (>55 mab), and was 20 m higher than that attained during the previous neap tide sampling. Enhanced dissipation rates of 10^{-6} W kg^{-1} were recorded within the BBL with highest dissipation rates near the seabed which sporadically reached 10^{-4} W kg^{-1} at some stages of maximum current flow. The growth of the BBL was asymmetric over the acceleration and deceleration stages of the quarter-diurnal period, with the phase lag increasing with height above the seabed. In comparison to the previous neap tidal cycle, the initial growth of the BBL in the accelerating stage was in phase with the initial acceleration of the tidal currents. As may be seen in Figure 5.10c, these tidal currents were also more symmetric in their acceleration and deceleration phases with no large vertical phase difference like was the case at neap tides.

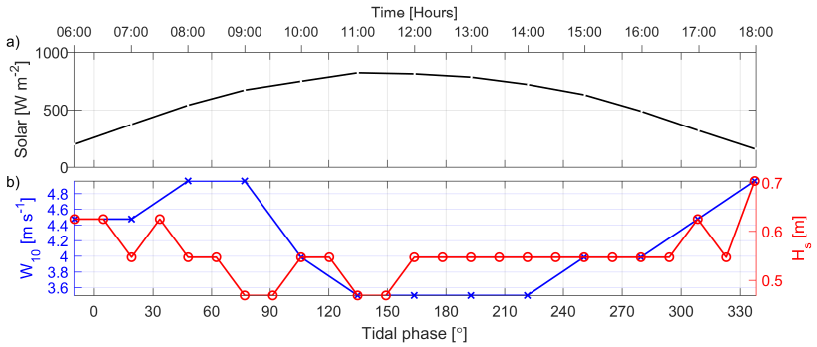

Figure 5.9: *Meteorological parameters for MSS tidal cycle on yearday 142.* ***a)*** *Solar short wave heat flux;* ***b)*** *wind speed measured at 10 m above the ground (blue,x) and significant wave height (red, o)*

The water column temperature was between 11.35–11.4°C and retained a well-mixed water column below a thin surface warm layer (>11.9°C) that was established between 60°–340°. The formation of this thin surface layer occurred during the morning increase in diurnal heat flux and also coincided with the maximum wind speed encountered over sampling (5 m s^{-1}). However, no significant deepening of the warm surface layer in response to the increased wind forcing was observed in the profiles following the initial appearance at 60°.

The maximum tidal current reached during this spring tidal cycle was ∼0.6 m s^{-1}. The sampling commenced near to the end of the flood tide and captured the subsequent ebb tide and most of the following flood tide. Minimal phase lag was observed in the vertical structure with a symmetric acceleration and deceleration phase.

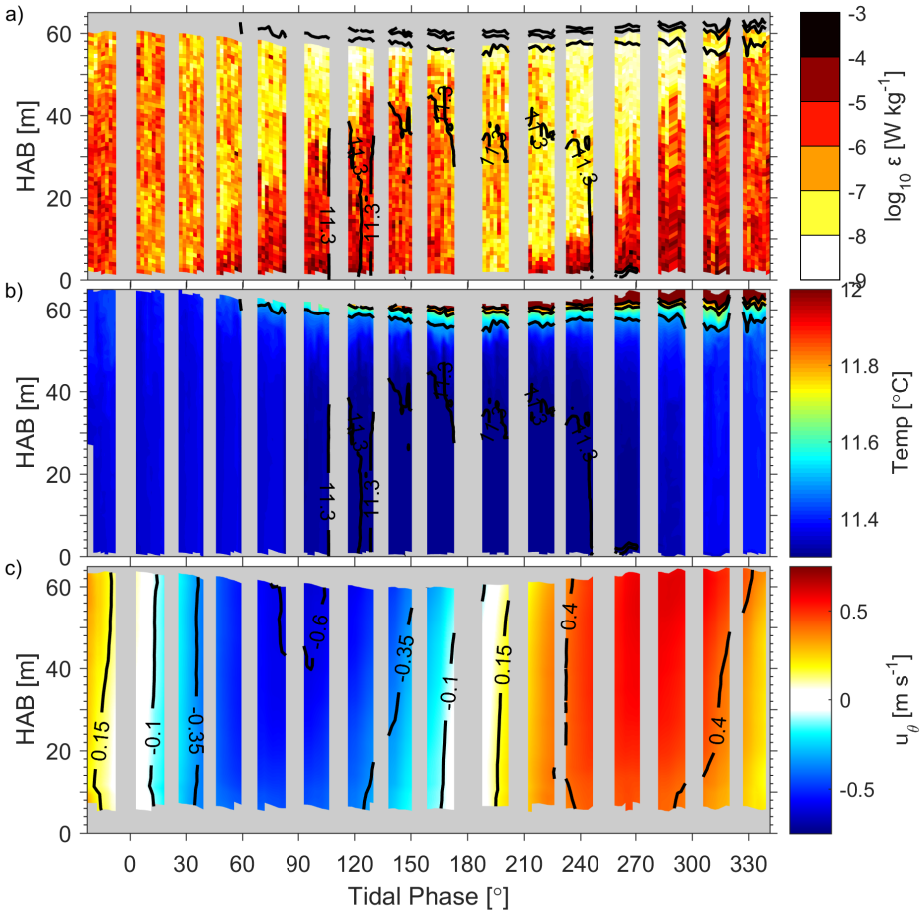

Figure 5.10: *MSS observations from Station 1 (offshore) on yearday 142 at spring tides.* ***a)*** *log base-10 turbulent dissipation rate with temperature contours overlaid,* ***b)*** *MSS temperature profiles,* ***c)*** *u-velocity rotated alongshore with velocity contours overlaid. The x-axis corresponds to the dominant M_2 tidal phase, whereby 0° refers to the minimum u-velocity near to the bed following the flood tide. Note the dissipation profiles were cropped near the surface to due to the more stringent data processing required to remove spurious shear measurements caused by the instrument's initial acceleration.*

5.3 Spring — the Turbulent Structure at the Inshore Station (St2)

5.3.1 Yearday 137 — Neap Tides

Sampling on yearday 137 occurred during neap tides. The inshore station (St2) was situated in 30 m water depth and the growth of the BBL was observed to extend up to the surface over the course of sampling (Figure 5.11a. Similar to the previous sampling, the growth of the BBL occurred at the quarter-diurnal

tidal period. For the majority of the tidal cycle, dissipation rates were $> 10^{-6}$ W kg^{-1} except for short periods following slack water when the rates dropped to 10^{-8} W kg^{-1}.

The water column was initially well-mixed with a temperature of 11.3°C. A significant increase in temperature was observed during the second stage of the tidal cycle (Δ0.15°C), commencing from the surface at 180° in the low dissipative region and rapidly deepening once dissipation rates increased during the peak flood tide.

The neap tidal currents reached a maximum velocity of 0.7^{-1} with surface intensification and a minimal vertical phase lag. Sampling commenced during an ebb tide and captured the transition to the subsequent flood tide and the initial stage of the following ebb tide.

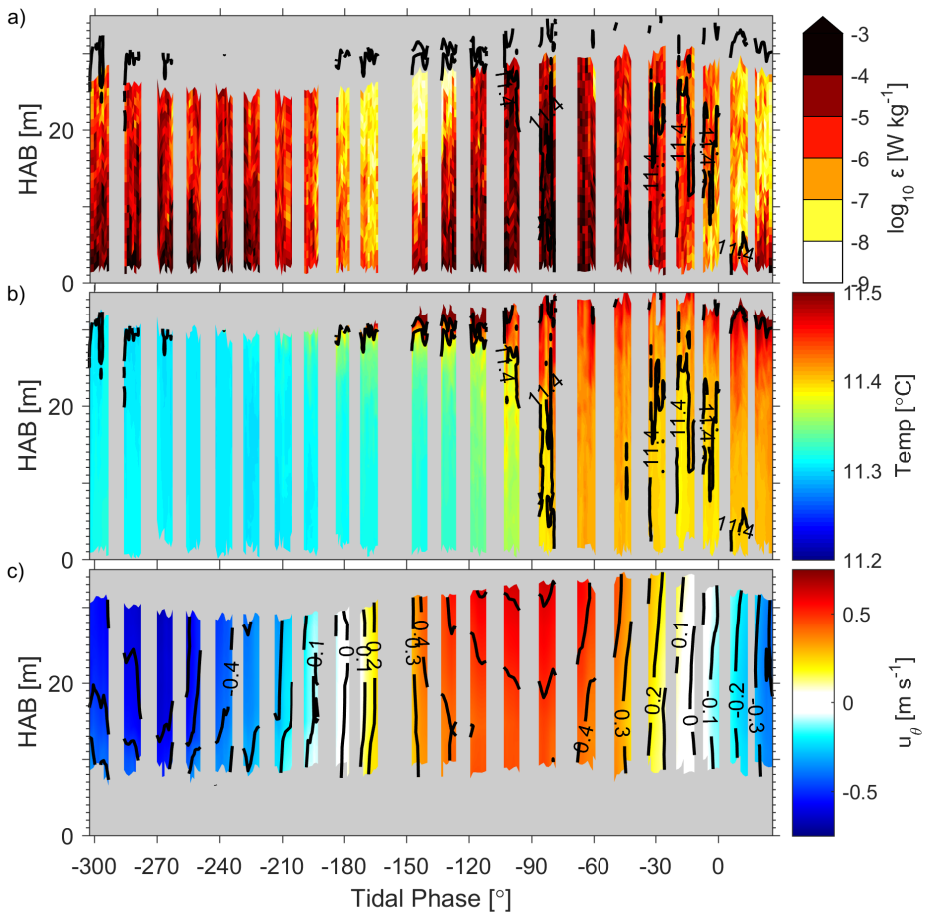

Figure 5.11: *MSS observations from Station 1 (offshore) on Yearday 137.* ***a)*** *log base-10 turbulent dissipation rate,* ***b)*** *temperature,* ***c)*** *u-velocity. The x-axis corresponds to the dominant M_2 tidal phase, where 0° is refers to the minimum u-velocity near the bed following the flood tide.*

5.3.2 Yearday 144 — Spring Tides

Sampling on yearday 144 occurred at spring tides. Once again, the BBL was observed to extend to the surface in response to the quarter-diurnal tidal current signal (Figure 5.12). The inshore station was controlled by a majority of high dissipation rates throughout the water column ($> 10^{-5}$ W kg^{-1}) with maximum dissipation $> 10^{-3}$ W kg^{-1}. Dissipation minima occurred at slack water in the upper water column (10^{-8} W kg^{-1}). The growth of the BBL was only slightly out of phase with the current minima preceding minimum dissipation by 20° in the vicinity of the seabed.

The water column structure was well-mixed with only slight stratification present near the surface between 175–240°. The temperature was initially 11.6°C and increased to 11.8°C over the course of sampling. The warming was associated and timed with the ebb tide and continued to warm to the flood tide before cooling slightly towards the end of sampling, suggesting that the warming was initially due to tidal advection while the surface stratification was due to solar heat input.

The spring tidal currents attained a maximum velocity of 0.95 m s^{-1}. The sampling commenced at the end of flood tide and captured the subsequent ebb and flood tides. There was minimal vertical phase lag observed in the current structure.

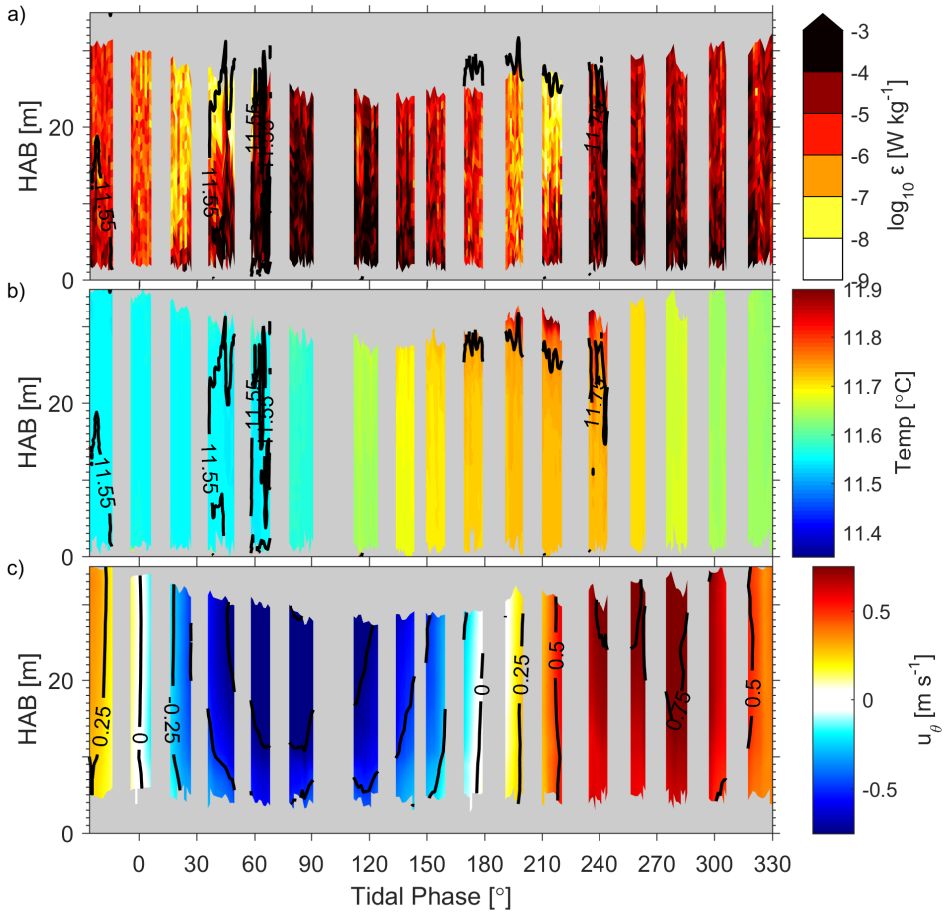

Figure 5.12: *MSS observations from Station 1 (offshore) on Yearday 144.* ***a)*** *log base-10 turbulent dissipation rate,* ***b)*** *temperature,* ***c)*** *u-velocity. The x-axis corresponds to the dominant M_2 tidal phase, where 0° is refers to the minimum u-velocity near the bed following the flood tide.*

5.4 The Strongly Stratified Conditions in Summer

The MSS field campaign in summer was conducted in a similar manner to that carried out in spring. Four complete tidal cycles were sampled in which sampling was alternated between St1 and St2 (at the same locations as May). The results from these sampling campaigns in summer are presented here and describe the MSS profiling with turbulent dissipation rates and associated variables presented from each tidal cycle.

5.4.1 Background Conditions during Turbulence Profiling

The meteorological conditions encountered during MSS sampling in August are presented in Figure 5.13. Sampling began at St2 on yearday 225 in wind speeds of 4–7 m s^{-1} with a significant wave height of less than 1 m. Sampling at St1 on the following day was preceded by a short peak in wind speed that attained a maximum of 13 m s^{-1}, after which the wind dropped rapidly to 5 m s^{-1} during sampling. The significant wave height was between 1.5–2.5 m. These two MSS sampling tidal cycles were conducted during a particular weak neap tide with a maximum barotropic current velocity of only 0.40 m s^{-1}. The conditions during spring tide sampling on yearday 232 was under low wind speeds of 2–4 m s^{-1} while the significant wave height was between 1.5–2 m. The maximum barotropic current velocity at spring tides were 1.1 m s^{-1}. The final sampling at Station 1 on yearday 234 recorded an increase in wind speed from 4 to 9 m s^{-1} over the duration of sampling. The significant wave height was 1–1.5 m.

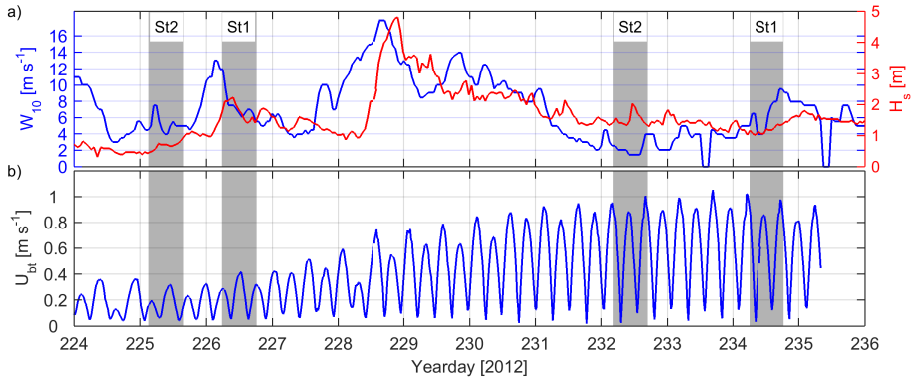

Figure 5.13: *Meteorological conditions for the during of MSS sampling (grey shade) in August.* ***a)*** *Wind speed (W_{10}) calculated for 10 m above the boundary and significant wave height (H_s).* ***b)*** *Depth-mean, barotropic tidal magnitudes as measured by the BM-ADCP situated approximately mid-way between St1 and St2.*

An overview of the water column temperature structure and stratification levels met during sampling is presented in Figure 5.14. The mean temperature on yearday 226 was 14.3 $\pm$1.78 °C and 15.3 $\pm$0.34 °C on yearday 234. These were both consistent with that measured at thermistor timeseries over the same time period. The vertical temperature profile on yearday 226 at the offshore station, St1, presented a warm surface layer separated by a strong

thermocline (Δ2.5°C) between 50–60 mab from the weakly stratified interior (15–50 mab), below which a well-mixed BBL was present (Figure 5.14a). The temperature within the BBL was 13.8°C while in the surface layer it was 16.3°C. The buoyancy frequency squared, N^2, profile reflected the level of stratification with maximum $N^2 = 6 \times 10^{-4}$ s^{-2} in the thermocline at 56 mab (Figure 5.14b). Stratification in the interior below the thermocline was approximately an order of magnitude less ($10^{-5} s^{-2}$), and significantly greater than that in the surface layer and BBL. Sampling at St1 during spring tides on yearday 234 presented weaker stratification in respect to the interior and thermocline. Nearly all the variability in temperature was above 40 mab. The upper water column saw a variation in structure with a warm surface layer present during low tide whilst the water column was well-mixed at high tide. During these stratified conditions, the temperature was approximately 1.8°C warmer in the surface layer with a sharp thermocline between 55–60 mab. The BBL temperature (<40 mab) was steady at 15.2°C over the course of sampling. The N^2 reflected the lack of stratification in the BBL with values 10^{-7} s^{-2} below 29 m above which N^2 increased steadily to a maximum in the surface layer of 8×10^{-5} s^{-2}.

Sampling at St2 in summer saw thermal stratification in the upper water column between 16–35 mab at neap tides while conditions were well-mixed at springs. On yearday 225 the surface layer above 30 mab was, on average, 15.2°C while the interior below the thermocline and BBL was 14.0°C. The N^2 profile echoed the increase in temperature in the thermocline with maximum $N^2 = 3 \times 10^{-4}$ at 27 mab. N^2 decreased below this to a minimum near the seabed (6×10^{-7} s^{-2}). The water column was well mixed at spring tides with a mean temperature of 15.0°C. An indication of some temporal variability was observed in the profiles with the presence of cooler waters at high tide (14.9°C), whilst warmer waters were recorded at low tide (15.4°C). The N^2 reflected the lack of a thermocline with low values ($< 10^{-5}$ s^{-2}) throughout the upper water column. An increase in N^2 was observed above the seabed in response to a slight decrease in temperature observed in this layer.

Potential Energy Anomaly

The potential energy anomaly calculated over the duration of the MSS tidal cycles in summer are presented in Figure 5.15. The deeper offshore station remained more stratified than the shallower inshore station at both neap and spring tides. The strongest stratification was during neap tides with

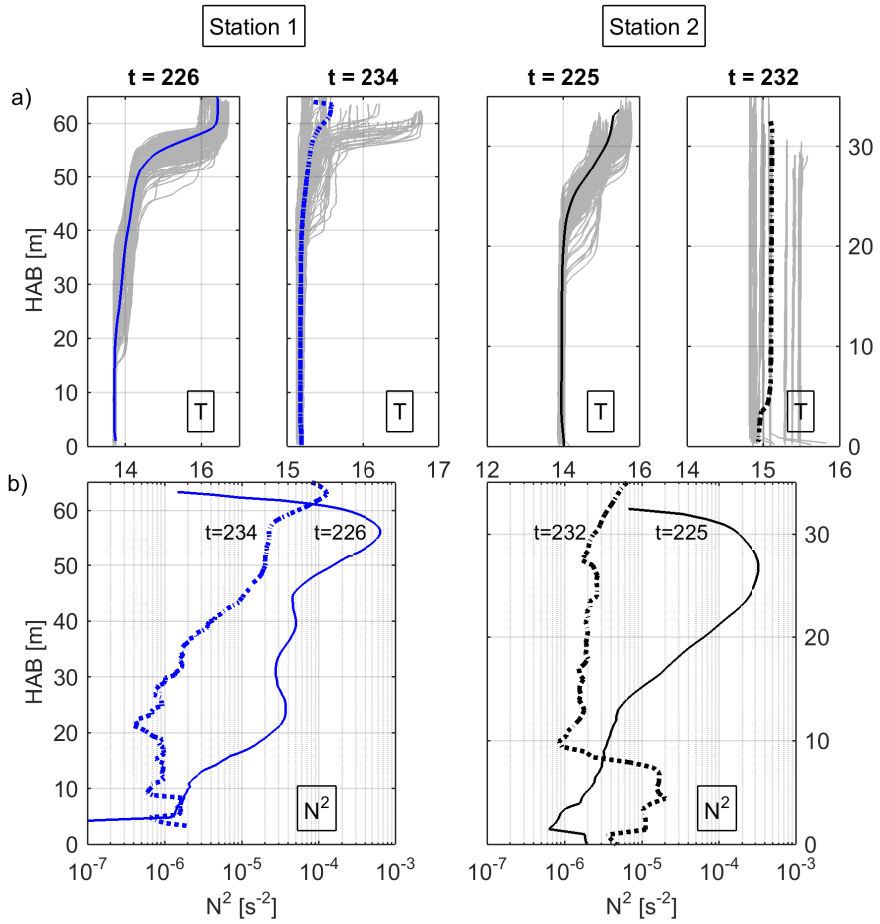

Figure 5.14: *The vertical temperature structure and squared buoyancy frequency for each 12.4 hour MSS tidal cycle in summer.* ***a)*** *Individual profiles of temperature (grey) and the tidal cycle mean (blue).* ***b)*** *The moderately-smoothed buoyancy frequency squared (N^2), indicating the level of vertical stratification present.*

values between 26–43 J m^{-3}. Spring tide values for the offshore station were significantly lower with values between 14–23 J m^{-3}. This was only slightly larger than the anomaly calculated for the inshore station at neap tides (8–13 J m^{-3}). The least stratified tidal cycle was at the inshore station at spring tides with relatively constant values of 2–5 J m^{-3}.

In summary, the background conditions during MSS sampling were variable with wind speeds between 1.5–12 m s^{-1} although wind speeds greater than 8 m s^{-1} were recorded only briefly during sampling at St1. The significant wave height varied between 0.5–2 m during sampling. It is worthwhile noting that the peak wind speed and significant wave height during the 11-day period occurred on yearday 228 in between sampling at neap tides and spring tides.

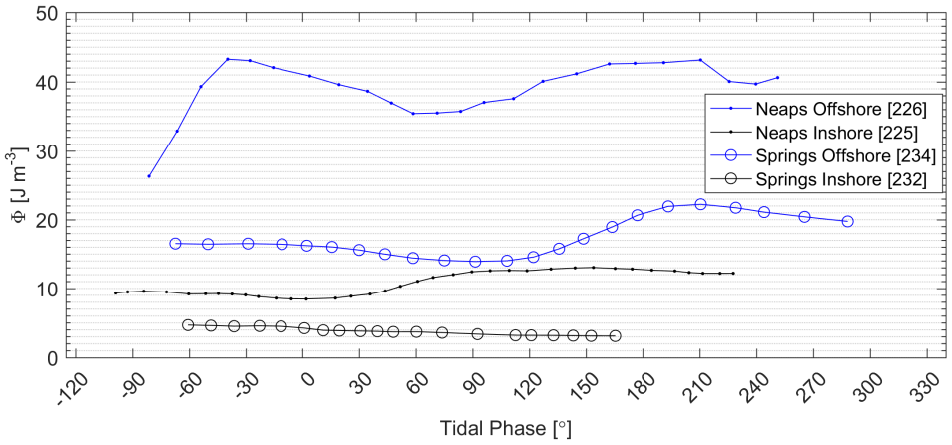

Figure 5.15: *The potential energy anomaly of the water column as calculated by the MSS density profiles during sampling at Station 1 & 2 in summer. The potential energy anomaly is a quantitative measure of stratification and represents the work required per unit volume to bring about the complete mixing of the water column.*

The impact of this storm was significant as was observed by the shift from stratified to well-mixed conditions in the thermistor data described in the previous Chapter. Neap tidal currents were 0.4 m s^{-1} while spring tidal currents reached 1.1 m s^{-1}.

The water column temperature during MSS sampling was between 13.9–16.8°C with the majority of the difference in the surface layer creating strong thermocline gradients. The offshore station was more stratified that the inshore station as was expected given the difference in water depth. St1 remained stratified at spring tide whilst St2 at spring tides was the only sampling to be well-mixed. The level of stratification was reflected in the potential energy anomalies. St1 at neap tides remained the most stratified throughout the tidal cycle whilst the St1 at spring tides was similar to St2 at neap tides. The lowest potential energy anomalies were at St2 at spring tides.

5.5 Summer — the Turbulent Structure at the Offshore Station (St1)

5.5.1 Yearday 226 — Neap Tides

Enhanced dissipation rates were observed within the turbulent BBL, interior and at the surface on yearday 226 (Figure 5.17a). Dissipation rates over the tidal cycle presented a quarter-diurnal signal in the turbulent BBL associated with the shear-driven turbulent mixing generated by the tidal current. The growth in BBL was significantly asymmetric over the acceleration and deceleration stages of the tidal flow. Maximum dissipation rates within the BBL were 10^{-5} W kg^{-1} close to the seabed. Typical values for the rest of the BBL were 10^{-6} W kg^{-1}. The maximum height of the BBL attained was approximately 28 mab during both the ebb and flood stages of the tidal cycle. However, during the latter part of the first ebb stage, between -180–$-120°$, a distinct period of elevated dissipation was observed in the outer BBL, which extended upwards and merged with a thin layer of elevated interior dissipation at 40 mab. This caused the 13.7 °C isotherm, situated on the outer layer of the BBL (Figure 5.16), to rise rapidly in height in response to the enhanced mixing in the outer BBL, observed in the decrease in the corresponding N^2 values between -160–-130(Figure 5.17a). The enhanced dissipation in the BBL during the second stage of the tidal cycle did not exhibit this upward offshoot and was depressed in comparison. Isotherms above the BBL during this stage (presented more clearly in Figure 5.17a), were observed to deepen with no interior source of elevated dissipation.

An thin layer of elevated dissipation was observed in the interior between -225–$-120°$. Maximum dissipation rates were 10^{-6} W kg^{-1} in this thin layer which was associated with an increase in mid-layer increase in the temperature gradient and N^2 values. This interior layer was also associated with enhanced shear-squared (S^2) observed in Figure 5.17b and the subsequent reduction in gradient Richardson numbers of <1, indicating weak instability in the water column was present.

Enhanced dissipation rates were also recorded above the sharp thermocline in the surface layer. Small-scale depressions in the thermocline at $-240°$, 15°, 60° were associated with enhanced dissipation in the surface layer above them. Similarly the depressions were observed in the isotherms in the interior.

Furthermore, increased shear (10^{-4} s^{-2}) was coincident with these depressions below the thermocline. These small interior vertical displacements mainly occurred at -240–210° and -60–30, which was associated with the reduction of current velocity at slack tide. This was a similar timing to that observed during the NLIW discussed in the previous Chapter. The vertical displacement was much less than that observed in the NLIW in the previous Chapter and was 4–6 m.

The vertical temperature structure over the tidal cycle showed the presence of a well-mixed BBL (approx. 0–25 mab) with a thermally stratified water column above (Figure 5.16b). A strong thermocline between 50–60 mab separated the surface layer, which was $\triangle$2–3°C warmer at 16–17°C. The temperature was 13.6°C within the BBL with low $N^2 =< 10^{-5}$ s^{-2} (Figure 5.17a). Temperatures increased outside the BBL with temperatures increasing by 0.7°C to 14.3°C immediately below the thermocline.

Sampling commenced during the mid-ebb tide and captured the flood and the first half of the subsequent ebb. Vertical shear in the velocity profiles were greatest near to the surface and creating a phase lag with depth. The maximum velocity of the flood current was $+0.4$ m s^{-1} whist the strongest current was recorded at the end with an ebb current of 0.6 m s^{-1}.

The strong thermocline between 50-60 mab limited the penetration of surface layer turbulence to depths shallower than the thermocline level. In addition, the frictional turbulent BBL is limited to between 20-30 mab in this instance. The thin band of enhanced turbulent dissipation between 35-40 mab occurs at the top of a weak thermocline and suggests the presence of thermocline shear rather than being directly related to either the near-surface turbulence or the turbulent BBL in a similar manner to that observed in Burchard and Rippeth (2009); Van Der Lee and Umlauf (2011).

Observations of the vertical structure of turbulent dissipation in the Irish Sea have shown the influence of stratification in inhibiting the growth of the BBL (Simpson et al., 1996). Figure 5.18 indicated a similar result when comparing observed BBL height at phase 90–180° to that at -85–0°. The height of the BBL was defined by the maximum gradient in dissipation rate within the outer layer of the BBL. The calculated height is shown in Figure 5.18 by red circles on the dissipation hourly profiles. Maximum BBL height attained between -85–0° was 30 mab. In comparison, the maximum observed between 90–180° was 24

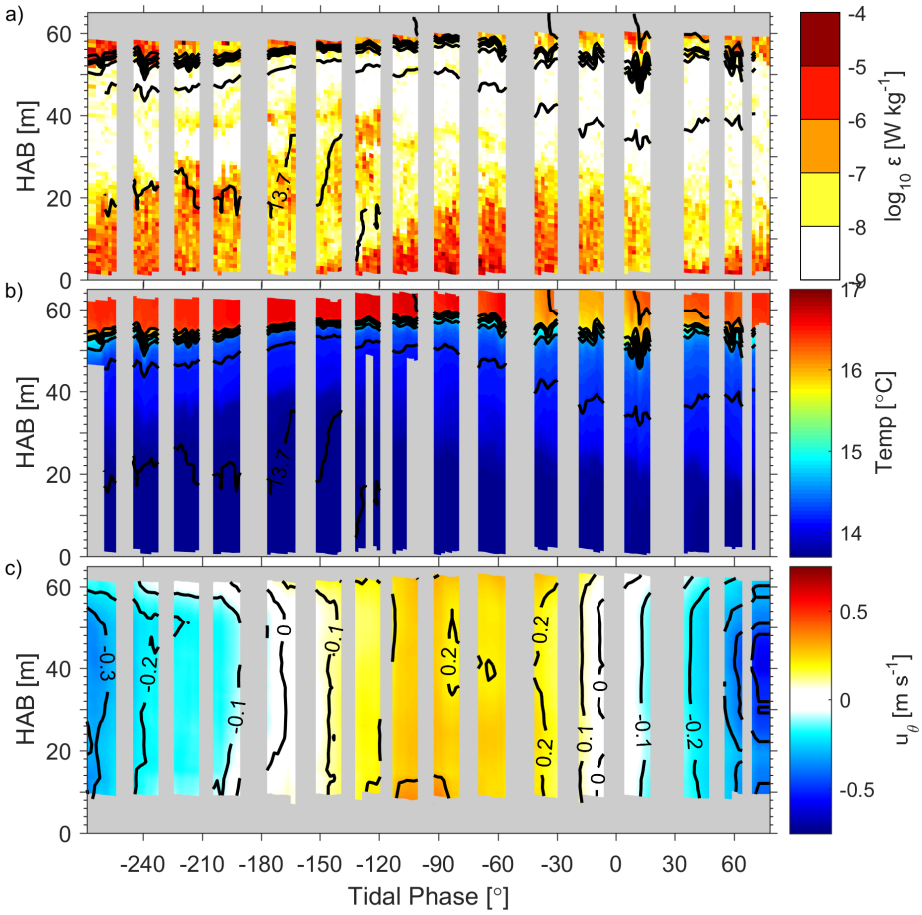

Figure 5.16: *MSS observations from Station 1 (offshore) on Yearday 226.* ***a)*** *log base-10 turbulent dissipation rate,* ***b)*** *temperature,* ***c)*** *u-velocity. The x-axis corresponds to the dominant M_2 tidal phase, where 0° is refers to the minimum u-velocity near the bed following the flood tide.*

mab. This can be related to the observed increase in N^2 levels in conjunction to the steady deepening of the stratified layer over the same period (90–180°). Similar results were obtained by Gayen et al. (2010) in model simulations of a BBL under stratified conditions.

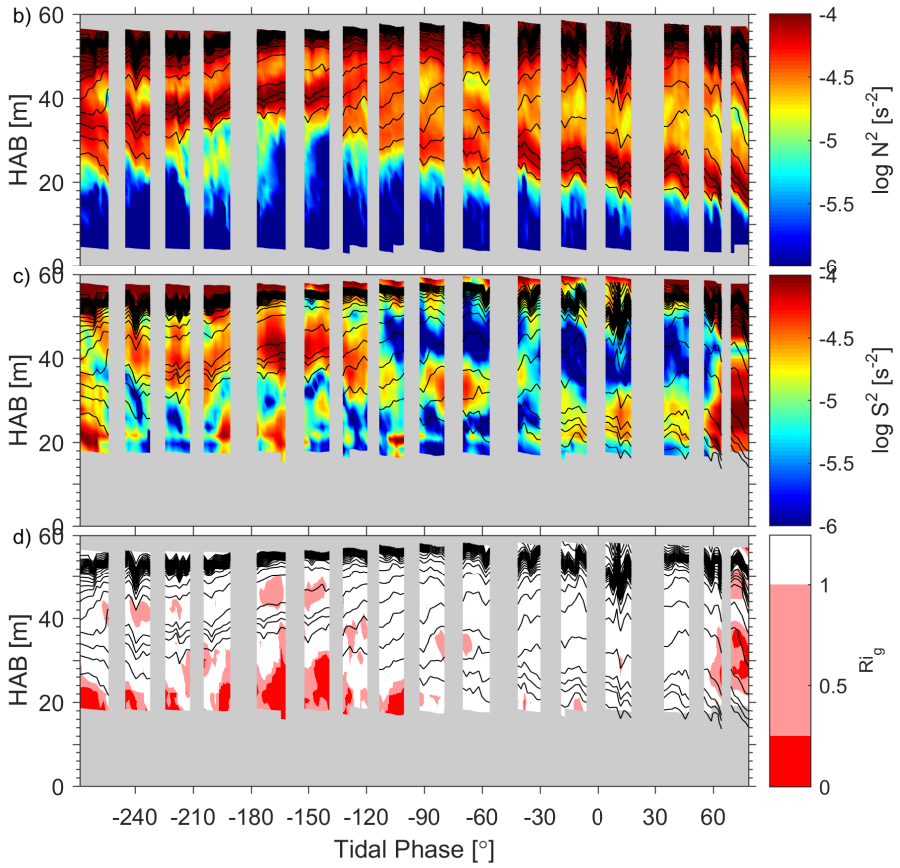

Figure 5.17: *Measured stratification and vertical shear at Station 1 (offshore) on Yearday 226.* ***a)*** *log base-10 buoyancy frequency squared (N^2),* ***b)*** *vertical shear squared (S^2),* ***c)*** *Gradient Richardson number showing a region of interior marginal stratification ($Ri < 1$) between 40-50 mab during the first half of the sampled tidal cycle. Temperature is contoured at 0.25°C and with actual values corresponding to those in previous figure. The x-axis corresponds to the dominant M_2 tidal phase, where 0° is refers to the minimum u-velocity near the bed following the flood tide.*

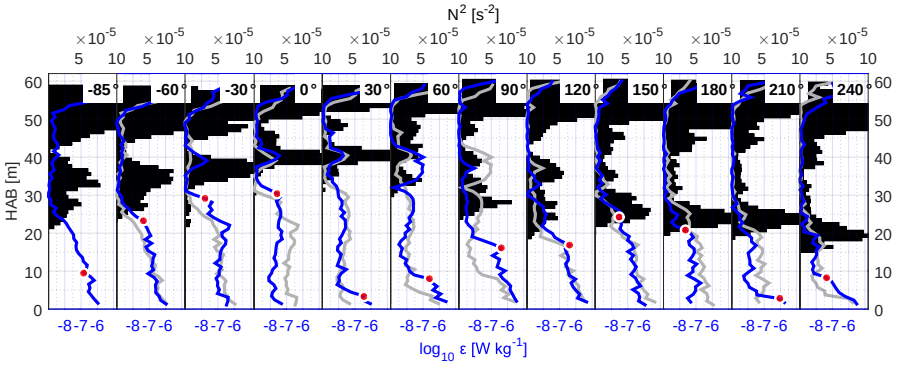

Figure 5.18: *Hourly profiles of turbulent dissipation from Yearday 226 with N^2 denoted by black horizontal bars. Corresponding tide phase is indicated at the top. The previous hour's profile is plotted in grey. Red circles denote height of the BBL based on maximum dissipation gradient in the upper region of the BBL.*

5.5.2 Yearday 234 — Spring Tides

Sampling on yearday 234 occurred at spring tides and the elevated dissipation rates arising from shear-driven turbulence at the seabed extended throughout the water column during peak flow (Figure 5.19a). Dissipation rates were predominately above 10^{-6} W kg^{-1} with maximum rates of 10^{-4} W kg^{-1} near the bed. In between the turbulent BBL, the background dissipation rates were 10^{-8} W kg^{-1} associated with slack tide. The growth of the BBL occurred at a quarter-diurnal periodicity with the flood and ebb flow of the tide. A minimal phase lag in dissipation rates was recorded along with tidal asymmetry between the acceleration and deceleration stages of the tide. Current velocities were strongest nearest the surface and reached maximum velocities of 0.9 m s^{-1} on the flood tide.

The water column was initially well-mixed with temperatures around 15.0°C (Figure 5.19b) that was related to the elevated dissipation rates throughout the water column. A period of near-surface stratification was observed between 160–240° preceded by sharp deepening of the isotherms on the leading edge of the warm water. The temperature was $>$16.5°C in this near-surface layer. The sharp depression in the isotherm was observed to occur again on the trailing end of the warm water with elevated dissipation rates on the upper side of the depression. A slight erosion at the base of the thermocline was observed although the near-surface isotherms remained intact.

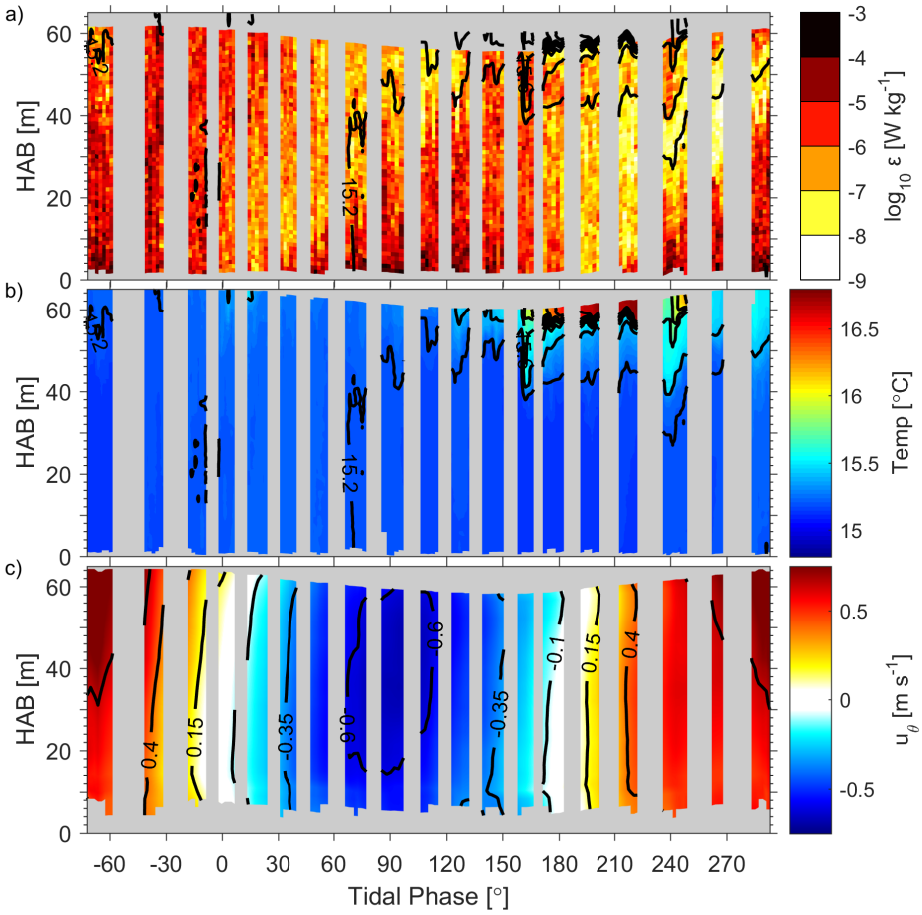

Figure 5.19: *MSS observations from Station 1 (offshore) on Yearday 234.* ***a)*** *log base-10 turbulent dissipation rate,* ***b)*** *temperature,* ***c)*** *u-velocity. The x-axis corresponds to the dominant M_2 tidal phase, where 0° is refers to the minimum u-velocity near the bed following the flood tide.*

5.6 Summer — the Turbulent Structure at the Inshore Station (St2)

5.6.1 Yearday 225 — Neap Tides

Sampling during neap tides at the inshore station was defined by weak surface stratification and the turbulent BBL extending up to the surface in the shallow water. The growth of the BBL occurred over a quater-diurnal period associated with the tide. Maximum dissipation rates were 10^{-5} W kg^{-1} near the bed with typical values of 10^{-6} W kg^{-1} within the BBL. Elevated dissipation rates were observed to extend up through the weak thermocline furing the first ebb stage of the tidal cycle. In comparison, the thermocline during the subsequent

flood stage prevented maintained lower dissipation rates above suggesting the thermocline acted as a barrier or there was not such a strong source of surface turbulence.

Weak stratification between 20–30 mab was recorded throughout the tidal cycle. The temperature in the interior was homogenous at 14°C whilst above the thermocline, in the surface layer, varied between 15–16°C. A singular sharp depression in the thermocline at $-110°$ deepened the isotherms by 9 m briefly. This was accompanied by enhanced turbulent dissipation above but no obvious signs of mixing below. Sampling commenced mid-way through the ebb tide and captured the subsequent flood tide. Maximum current velocities were recorded near the surface of the flood at 0.4 m s^{-1}.

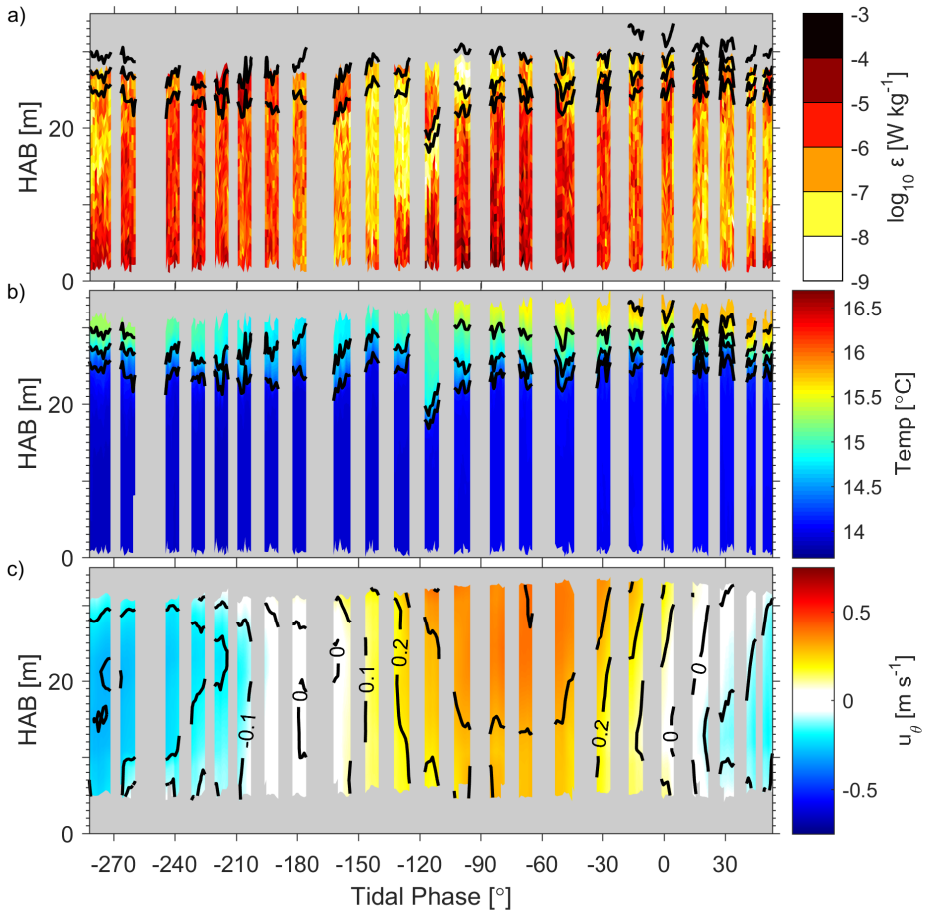

Figure 5.20: *MSS observations from Station 1 (offshore) on Yearday 225.* ***a)*** *log base-10 turbulent dissipation rate,* ***b)*** *temperature,* ***c)*** *u-velocity. The x-axis corresponds to the dominant M_2 tidal phase, where 0° is refers to the minimum u-velocity near the bed following the flood tide.*

5.6.2 Yearday 232 — Spring Tides

Sampling on yearday 232 occurred during spring tides and high levels of turbulent dissipation were observed throughout the tidal cycle originating from the turbulent BBL. Maximum dissipation rates were 10^{-3} W kg^{-1} near the seabed, though dissipation rates $>10^{-4}$ W kg^{-1} were observed to extend up to the surface.

The vertical temperature structure was well-mixed throughout the tidal cycle. A slight warmer was observed over the tidal cycle with temperatures initially at 15.0°C which and warmed to 15.5°C by the end. Sampling began during a flood tide and captured the subsequent ebb tide. Maximum current velocities were 1.1 m s^{-1} and contained a slight phase lead near to the surface.

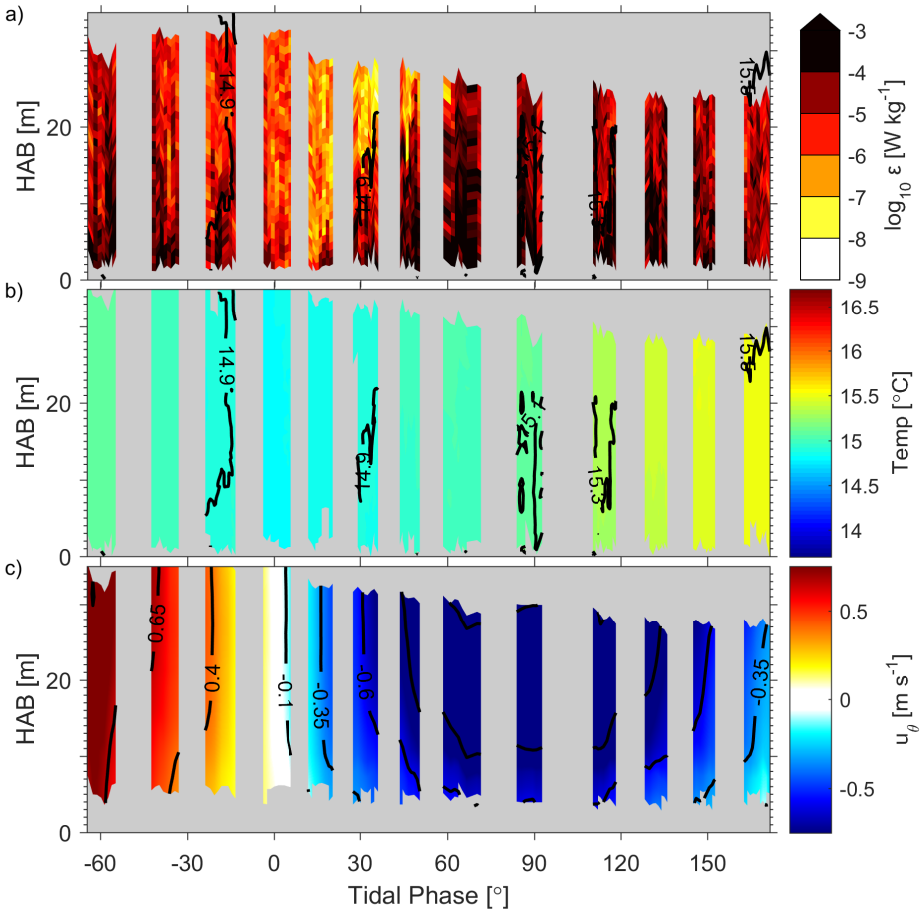

Figure 5.21: *MSS observations from Station 1 (offshore) on Yearday 232.* ***a)*** *log base-10 turbulent dissipation rate,* ***b)*** *temperature,* ***c)*** *u-velocity. The x-axis corresponds to the dominant M_2 tidal phase, where 0° is refers to the minimum u-velocity near the bed following the flood tide.*

5.7 The Impact of Stratification on the Bottom Boundary Layer

The shelf sea bottom boundary layer is influenced by the oscillatory tides, the Earth's rotation, stratification, and bottom topography (Dewey et al., 1988). The height of a bottom boundary layer formed in a stably stratified oceanic setting may be expressed as a planetary boundary layer with a stratification dependent factor. Weatherly and Martin (1978) derived the scaling law:

$$h_{bl} = 1.3\frac{u_\star}{f(1+\frac{N_0^2}{f^2})^{1/4}} \tag{5.2}$$

where $u_\star$, is the friction velocity, f, is the Coriolis frequency, and N_0, is the buoyancy frequency exterior to the BBL. In the limit of $N_0^2/f^2 >> 200$, the scaling law reduces to $h = 1.3u_\star/(fN_0)^{1/2}$. Figure 5.22 presents the scaling law applied to the MSS tidal cycles in which $u_\star$ was calculated using the dissipation method, $u_\star = (\varepsilon\kappa Z)^{1/3}$, where κ is the von Karmen constant and Z is height above the bed.

A marked variation in the height of the BBL between spring and neap tides was observed at both Station 1 & 2. In addition, Station 2 had BBLs three times greater than that at Station 1 at spring tides. The height of the BBL was observed to evolve in response to the oscillating tidal current with peak height around 90°and 270°. This corresponds to the period when the Reynolds stresses are largest during periods of strong velocity shear at peak current. Figure 5.22 shows sampling on yearday 135 (0514) and 226 (0813) to have similar BBL heights despite the difference in stratification between the two tidal cycles.

5.7.1 Phase Lag

An observation made of the turbulent dissipation rates from the MSS tidal cycles was the asymmetry between the acceleration and deceleration stages of the tide. Associated with it was a phase lag between the maximum current velocities and maximum turbulent dissipation that increased with height above the seabed. This has been reported elsewhere by Simpson et al. (1996) for both well-mixed and a stratified site in the Irish Sea. In these studies, the impact of stratification was observed to increase the phase lag from 1.5 hours in the well-mixed site (90 mab) to four hours in the stratified site at a height of 40 mab,

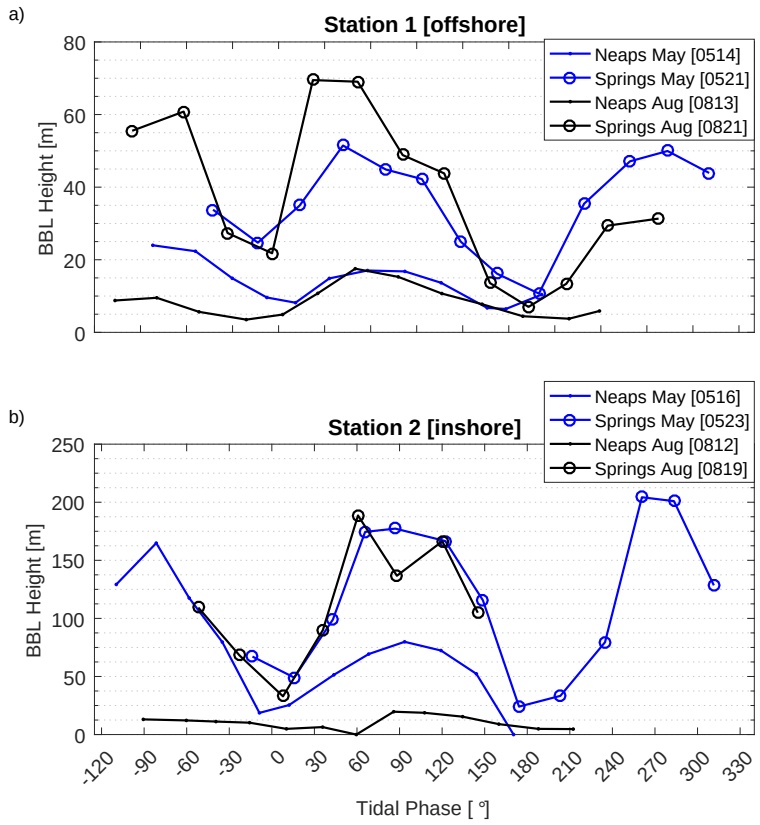

Figure 5.22: *The bottom boundary layer height as calculated from the Weatherly and Martin (1978) formula. Note the different depth range on the y-axis.*

relative to the near-bed. Above the turbulent BBL, the oscillatory M_4 signal of the dissipation rates diminished rapidly to nearly zero, indicating the lack of tidal influence on dissipation rates above the BBL. There have since been further studies which have confirmed these findings (Simpson et al., 2000). Lorke et al. (2002) also identified the phase lag increasing with height above the bed in the BBL of a lake under oscillatory seiching conditions, although suggests that the cause for this phase lag differed from that in a tidal boundary layer. In a model-observation comparison study using the same observational dataset used in Simpson et al. (1996), Burchard et al. (1998) reported both the $\kappa - \varepsilon$ and Mellor-Yamada turbulence closure scheme to reproduce the phase lag in dissipation rates. Another model study conducted by Gayen et al. (2010) using a LES model on a stratified water column forced by an oscillatory current further reported the phase lag in the outer layer of the BBL to be strongly influenced by the stratification. The cause of the phase lag in these tidally-driven oscillatory flows was indicated to be the delay in the velocity shear that delays the turbulence production the higher up the water column you ascend,

with only a small contribution from the effects of upward turbulent diffusion from the near-bed region (Simpson et al., 1996; Gayen et al., 2010). This conclusion was gained initially from a comparison of two model simulations that included and excluded the diffusive term whereby only a small difference was observed in the phase lag. The LES model by Gayen et al. (2010) was able to distinguish each individual term in the turbulence equation from which the phase lag in the production term was observed further supporting this notion. The influence of stratification in preventing the upward upward propagation of TKE production is to limit the turbulence in the mid-water column and focusing it instead to the near-bed region. This impacts the vertical structure of the water column with consequences for the turbulent mixing regime in marginally stratified shelf seas.

In order to calculate the tidally-driven phase lag encountered during the MSS sampling, the dissipation and current data were fitted to a quarter-diurnal (M_4) sinusoidal least-squares fit, following Simpson et al. (1996):

$$\varepsilon = a_0 + a_4 sin(\omega_4 t - \phi_4) \tag{5.3}$$

where, a_0, is the mean dissipation over the tidal cycle, a_4, the quarter-diurnal amplitude, ω_4, the quarter-diurnal frequency, and ϕ_4, the phase lag. The outcome of the fit is shown schematically in Figure 5.23.

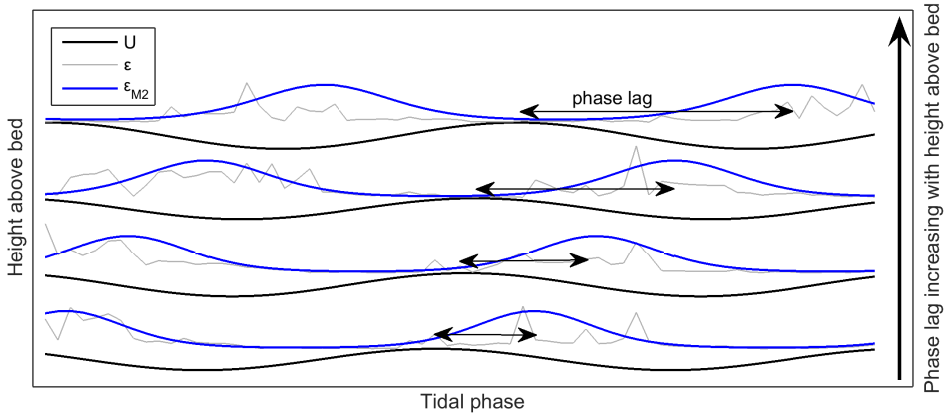

Figure 5.23: *Schematic of the dissipation rate tidal phase lag with respect to the current velocity. The diagram shows the increase in phase lag with height above the bed.*

Figure 5.24 presents the calculated M_4 amplitude dissipation profile, phase lag between it and the M_4 velocity and the measure of fit, R^2, at St1. The dissipation rate M_4 amplitude was high within the BBL and exhibited a

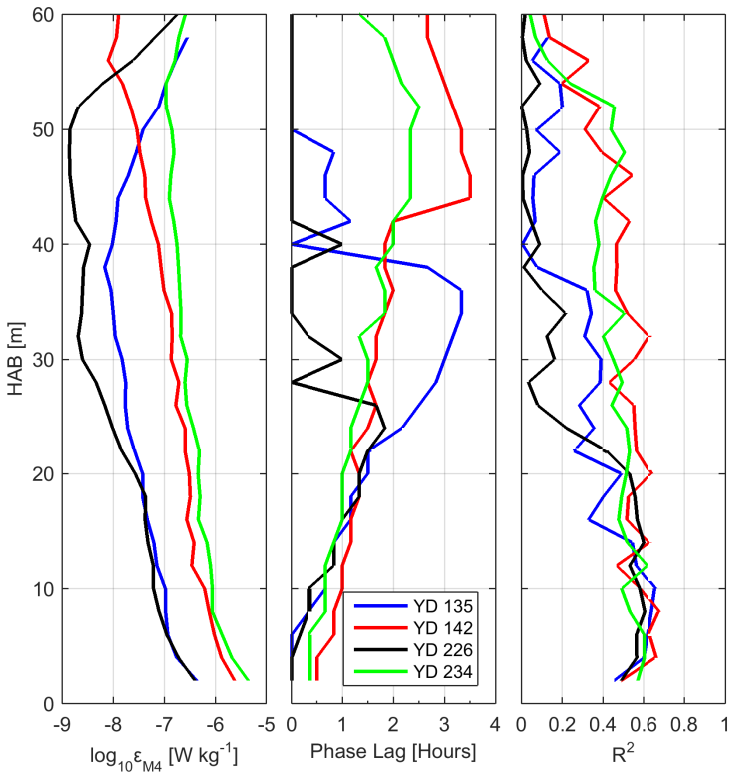

Figure 5.24: *The phase lag in dissipation rates with respect to tidal velocity for Station 1 during all four MSS sampling tidal cycles.* ***a)*** *M_2 dissipation rate fit;* ***b)*** *phase lag;* ***c)*** *R^2 correlation*

decrease from local maximum values at the bed to a minima in the mid-depth before increasing again near the surface. Amplitudes were largest during spring tides on yearday 142 and 234, with maximum near-bed dissipation rates of $10^{-5.5}$ W kg^{-1}. Neap tide dissipation rates within the BBL were maximum at $10^{-6.5}$ W kg^{-1}, an order of magnitude less. A greater range of minimum values were obtained in the mid-depths, with the highest minima at 10^{-7} W kg^{-1} during spring tides, and the lowest of $10^{-8.8}$ W kg^{-1} at neap tides. A distinct reduction in amplitude was present outside of the BBL as may be seen around 20 mab at neap tides on yeardays 135 & 226 and at 50–55 mab at spring tides on yeardays 142 & 234.

The phase lags generally increased with height above the bed for dissipation rates within the turbulent BBL. For all MSS tidal cycles, an increase in lag in the nearbed (20 mab) region was observed, with lags reaching between 1-1.5 hours. Above this, the phase lags was observed to differ between tidal cycles. On yearday 135, under weakly stratified conditions, the phase lag

in the outer layer of the BBL increased considerably, reaching a maximum at 3.25 hours at 36 mab whilst maintaining a correlation of >0.3. During stratified conditions on yearday 226, the height of the BBL was reduced to approximately 30 mab and phase lags were at maximum 1.8 hours at 24 mab, above which the correlation between dissipation rates and tidal velocity decreased significantly.

During spring tides, the phase lags presented a similar trend with increasing phase lags with height above the bed. Since the height of the BBL was considerably higher during spring tides, the maximum phase lags attained was also larger. The maximum phase lag on yearday 142 was 2.5 hours recorded at a height of 52 mab. On yearday 234 , this was 2 hours at 42 man. Above the maxima, the phase lags decreased towards the surface with an associated decrease in correlation indicating alternative sources of turbulence were prevalent.

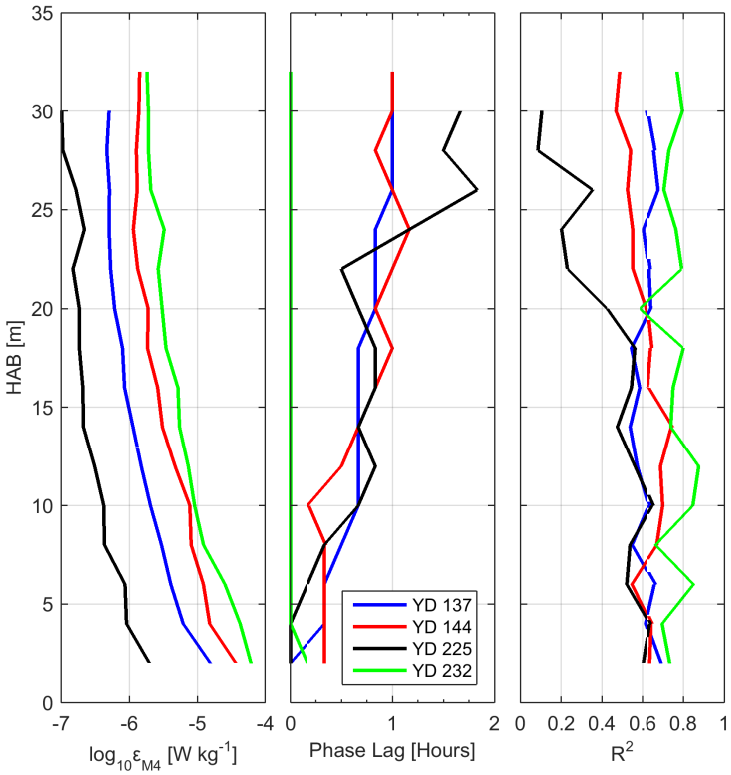

Figure 5.25: *The phase lag in dissipation rates with respect to tidal velocity for Station 2 during all four MSS sampling tidal cycles.* ***a)*** *M_2 dissipation rate fit;* ***b)*** *phase lag;* ***c)*** *R^2 correlation*

Figure 5.25 presents the M_4 amplitude, phase lag and correlation factor for

St2. A similar trend in M_4 amplitudes was observed to that at St1 in which the spring tide amplitudes were greatest. However, in comparison to St1 there was no discernible increase in the near-surface region given the lack of an interior minima and the surface increase due to surface forcing. In these profiles, the BBL extends for the length of the water column. Maximum dissipation rates within the near-bed region attained $10^{-4.4}$ W kg^{-1} during spring tides on yearday 232, reducing to a near-surface maxima of $10^{-5.5}$ W kg^{-1}. The profile exhibiting the minimum dissipation rates was on yearday 225 during which the lowest tidal velocities were recorded at neap tides. Maximum dissipation rates in the near-bed were $10^{-5.6}$ W kg^{-1} which decreased to 10^{-7} W kg^{-1} close to the surface.

A phase lag was observed at three of the four tidal cycles sampled that extended to the top of the profile. The calculated phase lag was altogether less than that observed for equivalent heights above the bed at St1. For example, the phase lag calculated 20 mab for St1 was between 1–1.5 hours, while for St2 it was 0.65–0.8 hours. For the majority of the profiles, the R^2 fit was >0.4 with a maximum of 0.7, indicating a good fit to the M_4 tidal cycle throughout the water column. This was confirmed by what is seen in the dissipation rate profiles for each station presented earlier in this Chapter — given the shallower water and stronger tidal currents, BBL height was more often extended to the surface. One particular reduction in R^2 values was seen in the upper water column, between 20–30 mab, on yearday 225. On this occasion weak stratification was observed at this height in the temperature data.The reduced R^2 coincident with the stratification supports the notion that stratification impacts the tidally driven BBL by suppressing its growth. Zero phase lag was recorded for yearday 232 at St2. This was due to the saturation of dissipation rates within the water column as was seen in Figure 5.21a. Consequently, the production of turbulence was directly related to the velocity magnitude with no vertical lag observed.

5.7.2 Dissipation Scaling outside the Frictional Boundary Layers

The MSS tidal cycles show the presence of well-defined frictional turbulent BBLs present at both the inshore and offshore stations as well as indications of other sources of dissipation in both the interior and surface layers. Turbulent dissipation in seasonally stratified shelf seas is much greater than in the

open-ocean due to the frictional influence of the seabed, stronger tidal currents, a larger percentage of the water column in the surface and bottom boundary layers. In fact, the open ocean is thought to dissipate only 0.9 TW of the barotropic tidal energy while shelf seas dissipate 2.6 TW of this energy (Munk and Wunsch, 1998). Egbert and Ray (2000) estimated that the Northwest European shelf accounts for more than 100 GW of the dissipation alone. There may also be the conversion from barotropic to baroclinic energy in shelf seas, with energy lost from the barotropic tide radiating away as internal waves in stratified waters predominantly along the seasonal thermocline. MacKinnon and Gregg (2003a) estimated that approximately 15% of observed dissipation on the New England shelf was related to the passage of internal solitary waves. This percentage was even higher in the thermocline with 50% of the dissipation attributed to internal waves. As such, some of the most successful models of open-ocean turbulence, away from the boundaries, draw on the relationship of internal wave shear and stratification and allow for the parameterization that relate turbulence to internal wave instabilities (Gregg, 1989; MacKinnon and Gregg, 2003a). One of the benefits of such parameterizations is in quantifying turbulent mixing in terms of more easily obtainable terms, such as the N^2 and S^2, which have been shown in the previous Sections to be obtained by profiles of density and current shear.

In this section, we progress on to the region above the well-defined BBL, where turbulent mixing is likely to be due to internal wave breaking driven by vertical shear or convective instabilities (Polzin et al., 1995). This was motivated by the NLIW packets observed in the thermistor data during stratified conditions and reported in Section 4.4.4. Here, the turbulent dissipation rates are parametrised in terms of physical properties, namely, stratification levels and vertical shear, to allow coherent patterns of turbulence to be identified based upon the water column structure. Furthermore, such parametrisations allow turbulent dissipation to be estimated from more easily measured quantities or explicitly resolved by numerical simulations (Henyey et al., 1986). The Gregg-Henyey parameterization (Equation 5.5), is one such parametrisation that is based on a variety of open ocean, mid-latitude, turbulent dissipation observations. This successful parameterization relates an increasing turbulent dissipation rate with increasing shear for all stratification values (Figure 5.26a). The basis of this dissipation scaling stems from open ocean turbulence where the energy cascades from the energy-containing production scales through the internal wave spectrum at a rate which may be adequately de-

scribed by the Garret-Munk internal wave spectrum (Garret and Munk, 1972, 1975). Gregg (1989) and Polzin et al. (1995) successfully compared it to ocean microstructure measurements at a variety of mid-latitude locations.

$$\varepsilon_{GH} = 1.8 \times 10^{-6} \left[f cosh^{-1} \left(\frac{N_0}{f} \right) \right] \left(\frac{S_{10}^4}{S_{GM}^4} \right) \left(\frac{N^2}{N_0^2} \right) \tag{5.4}$$

where, f is the Coriolis parameter, $N_0 = 3$ cph, S_{10}^4 is the measured 10 m shear, and S_{GM}^4;

$$S_{GM}^4 = 1.66 \times 10^{-10} \left(\frac{N^2}{N_0^2} \right)^2 \tag{5.5}$$

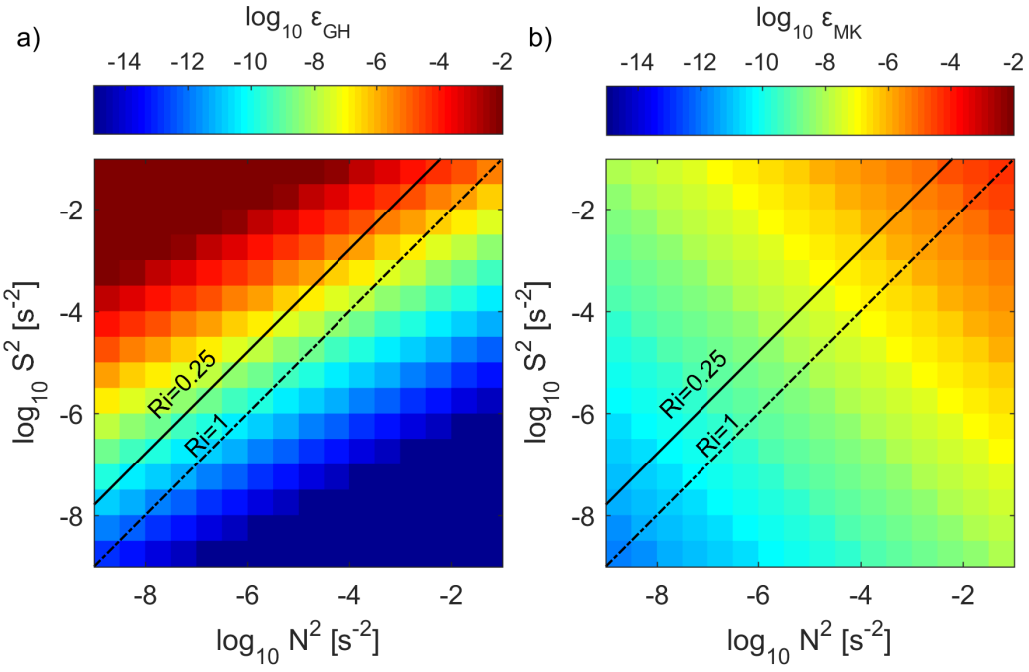

Figure 5.26: *The parameterizations of turbulent dissipation rates in terms of binned shear (S^2) and stratification (N^2). **a)** the parameterization of Gregg-Henyey for open ocean turbulent dissipation. **b)** the MacKinnon-Gregg parameterization based on continental shelf sea observations for interior mixing.*

More recently, MacKinnon and Gregg (2003a) proposed a new scaling to estimate turbulent dissipation in coastal environments from observations collected on the New England shelf (Figure 5.26b). Although based upon the internal wave energy cascade theory of the Gregg-Henyey parameterization, their model was modified to better fit the observed properties of internal waves on the continental shelf (MacKinnon and Gregg, 2003a). However, justification

for such a modification to the existing parameterization was based upon the intuitive appeal and empirical fit to observations. The main concern with the Gregg-Henyey open ocean scaling was a too strong dependence on shear and less so on stratification. Instead, the new parameterization of MacKinnon and Gregg (2003a) relates the increasing turbulent dissipation with increasing low frequency shear and increasing stratification (Equation 5.6).

$$\varepsilon_{MG} = \varepsilon_0 \left(\frac{N}{N_0}\right) \left(\frac{S_{lf}}{S_0}\right) \tag{5.6}$$

where $N_0 = S_0 = 3$ cph, S_{lf} is the low-frequency, low-mode resolved shear and $\varepsilon_0 = 1.1 \times 10^{-9}$.

Following the work of MacKinnon and Gregg (2003b), we evaluate the dependence of turbulent dissipation rates obtained from outside of the turbulent boundary layer on the physical characteristics of the vertical water column in terms of shear and stratification. A successful parameterization would point towards internal wave shear as being a candidate mechanism for internal mixing in the marginally stratified shelf sea front studied here.

Dissipation rates were plotted onto a grid of evenly spaced bins of N^2 from MSS profiles, and S^2, from the VM-ADCP, both with equal bin sizes of $\log_{10}0.5$. In order to attain a common vertical resolution, the datasets were averaged onto a 4 m vertical grid and the frictional BBL excluded by means of a tidal cycle average depth cutoff selected at 20 mab for neap tides, below which measurements were excluded from the scaling. During spring tides, the turbulent BBL routinely reached the surface excluding any interior layers and accordingly only the neap tidal cycles are presented.

Yearday 135

Interior turbulence parameterization for Station 1 on yearday 135 is presented in Figure 5.27 on the left hand side. The turbulent dissipation measurements range between 10^{-9}–10^{-6} W kg^{-1} and was contained within $-8.5 < N^2 < -4$ and $-6.5 < S^2 < -3$. The middle plots in Figure 5.27 present the Gregg-Henyey (top) and MacKinnon-Gregg (bottom) scaling for the equivalent N^2 and S^2 bins in the observations. When the measured turbulent dissipations were compared to the two parameterizations, no clear dependence on a particular scaling was observed over the other. Instead, observed dissipation rates above the black diagonal line in unstable Richardson number space ($\mathrm{Ri}_g < 0.25$) included the

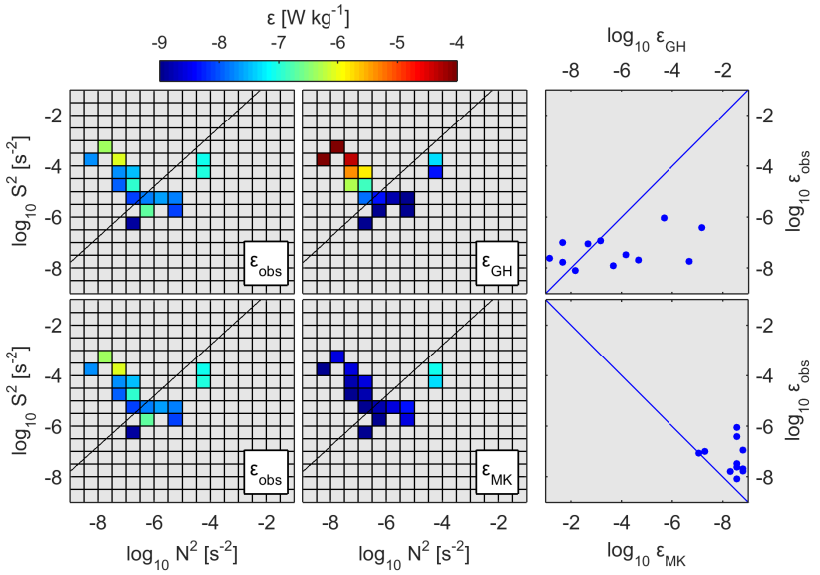

Figure 5.27: a) *Turbulent dissipation data averaged in bins of shear and stratification for yearday 135 at the offshore Station 1. Also included is the Gregg-Henyey model for dissipation data averaged in bins of shear and stratification (ε_{GH}) and the MacKinnon-Gregg scaling below (ε_{MK}). Black diagonal lines plotted on the scaling denote Ri_g = 0.25, with values above the line in unstable conditions. Modelled scaling have only the bins with observation data included. Observed dissipation plotted against modelled dissipation with a straight line 1:1 fit included (blue line).*

highest dissipation measurements ($\varepsilon = 10^{-6}$ W kg^{-1}) in a similar manner to the Gregg-Henyey scaling. However, dissipation rates in the Gregg-Henyey scaling were approximately 10^{-4} W kg^{-1}, and two-orders of magnitude greater than observed.

Under stable conditions (Ri$_g > 0.25$), the observed dissipation measurements tended to be smaller with values $< 10^{-7}$ W kg^{-1}. Under these stable conditions, the dissipation tended to follow the MacKinnon-Gregg scaling, with higher dissipation rates at high N^2 and of a similar magnitude to those calculated with the MacKinnon-Gregg parameterization (10^{-7} W kg^{-1}, N$^2 = 10^{-4.5}$ s^{-2}). A distinct high dissipation bin ($10^{-6.5}$ W kg^{-1}) was observed at low N^2 and S^2 that was uncharacteristic of both parameterizations. Plotting the dissipation measurements for Gregg-Henyey versus that observed and, similarly for MacKinnon-Gregg, showed a poor fit between the dissipation measurements and those parameterized (Figure 5.27 RHS). The correlation coefficient between the Gregg-Henyey scaling and measured dissipation rates was $+0.48$ and R$^2 = 0.19$. The MacKinnon-Gregg scaling did not fair any better with a correlation coefficient of $+0.42$ and R$^2 = 0.17$.

Plotting both N^2 and S^2 versus the observed dissipation rates in Figure 5.28 show dissipation rates tend to align with the MacKinnon-Gregg scaling for both N^2 and S^2 more so than the Gregg-Henyey scaling. The MacKinnon-Gregg scaling maintains a similar dissipation rate gradient across N^{-2} and S^{-2} bin values, although approximately two orders of magnitude lower. This discrepancy may be accounted for in the ε_0. By increasing $\varepsilon_0 = 2\times10^{-8}$ provided a better fit for the observed dissipation measurements to the Mackinnon-Gregg scaling for both N^2 and S^2.

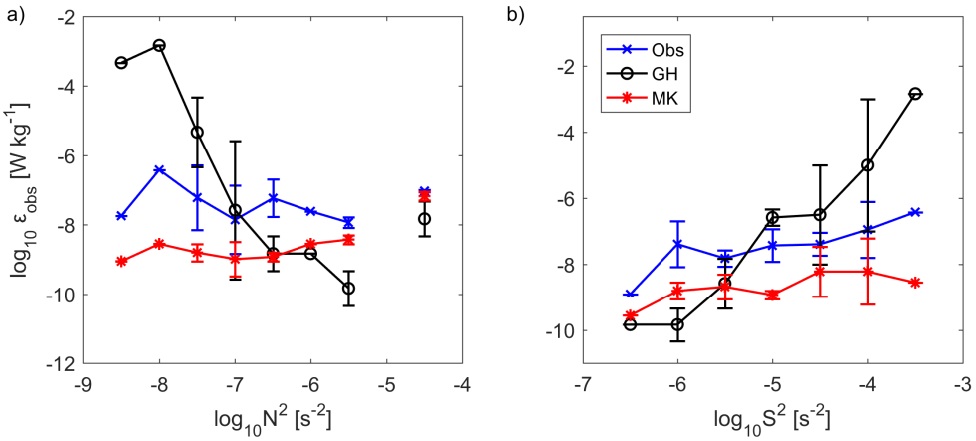

Figure 5.28: *Bin-sorted, average dissipation rates versus* ***a)*** N^2 *and,* ***b)*** S^2 *for observations on yearday 135 (blue), GH (black), and MK (red) scaling. The error bars presents the min and max dissipation rates for each bin (bin size =* log_{10} *0.5* N^2*,* S^2*).*

Yearday 226

Interior dissipation rates from Station 1 at neap tides in August were similarly scaled versus N^2 and S^2 and showed no particular correlation with either of the parameterizations (Figure 5.29). The turbulent dissipation measurements ranged between 10^{-9}–$10^{-6.7}$ W kg^{-1} and were contained within $-6.5 < N^2 < -2.5$ and $-6.5 < S^2 < -2.5$. In a similar arrangement to the scaling on yearday 135, high dissipation rates (10^{-7} W kg^{-1}) were observed at high shear values, especially under unstable Richardson numbers of $Ri_g < 0.25$. This pattern was suited to the Gregg-Henyey scaling although, in a similar manner to the previous scaling on yearday 135, the range of dissipation rates were much smaller than predicted by this parameterization. Correlation of the two parameterizations versus observations were again similar to that previously. The Gregg-Henyey scaling correlation coefficient versus observations was +0.48

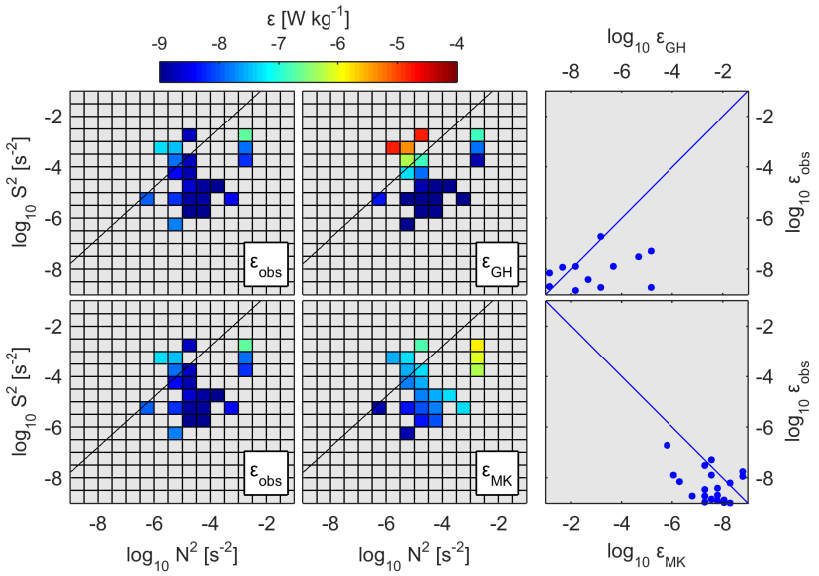

Figure 5.29: a) *Turbulent dissipation data averaged in bins of shear and stratification for yearday 226 at the offshore Station 1. Also included is the Gregg-Henyey model for dissipation data averaged in bins of shear and stratification (ε_{GH}) and the MacKinnon-Gregg scaling below (ε_{MK}). Black diagonal lines plotted on the scaling denote Ri_g = 0.25, with values above the line in unstable conditions. Modelled scaling have only the bins with observation data included. Observed dissipation plotted against modelled dissipation with a straight line 1:1 fit included.*

and $R^2 = 0.2$. A lower correlation between the MacKinnon-Gregg scaling and observations were found at +0.33 and $R^2 = 0.11$.

Plotting the observed, binned, interior dissipation rates versus N^2 and S^2, individually, showed that the observations were better represented by the MacKinnon-Gregg scaling than the open ocean alternative. Observed dissipation rates showed a positive trend towards both increased N^2 and S^2, contrary to the Gregg-Henyey scaling that scales to lower dissipation rates with increasing N^2.

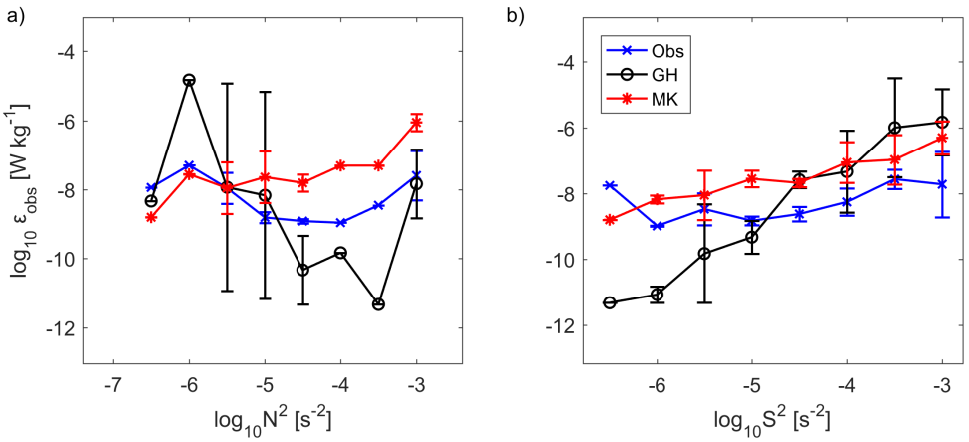

Figure 5.30: *Bin-sorted, average dissipation rates versus* ***a)*** N^2 *and,* ***b)*** S^2 *for observations on yearday 226 (blue), GH (black), and MK (red) scaling. The error bars presents the min and max dissipation rates for each bin (bin size* $= log_{10}$ *0.5* N^2*,* S^2*)*

5.8 Summary

This Chapter presented a detailed investigation into the vertical structure of turbulence over the tidal cycle at two stations in different mixing regimes. Observations were made using the MSS free-fall profiler allowing high-resolution measurements of finescale velocity shear from which an estimation of the dissipation rate of turbulent kinetic energy was made from the near-surface to the seabed. These profiles were conducted continuously for approximately 20–30 minutes before the instrument would be recovered to allow the vessel to reposition after drifting, thereby leading to a quasi-continuous sampling over the tidal cycle. The MSS sampling was conducted in both the spring and summer seasons and also at neap and spring tides. It was envisaged that such a sampling campaign would cover the weakly stratified spring season and the more strongly stratified summer season as well as comparing the weaker current conditions during neap tides to the stronger currents at spring tides.

Given the predominance of tidal mixing in shelf seas, the influence of the neap-spring cycle as well as the impact of stratification in summer on the BBL was investigated firstly. In addition, the influence of strong winds and relatively large waves were identified in the turbulence and temperature structure on yearday 135. During strongly stratified conditions on yearday 226, elevated dissipation rates within the interior and the vertical displacement of the

thermocline was identified, suggesting a source of internal mixing was present. The asymmetric growth of the BBL with the lag in turbulence production which increased with height above the bed was a predominant feature in all tidal cycles and was investigated here. Finally, two parameterizations for interior turbulence outside of boundary layers were tested against the data to determine the relative influence of internal mixing in stratified conditions. The key findings of this Chapter are summarised as follows:

1. **Bottom Boundary Layer —** The growth of the turbulent BBL was observed to predominantly occur at a quarter-diurnal (M_4) periodicity during all tidal cycles. This was visually demonstrated in the near-bed dissipation rates and also quantified in the M_4 fit of dissipation over the tidal cycle. The correlations (R^2) within the BBL were typically between 0.4–0.6, indicating a good fit between the observed dissipation rates and the M_4 dissipation fit. The largest amplitude dissipation rates were found within the BBL closest to the seabed with values between log-10 -6 to -4 W kg^{-1}. Dissipation rates were typically 1–3 orders of magnitude smaller at the interior minima, typically above the BBL and below the surface mixed layer. The height of the BBL was governed by the current magnitude with the spring tide BBL consistently larger than that observed at neap tides. The BBL was also more turbulent throughout the water column at the inshore station (St2).

A stratified water column directly above the BBL present on yearday 226 inhibited the growth of the BBL. This was reflected in the BBL scaling derived by Weatherly and Martin (1978) in which the tidal BBL is expressed as a planetary boundary layer with a stratification dependant factor. This scaling predicted the BBL on yearday 226 to reach a maximum height of 18 mab whereas in the observations it reached 28 mab. However, the scaling predicted it to be the lowest BBL at St1. The maximum height of the turbulent BBL was selected as the sharpest gradient in the dissipation profiles. Figure 5.18 showed that on yearday 226, the height of the BBL, as shown by the red circles, was inhibited by the region of high N^2. The growth of the BBL inhibited by the increase in stratification was reflected in the reduction of the vertical eddy diffusivity on yearday 135.

2. **Interior Mixing —** Evidence of mixing along the thermocline and outside of the frictional boundary layers was most evident on yearday 226 in the strongly stratified conditions at neap tides in summer. A mid-column layer of enhanced dissipation rates external to the BBL was observed which during the

first stage of the tidal cycle. This region was associated with increased N^2 and also S^2, which caused a local reduction in gradient Richardson numbers to <1, indicating an unstable water column capable of maintained turbulent mixing. Also observed was six significant vertical displacements of the thermocline which occurred during slack tide in a similar manner to the NLIW observed in the thermistor data in the previous Chapter. The maximum displacement during the first set was 4.5 m over 16 minutes while the second was 7 m over 8 minutes and were associated with increased vertical shear observed in the S^2 although no discernible increase in dissipation rates were observed below the thermocline. There was, however, a suggestion of increased dissipation rates in the surface layer associated with these vertical displacements.

Turbulence scaling appropriate for interior mixing away from the frictional boundary layers were presented to establish internal wave shear as an candidate mechanism for mixing at the study site. The turbulent dissipation data were fit to two parameterizations, the Gregg-Henyey and MacKinnon-Gregg scaling. Overall, a better fit to the MacKinnon-Gregg scaling was observed for the two tidal cycles used in this analysis.

3. **Surface Mixing —** The influence of strong surface forcing was observed on yearday 135 as sampling was conducted during a significant wind event with wind speed above 10 m s^{-1} on occasion. A significant deepening of the surface mixed layer was observed. Within the surface mixed layer, there were high dissipation rates of similar magnitude to that in the BBL ($10^{-}6$ W kg^{-1}). The surface layer was $\triangle 0.6$°C warmer than the BBL.

CHAPTER 6

INVESTIGATING THE VERTICAL MIXING MECHANISMS IN A MARGINALLY STRATIFIED SHELF SEA SETTING USING A 1-D NUMERICAL TURBULENCE MODEL — GOTM

In this Chapter, model simulations using the General Ocean Turbulence Model (GOTM) are presented for the three locations at the study site; the thermistor mooring, and the offshore (St1) and inshore (St2) MSS sampling sites. Both spring and summer deployments were modelled using initial conditions from observations, while surface forcing from both heat fluxes and wind stress were obtained from the Met Office Unified Model output. The aim of this chapter was to test the accuracy of a 1-D turbulence model in simulating the vertical mixing and restratification processes identified in the observations and to consider independently the otherwise integrated effects of the various mixing processes. This is particularly relevant for marginally stratified locations with the purpose of addressing discrepancies in current shelf sea models for future modelling efforts.

As was identified in Chapter 4, intense storm conditions on yearday 228 generated significant mixing and horizontal advection that caused sudden changes to the water column structure from stratified to well-mixed conditions. In addition, NLIW were observed in summer during stratified conditions reducing the stability of the water column and potentially generating turbulent mixing. These advective and mixing processes are currently not resolved in GOTM and have been identified as an source of uncertainty due to their non-local and intermittent character (Burchard et al., 2008). In these simulations, the 1-D model does not account for lateral advection which, in tidally dominant regions, may be a source of large uncertainty. In itself, this could be construed as a major disadvantage of 1-D models, however, in this case, it can benefit the interpretation of the observations and distinguish between local and non-local processes.

6.1 Model Experiment Objectives

The particular objectives of the modelling experiments were to:

1. Case 1 — Determine to what extent a 1-D model can represent the conditions in a marginally stratified shelf sea location.

1.1. Case 1a: Simulation of thermistor location in Spring (depth: 55 m).

1.2. Case 1b: Simulation of thermistor location in Summer (depth: 55 m).

2. Determine to what extent a 1-D model can reproduce the vertical mixing regime at Stations 1 & 2 in Spring and Summer.

2.1. Case 2a: Simulation of Station 1 in Spring (depth: 65 m).

2.2. Case 2b: Simulation of Station 2 in Spring (depth: 35 m).

2.3. Case 2c: Simulation of Station 1 in Summer (depth: 65 m).

2.4. Case 2d: Simulation of Station 2 in Summer (depth: 35 m).

3. Case 3 — Investigate the parameterization of internal waves in GOTM.

6.2 Case 1 — Simulations of Thermistor and MSS Stations

6.2.1 Comparing Simulations with Thermistor Observations in Spring — Case 1a

Model simulations of the weakly stratified conditions in spring were run over the same 12-day period as the thermistor deployments. The model time step was 1 second with the simulation results output every ten minutes. In this simulation, the vertical temperature structure was initialized from thermistor data, averaged over a 24 hour period in order to remove the variability associated with tidal advection (yearday 134.75–135.75). Meteorological forcing and the heat fluxes were assigned as described in Section 3.3.2. The water depth was set to 55 m and the external pressure gradients were calculated from the bed-moored ADCP located nearby.

Modelled Temperature in Spring

The observed and simulated temperature structure over the thermistor deployment is presented in Figure 6.1. Overall, the observations were well represented by the model with the observed increase in temperature captured by the model though with less temporal variability as is evident by the fewer temperature contours. The predominantly vertical orientation of the contours show both the observations and model simulation maintained a well-mixed water column below the near-surface layer.

A key benefit of the numerical model over the observations was its ability to capture the evolution of the surface layer; the uppermost temperature sensor on the thermistor mooring was located at a depth of $<$10 m due to the requirement of a subsurface float to maintain buoyancy. As such, the

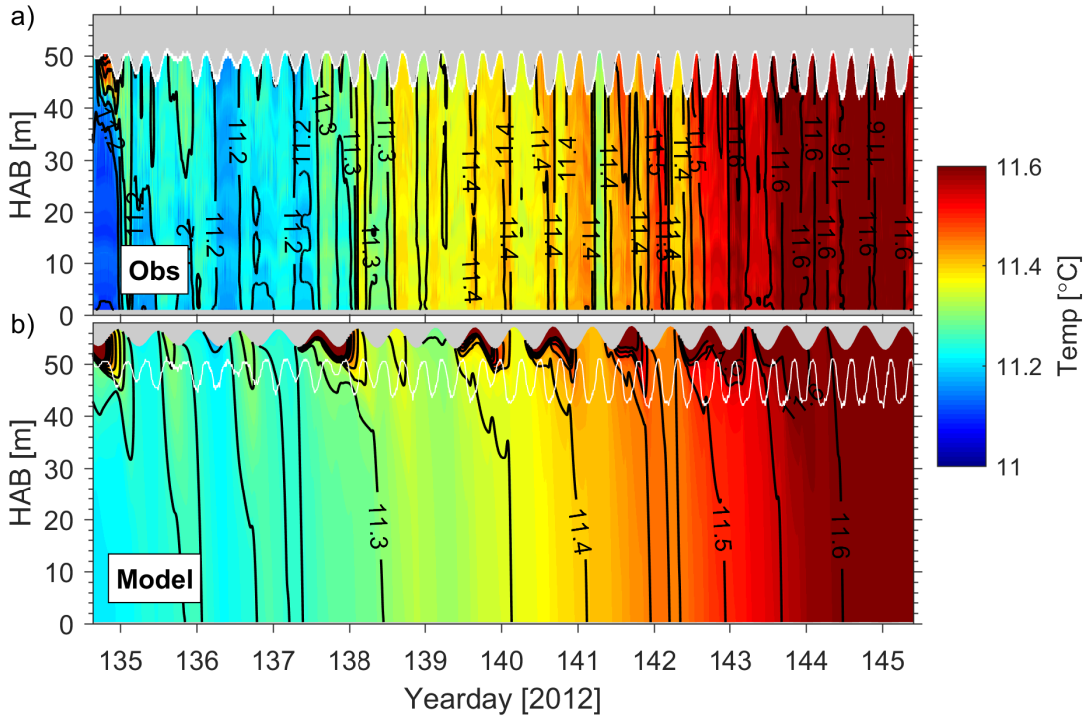

Figure 6.1: *The observed* ***(a)*** *and modelled* ***(b)*** *temperature field for the thermistor mooring location in May (Case 1a). Temperature contours were set at 0.05°C and labelled every 0.1°C. The surface region not included in the thermistor observations is denoted above the white line. The white line oscillates at an* M_4 *periodicity in response to the thermistor knock-down due to the tidal current.*

observations provide no information in the surface layer where the warming effects of insolation were most significant. The model simulation of the near-surface region did produce periodic stratification in the top 4 m of the water column during periods of strong positive day time heat flux (e.g. yearday 137.4). The stratified warm layer was mixed downwards at night, indicating convective mixing due to the negative night time heat flux (surface cooling). The simulated temperature increases throughout the water column were associated with the daytime positive heat flux and therefore maintained a strong diurnal periodicity. During periods of strong wind stress on yearday 135–136 & 138–139, the near-surface stratification was not formed although an increase in water column temperature was still observed in the model indicating the increased surface mixing due to the increased surface wind stress generated significant surface mixing of heat.

The good agreement between observations and model simulation may be seen in the depth-mean temperature presented in Figure 6.2 (excluding the near-

surface region not included in the thermistor data). The initial temperature in the observations was 11.14°C and increased over the course of the deployment to a maximum of 11.66°C towards the end of the deployment. In comparison, the depth-mean modelled temperature was initially 11.19°C and increased to 11.65°C. The average rate of heat increase over the deployment period was 0.045°C day^{-1} in the observations and 0.036°C day^{-1} in the model. As was described in Chapter 4, the largest variability in the thermistor data was associated with the horizontal tidal advection at semi-diurnal periodicity, a process not included in the model due to its 1-D setup.

The root-mean-square error (RMSE), or standard deviation of the residuals, provides an indication of the mean variability associated with residuals from the long-term linear temperature increase. The RMSE bounds were ±0.04°C and may be considered as encompassing the natural variability associated with this advection. During periods of small semi-diurnal variability the model matched the observations to within the RMSE bounds as was seen between yearday 135–138. However, as the semi-diurnal variability increased with a sudden warming of 0.1°C on yearday 138, the model deviated outside the RMSE bounds. The similarity between the modelled and observed long-term increase in temperature meant that the deviation was not large and on many instances decreases in observed temperature meant the model intersected the observed timeseries. Towards the end of the deployment, the observed semi-diurnal variability had decreased and the model recovered to within the RMSE bounds.

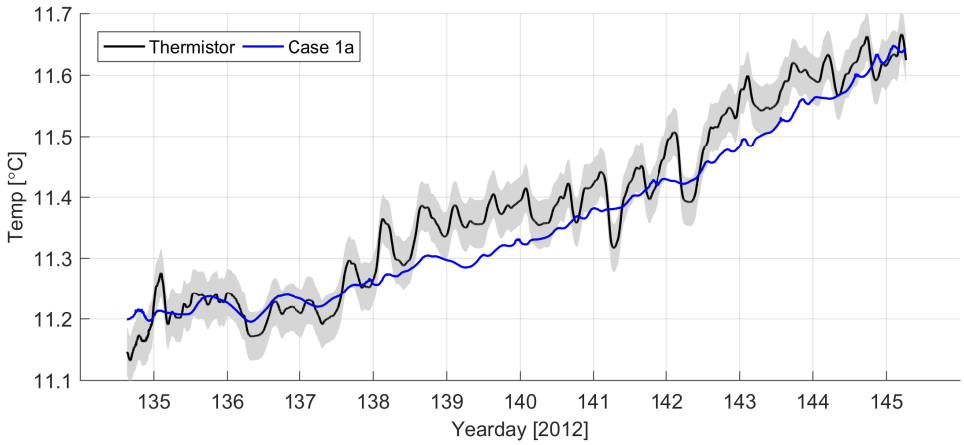

Figure 6.2: *The depth-mean temperature for both thermistor and model simulation timeseries (Case 1a). The thermistor data includes a shaded RMSE denoting the mean variability about the long-term linear increase in temperature.*

Diurnal Convective Mixing and Restratification

The close agreement between the observed and simulated temperature depth-mean temperature timeseries in Figure 6.2 suggests that much of the heating was from heat input at the surface rather than from an advective source. Figure 6.3 presents an example period of yearday 137–142 of the near-surface layer which shows the impact of convective mixing on the temperature and turbulent dissipation.

The diurnal heat cycle was present in the model simulations with daytime warming evident in the negative buoyancy flux followed by a positive buoyancy flux at night (Figure 6.3b). The near-surface stratification was observed to follow this diurnal cycle with the rise in near-surface temperature related to the buoyancy flux magnitude. On yearday 138, the conditions were windy as shown by the enhanced surface wind stress (0.25 N m^{-2}), which acted to reduce the buoyancy flux (Figure 6.3). Here, the near-surface stratification did not form due to the combination of a weaker buoyancy flux and stronger surface mixing, evident in the near-surface turbulent dissipation rates (Figure 6.3d). During periods of stratification, the convective mixing enhanced dissipation rates in the near surface which was linked to the deepening of the temperature contours. In addition to the surface forcing, the influence of the tidally generated enhanced turbulent mixing may be seen in Figure 6.3d to impact on the downward trend of the temperature contours, e.g., at yearday 138.0 & 141.9.

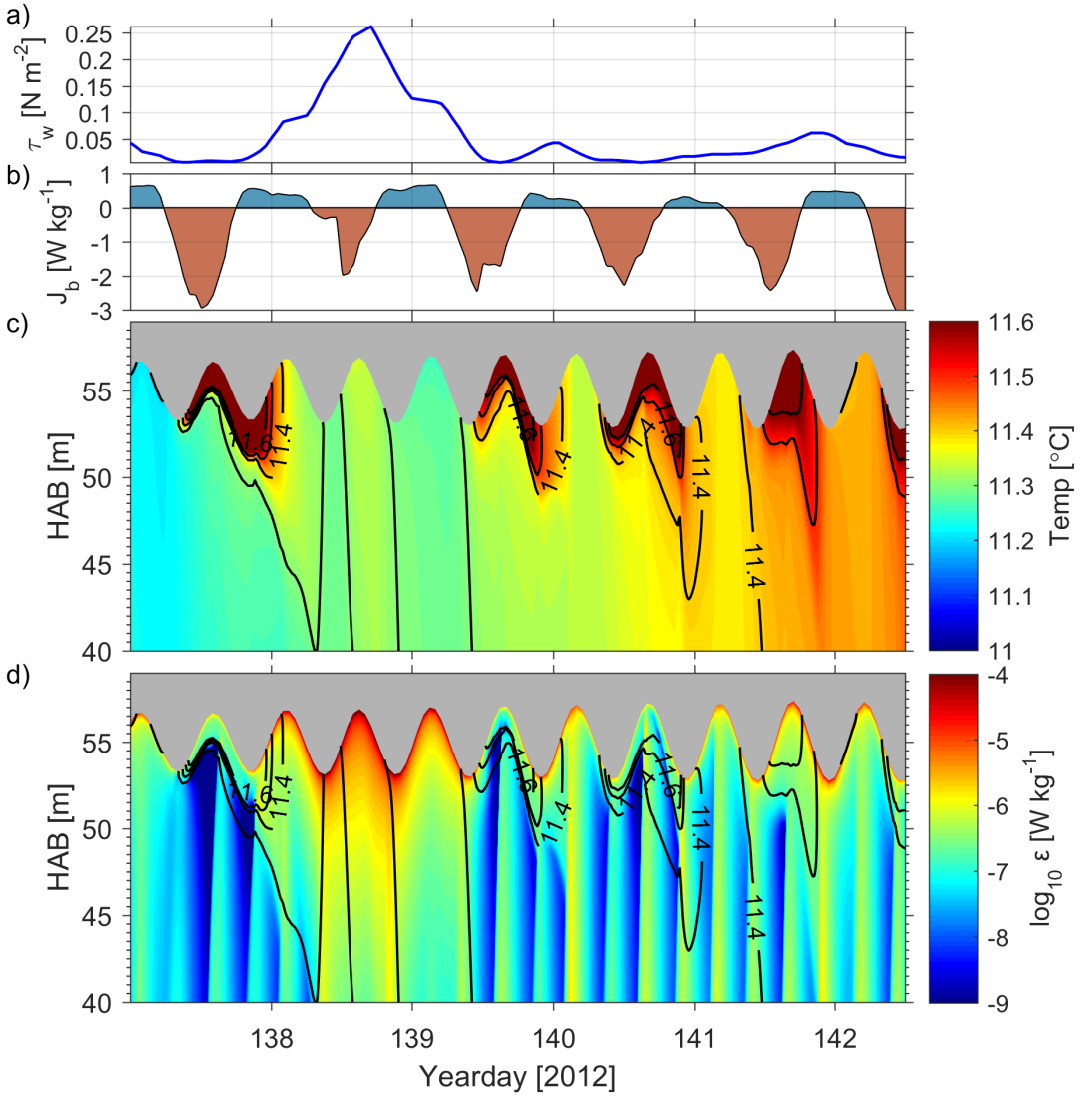

Figure 6.3: *A subset of the modelled near-surface region in simulation Case 1a showing the impact of convective mixing (yearday 137–142).* ***a)*** *surface wind stress;* ***b)*** *buoyancy flux ($\times 10^{-7}$);* ***c)*** *temperature field* ***d)*** *turbulent dissipation rates. The modelled temperature near-surface region shows the near-surface warming during periods of negative buoyancy flux as a result of insolation. After sunset it is mixed down with the positive buoyancy flux due to surface cooling. During periods of strong wind stress, the near-surface stratification does not develop due to high levels of turbulent mixing in the near-surface region.*

Modelled Turbulent Dissipation Structure

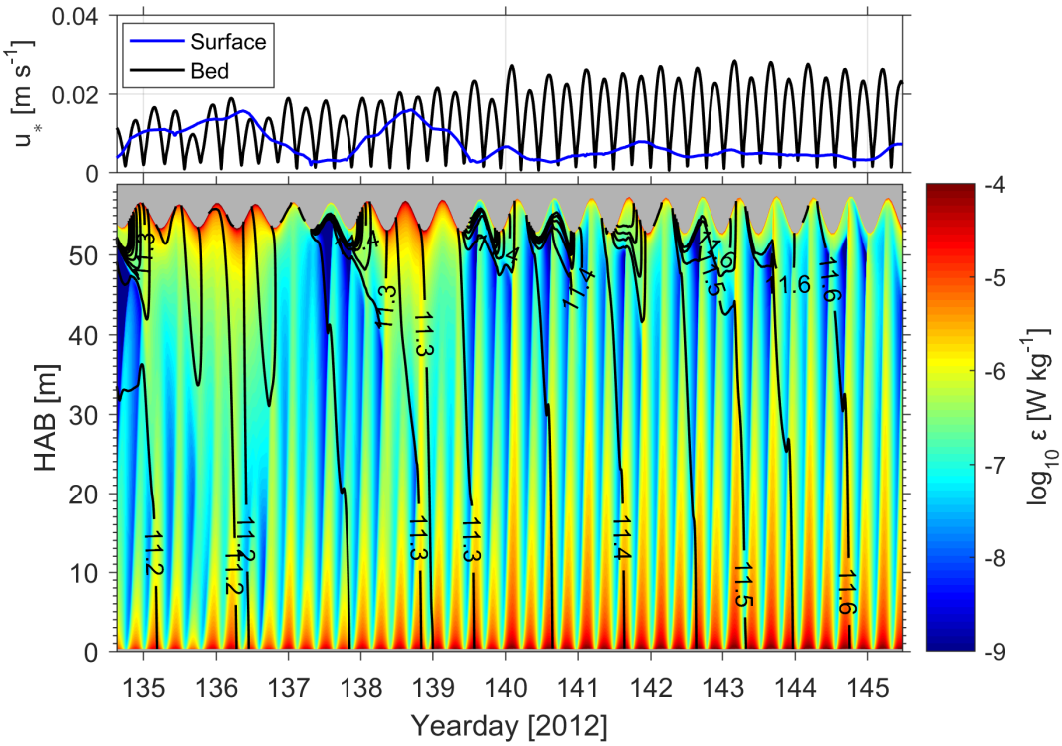

Figure 6.4: *Case 1a: the modelled turbulent dissipation rates with temperature contours overlaid at 0.05°C intervals and labelled every 0.1°C. The friction velocity, from which the boundary layer turbulent Reynolds stresses are derived, are presented above the main figure. The friction velocity, from which the boundary layer turbulent Reynolds stresses are derived, are presented above the main figure.*

Figure 6.4 presents the full-depth, simulated, turbulent dissipation rates and boundary friction velocities from which the turbulent shear stresses are derived under the assumption of an unstratified logarithmic boundary layer, in which turbulent shear production is equal to the turbulent dissipation ($p = \varepsilon$). The tidally driven quarter-diurnal bed friction was the predominant source of turbulent dissipation in the model. However, periods of elevated surface stress generated significant turbulent dissipation in the upper half of the water column where the seabed generated turbulent dissipation was weakest. Figure 6.5 presents profiles of turbulent dissipation from three time slices to highlight the influence of convective mixing and wind stress on yearday 138.05 and 138.57. Turbulent dissipation reached $5{\times}10^{-5}$ W kg^{-1} in the tidally driven BBL while the same magnitude of turbulent dissipation was simulated in the near-surface region during periods of strong surface wind stress and convective mixing. In these instances, the elevated levels of turbulent dissipation were

observed to be greater than that of tidal mixing alone. Turbulent dissipation during convection mixing were 10^{-7} W kg^{-1} in the top 10 m before decreasing to a local minimum. In comparison, the wind mixing increased mixing in the near-surface region and attained similar levels as those in the BBL.

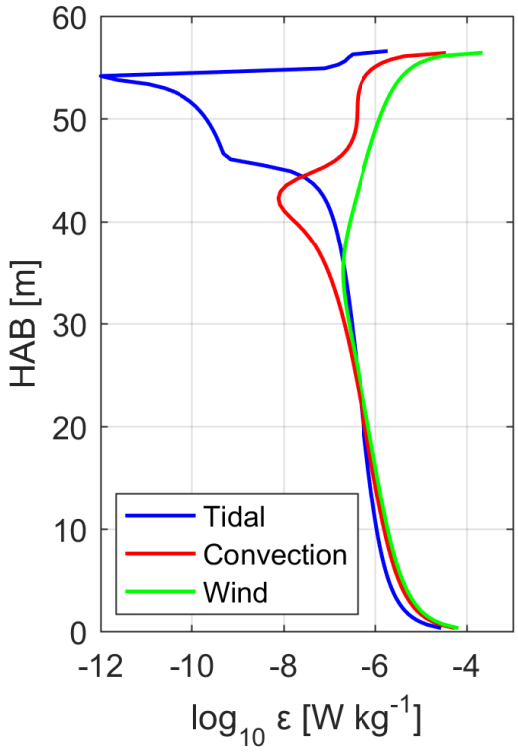

Figure 6.5: *Example profiles of turbulent dissipation during periods of tidal mixing (yearday 137.57); convective mixing (yearday 138.05); and strong wind mixing (yearday 138.57). Enhanced dissipation rates during periods of wind and convective mixing were evident at levels equivalent to those in the tidally driven BBL ($\geq 10^{-7}$ W kg^{-1}).*

6.2.2 Comparing Simulations with Thermistor Observations in Summer — Case 1b

Stratified Conditions

The simulation for the August thermistor deployment is presented in Figure 6.6. In this instance, the most significant noticeable difference between the modelled temperature and observations developed following yearday 228 with the modelled temperatures not increasing in line with observations, although the model did simulate the same transition to a well-mixed water column. Both the model and observations contain a stratified water column at the

beginning of the timeseries between yearday 223–229. Much of the stratified layer in the model resided above the thermistor mooring though with the base of the thermocline just below (indicated by the white line). The observations suggest that a similar warm layer resided above the top-most thermistor, as was evident by slight warming in the upper layer of the thermistor. The thermistor, however, contained periodic deepening of the isotherms by up to 10 m during the stratified period. On one occasion, the isotherm deepened by 40 m on yearday 227. In comparison, the model did not contain any variability in the thermocline except for that associated with the semi-diurnal variation with sea surface height.

Following the storm on yearday 228, both the model and observations transitioned to a well-mixed water column. In the observations, this was accompanied by much warmer waters that was not simulated by the model. Such a sudden increase in temperature was greater than that possible by the heat flux as was described in Chapter 4. The model did simulate a warming and the complete breakdown of the seasonal thermocline.

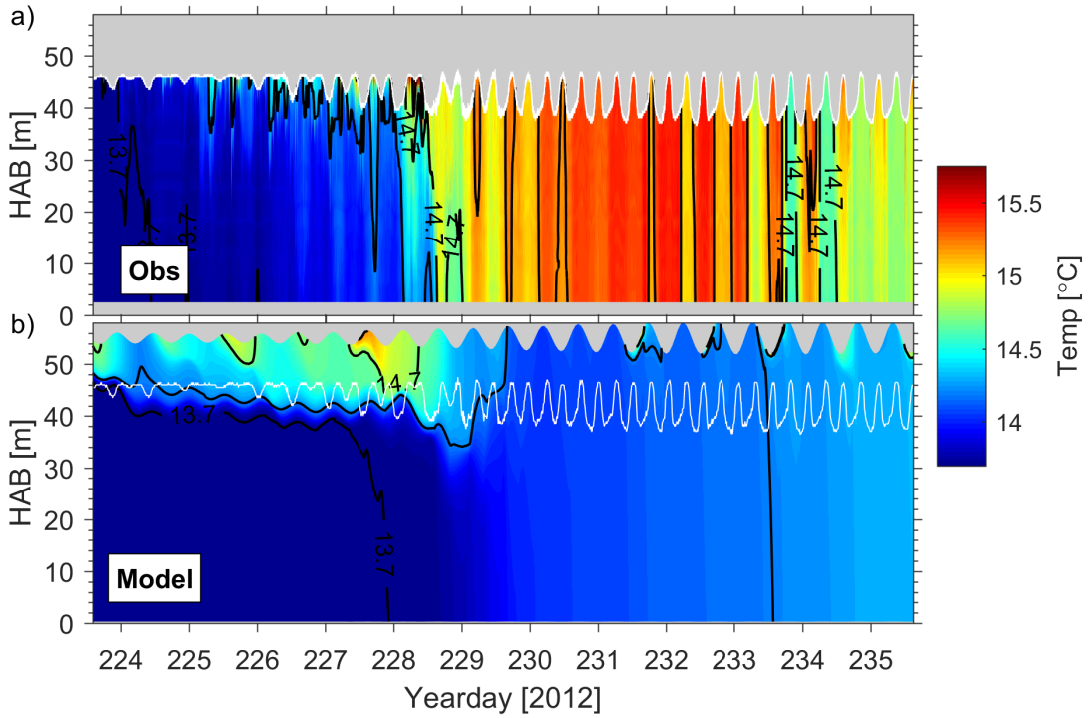

Figure 6.6: *The observed* ***(a)*** *and modelled* ***(b)*** *temperature field for the thermistor mooring location in August (Case 1b). Temperature contours were set at 0.5°C and labelled every 1°C. The surface region not included in the thermistor observations is denoted above the white line.*

The top and bottom timeseries presented in Figure 6.7 show the simulation matched the beginning of the thermistor timeseries well but soon deviated from it. The simulated water column did not gain enough heat over the period as was observed. This was seen both in the upper water column at 37 mab as well as 10 mab. Simulations hardly had any diurnal variability unlike that observed in the weakly stratified conditions and that observed in the observations. During the storm on yearday 228, the increase in temperature was not to the same extent as observed in the thermistor timeseries.

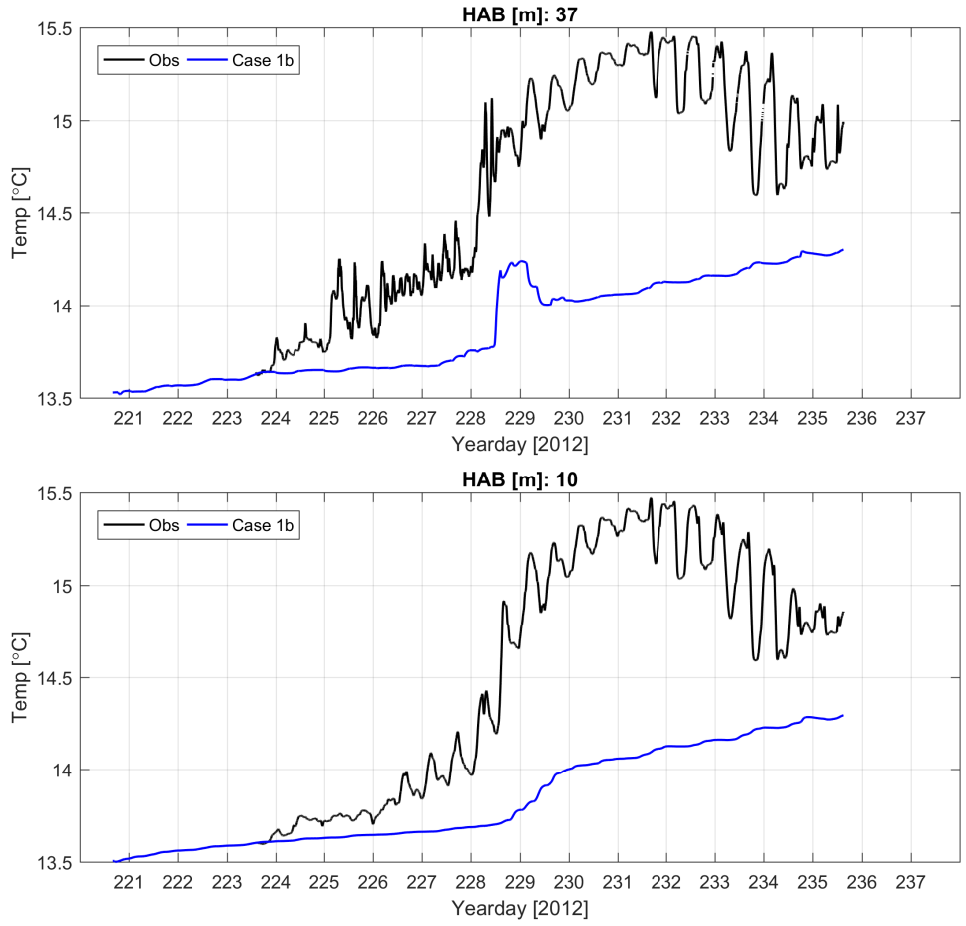

Figure 6.7: *Temperature timeseries of upper (43 HAB) and lower (10 HAB) water column from thermistor observations (black) and the Case 1b simulation (blue).*

Modelled Turbulent Dissipation in Summer

Simulated turbulent dissipation rates are presented in Figure 6.8. The transition from neap to spring tides is evident in the bed stress and tidally-driven dissipation rates. The tidally-driven turbulent BBL, shown here by the enhanced turbulent dissipation, exhibits significant variability in height with the

tidal asymmetry and transition to spring tides. The formation of stratification between yearday 223–229 occurs during weak tidal forcing and is evident in the temperature contours during neap tides with low bed stress generating weak turbulence in the interior below the thermocline.

The impact of the storms in deepening the upper mixed layer is also evident and the transition to well-mixed waters may be seen in the dissipation rates covering the whole water column.

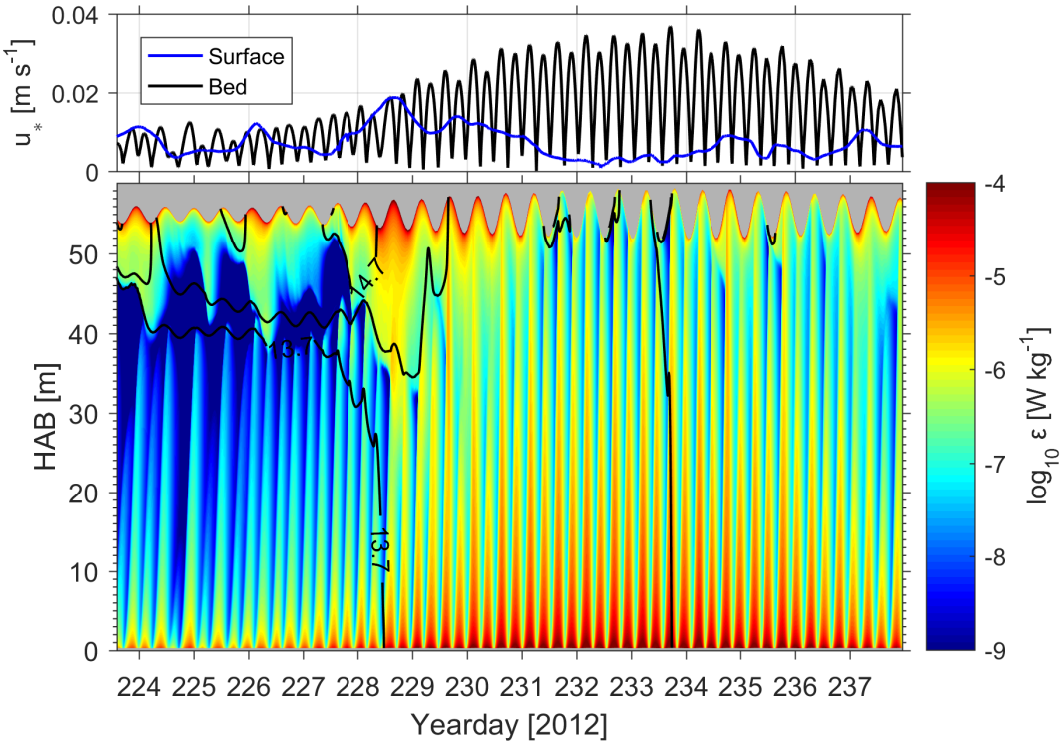

Figure 6.8: *Case 1b: the modelled turbulent dissipation at the thermistor station with temperature contours overlaid at 0.5°C and labelled every 1°C. The boundary stresses are presented above the main figure.*

6.3 Case 2 — The Vertical Water Column Structure at the Inshore and Offshore Stations

6.3.1 Case 2a & b: Comparing Simulations with MSS Tidal Cycles in Spring

Model simulation were run for the two MSS sampling stations; St1 and St2. In these simulations, the same model physics were used though the initial

conditions were obtained from the MSS tidal cycles at neap tides for each station in both spring and summer. In addition, the water depth for the respective stations were different, with St1 set in 65 m and St2 in 35 m.

The temperature field from both St1 & St2 in spring season are presented in Figure 6.9. The two stations show the similar warming trend as was observed at the thermistor mooring. The rise in temperature was the same for both stations though St2 was warmer (11.55–12.2°C) than the offshore station (11.15–11.6°C). Both simulations maintained well-mixed water columns with periodic stratification in the near-surface during periods of strong heat flux. Both stations were affected by significant wind events and St1, maintained deeper stratification.

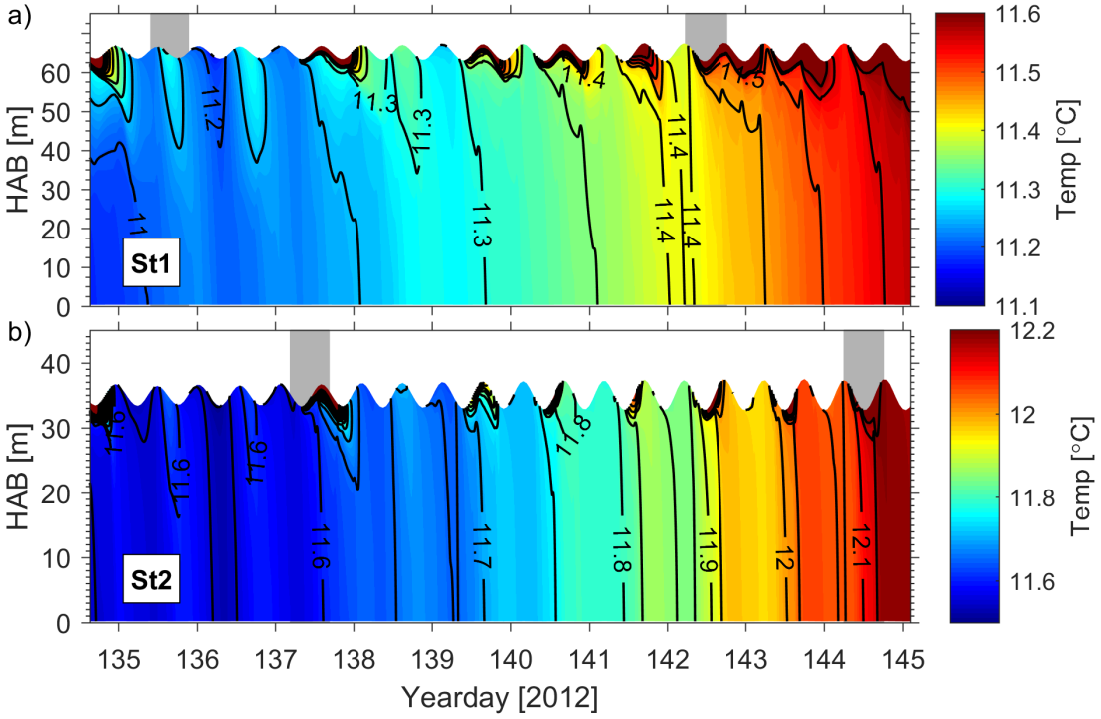

Figure 6.9: *The modelled temperature at Station 1 and 2 in weakly stratified conditions in May. The timings of MSS tidal cycles are shown in grey. Temperature contours were set at 0.05°C and labelled every 0.1°C.*

The simulated turbulent dissipation for both Stations are presented in Figure 6.11. Enhanced turbulent mixing was observed throughout the water column with a combination of both surface stress and tidal stress acting to mix the water column. It is worthwhile to note that the two stations used different current forcing from observations, with the inshore station using an bed-

moored ADCP located at St2 as part of a separate project (Figure 6.10). The simulated bed shear stress was consistently greater for the inshore station by approximately 0.025–0.01 m s^{-1} and a general trend towards larger bed shear stresses during spring tides was present at both Stations.

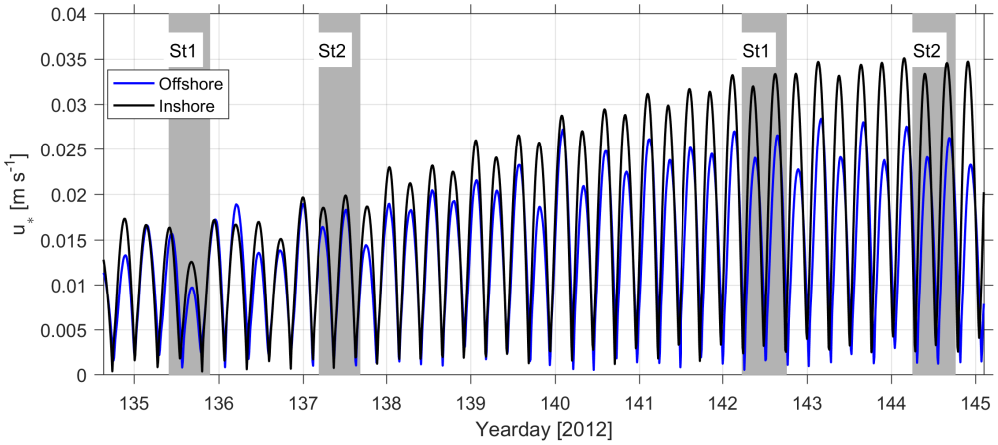

Figure 6.10: *Simulated bed shear stresses for the offshore (St1) and inshore (St2) MSS stations during deployment in spring. The timings of the alternate MSS tidal cycles at station 1 & 2 are indicated.*

The simulated dissipation rates for St1 and St2 highlights the difference in water column structure predominantly produced by the difference in water depth and tidal forcing. The turbulent BBL, once again identified by the enhanced dissipation rates, was evident at both stations generated at a M_4 periodicity with an increase in BBL towards spring tides. The significant wind events on yearday 136 & 138 were evident in the elevated dissipation rates in the upper $\sim$15 m of the water column. Given the shallower water depth at St2, dissipation rates throughout the water column were consistently higher than at St1. The temperature contours show that weak stratification was more easily attained at St1 although it was also present at St2 on occasions where the dissipation rates were reduced.

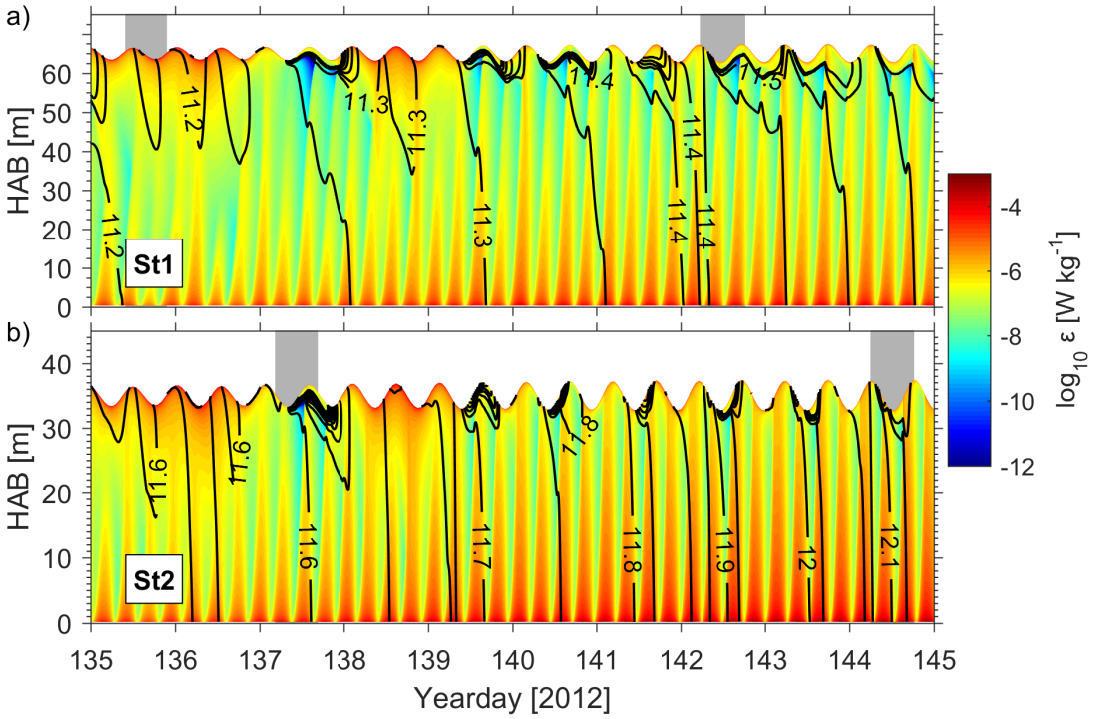

Figure 6.11: *The modelled dissipation rate at Station 1 and 2 in weakly stratified conditions in May. The timings of MSS tidal cycles are shown in grey. Temperature contours were set at 0.05°C and labelled every 0.1°C.*

Case 2a — Station 1 — Increased Surface Wind Stress Conditions

The MSS tidal cycle on yearday 135 was conducted under increasing wind stress conditions and a deepening of the warmer surface mixed layer was observed in response to the increased forcing. The modelled temperature and dissipation shown in the previous section of this chapter in Figure 6.9a & 6.11a show downwards mixing of warm water was simulated within a region of enhanced dissipation in the upper water column on yearday 135. In this section, a direct comparison between the modelled dissipation rates and that measured during the MSS tidal cycles is made in order to assess the accuracy of the modelled vertical turbulent mixing under strong surface winds and at neap tides (Figure 6.12).

Enhanced dissipation rates within the tidally-generated turbulent BBL were in good phase agreement with those in the observations (Figure 6.12a & b). Enhanced dissipation rates within the first turbulent BBL, established prior to the beginning of sampling, decreased in the near-bed region at approximately 20° in the simulation (10^{-7} W kg^{-1} contour) which matched that seen in the

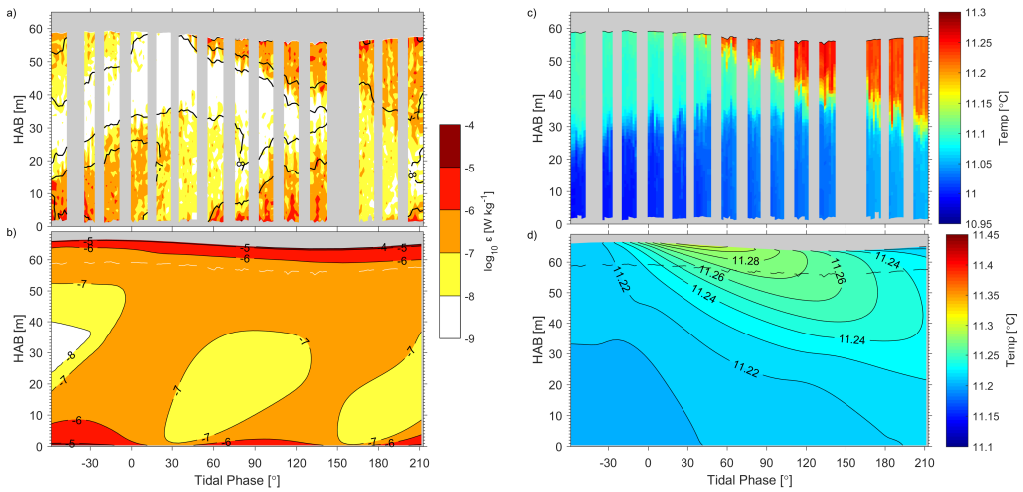

Figure 6.12: *The observed and simulated MSS tidal cycle at neap tides on yearday 135.* ***a)*** *Observed dissipation rates;* ***b)*** *modelled dissipation rates;* ***c)*** *observed temperature* ***d)*** *modelled temperature.*

observations. The turbulent BBL height (contours of 10^{-7} W kg^{-1}) was also well replicated in the simulation and may be seen at the beginning of the measured tidal cycle between -50– -30°. The growth of the BBL was captured by the model although no discernible decrease in dissipation rates were seen in the water column's interior. The second region of enhanced turbulence in the BBL commenced around 50° and lasted until 150° in both simulations and observations. Dissipation rates in between the enhanced BBL layers were of the same magnitude in simulations and observations (10^{-8} W kg^{-1}). The phase lag in the growth of the turbulent BBL with height was also correctly replicated. Enhanced dissipation rates in the simulated near-surface region was seen in the model at levels comparative in magnitude to the BBL. The wind-driven enhancement between 30–210° observed in the MSS was not evident in the model since dissipation rates were elevated throughout the interior. However, dissipation rates in the wind-enhanced layer matched those simulated in the near-surface region and is investigated in hourly profiles below (Figure 6.13).

The result of the enhanced surface wind stress was observed in the modelled temperature structure. The downward flux of heat was observed over the tidal cycle in the near-surface layer although the model did not show the level of warming in this layer in comparison to observations. Overall, observed temperatures were slightly cooler at 11.0–11.3°C, whereas the modelled temperature was between 11.2–11.3°C. The observed mid-water temperature

gradient that maintained cooler temperatures within the BBL did not endure in the simulation unlike the observations. The cooler BBL was initially simulated between -50– 0° but the downward mixing of warmer near-surface waters quickly enveloped the BBL. Given the reduced temperature gradients in the simulation, this reduction of stratification could have likely allowed the increased temperature diffusion in the simulation.

Profiles of dissipation rates for both model simulation and observations at approximately 30° (1 hour) intervals show the good agreement in dissipation rates in the bottom and surface boundary layers (Figure 6.13). Outside of the turbulent BBL layer, the model simulation departed from observations and did not simulate the observed interior minima. As opposed to the observations, modelled dissipation rates remained above 10^{-7} W kg^{-1} in the interior, which was not the case in observations that decreased to 10^{-9} W kg^{-1}. The effect of the increased wind stress, which enhanced surface dissipation rates starting at 50° in observations, increased observed dissipation rates to match the simulation. Towards the end of the tidal cycle (190–210°), the surface source of dissipation had diffused down and the model simulation levels matched that in observations.

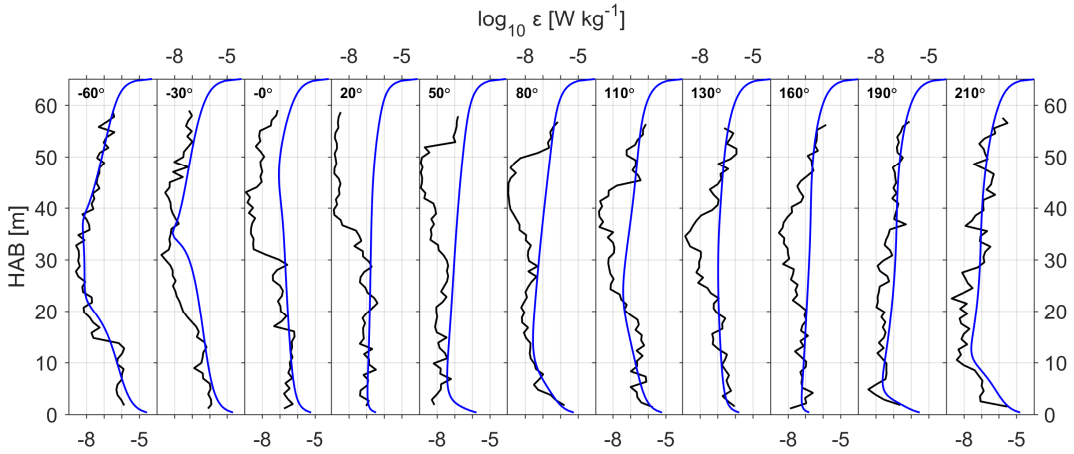

Figure 6.13: *The modelled (blue) and MSS profiles (black) turbulent dissipation at Station 1 on yearday 135 showing the near-surface warming associated with the downward mixing of warm water due to an increase in wind stress.*

Temperature profiles in Figure 6.14 show the simulation temperatures to be warmer and with less vertical gradient throughout the tidal cycle than in the observations. The lack of the mid-water column temperature gradient is evident in the model profiles in comparison to those observed. This may also be seen in the upper water column gradients during the enhanced surface wind

stress.

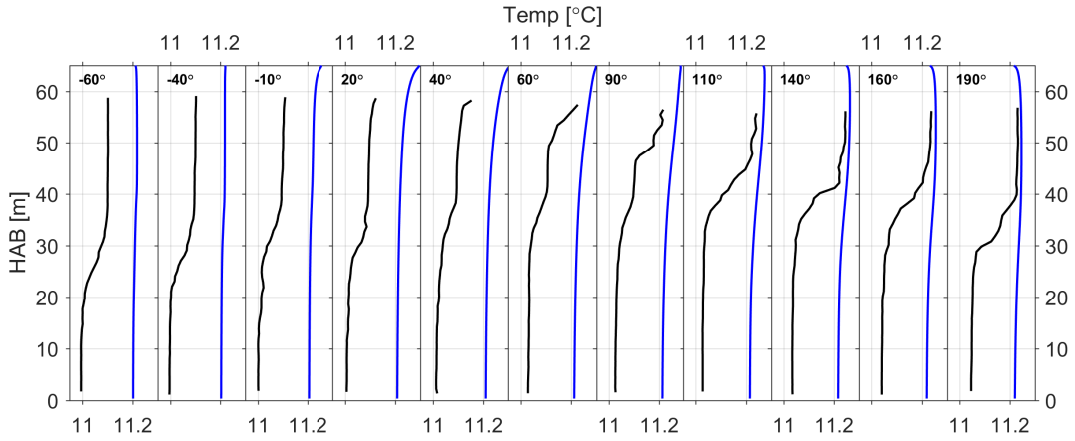

Figure 6.14: *The modelled (blue) and MSS profiles (black) temperature at Station 1 on yearday 135 showing the near-surface warming associated with the downward mixing of warm water due to an increase in wind stress.*

Increased Bed Stress Conditions at Spring Tides

Modelled turbulent dissipation rates in the BBL show good phase and height agreement with those measured by the MSS during spring tides on yearday 142 (Figure 6.15). The phase properties of the BBL were well represented in the model with the timing of the enhanced turbulent BBL and phase lag with height above the bed closely matching that in the observations. The increase in BBL height in comparison to neap tides was also well represented by the model. This may be seen by comparing the dissipation contours of the first turbulent BBL cycle between 0–180°. Here, the 10^{-6} W kg^{-1} contour from MSS observations and model reached a height of 25 m at approximately 110°. During the second cycle, the maximum 10^{-6} W kg^{-1} contour height reached 31 mab in observations and 33 mab in the model simulation. The predominantly well-mixed temperature structure with some near-surface warming during the second half of the tidal cycle matched that seen in the observations although the simulated temperature was cooler than observed.

The hourly profiles of dissipation rates are presented in Figure 6.16 and show good agreement in the dissipation rates within the BBL.

The hourly temperature profiles presented in Figure 6.17 show the well-mixed water column. The surface warming that started to appear in both observations and simulations at 50° was not adequetly captured by the model in depth. This

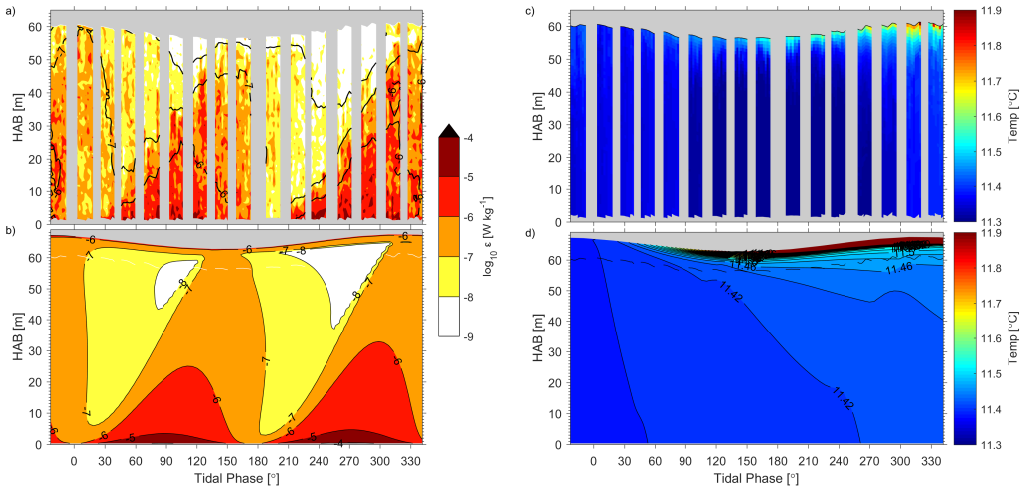

Figure 6.15: *The observed and simulated MSS tidal cycle at spring tides on yearday 142.* ***a)*** *Observed dissipation rates;* ***b)*** *modelled dissipation rates;* ***c)*** *observed temperature* ***d)*** *modelled temperature.*

suggests a lack of mixing in the near-surface layer. However, given the warmer simulated temperatures, the increase in observed temperature minimizes the difference in temperature in the water column.

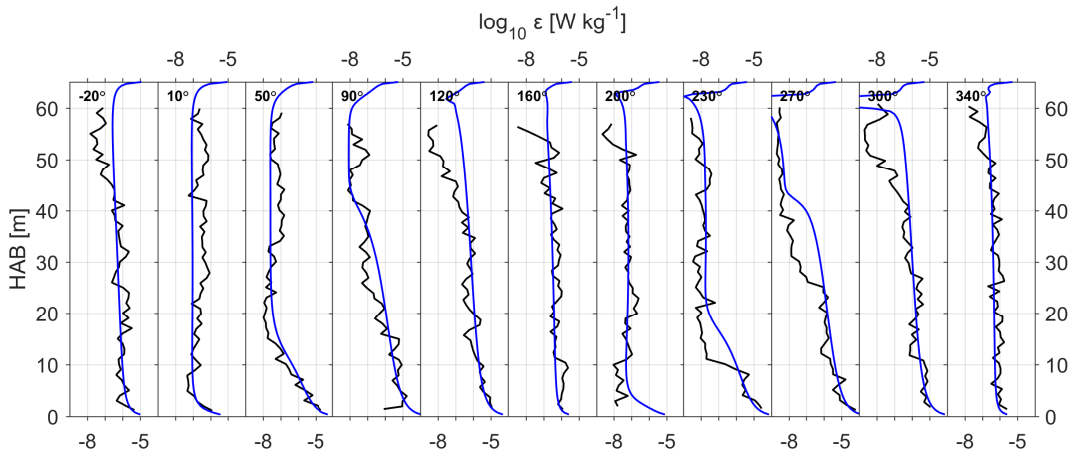

Figure 6.16: *The modelled (blue) and MSS profiles (black) turbulent dissipation at Station 1 on yearday 142.*

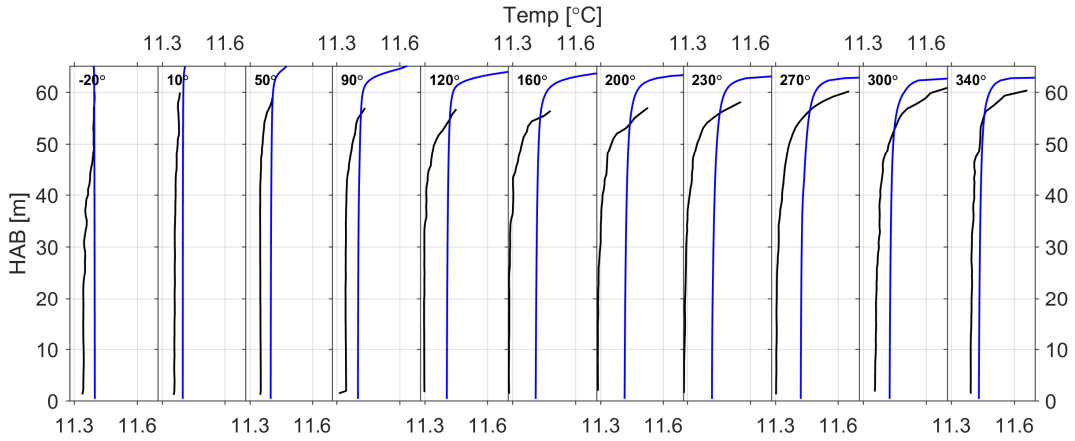

Figure 6.17: *The modelled (blue) and MSS profiles (black) temperature at Station 1 on yearday 142 showing the near-surface warming associated with the downward mixing of warm water due to an increase in wind stress.*

Case 2b — Station 2 — Neap Tide Conditions

The shallow water depth at Station 2 altered the dynamics of the water column. Here, the tidally driven BBL was observed to reach the top of the MSS measurements during both neap and spring tides. The water column was mainly well-mixed and situated inshore of the seasonally stratification and frontal region.

MSS dissipation rates within the tidal BBL during neap tides (yearday 137) at Station 2 were observed to extend throughout the water column as is evident in Figure 6.18a. Elevated dissipation rates of 10^{-6} W kg^{-1} were recorded through out the water column between -300– - 180°and -120– -20°. In comparison,

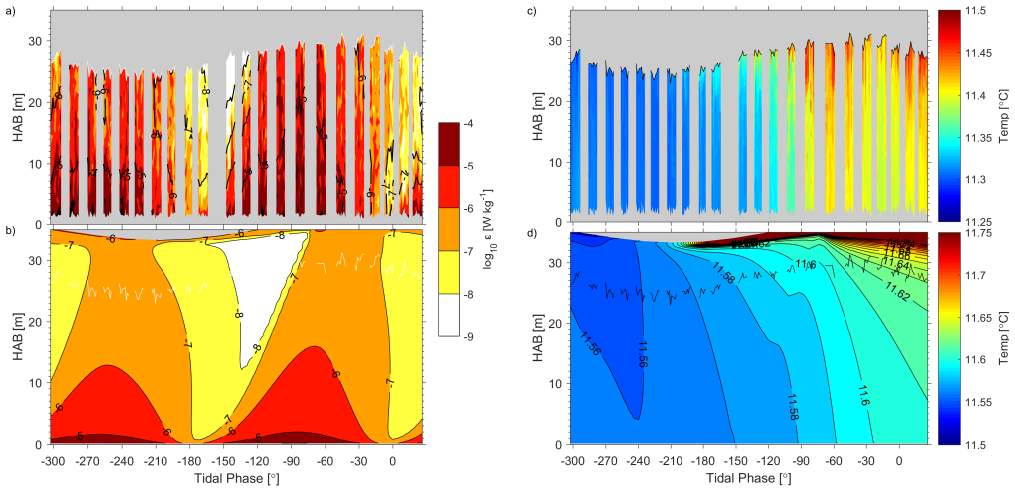

Figure 6.18: *The observed and simulated MSS tidal cycle at neap tides on yearday 137.* ***a)*** *Observed dissipation rates;* ***b)*** *modelled dissipation rates;* ***c)*** *observed temperature* ***d)*** *modelled temperature.*

the modelled dissipation rates for the equivalent tidal phases were 10^{-7} W kg^{-1} in the upper water column. The dissipation minima observed in the MSS sampling during slack water was evident in the simulation though overdue by approximately 30° (1 hour).

The modelled temperature field attempted a similar warming pattern during the second half of the MSS tidal cycle though was unable to achieve the correct degree of warming within the water column. The simulation obtained the correct vertical structure, developing a homogeneous, vertically well-mixed water column at the same time as that observed in the MSS. However, the increase in temperature was not hot enough in comparison to the observations.

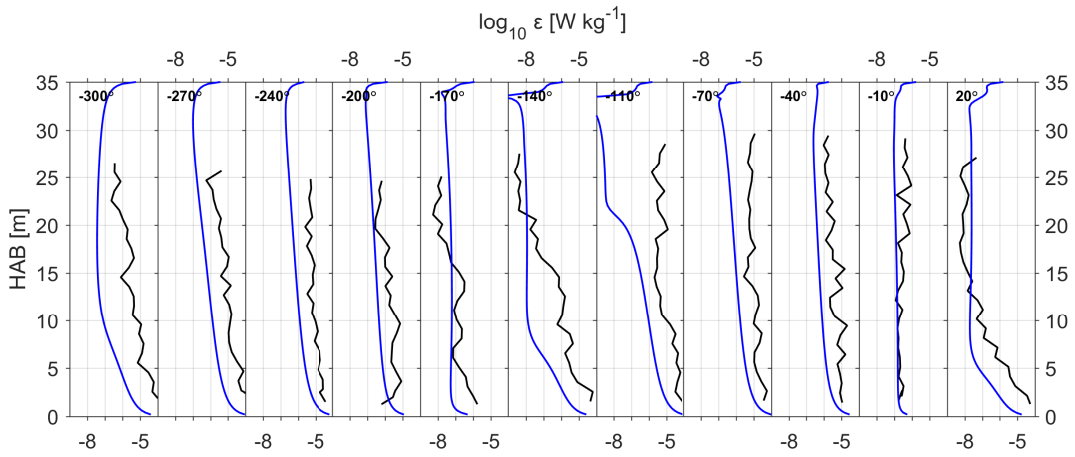

Figure 6.19: *The modelled (blue) and MSS profiles (black) turbulent dissipation at Station 1 on yearday 137 showing the near-surface warming associated with the downward mixing of warm water due to an increase in wind stress.*

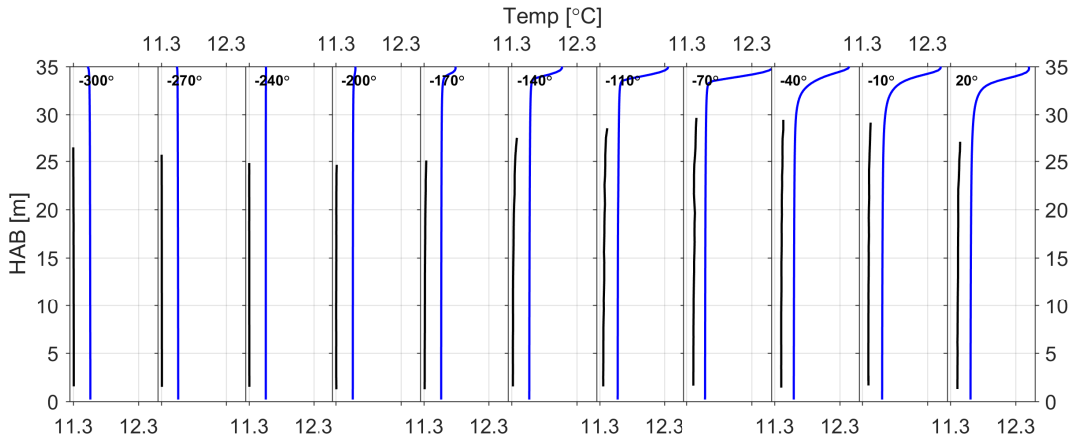

Figure 6.20: *The modelled (blue) and MSS profiles (black) temperature at Station 1 on yearday 135 showing the near-surface warming associated with the downward mixing of warm water due to an increase in wind stress.*

6.3.2 Case 2c & d: Comparing Simulations with MSS Tidal Cycles in Summer

Under Stratified Conditions

The temperature structure and levels of stratification differ greatly between Station 1 & 2 in summer (Figure 6.21). The offshore station, Station 1, maintained stratification and a strong thermocline through the deployment period, while Station 2 was well-mixed even under weak tidal forcing at neap tides. Unlike at the thermistor station, the storm on yearday 229 did not completely breakdown the stratification although a significant reduction in the strength

of the stratification ensued as well as a deepening of the seasonal thermocline by 6 m. In comparison to the offshore station, the inshore station was well mixed except for periods of near-surface stratification during neap tides.

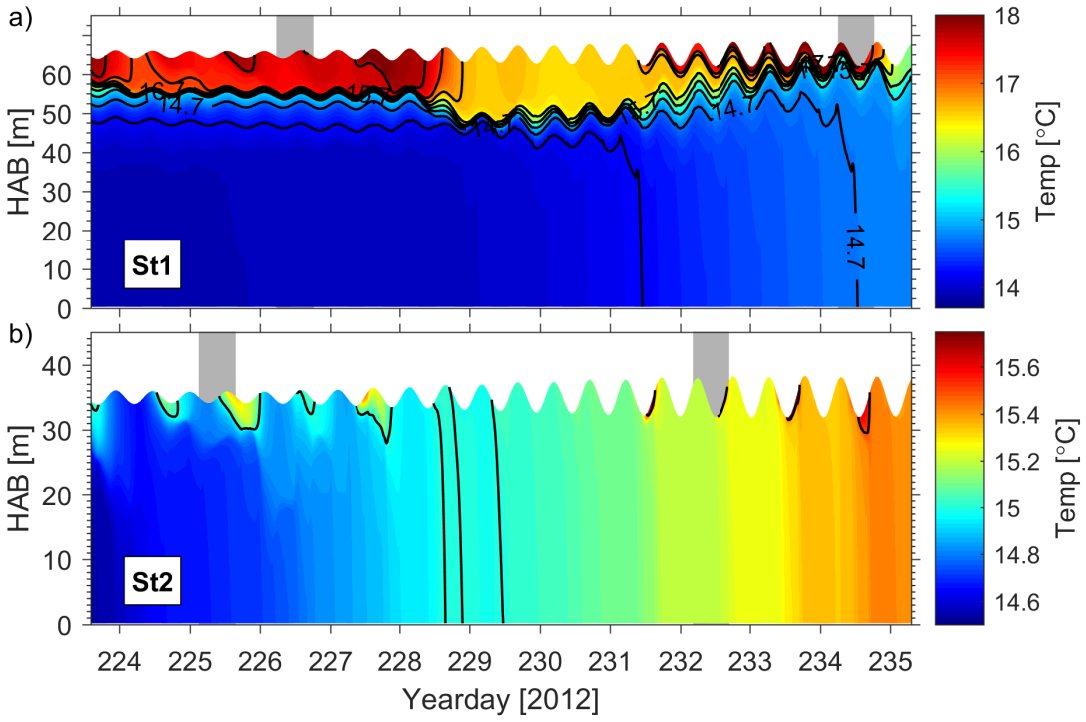

Figure 6.21: *The modelled temperature timeseries at Station 1* ***(a)*** *and 2* ***(b)*** *in summer. The model water depth was 65 m. Grey shade denotes the timing of MSS tidal cycles conducted at each station. Modelled temperature contours are overlaid every 0.5°C and labelled every 1°C.*

The modelled turbulent dissipation rates presented in Figure 6.22 show how the differing water depth impacts on the water column structure. During neap tides at the beginning of the simulation, the turbulent mixing in the tidally driven BBL was reduced and the BBL reached a maximum height of 44 mab. Surface forcing during this period was constrained to the top 10 m above the thermocline. Unlike at the thermistor station, this left a 10 m high section in the interior that contained very low levels of simulated dissipation rates. Unlike the unstratified conditions in spring presented above in Figure 6.11, the turbulent dissipation in the upper water column was unable to penetrate the seasonal stratification. Enhanced dissipation during the storm on yearday 228, caused a deepening of the thermocline by 6 m and an increase in the turbulent BBL increased dissipation rates in the interior. During the period of increased surface wind stress, the thermocline deepened but did not get eroded. Further

erosion of the seasonal thermocline occurred after the reduction in upper dissipation under increased BBL mixing conditions. This occurred because the reduction in near-surface mixing allowed the development of near-surface stratification, observed to develop around yearday 231, which prevented the downward diffusion of heat to maintain the temperature gradients in the seasonal thermocline below it.

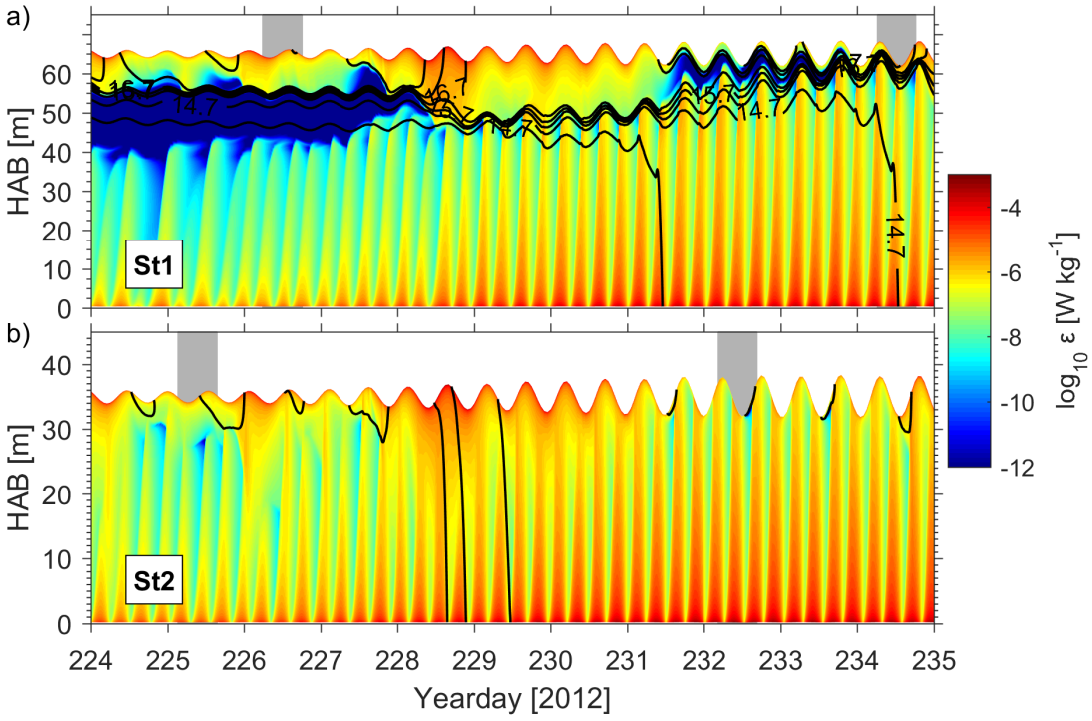

Figure 6.22: *The modelled turbulent dissipation rates for Station 1* ***(a)*** *and 2* ***(b)*** *in summer. The model water depth was 35 m. Grey shade denotes the timing of MSS tidal cycles conducted at each station. Modelled temperature contours are overlaid every 0.5°C and labelled every 1°C.*

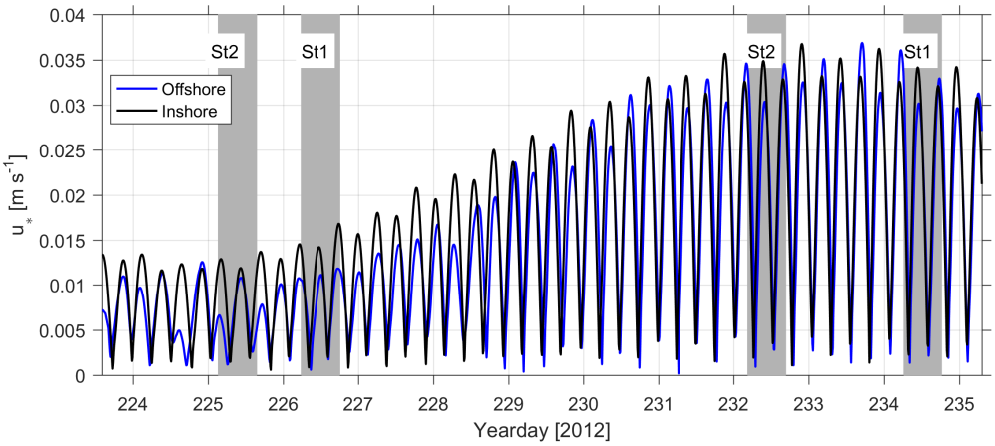

Figure 6.23: *Simulated bed shear stresses for the offshore (St1) and inshore (St2) MSS stations during deployment in summer. The timings of the alternate MSS tidal cycles at station 1 & 2 are indicated.*

Case 2c — Station 1 — Under Stratified Conditions at Neap Tides

The MSS tidal cycle in summer at neap tides maintained the strongest stratification. This was due to a combination of weak neap tidal currents (Figure 6.23) and seasonal increase in surface heat flux. Figure 6.24 presents the observed and simulated tidal cycle of turbulent dissipation and temperature. Although the phase timing of the turbulent BBL structure was well matched, the outer region of the simulated turbulent BBL presented significant differences to that of the observations. During the first half of the tidal cycle, the outer region (10^{-8} W kg^{-1}) increased in height more than observed. Furthermore, the outer BBL in the second half of the tidal cycle was significantly higher than in observations. The observations in the BBL were kept low due to interior stratification as described in Chapter 5. This was not replicated in the model most likely due to the lack of interior stratification that is evident in Figure 6.24d. Low levels of turbulent dissipation were consistent with observations in the interior although an elevated patch of turbulent dissipation along an isotherm, between -240– -120°, seen in the observations was not simulated in the model. Enhanced near-surface turbulent dissipation rates matched the observations with the base of the near-surface layer between 50–60 mab.

The modelled temperature structure successfully simulated the warm surface mixed layer with the thermocline at the base of the mixed layer at 55 mab. The surface mixed layer waters were warmer in the model than observed and the thermocline gradients were much sharper. Below the surface mixed layer, the modelled temperature structure lacked the interior stratification that was

seen to regulate the height of the turbulent BBL in the observations.

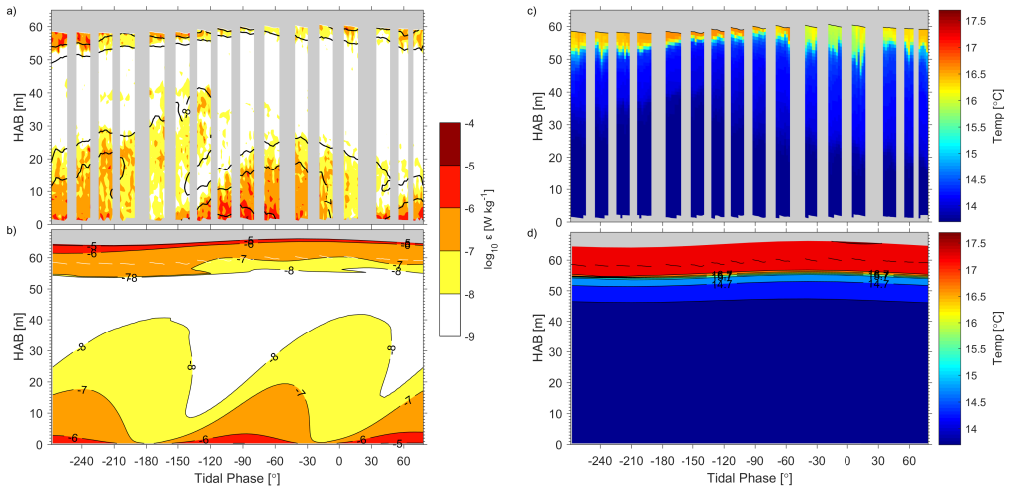

Figure 6.24: *The observed and simulated MSS tidal cycle at neap tides on yearday 226.* ***a)*** *Observed dissipation rates;* ***b)*** *modelled dissipation rates;* ***c)*** *observed temperature* ***d)*** *modelled temperature.*

The turbulent dissipation profiles presented at approximately hourly intervals show the close agreement in the lower section of the turbulent BBL between the model and observations (Figure 6.25). At tidal phase -230 and -200°, the deviation between model and observations, between 25–37 mab, in the upper BBL region is evident. The difference in height of the turbulent BBL during the second half of the tidal cycle was evident between the depths of 20–40 mab at tidal phase -30– 40°. The decrease in turbulent dissipation above the BBL is evident in the profiles and the height at which the BBL decreases to background interior levels are well replicated in the model (e.g. at tidal phase 160 & 130° at 42 mab). The increase in surface layer turbulent dissipation in the upper part of the profiles shows some variability in magnitude and height not seen in the model simulation profiles.

The temperature profiles in Figure 6.26 and N^2 profiles in Figure 6.27 show the difference in thermocline structure between the model and observations. The modelled thermocline structure remains relatively steady over the tidal cycle whereas the MSS temperature profiles show a distinctive decrease in thermocline gradient coinciding with a cooling of the surface layer and a slight warming of the deeper layer. The buoyancy frequency reflects this difference with maximum N^2 values within the modelled thermocline of $10^{-2.2}$ s^{-2}, whereas the maximum observed frequency was $10^{-2.7}$ s^{-2}. The observed N^2 in the thermocline decreased between -90– 10°in line with the weakening

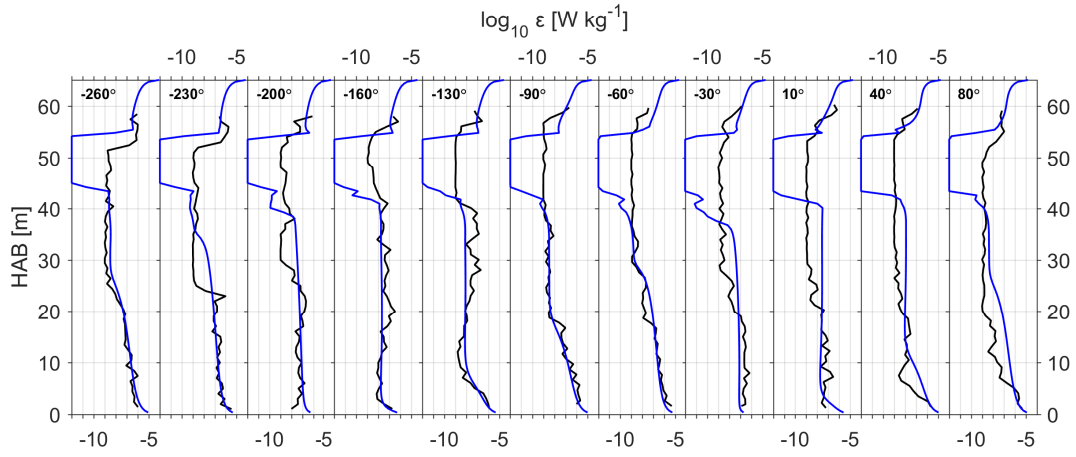

Figure 6.25: *The modelled (blue) and MSS profiles (black) turbulent dissipation at Station 1 on yearday 226.*

of the thermocline observed in Figure 6.24c at the same tidal phase. This was not replicated in the model and indicates enhanced mixing either from a surface source or along the thermocline that was not incorporated in the model. Enhanced dissipation rates were also observed during the same period in Figure 6.24a.

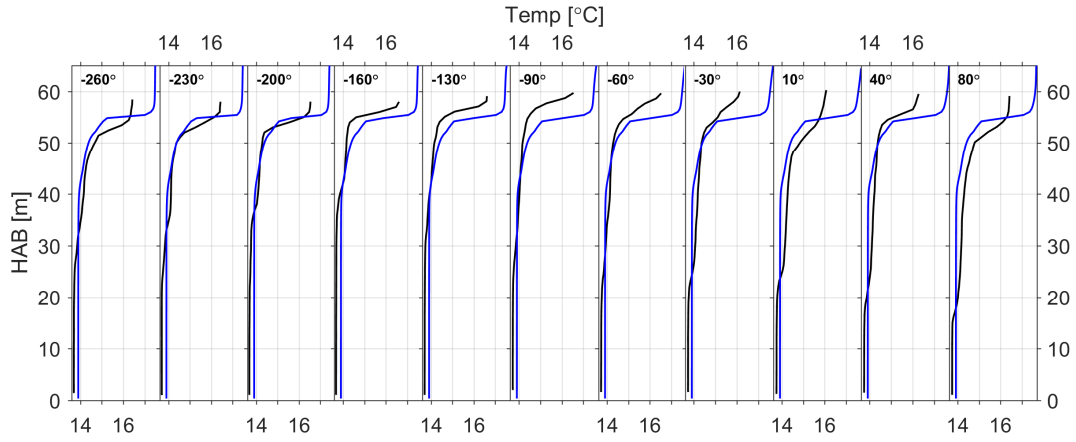

Figure 6.26: *The modelled (blue) and MSS profiles (black) temperature at Station 1 on yearday 226.*

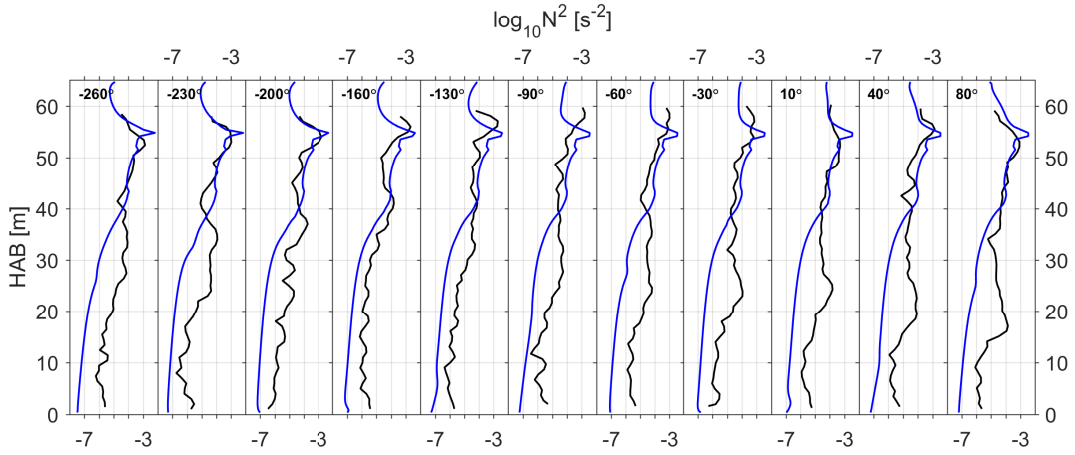

Figure 6.27: *The modelled (blue) and MSS profiles (black) buoyancy frequency squared at Station 1 on yearday 226.*

Case 2d — Station 1 — Under Stratified Conditions at Spring Tides

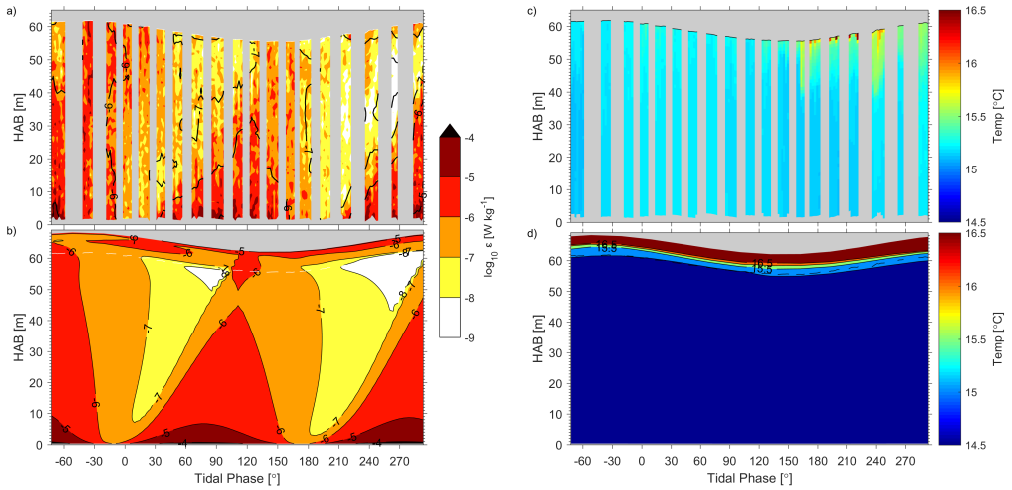

Figure 6.28: *The observed and simulated MSS tidal cycle at neap tides on yearday 234.* ***a)*** *Observed dissipation rates;* ***b)*** *modelled dissipation rates;* ***c)*** *observed temperature* ***d)*** *modelled temperature.*

The turbulent dissipation measured at the MSS tidal cycle on yearday 234 at spring tides were well modelled. The overall height of the BBL was matched in observations with that modelled. Between -60–0° tidal phase there were elevated dissipation rates throughout the water column (10^{-6} W kg^{-1}). However, the timing of the dissipation in the model was advanced by 30°. The following tidal cycle presented a depressed BBL, with the 10^{-6} W kg^{-1} contour in observations reaching a maximum height of 32 m while, in comparison, in the model reached 44 m hab.

During the latter stages of the tidal cycle, between 210–280°, abrupt intrusions of upper water column warm water were observed. These were coincident with elevated dissipation rates (10^{-7} W kg $^{-1}$) in the upper water column that were not present in the model. These warm water intrusions are illustrative of the missing physics in the model, either originating from an advective source or upper water column turbulent mixing process not included. Such small-scale, secondary mixing mechanisms may be seen to play an important role in the upper water column mixing; the modelled temperature contains much too strong a thermocline with temperatures $\triangle 1$ °C across the thermocline. Although the thermocline resided above the upper limit of the MSS profiles and subsequently was not recorded, the consequential lack of downward mixing of warm surface water caused the water below the thermocline in the model to be cooler than that observed in the MSS profiling. Below the thermocline in the model, temperatures were on average 14.5°C whilst in observations, they were on average 15.25°C.

6.4 Case 3 — Internal Wave Mixing

6.4.1 Internal Wave Mixing Parameterization

As may be seen in Figure 6.22, under strongly stratified conditions, the model predicts minimal levels of turbulent dissipation in the interior below the thermocline. In reality, observations from the MSS tidal cycles have shown that levels of turbulent dissipation in the interior may be higher than predicted by the model. Studies have found interior mixing processes, shear instabilities or internal wave breaking, that are not considered in GOTM increase the level of mixing in the interior (Simpson et al., 1996; Burchard et al., 1998; Rippeth et al., 2005). Simple algebraic parameterizations have been implemented in GOTM in order to account for the increasing effect of shear instability and internal wave breaking in the presence of stable stratification. The difficulty in implementing internal mixing is that turbulence in stratified fluids is highly intermittent and therefore it is only the mean effect of these processes on the mixing that may be modelled in GOTM (Burchard et al., 2000).

Stable stratification acts to reduce the size of turbulent eddies and cause the largest turbulent eddies to decay into internal waves (Luyten et al., 1996a). In order to account for this, Galperin et al. (1988) argued limiting the turbulent macro length scale by the buoyancy length scale to account for the reduced

mixing in stably stratified flows:

$$L^2 \leq L^2_{min} = \frac{0.56k}{N^2} \quad \text{for} N^2 > 0 \tag{6.1}$$

In all simulations conducted in this investigation, including those in Case 1 presented in the previous Section, the macro length scale was limited following the original implementation in the Fladenground testcase scenario. Further limitations on the TKE was necessary in simulations by Luyten et al. (1996b), since the limiting conditions set by the macro length scale made no significant change to their results. The empirical limit of TKE (k) was selected as $k_{min} = 10^{-6}$ m^2 s^{-2} by comparing model predictions to turbulent dissipation rates collected in the Irish Sea by Simpson et al. (1996). In a comparison simulation for the same observational data, Burchard et al. (1998) found $k_{min} = 7.6 \times 10^{-6}$ m^2 s^{-1} to best match observations.

An alternative to imposing limiting conditions on turbulence generation in stably stratified flows is also considered in GOTM by parameterizing internal mixing more directly. The introduction of internal wave mixing as an extra term in the turbulence equations as an additional source of shear was implemented by Mellor (1989). Here, the internal wave shear is dependent on N^2 and modelled as αN^2, where an empirical value of $\alpha = 0.7$ is set from comparison to observed shear profiles (Burchard et al., 1999). The extra term is added to the turbulent shear production term (P) in GOTM under stable stratification ($N^2 > 0$):

$$P = \nu_t(S^2 + \alpha N^2) \tag{6.2}$$

where, S, is the modelled vertical shear.

IW Thermistor Timeseries

Figure 6.29 presents the simulations with the various internal wave parametrisations in comparison to the thermistor timeseries for the summer deployment. No significant improvement was observed as a result of the inclusion of stratified mixing, though the paramitrisation of Mellor (1989) caused a slight increase in temperature during stratified conditions between yearday 226–228.

Figure 6.30 presents the vertical profiles of temperature, TKE and turbulent diffusivity for two times indicated by the vertical dashed lines in Figure 6.29

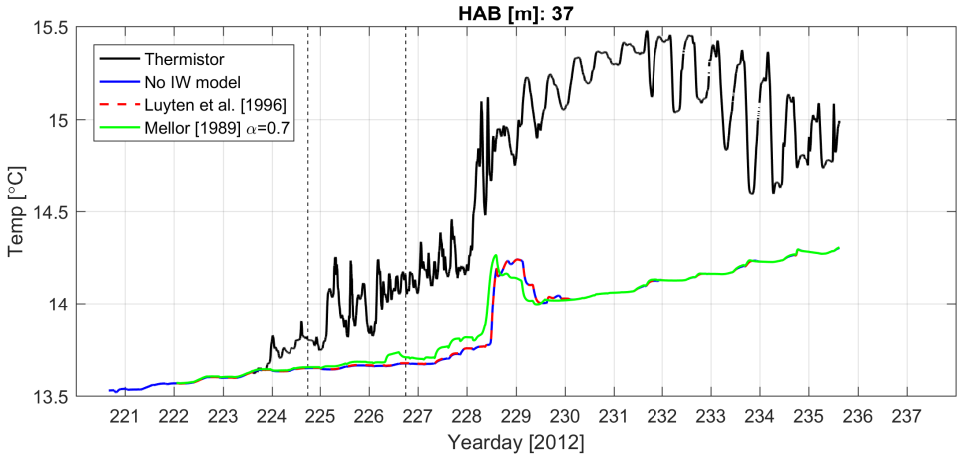

Figure 6.29: *Temperature timeseries from model and observations at HAB 37 m with the various internal mixing parameterizations. The vertical dashed lines denote the timing of the profiles included below on yearday 224.75 and yearday 226.75.*

(yearday 224.75 & 226.75). The results of the internal wave parametrisation did not show any improvement in the vertical structure of the temperature profile for the simulations. The simulations maintained a cooler interior with a stronger thermocline than that observed. Furthermore, the surface layer temperature was much warmer than indicated although it is imperative to consider that the thermistor profile excluded the top $\sim$ 5–10 m of the water column. Nevertheless, the indications were that the simulated surface layer was significantly warmer than observed. The significant differnence between the two internal wave parametrisations was observed in the profiles of TKE and turbulent diffusivity. Here, the parametrisation of Luyten et al. (1996b) contained significantly elevated levels in the interior ($k_{min} = 10^{-6}$ m^2 s^{-2}) in response to the minimum TKE limit set.

As was observed in Figure 6.30, no discernible difference was made by setting $k_{min} = 10^{-6}$ m^2 s^{-2} in the temperature profiles suggesting that this background value was too low. In Figure 6.31 the result of increasing this background value are presented in comparison to the observed temperature profile. The best fit to the observed temperature profile was attained with a background $k_{min} = 10^{-4}$ m^2 s^{-2} although there was still an absolute difference in temperature between that observed and simulated. Furthermore, TKE levels were exceptionally large which caused anomalously large TKE levels in the boundary layer during low turbulent conditions (Figure 6.31a). Such a condition of anomalously large values was further illustrated when $k_{min} = 10^{-3}$ m^2 s^{-2}. In this case, the water

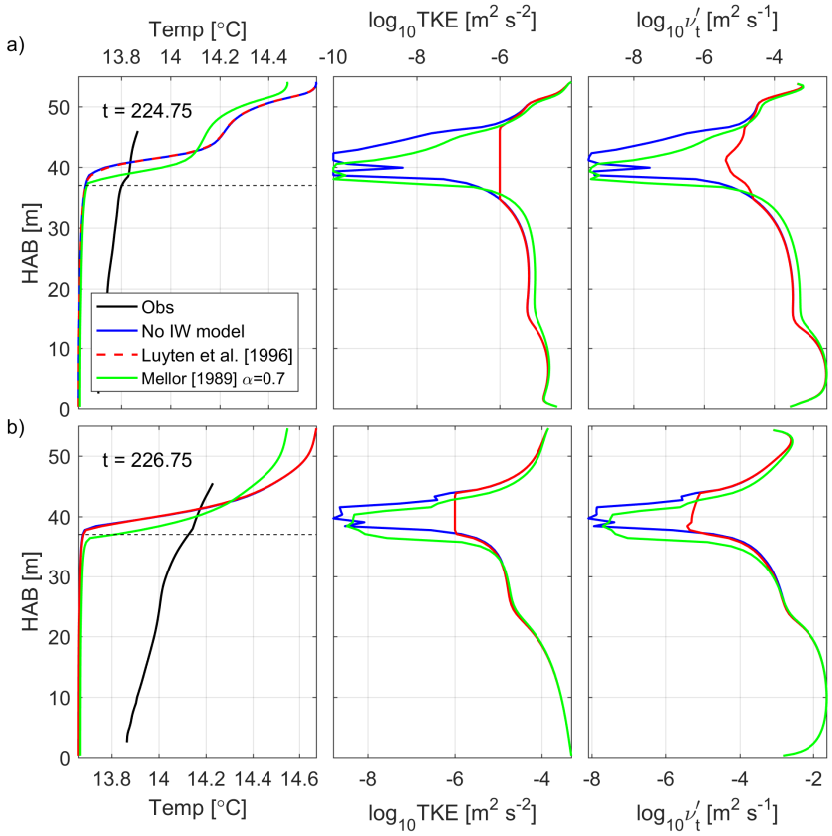

Figure 6.30: *Profiles of temperature, TKE, and turbulent diffusivity for the various internal mixing parameterizations implemented in GOTM.* ***a)*** *Profiles during yearday 224.75;* ***b)*** *profiles during yearday 226.75. The horizontal dashed line shows the depth of the temperature timeseries (HAB 37 m) presented in the previous Figure.*

column became completely vertically well-mixed and TKE levels ceased to represent the vertical profile including the with the elevated levels in the BBL.

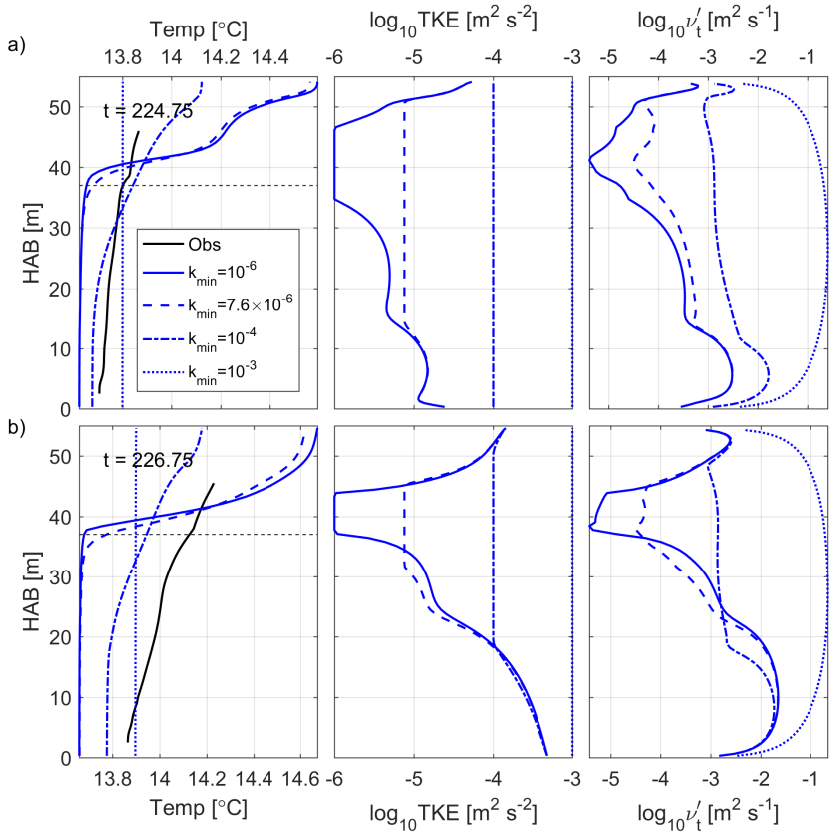

Figure 6.31: *Profiles of temperature, TKE and turbulent viscosity simulated under various empirical minimum TKE values under the parameterization put forward by Luyten et al. (1996b). The black horizontal dashed line denotes the height of the thermistor timeseries graph presented above.*

6.5 Summary

This Chapter presented the results of the simulations made using a 1-D, vertical-resolving, General Ocean Turbulence Model which was run to investigate the details of the vertical mixing regime identified in the observations. The model was set up for the three locations; the two MSS sampling sites, and the thermistor mooring, situated in between the MSS sites. Initial conditions were selected from observation and the vertical boundaries set to the free surface and the water depth for the required location. The numerical model only considered the vertical fluxes and no advective processes were included since no internal pressure gradients were prescribed, primarily to focus on the vertical mixing but also since there was no spatial sources of full water column data available to quantify the advection. The model was run for the periods of the field campaign giving a good dataset to compare against. Overall, the model comparison with the observation data was impressive with the model

able to accurately model the boundary layer mxing processes. The model fell short of expectations in two areas. Firstly, the parameterized interior mixing and surface wave mixing was inadequate. Secondly, as was expected, the lack of advective processes meant deviation from observations was found, especially in August when a large increase in temperature was observed on yearday 228 that was not reproduced in the model. Also, small-scale variability in the temperature field over a semi-diurnal periodicity was absent in the model though was consistently present in the observations. The principal findings of this Chapter are summarised as follows:

1. **Comparisons with observation data —** In comparison to the thermistor data, the model performed well in capturing the rate of temperature increase associated with surface heat input. The model fell short of the observed warming in August due to the advective of warm water following the significant wind event on yearday 228. In addition, the model also lacked the semi-diurnal advective variability observed, although performed well with the diurnal variability associated with convective mixing and surface heat input. The model also responded well to surface forcing conditions with deepening of the surface warm layer, and thermocline in summer, in response to stronger wind stress and conversely generated more surface warming in a thin surface layer during weak surface forcing conditions.

2. **Simulating the vertical turbulent mixing regime —** Turbulent dissipation levels were well replicated in the model in comparison to the MSS sampling. The model performed well in simulating the growth of the BBL and its phase properties, including the phase lag and its asymmetric response over the acceleration and deceleration stages of the tide. The height of the BBL was well reproduced also. Sources of interior mixing were particularly absent, though this was to be expected given the lack of internal wave mixing included in the model. By in large, GOTM is unable to reproduce background stratification levels in stratified conditions in the interior although as was seen in the internal wave parametrisation analysis, by setting an artificially high background TKE rate (k_{min}), the interior representation improved although with a detrimental affect on low turbulent conditions during slack tide (when the natural state of k_{min} was less than the prescribed k_{min}). A lack of stratification in the water column below the thermocline in summer was most likely why no impact of stratification on the BBL was observed on yearday 226. The lack of stratification in the simulation was evident in the profiles of N^2

in comparison to the observation profiles. Strong surface forcing conditions generated significant turbuent mixing in the surface layer that was of the same magnitude as the BBL and contributed significantly to the downward mixing of temperature. The levels of turbulent dissipation in the surface layers matched well with those from MSS sampling. The deepening of the surface mixed layer on yearday 135 with the associated turbulent conditions was well reproduced in the model simulation.

3. **Parameterization of internal wave mixing —** Two applications of internal wave parameterization were tested in this study. The simple case of an empirical limit to the TKE (k) as described by Luyten et al. (1996b) was firstly tested and, secondly, the introduction of an additional source of vertical shear dependent on the level of stratification as established by the buoyancy frequency, as described by Mellor (1989) was investigated. The various parametrisation were not successful in improving the fit of the modelled temperature timeseries to observations in summer. A slight increase in temperature in the timeseries was associated with the Mellor (1989) parametrisation during stratified conditions (yearday 226–228) although it was not enough to cause any significant improvement to the fit to observations. This was further illustrated in a comparison of the vertical structure of temperature between the various internal wave parametrisations and the thermistor mooring. The alternate parametrisation of Luyten et al. (1996b) did not cause a noticeable change in the temperature timeseries in summer although performed better in the interior in respect to the levels of turbulent dissipation rates. However, no noticeable change in the temperatre profiles were observed in this case either.

CHAPTER 7

SYNTHESIS & CONCLUSIONS

This chapter initially synthesizes the main findings of the research in relation to the aims and objectives of this study. The implications of the research on our current understanding of shelf sea mixing is discussed and the conclusions drawn from our results are summarized in the closing remarks.

7.1 Synthesis of Results

The Celtic Sea is a seasonally stratified shelf sea that thermally stratifies in summer in response to the seasonal increase in solar irradiance. The location for this study was chosen in the shallow shelf sea off the north coast of Cornwall. The presence of a seasonal frontal structure was observed in composite SST, which developed in May, remained over the summer, and broke down in Autumn. Empirical analysis of the study site using a 1-D heating-stirring analytical model showed that the location was conducive to a tidal-mixing front given the water depth at the study site (< 80 m), strong tidal currents, and local synoptic-scale meteorological forcing. The aim of this study was to investigate the role of tidal mixing at the site an identify secondary mixing mechanisms that contribute to the evolution of the water column in a manner not consistent with tidally-driven bottom boundary layer (BBL) mixing alone. The collective impact of these processes on the vertical mixing profile is hugely important because of the sensitivity of the water column structure to the form of the mixing profile. In such marginally stratified areas of the shelf sea, the impact of the secondary mixing mechanisms could potentially tip the balance between a well-mixed and stratified water column, with further repercussions to the physical and biological regimes (Holt et al., 2017; Franks, 1992b,a).

7.1.1 Spatio-Temporal Variability at the Study Site

The fieldwork campaign consisted of sampling at two sites, situated either side of the transient front (Figure 5.1). The offshore shore site (St1) was situated at a mean water depth of 65 m and was typically thermally stratified in the near surface region. The typical depth of the thermocline was between 50–60 metres above the bed (mab) as may be seen in the mean temperature profiles in Figures 5.3 & 5.14. In spring, St1 was weakly stratified at both neap and spring tides with the surface layer approximately 0.2 warmer at neap tides and 1.0°C warmer at spring tides. Whereas in summer, the stratification was stronger with the surface layer approximately 2°C warmer during MSS sampling. The

large variability in the surface warm layer between neap and spring tides in the spring season was due to surface forcing generating strong turbulent mixing in the upper water column and mixing the warm water downwards. In summer, the main surface forcing event occurred on yearday 228 and caused a significant change in the water column structure. The outcome of the strong wind forcing was to completely mix the water column. The results of the analysis show that vertical mixing was only partly responsible for the abrupt shift in structure. This was evidenced by the cumulative surface heat input timeseries (Figure 4.21) that did not reproduce the sudden warming, nor the 1-D model simulations that could also not replicate the temperature increase due to the lack of horizontal advection included in the model (Figure 6.7). Furthermore, SST imagery from a few days before and after the event showed a complete change in horizontal structure with the frontal region advancing offshore (Figures 4.32 & 4.34).

The inshore station (St2) was situated at a mean water depth of 35 m and was typically well-mixed during sampling though periods of weak near-surface stratification was present at neap tides. Given the shallow water depth, the predominant mixing mechanism was tidal mixing originating in the frictional turbulent BBL. The growth of the BBL occurred at a quarter-diurnal periodicity associated with the magnitude of current velocity during the flood and ebb tide. Model simulations of St2 in Figure 6.9 and Figure 6.21 show intermittent periods of weak stratification in the near-surface layer, including during the three of the four MSS tidal cycles (excluding yearday 232). This near-surface weak stratification was also observed in the MSS sampling on the same days. These simulations aid in interpreting these results and indicate the source of the warm surface layer to be from periods of increased surface heat input. The simulations show that these were short lived events and that the enhanced turbulent mixing from the BBL and convective mixing rapidly deteriorated the weakly stratified surface layer.

The contrast in the water column structure between the inshore and offshore station was illustrated in the Minibat transects run between the two stations. Transects in both spring and summer seasons show the well-mixed inshore waters separated from the typically stratified offshore waters. The transect on yearday 137 show the inshore waters to be much warmer which was suggested to be due to surface forcing causing the pile up of warm surface waters along the north coast of Cornwall, while the south coast experienced cooler upwelling

water (Figure 4.15). During the transects in summer, a substantial transition in the position of the front was observed in the SST. Such variability was caused by horizontal advection at time scales not associated with tidal excursions. In an attempt to distinguish the cause of such variability, the low-frequency, sub-diurnal, residual currents were extracted from the bed-moored ADCP timeseries and a consistent residual current was observed in both spring and summer with maximum velocities of 9.5 cm s^{-1} in spring and 11 cm s^{-1} during the strong wind event on yearday 228 in summer. A residual current predominantly directed to the east was present in bottom, top and depth-mean residual vectors. The bottom currents were orientated approximately 30–45° to the right of the surface currents with depth-mean average daily speed of 3.5 cm s^{-1} in May and 5.0 cm s^{-1} in August.

A number of possible mechanisms are put forward for the increase in sub-tidal residual velocity observed in summer compared to spring. The direction and magnitude of surface forcing in summer was predominantly directed from the west-southwest, thereby potentially enabling a stronger wind and wave driven flow. Additionally, the stronger density gradients in summer also produce stronger density driven flows, especially in the vicinity of the front, which are known to produce strong frontal jets running parallel to the front. In order to assess the potential contribution of the density driven flow, the thermal wind equation was employed to calculate the geostrophic flow associated with the frontal density gradients recorded in the Minibat transects. The results of the de-tided residual ADCP velocities show that, in some instances, enhanced residuals in the near-surface layer were evident at the point of maximum horizontal density gradients. Although these results were indicative of flow enhancement in relation to the front, the variability in the residual field make it difficult to conclude that what was seen was indeed a frontal jet, rather than potential small-scale baroclinic eddies or instabilities associated with the front.

7.1.2 The Vertical Structure of Turbulent Mixing

In order to differentiate the various forcing mechanisms, the vertical profile of turbulence may be divided into three broad categories depending on their predominant method of forcing. The tidally-driven turbulent BBL is known to have a dominant influence in tidally-driven shelf seas since its forcing mechanism, the barotropic tide, generates a regular frictional shear stress at

the seabed. The magnitude of this shear stress may vary at tidal periodicities though generally remains dominant in tidally-driven shelf seas. Investigation of the turbulent BBL in this study determined the a prevailing M_4 periodicity was present at both the inshore and offshore stations. This was associated with the accelerating and decelerating stages of the predominant M_2 tidal constituent which generated the strongest turbulent dissipation near the bed. Background levels of turbulent dissipation was generally achieved at slack tide. The strength and height of the BBL varied over the neap-spring cycle with the stronger spring tides generating stronger turbulent mixing and a higher BBL. This description characterises what is postulated in the h/U^3 parameter and broadly describes with good accuracy the extent to which tidal mixing controls stratification in tidally-driven shelf seas (Simpson and Hunter, 1974). However, as was evident in this study, the strength and height of the BBL was strongly influenced by the subtle variations in current and water column stratification meaning that this parametrisation is constrained in its application.

The structure of the turbulent BBL was asymmetric over the accelerating and decelerating stages of the tidal cycle. During the acceleration stage, turbulence was generally confined to the near-bed region whilst uniformly increasing with height over the stage. During the deceleration stage, the turbulent BBL continued to grow with elevated turbulent dissipation levels throughout the BBL before an observed decrease in turbulence commencing in the near-bed region. The growth of the BBL typically occurred faster during spring tides, whilst the neap tides had larger phase lags associated with the upward propagation of the BBL (Figures 5.24 & 5.25). The results of this study show that an increase in phase lag in the BBL with height above the bed was evident in seven of the eight tidal cycles (0° was computed for yearday 232 at spring tides at St2). At St1, the neap tide phase lag profile was minimum near the bed but increased more rapidly with height than the spring tide profiles, resulting a larger phase lag than at spring tides by the top of the BBL. The maximum phase lag was 3.25 hours on yearday 135, whilst the equivalent phase lag for spring tides was 1.75–2 hours. The growth of the BBL was curtailed in the stratified water column on yearday 226 though no apparent increase in phase lag relative to the other tidal cycles was evident unlike that reported by Simpson et al. (1996, 2000). A similar situation was evident at St2 with phase lags increasing with height above the bed though the maximum lag remained at 1 hour.

The impact of stratification on the growth of the BBL was most evident on yearday 226 when the interior of the water column was stably stratified. Figure 5.18 showed the impediment of the BBL growth between 0–210° tidal phase as a result of strengthening stratification immediately above the BBL. Figure 7.1 presents a summary of the BBL heights attained during all MSS sampling at both St1 and St2. The BBL height was computed by identifying the maximum gradient in dissipation rates in the outer layer of the BBL. A distinct separation between neap tide and spring tide heights is noticeable at St1 while St2 was typically well-mixed and the BBL height reflected the water column depth. The neap-spring contrast was reflected in the BBL heights calculated using the Weatherly and Martin (1978) formula though the timing of the maximum BBL height was significant different since the Weatherly and Martin (1978) formula was calculated using the friction velocity at the seabed and hence did not account for the observed phase lag. A slight discrepancy in the calculated heights of the BBL was also evident which was primarily due to the water column structure and possible stratification (e.g. yearday 226 (0813), Figure 7.1).

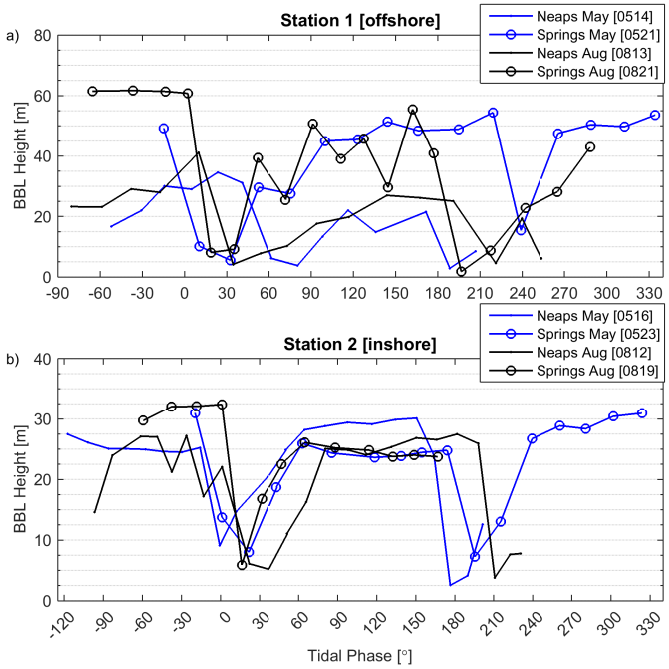

Figure 7.1: *The computed height of the BBL during all MSS tidal cycles at both St1 and St2. The height was computed by identifying the maximum gradient in dissipation rate immediately above the BBL.* ***a)*** *Sampled MSS tidal cycles at St1;* ***b)*** *Sampled MSS tidal cycles at St2.*

Evidence of mixing within the stratified interior was observed during neap

tides in August. NLIW were observed propagating along the thermocline on yearday 225 in two discreet packets producing vertical isotherm displacements of 11 m each with a duration of between 23–26 minutes. The vertical displacement of the isotherms were associated with increased vertical velocities in the thermocline region as measured by the bed-moored ADCP (Figure 4.22). Further spikes in vertical velocity were observed on the following days associated with the downward displacements of the isotherms. One such occasion occurred during MSS sampling on yearday 226.29–226.65 at St1 and was captured in the MSS temperature profiles. These displacements were 8 m and associated with the reduction in tidal velocity at slack tide. Analysis of the NLIW packets on yearday 225 showed that their displacements of the isotherms caused enhanced shear in the thermocline region as well as the reduction of gradient Richardson numbers indicating instability of the water column. The presence of shear instability and stratified turbulence was further indicated by the local increase in ADCP echo intensity during the passage of the NLIW as described by Jones et al. (2014). A distinct lack of interior turbulence ensued in the model simulations that did not account for any interior mixing processes. However, two attempts to parametrise the interior mixing were investigated with discordant results. One method involved an additional source of shear in the turbulence equations dependent of the level of N^2 as implemented by Mellor (1989). This parametrisation promoted a slight diffusion of the thermocline towards the levels observed and also increased temperatures in the interior slightly. However, the temperature timeseries nor profile were proportionate to that observed in-situ (Figure 6.30). The second method employed was that of Luyten et al. (1996b) which set a minimum level of turbulence. In order to sustain a temperature profile proportionate to that observed, background TKE was required to set at a disproportionately high level ($k_{min} = 10^{-4}$ m^2 s^{-2}). Such high TKE levels impaired boundary values during weak turbulent conditions ($k_{BBL} < k_{min}$). As such, no satisfactory parametrisation was established and further investigation is warranted.

7.2 Discussion

The aim of this study was to determine the sensitivity of marginally stratified shelf seas to the key processes that govern turbulent mixing and that contribute to the evolution of the water column in a manner that is not consistent with tidally-driven mixing alone. Numerical modelling studies have identified

a recent trend towards earlier seasonal stratification in temperate shelf seas, with the consequential advancement in the timing of the biological spring bloom (Young and Holt, 2007). Spring air time temperatures are now 1.5°C warmer around the UK and are indicated to be the cause for the earlier onset of stratification, demonstrating the delicate connection between shelf seas and the regional-scale climate (Sharples et al., 2006). An accurate understanding of turbulent mixing processes controlling shelf sea stratification is now essential given that UK climate projections predict strengthening stratification on Northwest European Shelf over this century with a consequential biological implications given the predicted reduction in the vertical nutrient flux across the seasonal thermocline (Sharples et al., 2013). This study is particularly relevant in the present climate given we currently do not fully understand the combined role played by turbulent mixing processes in shelf seas which impact our ability to accurately model these delicately balanced shelf sea systems (Holt and Proctor, 2003; Siddorn and Icarus Allen, 2003; Holt and Umlauf, 2008).

An Assessment of the Fieldwork Campaign

This study set out to collect in-situ observations to determine the hydrodynamic spatio-temporal variability at the study site. In total, a comprehensive fieldwork campaign was mounted sampling spring and summer season regimes at both neap and spring tides. A substantial aspect of the fieldwork campaign was the intensive MSS turbulence profiling which, with eight complete semi-diurnal tidal cycles sampled, consists a large dataset of which not many of the like have been reported in the literature. The coherence in sampling location and variety of conditions (inshore-offshore, neap-springs, spring-summer) made it a successful dataset capable of quantifying turbulent dissipation throughout the water column with great potential for further study. The MSS profiler benefits from two methods of deployment. Firstly, as was employed in this study, the profiler can be deployed at the surface and profiled in a descending mode, capturing the interior and near bed regions. The alternate method consists of tethering the profiler to the seabed and profiling in an ascending manner, which would capture the interior and and near-surface region. Given the influence of surface waves on injecting TKE in the near surface, and being particularly enigmatic despite having long been known to exert an influence on shelf sea mixing, an additional aspect of this study focusing on surface wave mixing would have benefited from the second deployment

method. However, the potential inaccuracies associated with such a deployment would have diminished the usability of the dataset given the difficulty in deploying a tethered profiler to the seabed in such energetic hydrodynamic conditions.

In addition to the MSS sampling, the bed-moored ADCP, thermistor mooring and wave buoy, provided high-resolution timeseries of current velocity, temperature and wave height for a single location situated in between the MSS sampling locations. These timeseries provided a good picture of the temporal evolution of the water column over the neap-spring transition, as well as recording changes due to the shorter-scale synoptic weather events. In retrospect, analysis would have benefited from more conductivity sensors to measure salinity, as well as the thermistor mooring covering the near-surface region. This caused problems when computing the water column heat content and describing the evolution of the surface layer. Surface waves contribute to mixing even when non-breaking although the depth of their intrusion is not well-known (Babanin and Haus, 2009). Here, the thermistor string's high-resolution may have been influential in determining the small-scale convection and turbulent mixing in this near surface layer, significantly expanding the scope of this study in a very pertinent area of research — the impact of non-breaking surface waves on the levels of stratification in a marginally stratified frontal region. This study site is particularly suited in this regard since it is highly exposed to large swell from the Atlantic. Additionally, the observed NLIW packets during the stratified period also highlights the important processes occurring in the interior that may have been better resolved had the thermistor string extended closer to the surface.

In addition, although care was taken to ascertain that the meteorological conditions obtained from Sevenstones were representative of the study site, it was difficult in identifying the finescale variability in wind speed and direction and relating it with near-surface processes due to the time lag between the two sites — it is suggested that a met-station be installed on the wave buoy for future studies. The spatial coverage of the frontal region was obtained from the Minibat surveys which also contained a vessel-mounted ADCP. The vertical dive depth of the Minibat achieved during this study was $\sim$5–20 m which successfully captured the thermocline region ($\sim$10 m) and the waters immediately above and below. As was observed in the transects and subsequently highlighted in the geostrophic velocity calculations, the presence of a bottom

front on yearday 227 (Figure 4.32) would have benefited from a deeper profile. However as is most often the case, the deeper dive depth would have been gained at the expense of horizontal resolution, which given the sharp density gradients in the surface front was considered a priority in this study. All in all, the study objective to collect in-situ observations of the hydrodynamics at the study site was well met with good quality observations detailing the spatio-temporal variability at a marginally stratified location of the Celtic Sea.

An Assessment of the Numerical Simulations

This study also implemented a vertical turbulent mixing model — the General Ocean Turbulence Model (GOTM) — in order to elucidate the results of the in-situ observations and to aid in determining to what extent the site was controlled by vertical turbulent mixing mechanisms or horizontal advective mixing. By selectively tweaking the model forcing mechanisms, for example turning on internal wave parameterization or increasing the background dissipation rates, this model study was somewhat capable of disentangling the complexities observed in-situ.

Initial confirmation that the model produced good results was achieved by comparing the modelled temperature against the thermistor mooring over the period of deployments in spring and summer (Section 6.2.1 & 6.2.2 — Figures 6.1 & 6.6). Results show that in May the rate of temperature increase was well captured by the model although the observed variability, mainly at semi-diurnal periodicity, was absent from the model. Given that variability at a semi-diurnal frequency is highly likely to be advective in nature, as opposed to a quarter diurnal signal which was most likely to be generated by tidal shear stress and hence vertical mixing, the lack of the semi-diurnal signal in the model was expected since no internal pressure gradients simulating advection were prescribed in the model runs. Such quarter-diurnal signals was observed in the in-situ turbulent boundary layer in Chapter 5 which was in phase and controlled by the tidal velocities near the seabed. The similar growth of the BBL was simulated by the model indicating the model was able to also faithfully reproduce the turbulent dynamics of the regular tidal forcing.

In August, the model results comparison was not so successful due to the in-situ temperatures increasing rapidly in comparison to the modelled temperature;

the results from the residual current analysis show that there was a strong residual current during the strong wind event on yearday 228. However, the strong wind event was also observed to generate increased turbulent mixing at the surface thereby increasing the downward heat flux from the surface layer. This strong wind event had three implications: 1) the residual currents responded to both the magnitude and direction of the wind stress; 2) the water column structure was altered for the remainder of the observations with a previously stratified water column revoking to well-mixed conditions; 3) the depth-mean temperature increased rapidly as a result of the downward mixing of warm surface water in conjunction with the lateral advection of the water mass, presumably due to the intensified residual currents.

The Vertical Mixing Regime

The evolution of the turbulent BBL recorded here had many aspects identified previously in other studies. Simpson et al. (1996) identified turbulent dissipation within the BBL to have a significant M_4 periodicity with a pronounced phase lag that increased with height above the bed. In the well-mixed site, the phase lag attained 1.2 hours at 30 mab (total water depth =70 m). In stratified waters, the growth of the M_4 signal was limited in height and the observed phase lag increased to four hours at 37 mab (total water depth =90 m). In contrast to the results of Simpson et al. (1996), the phase lag obtained in this study was $\sim$3.5 hours at St1 (at 37 mab) and $\sim$1 hour (at 30 mab) at St2. What was not made clear in these results was whether the variation in phase lag was due to changes in current velocity or stratification since the neap tide profiles were similar in profile and likewise the spring tide profiles. However, the predominance of the M_4 signal in both this study and Simpson et al. (1996, 2000) was due to the occurrence of degenerate M_2 tidal ellipses and a subsequent rectilinear tidal flow. Phase lags have also been observed in other shelf seas and reported in other studies, including on the Oregon shelf (Perlin et al., 2005), and the Yellow Sea (Zhang and Wu, 2018), as well as other numerical studies (Burchard et al., 1998; Gayen et al., 2010). Furthermore, tidal asymmetry between the accelerating and decelerating stages have also been clearly identified in TKE production and dissipation rates and buoyancy flux (Gayen et al., 2010).

Given these results were reproduced in a vertical turbulence model that did not include turbulent diffusion (i.e. local equilibrium between TKE production and TKE dissipation), the inference for the phase delay was primarily due

to the progressive delay of the turbulent production term with height above the bed (Simpson et al., 1996, 2000). Burchard et al. (2002) concluded that one-equation model underestimated the phase lag in comparison to both the observations and equivalent two-equation model simulations. It was suggested this was due to inaccurate turbulence time scales although they were unsure whether this would affect all one-equation models. However, the general consensus in the literature is that two-equation models, like that used in this study, better represent the phase lag properties and the tidal asymmetry of the turbulent BBL.

The density driven circulation for the Celtic Sea has been reported by Hill et al. (1994). The internal dynamics of fronts have shown the presence of frontal jets and weak cross frontal circulation (Garret and Loder, 1981). Direct observation of frontal jets have been reported by Lwiza et al. (1991); Brown et al. (2003), whilst Simpson et al. (2009) used the thermal wind equation to derive frontal jets of up to 0.2 m s^{-1} from the observed density distribution along the western Irish Sea front. The results of the thermal wind shear and current residuals presented in this study is indicative of a frontal jet though its structure may more transient than that reported along the stronger fronts. In shelf seas, the available potential energy for baroclinic motions is provided by the combination of buoyancy forcing, tidal and wind mixing and is affected by the seasonality in buoyancy forcing (Badin et al., 2009). Shelf sea fronts can become baroclinically unstable causing them to meander and shed eddies on the scale of the internal Rossby radius (Simpson et al., 1978; Hill et al., 1993; Badin et al., 2009). The meandering structure forming a 'tongue'-like feature observed in the SST imagery from yearday 227 suggests the presence of baroclinic instabilities in the front. The characteristic length scale of a baroclinic disturbance is given by the Rossby radius of deformation, $R_d = (g\prime H)^{1/2}/f$, where $g\prime = g\partial\rho/\rho$ is the reduced gravity, H is the depth of the upper layer (based on a two-layer calculation) in stratified waters and f is the Coriolis parameter. The wavelength of the fastest growing disturbance predicted by the stability analysis of Eady is $\lambda_E = 4R_d$, which for yearday 227 was 4×2.2 km $= 8.8$ km. The diameter of the tongue surrounding St1 was approximately 8 km indicating that the frontal structure observed at the study site was potentially at times baroclinically unstable (Simpson et al., 1981).

Two main mechanisms for generating elevated shear along the thermocline

in shelf seas include propagating waves along the isotherms (MacKinnon and Gregg, 2003a; Shroyer et al., 2011) and interfacial shear driven by surface flows (van Haren et al., 1999; MacKinnon and Gregg, 2005). No significant kinetic energy was observed associated with the inertial period during the study and hence the influence of inertial forcing in the surface layer did not attract further attention. This is not to say that inertial forcing was discounted as a candidate mechanism for shelf sea mixing. Significant levels of baroclinic energy at the local inertial period have been reported for seasonally stratified locations in the Celtic Sea (Palmer et al., 2008), the North Sea (Burchard and Rippeth, 2009), and the New England Shelf (MacKinnon and Gregg, 2005).

On the other hand, the presence of NLIW in the thermistor data on yearday 225 suggests turbulence through shear instabilities, most probably generated by the release of lee waves with the interaction of topography irregularities on the nearby bank. Similar observations were made by Klymak and Gregg (2004) on Knight Inlet sill in which water upstream of the sill accumulated in a dense lower layer, lifting the interface upstream, until enough potential energy was gained in the lower layer to release the fluid over the obstacle. The vertical heave related to the release propagates away from the obstacle in the form of internal waves. This hydraulic control was an attractive mechanism given the timing of the NLIW being consistently aligned with the slack tide and the composite internal Froude number reaching super-critical conditions during the passage of the NLIW. Jones et al. (2014) reported a transition from subcritical to supercritical hydraulic flow at the eastern side of Runnelstone Reef (south Cornwall) and the development of a subsequent internal lee wave that was associated with the greatest number of porpoise sightings. The transition between sub- and super-critical flows has been reported to usually be associated with shear instability and turbulent mixing (Moum and Nash, 2000). Although no direct turbulent measurements were made during the passage of the NLIW on yearday 225, the waves were associated with increased vertical shear and reduced gradient Richardson numbers within the thermocline. Furthermore, ADCP echo intensity has been previously used as a proxy for stratified turbulence (van Haren, 2009; Jones et al., 2014; Hosegood et al., 2019) and in these instances the NLIW caused local increases in echo intensity within the thermocline as well.

Following the work of MacKinnon and Gregg (2003a) on the New England

shelf, the interior dissipation rates were evaluated in N^2–S^2 space to determine whether any coherency with the physical properties of the water column were seen. The results of the separate shear and stratification dependence suggested a better fit to the MacKinnon-Gregg scaling as opposed to the alternate scaling considered, the Gregg-Henyey scaling. This appears to be due to the MacKinnon-Gregg scaling having the correct functional dependence on stratification and shear with a better predicted magnitude and variability, where as the Gregg-Henyey scaling was too dependent on decreasing dissipation with increasing stratification. This result was reflected in dye-release experiments that reported the MacKinnon-Gregg scaling was consistent with the diapycnal diffusivities inferred from dye-spreading. Palmer et al. (2008) also found thermocline dissipation rates to suit the MacKinnon-Gregg scaling for the Celtic Sea. Further examples of shelf sea interior dissipation rates fitting the MacKinnon-Gregg scaling better than the open-ocean Gregg-Henyey scaling are found in the literature (e.g. Van Der Lee and Umlauf (2011); Wang et al. (2014)). However, we hesitate to draw any firm conclusions from this since the dissipation rate fit to either parametrization was weak. The presence of high frequency NLIW in our data may point towards a reason for this. The scalings are based upon stable, large-scale, low-mode shear dominating turbulence production, as small-scale internal waves tend to break and dissipate too easily. It may be the case that the energy containing waves at our study site are unstable and hence the open-ocean scaling based upon wave-wave interaction through the internal wave spectrum may not applicable to this data. Given the proximity of the frictional boundary layers, a gradient Richardson number based parametrisation may be warranted in further investigations. The issue of the poor scaling fit has been echoed in Carter et al. (2005) for dissipation measurements on the Monterey shelf. Here, the authors suggest local internal tide generation to be a source of high mode unstable shear making the parametrisation unsuitable for the location.

7.3 Conclusions

In conclusion, the principal findings of this research are:

1. Weak stratification was established in spring ($\Delta T =$) at the offshore site (St1) while the inshore site (St2) was typically well-mixed due to stronger tidal currents combined with a shallower water depth. Weaker tidal forcing allowed limited stratification to develop at the inshore station in summer. During the

more strongly stratified conditions in summer, the transition from stratified to well-mixed waters occurred over the neap-spring cycle although the timing was controlled by strong surface forcing conditions which increased surface mixing and also advected well-mixed waters over the study site.

2. The general water column structure and stratification level was well reproduced in the simulations using a 2-equation, $\kappa - \varepsilon$, turbulence closure model incorporated in the General Ocean Turbulence Model (GOTM). However, given the 1-D vertical setup of the model, it fell short of simulating the advective signals that dominated the semi-diurnal tidal periodicity and summer time transition from stratified to well-mixed waters in response to the significant wind event.

3. The phase lag and tidal asymmetry present in a turbulent bottom boundary layer (BBL) was observed in the turbulent dissipation profiles conducted with the MSS profiler as well as being well reproduced by the 2-equation turbulence model. The phase lag was observed to increase with height above the bed with neap tides generating a larger phase lag at the top of the BBL than at spring tides. The impact of a stratified water column was observed in the maximum height attained by the BBL in summer although there was no observable increase in the phase lag unlike that reported in other turbulent shelf sea BBLs. A lack of an internally stratified water column in the model meant that it did not reproduce the stratification effects on the growth of the BBL.

4. Turbulent dissipation levels in the numerical simulations digressed from that observed in the interior supporting the notion of a missing mixing mechanism. Observations of non-linear internal waves (NLIW) suggested to be generated by hydraulic control and released during the transition from sub-critical to super-critical flow in the form of lee waves point to one candidate mechanism considered here. The vertical displacement of the leading wave was 11 m with the period between successive troughs of approximately 23–36 minutes. Such NLIW have been described to enhance shear and cause turbulent mixing in the thermocline in shelf seas. The passage of the NLIW were observed to increase shear, reduce the gradient Richardson numbers to values less than unity in the thermocline that is indicative of instability, and increase the ADCP echo intensity return which is reported to be indicative of enhanced stratified turbulence.

5. The passage of a synoptic scale wind event controlled the transition from

stratified to well-mixed waters and was observed on previous occasion in the MSS sampling to deepen the surface turbulent mixed layer to within contact with the BBL.

6. Baroclinic residual velocities identified the intensification of surface currents associated with the sharpest frontal gradients. The finescale structure of the residuals suggested baroclinic instabilities at the front, a premise supported by the SST signature of the study site that showed a warm tongue of water extending shoreward that had a diameter ($\sim$8 km) equivalent to the wavelength of the fastest growing disturbances as derived from the Rossby Eady length ($\sim$8.8 km).

7.4 Further Work

This research has identified a number of complex turbulent mixing regimes present at a marginally stratified shelf sea site. However, it became apparent through the course of this research that, by virtue of the complexities themselves, further work is inevitable.

The in-situ observations were an excellent data set and may be used to either investigate questions that were not posed, or advance on what has been interrogated in this study. Alternatively, this study site could benefit from an ongoing, regular fieldwork campaign, for which this fieldwork would form the initial baseline survey. This would be pertinent in regards to the Wave Hub energy extracting site located in the vicinity of the study site. In fact, the choice of study site was in part motivated by the Wave hub since studies have suggested that the energy extraction by wave energy devices would result in a change in surface wave field characteristics with the consequent alterations to the vertical turbulent mixing regime. Concerns raised by stakeholder groups that the energy extraction by the offshore wave farm may lead to reduced wave heights at the shoreline and thus adversely affect the north Cornish coast's economically important surfing industry (Millar et al., 2007; Stokes, 2015).

An extension of the fieldwork is envisaged to include further investigation into the spatial structure of the thermal front using the HF radar data available for the region (Lopez, 2017). Furthermore, the impact of surface wave forcing on the vertical turbulence structure could make use of the application of wave products retrieved from the HF radar in combination with the wave buoy,

ADCP and MSS profiling data to distinguish, for example, the extent to which turbulent mixing from surface wave forcing penetrates through the water column. In such marginally stratified conditions, the additional influence of surface wave mixing so close to the thermocline observed here may prove to be highly influential in controlling the vertical structure. This may also lead to improved parametrisation for surface wave forcing in GOTM. The difficulty remains, however, to appropriately separate the influence of wind forcing from that of the waves.

The impact of an internally stratified water column on the growth of the turbulent BBL was not observed in GOTM since there was too little diffusion across the thermocline and the interior water remained homogeneous. It would be worthwhile investigating the turbulent dissipation structure simulated by GOTM in a stratified water column over the period of a MSS tidal cycle in which the modelled water column structure could be nudged to produce the stratification using the MSS density data. To this end, the influence of stratification as modelled by the variety of 1-equation, 2-equation and the empirical KPP turbulence models may be assessed in relation to observational data.

Finally, in mind of the complexities in the spatial structures observed along the front in summer — and their impact on cross-frontal exchanges and nutrient availability — we propose further spatial surveys either with profiling instruments on Lagrangian floats in order to minimise the advective influence of the semi-diurnal tide or dye-release experiments to quantify the diapycnal fluxes in the vicinity of the front.

Bibliography

Agrawal, Y. C., Terray, E. a., Donelan, M. a., Hwang, P. a., Williams, A. J., Drennan, W. M., Kahma, K. K., and Kitaigorodskii, S. a. (1992). Enhanced dissipation of kinetic energy beneath surface waves. *Nature*, 359:219–220.

Allen, C. M., Simpson, J. H., and Carson, R. (1980). The structure and variability of shelf sea fronts as observed by an undulating CTD system. *Oceanologica Acta*, 3(1):59–68.

Andersen, O. B. (1999). Shallow water tides in the northwest European shelf region from TOPEX/POSEIDON altimetry. *Journal of Geophysical Research*, 104(C4):7729–7741.

Anis, A. and Moum, J. N. (1995). Surface wave-turbulence interactions: scaling epsilon(z) near the sea surface. *Journal of Physical Oceanography*, 25:2025–2045.

Ashton, I., Saulnier, J.-B., and Smith, G. (2013). Spatial variability of ocean waves, from in-situ measurements. *Ocean Engineering*, 57:83–98.

Babanin, A. V. and Haus, B. K. (2009). On the Existence of Water Turbulence Induced by Nonbreaking Surface Waves. *Journal of Physical Oceanography*, 39(10):2675–2679.

Badin, G., Williams, R. G., Holt, J. T., and Fernand, L. J. (2009). Are mesoscale eddies in shelf seas formed by baroclinic instability of tidal fronts? *Journal of Geophysical Research: Oceans*, 114(10):C10021.

Bakun, A. (2006). Fronts and eddies as key structures in the habitat of marine fish larvae: opportunity, adaptive response and competitive advantage. *Scientia Marina*, 70S2(October):105–122.

Batchelor, G. K. (1953). *The theory of homogeneous turbulence*. Cambridge University Press, Cambridge.

Belkin, I. M., Cornillon, P. C., and Sherman, K. (2009). Fronts in Large Marine Ecosystems. *Progress in Oceanography*, 81(1-4):223–236.

Belkin, I. M. and Helber, R. W. (2015). Physical oceanography of fronts: An editorial. *Deep-Sea Research Part II: Topical Studies in Oceanography*, 119:1–2.

Bouffard, D. and Boegman, L. (2013). A diapycnal diffusivity model for stratified environmental flows. *Dynamics of Atmospheres and Oceans*, 61-62:14–34.

Bowers, D. G. and Simpson, J. H. (1987). Mean position of tidal fronts in European-shelf seas. *Continental Shelf Research*, 7(1):35–44.

Bowman, M. J. and Esaias, W. (1981). Fronts, stratification, and mixing in Long Island and Block Island sounds. *Journal of Geophysical Research*, 86(C5):4260–4264.

Bowman, M. J., Kibblewhite, A. C., and Chiswell, S. (1983). Shelf fronts and tidal stirring in Greater Cook Strait , New Zealand. *Oceanologica Acta*, 6(2):119–129.

Bradford, J. M., Lapennas, P. P., Murtagh, R. A., Chang, F. H., and Wilkinson, V. (1986). Factors controlling summer phytoplankton production in greater Cook Strait, New Zealand. *New Zealand Journal of Marine & Freshwater Research*, 20(2):253–279.

Brown, J., Bolaños, R., Howarth, M. J., and Souza, A. J. (2012). Extracting sea level residual in tidally dominated estuarine environments. *Ocean Dynamics*, 62(7):969–982.

Brown, J., Carrillo, L., Fernand, L., Horsburgh, K. J., Hill, A. E., Young, E. F., and Medler, K. J. (2003). Observations of the physical structure and seasonal jet-like circulation of the Celtic Sea and St. George's Channel of the Irish Sea. *Continental Shelf Research*, 23(6):533–561.

Brown, J. and Gmitrowicz, E. M. (1995). Observations of the transverse structure and dynamics of the low frequency flow through the North Channel of the Irish Sea. *Continental Shelf Research*, 15(9):1133–1156.

Burchard, H. (2001). Simulating the Wave-Enhanced Layer under Breaking Surface Waves with Two-Equation Turbulence Models. *Journal of Physical Oceanography*, 31(11):3133–3145.

Burchard, H. and Bolding, K. (2001). Comparative Analysis of Four Second-Moment Turbulence Closure Models for the Oceanic Mixed Layer. *Journal of Physical Oceanography*, 31(8):1943–1968.

Burchard, H., Bolding, K., Rippeth, T. P., Stips, A., Simpson, J. H., and Sündermann, J. (2002). Microstructure of turbulence in the northern North Sea: A comparative study of observations and model simulations. *Journal of Sea Research*, 47(3-4):223–238.

Burchard, H., Bolding, K., and Ruiz Villarreal, M. (1999). GOTM - a general ocean turbulence model. Theory, applications and test cases. Technical report, European Commission.

Burchard, H., Bolding, K., Ruiz Villarreal, M., Rippeth, T. P., Fisher, N. R., and Stips, A. (2005a). The GOTM Modeling System. In Baumert, H. Z., Simpson, J. H., and Sundermann, J., editors, *Marine Turbulence: Theories, Observations and Models*, chapter 25, pages 213–224. Cambridge University Press, Cambridge.

Burchard, H., Craig, P. D., Gemmrich, J. R., van Haren, H., Mathieu, P. P., Meier, H. E. M., Nimmo Smith, W. A. M., Prandke, H., Rippeth, T. P., Skyllingstad, E. D., Smyth, W. D., Welsh, D. J. S., and Wijesekera, H. W. (2008). Observational and numerical modeling methods for quantifying coastal ocean turbulence and mixing. *Progress in Oceanography*, 76(4):399–442.

Burchard, H., Deleersnijder, E., and Stoyan, G. (2005b). Some Numerical Aspects of Turbulence-Closure Models. In Baumert, H. Z., Simpson, J. H., and Sundermann, J., editors, *Marine Turbulence: Theories, Observations and Models*, chapter 23, pages 197–206. Cambridge University Press, Cambridge.

Burchard, H. and Petersen, O. (1999). Models of turbulence in the marine environment - A comparative study of two-equation turbulence models. *Journal of Marine Systems*, 21(1-4):29–53.

Burchard, H., Petersen, O., and Rippeth, T. P. (1998). Comparing the perfor-

mance of the Mellor-Yamada and the κ-ϵ two-equation turbulence models. *Journal of Geophysical Research*, 103(C5):10543.

Burchard, H. and Rippeth, T. P. (2009). Generation of Bulk Shear Spikes in Shallow Stratified Tidal Seas. *Journal of Physical Oceanography*, 39(4):969–985.

Burchard, H., Stips, A., Eifler, W., Bolding, K., and Villarreal, M. (2000). Numerical simulation of dissipation measurements in nonstratified and strongly stratified estuaries.

Burgett, R. L., Hebert, D., and Oakey, N. S. (2001). Vertical structure of turbulence on the southern flank of Georges Bank. *Journal of Geophysical Research: Oceans*, 106(C10):22545–22558.

Canuto, V. M., Howard, A. M., Cheng, Y., and Dubovikov, M. S. (2001). Ocean Turbulence. Part I: One-Point Closure Model - Momentum and Heat Vertical Diffusivities. *Journal of Physical Oceanography*, 31(6):1413–1426.

Carlson, D. F., Muscarella, P. A., Gildor, H., Lipphardt, B. L., and Fredj, E. (2010). How useful are progressive vector diagrams for studying coastal ocean transport. *Limnology and Oceanography: methods*, 8(1989):98–106.

Carpenter, J. R., Merckelbach, L., Callies, U., Clark, S., Gaslikova, L., and Baschek, B. (2016). Potential Impacts of Offshore Wind Farms on North Sea Stratification. *PloS one*, 11(8):1–28.

Carrillo, L., Souza, A. J., Hill, A. E., Brown, J., Fernand, L., and Candela, J. (2005). Detiding ADCP data in a highly variable shelf area: The Celtic Sea. *Journal of Atmospheric and Oceanic Technology*, 22(1):84–97.

Carter, G. S., Gregg, M. C., and Lien, R. C. (2005). Internal waves, solitary-like waves, and mixing on the Monterey Bay shelf. *Continental Shelf Research*, 25(12-13):1499–1520.

Castelao, R., Chant, R., Glenn, S., and Schofield, O. (2010). The Effects of Tides and Oscillatory Winds on the Subtidal Inner-Shelf Cross-Shelf Circulation. *Journal of Physical Oceanography*, 40(4):775–788.

Cox, S., Miller, P. I., Embling, C. B., Scales, K. L., Bicknell, A. W. J., Hosegood, P. J., Morgan, G., Ingram, S., and Votier, S. C. (2016a). Seabird diving

behaviour reveals the functional significance of shelf-sea fronts as foraging hotspots. *Royal Society Open Science*, 3(160317).

Cox, S., Witt, M. J., Embling, C., Godley, B., Hosegood, P. J., Miller, P. I., Votier, S., and Ingram, S. (2016b). Temporal patterns in habitat use by small cetaceans at an oceanographically dynamic marine renewable energy test site in the Celtic Sea. *Deep Sea Research Part II: Topical Studies in Oceanography*, pages 1–13.

Craig, P. D. and Banner, M. L. (1994). Modeling Wave-Enhanced Turbulence in the Ocean Surface Layer.

Cross, J., Nimmo Smith, W. A. M., Hosegood, P. J., and Torres, R. (2015). The Role of Advection in the Distribution of Plankton Populations at a Moored 1-D Coastal Observatory. *Progress in Oceanography*, 137:342–359.

Cushman-Roisin, B. and Beckers, J.-M. (2011). *Introduction to Geophysical Fluid Dynamics - Physical and Numerical Aspects*, volume 101. Academic Press.

D'Asaro, E. A. (2001). Turbulent Vertical Kinetic Energy in the Ocean Mixed Layer. *Journal of Physical Oceanography*, 31(12):3530–3537.

D'Asaro, E. A. and Dairiki, G. T. (1997). Turbulence intensity measurements in a wind-driven mixed layer. *Journal of Physical Oceanography*, 27(9):2009–2022.

D'Asaro, E. A., Thomson, J., Shcherbina, A. Y., Harcourt, R. R., Cronin, M. F., Hemer, M. A., and Fox-Kemper, B. (2014). Quantifying upper ocean turbulence driven by surface waves. *Geophysical Research Letters*, 41(1):102–107.

De Haas, H., Van Weering, T. C. E., and De Stigter, H. (2002). Organic carbon in shelf seas: Sinks or sources, processes and products. *Continental Shelf Research*, 22(5):691–717.

Dewey, R. K., Leblond, P. H., and Crawford, W. R. (1988). The turbulent bottom boundary layer and its influence on local dynamics over the continental shelf. *Dynamics of Atmospheres and Oceans*, 12(2):143–172.

Dietrich, G. (1951). Influences of tidal streams on oceanographic and climatic conditions in the sea as exemplified by the English Channel. *Nature*, 168:8–11.

Dolmer, P. (2000). Algal concentration profiles above mussel beds. *Journal of Sea Research*, 43(2):113–119.

Dye, S., Holliday, N. P., Hughes, S. L., Inall, M., Kennington, K., Smyth, T., Tinker, J., Andres, O., and Beszczynska-Möller, A. (2013). Climate change impacts on the waters around the UK and Ireland: Salinity. Technical Report November 2015, MCCIP.

Edinger, J. E., Duttweiller, D. W., and Geyer, J. C. (1968). The response of water temperatures to meteorological conditions. *Water Resources Research1*, 4(5):1137–1143.

Egbert, G. D. and Erofeeva, S. Y. (2002). Efficient inverse modeling of barotropic ocean tides. *Journal of Atmospheric and Oceanic Technology*, 19(2):183–204.

Egbert, G. D. and Ray, R. D. (2000). Significant Dissipation of Tidal Energy in the Deep Ocean Inferred from Satellite Altimeter Data. *Nature*, 405(1993):775–778.

Ekman, V. W. (1905). On the Influence of the Earth's Rotation on Ocean-Currents.

Emery, W. J. and Thomson, R. E. (2001). *Data Analysis Methods in Physical Oceanography*. Elsevier, Amsterdam, second edition.

Farmer, D. and Armi, L. (1999). Stratified flow over topography: the role of small-scale entrainment and mixing in flow establishment. *Proceedings of the Royal Society A: Mathematical, Physical and Engineering Sciences*, 455(1989):3221–3258.

Farmer, D. and Li, M. (1995). Patterns of Bubble Clouds organized by Langmuir Circulation. *Journal of Physical Oceanography*, 25(6):1426–1440.

Fearnhead, P. G. (1975). On the formation of fronts by tidal mixing around the British Isles. *Deep-Sea Research and Oceanographic Abstracts*, 22(5):311–321.

Franks, P. J. S. (1992a). Phytoplankton blooms at fronts: patterns, scales, and physical forcing mechanisms. *Reviews in Aquatic Sciences*, 6(2):121–137.

Franks, P. J. S. (1992b). Sink or swim: Accumulation of biomass at fronts. *Marine Ecology Progress Series*, 82:1–12.

Frost, M., Baxter, J. M., Buckley, P. J., Cox, M., Dye, S., and Withers Harvey, N. (2012). Impacts of climate change on fish, fisheries and aquaculture. *Aquatic Conservation: Marine and Freshwater Ecosystems*, 22(3):331–336.

Galperin, B., Kantha, L. H., Hassid, S., and Rosati, A. (1988). A Quasi-equilibrium Turbulent Energy Model for Geophysical Flows.

Garret, C. J. R., Keeley, J., and Greenberg, D. A. (1978). Tidal mixing versus thermal stratification in the Bay of Fundy and gulf of Maine. *Atmosphere-Ocean*, 16(4):403–423.

Garret, C. J. R. and Loder, J. W. (1981). Dynamical aspects of shallow sea fronts. *Philosophical Transactions of the Royal Society of London*, A302(September):563–581.

Garret, C. J. R. and Munk, W. (1972). Space-Time Scales of Internal Waves. *Geophysical & Astrophysical Fluid Dynamics*, 3(1):225–264.

Garret, C. J. R. and Munk, W. (1975). Space-time scales of internal waves: a progress report. *Journal of Geophysical Research*, 80:291–297.

Gayen, B., Sarkar, S., and Taylor, J. R. (2010). Large eddy simulation of a stratified boundary layer under an oscillatory current. *Journal of Fluid Mechanics*, 643:233–266.

Glorioso, P. D. and Simpson, J. H. (1994). Numerical modelling of the M2 tide on the northern Patagonian Shelf. *Continental Shelf Research*, 14(2-3):267–278.

Godin, G. (1972). *The Analysis of Tides*. University of Toronto Press, Toronto.

Gómez-Gesteira, M., DeCastro, M., Alvarez, I., Gómez-Gesteira, J. L., Comez-Gesteira, M., DeCastro, M., Alvarez, I., and Gomez-Gesteira, J. L. (2008). Coastal sea surface temperature warming trend along the continental part of the Atlantic Arc. *Journal of Geophysical Research*, 113(4):1–9.

Green, J. A. M., Simpson, J. H., Thorpe, S. A., and Rippeth, T. P. (2010). Observations of internal tidal waves in the isolated seasonally stratified region of the western Irish Sea. *Continental Shelf Research*, 30(2):214–225.

Gregg, M. C. (1989). Scaling turbulent dissipation in the thermocline. *Journal of Geophysical Research*, 94(C7):9686–9698.

Hardisty, J. (1990). *The British Seas: An introduction to the oceanography and resources of the north-west European continental shelf.* Routledge, New York, 1 edition.

Heinz, S. and Roekaerts, D. (2001). Reynolds number elects on mixing and reaction in a turbulent pipe flow. *Chemical Engineering Science*, 56:3197–3210.

Henyey, F. S., Wright, J., and Flatte, S. M. (1986). Energy and action flow through the internal wave field: An eikonal approach. *Journal of Geophysical Research: Oceans*, 91(C7).

Hickman, A. E., Moore, C. M., Sharples, J., Lucas, I. M., Tilstone, G. H., Krivtsov, V., and Holligan, P. M. (2012). Primary production and nitrate uptake within the seasonal thermocline of a stratified shelf sea. *Marine Ecology Progress Series*, 463:39–57.

Hill, A. E., Brown, J., Fernand, L., Holt, J. T., Horsburgh, K. J., Proctor, R., Raine, R., and Turrell, W. R. (2008). Thermohaline circulation of shallow tidal seas. *Geophysical Research Letters*, 35(11):L11605.

Hill, A. E., Durazo, R., and Smeed, D. A. (1994). Observations of a cyclonic gyre in the western Irish Sea. *Continental Shelf Research*, 14(5):479–490.

Hill, A. E., Horsburgh, K. J., Garvine, R., Gillibrand, P., Slesser, G., Turrell, W. R., and Adams, R. (1997). Observations of a Density-driven Recirculation of the Scottish Coastal Current in the Minch. *Estuarine, Coastal and Shelf Science*, 45(4):473–484.

Hill, A. E., James, I. D., Linden, P. F., Matthews, J. P., Prandle, D., Simpson, J. H., Gmitrowicz, E. M., Smeed, D. A., Lwiza, K. M. M., Durazo, R., Fox, A. D., Bowers, D. G., and Weydert, M. (1993). Dynamics of Tidal Mixing Fronts in the North Sea [and Discussion]. *Philosophical Transactions of the Royal Society of London A: Mathematical, Physical and Engineering Sciences*, 343(1669):431–446.

Holford, J. and Linden, P. (1999). Turbulent mixing in a stratified fluid. *Dynamics of atmospheres and oceans*, 30:173–198.

Holligan, P. M. (1984). Vertical distribution and partitioning of organic carbon in mixed, frontal and stratified waters of the English Cannel. *Marine Ecology Progress Series*, 14:111–127.

Holt, J. T., Hyder, P., Ashworth, M., Harle, J., Hewitt, H. T., Liu, H., New, A. L., Pickles, S., Porter, A., Popova, E., Icarus Allen, J., Siddorn, J. R., and Wood, R. (2017). Prospects for improving the representation of coastal and shelf seas in global ocean models. *Geoscientific Model Development*, 10(1):499–523.

Holt, J. T., Icarus Allen, J., Proctor, R., and Gilbert, F. (2005). Error quantification of a high-resolution coupled hydrodynamicâ€“ecosystem coastalâ€“ocean model: Part 1 model overview and assessment of the hydrodynamics. *Journal of Marine Systems*, 57(1-2):167–188.

Holt, J. T. and Proctor, R. (2003). The Role of Advection in Determining the Temperature Structure of the Irish Sea. *Journal of Physical Oceanography*, 33(11):2288–2306.

Holt, J. T. and Proctor, R. (2008). The seasonal circulation and volume transport on the northwest European continental shelf: A fine-resolution model study. *Journal of Geophysical Research: Oceans*, 113(6).

Holt, J. T. and Umlauf, L. (2008). Modelling the tidal mixing fronts and seasonal stratification of the Northwest European Continental shelf. *Continental Shelf Research*, 28(7):887–903.

Holt, J. T., Wakelin, S., Lowe, J. A., and Tinker, J. (2010). The potential impacts of climate change on the hydrography of the northwest European continental shelf. *Progress in Oceanography*, 86(3-4):361–379.

Horsburgh, K. J., Hill, A. E., and Brown, J. (1998). A Summer Jet in the St George's Channel of the Irish Sea. *Estuarine , Coastal and Shelf Science*, 47(3):285–294.

Horsburgh, K. J., Hill, A. E., Brown, J., Fernand, L., Garvine, R. W., and Angelico, M. M. P. (2000). Seasonal Evolution of the cold pool gyre in the western Irish Sea. *Progress in Oceanography*, 46(1):1–58.

Horwitz, R. M. and Lentz, S. J. (2016). The effect of wind direction on cross-shelf transport on an initially stratified inner shelf. *Journal of Marine Research*, 74:201–227.

Hosegood, P. J., Nimmo-smith, W. A. M., Proud, R., Adams, K., and Brierley, A. S. (2019). Internal lee waves and baroclinic bores over a tropical seamount shark hotspot. *Progress in Oceanography*, 172:34–50.

Hosegood, P. J. and van Haren, H. (2003). Ekman-induced turbulence over the continental slope in the Faeroe-Shetland Channel as inferred from spikes in current meter observations. *Deep-Sea Research Part I: Oceanographic Research Papers*, 50(5):657–680.

Howarth, M. J. (1975). Current surges in St George's Channel. *Estuarine, Coastal and Shelf Science*, 3:57–70.

Howarth, M. J., Simpson, J. H., Sündermann, J., and Van Haren, H. (2002). Processes of vertical exchange in shelf seas (PROVESS). *Journal of Sea Research*, 47(3-4):199–208.

Hub, W. (2006). The wave power climate at the Wave Hub site. Technical Report November, SWRDA.

Huisman, J., Sharples, J., Stroom, J. M., Visser, P. M., Kardinaal, W. E. A., Verspagen, J. M., and Sommeijer, B. (2004). Changes in turbulent mixing shift competition for light between phytoplankton species. *Ecology*, 85(11):2960–2970.

Huthnance, J. M., Coelho, H., Griffiths, C. R., Knight, P. J., Rees, A. P., Sinha, B., Vangriesheim, A., White, M., and Chatwin, P. G. (2001). Physical structures, advection and mixing in the region of Goban Spur. *Deep-Sea Research Part II: Topical Studies in Oceanography*, 48(14-15):2979–3021.

Icarus Allen, J., Siddorn, J. R., Blackford, J. C., and Gilbert, F. J. (2004). Turbulence as a control on the microbial loop in a temperate seasonally stratified marine systems model. *Journal of Sea Research*, 52(1):1–20.

Jones, A. R., Hosegood, P. J., Wynn, R. B., De Boer, M. N., Butler-Cowdry, S., and Embling, C. B. (2014). Fine-scale hydrodynamics influence the spatio-temporal distribution of harbour porpoises at a coastal hotspot. *Progress in Oceanography*, 128:30–48.

Kantha, L. H. and Clayson, C. A. (1994). An improved mixed layer model for geophysical applications. *Journal of Geophysical Research*, 99:25235–25266.

Klymak, J. M. and Gregg, M. C. (2004). Tidally generated turbulence over the Knight Inlet Sill. *Journal of Physical Oceanography*, 34(5):1135–1151.

Kolmogorov, A. N. (1991). The local structure of turbulence in incompressible

viscous fluid for very large Reynolds numbers. *Proceedings of the Royal Society of London A*, 434:9–13.

Korotenko, K. A., Sentchev, A., Schmitt, F. G., and Jouanneau, N. (2013). Variability of turbulent quantities in the tidal bottom boundary layer: Case study in the eastern English Channel. *Continental Shelf Research*, 58:21–31.

Kukulka, T., Plueddemann, A. J., Trowbridge, J. H., and Sullivan, P. P. (2009). Significance of Langmuir circulation in upper ocean mixing: Comparison of observations and simulations. *Geophysical Research Letters*, 36(10):2–6.

Kurapov, A. L., Allen, J. S., Egbert, G. D., Miller, R. N., Kosro, P. M., Levine, M., and Boyd, T. (2005). Distant effect of assimilation of moored currents into a model of coastal wind-driven circulation off Oregon. *Journal of Geophysical Research C: Oceans*, 110(2):1–20.

Kwong, S. C. M., Davies, A. M., and Flather, R. A. (1997). A three-dimensional model of the principal tides on the European shelf. *Progress in Oceanography*, 39(3):205–262.

Langmuir, I. (1938). Surface Motion of Water Induced By Wind.

Lapworth, A. and McGregor, J. (2008). Seasonal variation of the prevailing wind direction in Britain. *Weather*, 63(12):361–364.

Large, W. G. and Pond, S. (1981). Open ocean momentum flux measurements in moderate to strong winds. *Journal of Physical Oceanography*, 11:324–336.

Lawrence, G. A. (1990). On the hydraulics of boussinesq and non-boussinesq two-layer flows. *Journal of Fluid Mechanics*, 215:457–480.

Le Boyer, A., Cambon, G., Daniault, N., Herbette, S., Le Cann, B., Mari??, L., and Morin, P. (2009). Observations of the Ushant tidal front in September 2007. *Continental Shelf Research*, 29(8):1026–1037.

Lee, M.-a., Chang, Y., and Shimada, T. (2015). Seasonal evolution of fine-scale sea surface temperature fronts in the East China Sea. *Deep Sea Research Part II: Topical Studies in Oceanography*, 119:20–29.

Lentz, S. J. (2001). The Influence of Stratification on the Wind-Driven Cross-Shelf Circulation over the North Carolina Shelf*. *Journal of Physical Oceanography*, 31(9):2749–2760.

Lentz, S. J. and Trowbridge, J. H. (1991). The Bottom Boundary Layer over the Northern Californian Shelf.

Li, M., Zahariev, K., and Garret, C. J. R. (1995). Role of Langmuir Circulation in the Deepening of the Ocean Surface Mixed Layer. *Science*, 270(5244):1955–1957.

Loder, J. W. and Greenberg, D. A. (1986). Predicted position of tidal fronts in the Gulf of Maine. *Continental Shelf Research*, 83(3):4615–4622.

Lopez, G. (2017). *Evaluation, analysis, and application of the HF Radar Wave and Current Measurments*. Phd thesis, University of Plymouth.

Lorke, A., Umlauf, L., Jonas, T., and Wüest, A. (2002). Dynamics of turbulence in low-speed oscillating bottom-boundary layers of stratified basins. *Environmental Fluid Mechanics*, 2(4):291–313.

Lowe, J. A., Howard, T. P., Pardaens, A., Tinker, J., Holt, J. T., Wakelin, S., Milne, G., Leake, J., Wolf, J., Horsburgh, K. J., Reeder, T., Jenkins, G., Ridley, J., Dye, S., and Bradley, S. (2009). *Changes to mean sea level*. Met Office Hadley Centre, Exeter, UK.

Lueck, R. G. (2005). Horizontal and vertical turbulence profilers. In Baumert, H. Z., Simpson, J. H., and Sundermann, J., editors, *Marine Turbulence: Theories, Observations and Models*, chapter 11, pages 89–100. Cambridge University Press, Cambridge.

Luyten, P. J., Deleersnijder, E., Ozer, J., and Ruddick, K. G. (1996a). Presentation of a family of turbulence closure models for stratified shallow water flows and preliminary application to the Rhine outflow region. *Continental Shelf Research*, 16:101–130.

Luyten, P. J., Simpson, J. H., and Rippeth, T. P. (1996b). Comparison of turbulence models for homogenous and stratified flows with turbulence measurements in the Irish Sea. In *MAST Workshop on Turbulence Modelling*, Bergen, Norway.

Luznik, L., Zhu, W., Gurka, R., Katz, J., Nimmo Smith, W. a. M., and Osborn, T. R. (2007). Distribution of Energy Spectra, Reynolds Stresses, Turbulence Production, and Dissipation in a Tidally Driven Bottom Boundary Layer. *Journal of Physical Oceanography*, 37(6):1527–1550.

Lwiza, K. M. M., Bowers, D. G., and Simpson, J. H. (1991). Residual and tidal flow at a tidal mixing front in the North Sea. *Continental Shelf Research*, 11(11):1379–1395.

MacKinnon, J. A. and Gregg, M. C. (2003a). Mixing on the Late-Summer New England Shelfâ€"Solibores, Shear, and Stratification. *Journal of Physical Oceanography*, 33(7):1476–1492.

MacKinnon, J. A. and Gregg, M. C. (2003b). Shear and Baroclinic Energy Flux on the Summer New England Shelf. *Journal of Physical Oceanography*, 33(7):1462–1475.

MacKinnon, J. A. and Gregg, M. C. (2005). Near-Inertial Waves on the New England Shelf: The Role of Evolving Stratification, Turbulent Dissipation, and Bottom Drag. *Journal of Physical Oceanography*, 35(12):2408–2424.

Masselink, G., Austin, M. J., Scott, T., Poate, T., and Russell, P. (2014). Role of wave forcing, storms and NAO in outer bar dynamics on a high-energy, macro-tidal beach. *Geomorphology*, 226:76–93.

Matthews, D. J. (1911). Report on the physical conditions in the English Channel and adjacent waters, 1906, with a note on the mean conditions for 1903-1909. Technical report, Marine Biological Association.

Mellor, G. L. (1989). Retrospect on oceanic boundary layer modelling and second moment closure. In Muller, editor, *Parametrization of Small-scale processes*, pages 251–272, Honolulu.

Mellor, G. L. and Yamada, T. (1982). Development of a turbulence closure model for geophysical fluid problems. *Reviews of Geophysics*, 20(4):851–875.

Millar, D. L., Smith, H. C., and Reeve, D. E. (2007). Modelling analysis of the sensitivity of shoreline change to a wave farm. *Ocean Engineering*, 34(5-6):884–901.

Miller, P. I. (2009). Composite front maps for improved visibility of dynamic sea-surface features on cloudy SeaWiFS and AVHRR data. *Journal of Marine Systems*, 78(3):327–336.

Miller, P. I. (2011). Detection and visualisation of oceanic fronts from satellite data, with applications for fisheries, marine megafauna and marine protected areas. In Morales, J., Stuart, V., Platt, T., and Sathyendranath,

S., editors, . . . *Applications for Marine Living Resources Conservation . . .*, chapter 16, pages 229–239. EU PRESPO, Darthmouth, Canada.

Moum, J. N., Gregg, M. C., Lien, R. C., and Carr, M. E. (1995). Comparison of Turbulence Kinetic Energy Dissipation Rate Estimates from Two Ocean Microstructure Profilers.

Moum, J. N., Nash, J., and Klymak, J. (2008). Small-Scale Processes in the Coastal Ocean. *Oceanography*, 21(4):22–33.

Moum, J. N. and Nash, J. D. (2000). Topographically Induced Drag and Mixing at a Small Bank on the Continental Shelf. *Journal of Physical Oceanography*, 30(8):2049–2054.

Muller-Karger, F. E., Varela, R., Thunell, R., Luerssen, R., Hu, C., and Walsh, J. J. (2005). The importance of continental margins in the global carbon cycle. *Geophysical Research Letters*, 32(1):1–4.

Munk, W. and Wunsch, C. (1998). Abyssal recipes II: Energetics of tidal and wind mixing. *Deep-Sea Research Part I: Oceanographic Research Papers*, 45(12):1977–2010.

Nystrom, E. and Oberg, K. (2002). Measurement of turbulence with acoustic doppler current profilers - sources of error and laboratory results. *Hydraulic Measurements and Experimental Methods*, 55:1–10.

Osborn, T. R. (1974). Vertical profiling of velocity microstructure. *Journal of Physical Oceanography*, 4(1):109–115.

Osborn, T. R. (1980). Estimates of the Local Rate of Vertical Diffusion from Dissipation Measurements.

Palmer, M. R., Rippeth, T. P., and Simpson, J. H. (2008). An investigation of internal mixing in a seasonally stratified shelf sea. *Journal of Geophysical Research: Oceans*, 113(12):1–14.

Paskyabi, M. B. and Fer, I. (2010). Ocean near-surface boundary layer : processes and turbulence measurements. Technical report, University of Bergen.

Pauly, D., Christensen, V., Guénette, S., Pitcher, T. J., Sumaila, U. R., Walters, C. J., Watson, R., and Zeller, D. (2002). Towards sustainability in world fisheries. *Nature*, 418(6898):689–695.

Pemberton, K., Rees, A. P., Miller, P. I., Raine, R., and Joint, I. (2004). The influence of water body characteristics on phytoplankton diversity and production in the Celtic Sea. *Continental Shelf Research*, 24(17):2011–2028.

Perlin, A., Moum, J. N., Klymak, J. M., Levine, M. D., Boyd, T., and Kosro, P. M. (2005). A modified law-of-the-wall applied to oceanic bottom boundary layers. *Journal of Geophysical Research C: Oceans*, 110(10):1–9.

Pingree, R. D. (1980). Physical Oceanography of the Celtic Sea and English Channel. In Banner, F., Collins, M., and Massie, K., editors, *The North-West European shelf seas: The sea bed and the Sea in motion. Physical and Chemical Oceanography and Physical Resources*, chapter 13, pages 415–465. Elsevier Ltd, Amsterdam.

Pingree, R. D. and Griffiths, D. K. (1978). Tidal fronts on the shelf seas around the British Isles. *Journal of Geophysical Research*, 83(C9):4615.

Pingree, R. D., Holligan, P. M., Mardell, G. T., and Head, R. (1976). The Influence of Physical Stability on Spring, Summer and Autumn Phytoplankton Blooms in the Celtic Sea. *Journal of the Marine Biological Association of the United Kingdom*, 56:845–873.

Pisoni, J. P., Rivas, A. L., and Piola, A. R. (2015). On the variability of tidal fronts on a macrotidal continental shelf, Northern Patagonia, Argentina. *Deep-Sea Research Part II: Topical Studies in Oceanography*, 119:61–68.

Plueddemann, A. J., Smith, J. a., Farmer, D., Weller, R. a., Crawford, W. R., Pinkel, R., Vagle, S., and Gnanadesikan, A. (1996). Structure and variability of Langmuir circulation during the Surface Waves Processes Program. *Journal of Geophysical Research*, 101(C2):3525.

Polzin, K. L. and Montgomery, E. (1998). Microstructure profiling with the High Resolution Profiler. Technical report, Woods Hole Oceanographic Institution.

Polzin, K. L., Toole, J. M., and Schmitt, R. W. (1995). Finescale parametrizations of turbulent dissipation. *J. Phys. Oceanogr.*, 25(November):306–328.

Pope, S. B. (2000). *Turbulent Flows*. Cambridge University Press.

Prandke, H. (2009a). Microstructure Profiler MSS90 Operating Instructions and User's Manual. Technical report, ISW Wassermesstechnik, Sun & Sea Technology.

Prandke, H. (2009b). MSSpro microstructure data evaluation tool user manual - version 1.21. Technical report, ISW Wassermesstechnik.

Prandke, H., Holtsch, K., and Stips, A. (2000). MITEC technology development: the microstructure/turbulence measuring system MSS. Technical report, Space Applications Institute.

Prandle, D. (1982). The vertical structure of tidal currents and other oscillatory flows. *Continental Shelf Research*, 1(2):191–207.

Prestidge, M. C. and Taylor, A. H. (1995). A modeling investigation of the distribution of stratification and phytoplankton abundance in the Irish Sea. *Journal of Plankton Research*, 17(7):1397–1420.

RDInstruments (1996). Principles of operation. A practical primer. Technical report, RD Instruments, San Diego.

RDInstruments (2009). Workhorse Monitor Datasheet. Technical report, RD Instruments, San Diego.

Reeve, D. E., Chen, Y., Pan, S., Magar, V., Simmonds, D. J., and Zacharioudaki, A. (2011). An investigation of the impacts of climate change on wave energy generation: The Wave Hub, Cornwall, UK. *Renewable Energy*, 36(9):2404–2413.

Rippeth, T. P. (2005). Mixing in seasonally stratified shelf seas: a shifting paradigm. *Philosophical transactions. Series A, Mathematical, physical, and engineering sciences*, 363(1837):2837–2854.

Rippeth, T. P. and Inall, M. (2002). Observations of the internal tide and associated mixing across the Malin Shelf. *Journal of Geophysical Research*, 107(C4):3028.

Rippeth, T. P. and Meier, H. M. (2005). The four shelf-sea regimes. In Baumert, H., Simpson, J. H., and Sündermann, J., editors, *Marine Turbulence: Theories, Observations and Models*, chapter 46, pages 369–375. Cambridge University Press, Cambridge.

Rippeth, T. P., Palmer, M. R., Simpson, J. H., Fisher, N. R., and Sharples, J. (2005). Thermocline mixing in summer stratified continental shelf seas. *Geophysical Research Letters*, 32(5):1–4.

Rippeth, T. P., Simpson, J. H., Player, R. J., and Garcia, M. (2002). Current

oscillations in the diurnal-inertial band on the Catalonian shelf in spring. *Continental Shelf Research*, 22(2):247–265.

Rivas, A. L. and Pisoni, J. P. (2010). Identification, characteristics and seasonal evolution of surface thermal fronts in the Argentinean Contiental Shelf. *Journal of Marine Systems*, 79:134–143.

Rodi, W. (1980). Turbulence models and their applications in hydraulics. Technical report, International Association for Hydraulic Research, Delft.

Rodi, W. (1987). Examples of calculation methods for flow and mixing in stratified fluids. *Journal of Geophysical Research: Oceans*, 92(C5):5305–5328.

Ross, O. N. and Sharples, J. (2008). Swimming for survival: A role of phytoplankton motility in a stratified turbulent environment. *Journal of Marine Systems*, 70(3-4):248–262.

Schumacher, J. D., Kinder, T. H., Pashinski, D. J., and Charnell, R. L. (1979). A Structural Front Over the Continental Shelf of the Eastern Bering Sea. *Journal of Physical Oceanography*, 9(1):79–87.

Scully, M. E. and Friedrichs, C. T. (2007). The Importance of Tidal and Lateral Asymmetries in Stratification to Residual Circulation in Partially Mixed Estuaries*. *Journal of Physical Oceanography*, 37(1994):1496–1511.

Sharples, J. (2008). Potential impacts of the spring-neap tidal cycle on shelf sea primary production. *Journal of Plankton Research*, 30(2):183–197.

Sharples, J. and Dye, S. (2008). Shelf Sea Stratification and the Spring Bloom. *Mccip.Org.Uk*, pages 1–5.

Sharples, J., Holt, J. T., and Dye, S. (2010). MCCIP ARC Science Review 2010-11 Shelf Sea Stratification. Technical report, MCCIP Science Review.

Sharples, J., Holt, J. T., and Dye, S. (2013). Impacts of climate change on shelf sea stratification. *MCCIP Science Review*, pages 67–70.

Sharples, J., Moore, M. C., Rippeth, T. P., Holligan, P. M., Hydes, D. J., Fisher, N. R., and Simpson, J. H. (2001). Phytoplankton distribution and survival in the thermocline. *Limnology and Oceanography*, 46(3):486–496.

Sharples, J., Ross, O. N., Scott, B. E., Greenstreet, S. P. R., and Fraser, H. (2006).

Inter-annual variability in the timing of stratification and the spring bloom in the North-western North Sea. *Continental Shelf Research*, 26(6):733–751.

Sharples, J. and Simpson, J. H. (1993). Periodic Frontogenesis in a Region of Freshwater Influence. *Estuaries*, 16(1):74.

Shi, R., Guo, X., Wang, D., Zeng, L., and Chen, J. (2015). Seasonal variability in coastal fronts and its influence on sea surface wind in the Northern South China Sea. *Deep Sea Research Part II: Topical Studies in Oceanography*, 119(1987):30–39.

Shirahata, K., Yoshimoto, S., Tsuchihara, T., and Ishida, S. (2016). Digital filters to eliminate or separate tidal components in groundwater observation time-series data. *Japan Agricultural Research Quarterly*, 50(3):241–252.

Shroyer, E. L., Moum, J. N., and Nash, J. D. (2011). Nonlinear internal waves over New Jersey's continental shelf. *Journal of Geophysical Research: Oceans*, 116(3):1–16.

Siddorn, J. R. and Icarus Allen, J. (2003). Surface heat fluxes and ecosystem function in the Cretan Sea (eastern Mediterranean): a modelling study. *Annales Geophysicae*, 21:377–388.

Simpson, J. H. (1997). Physical processes in the ROFI regime. *Journal of Marine Systems*, 12(1-4):3–15.

Simpson, J. H., Allen, C. M., and Morris, N. C. G. (1978). Fronts on the continental shelf. *Journal of Geophysical Research*, 83(8):4607.

Simpson, J. H. and Bowers, D. G. (1981). Models of stratification and frontal movement in shelf seas. *Deep Sea Research Part A, Oceanographic Research Papers*, 28(7):727–738.

Simpson, J. H. and Bowers, D. G. (1984). The role of tidal stirring in controlling the seasonal heat cycle in shelf seas. *Annales Geophysicae*, 2:411–416.

Simpson, J. H., Burchard, H., Fisher, N. R., and Rippeth, T. P. (2002). The semi-diurnal cycle of dissipation in a ROFI: Model-measurement comparisons. *Continental Shelf Research*, 22(11-13):1615–1628.

Simpson, J. H., Crawford, W. R., Rippeth, T. P., Campbell, A. R., and Cheok, J. V. S. (1996). The Vertical Structure of Turbulent Dissipation in Shelf Seas. *Journal of Physical Oceanography*, 26(8):1579–1590.

Simpson, J. H., Crisp, D. J., and Hearn, C. (1981). The Shelf-Sea Fronts: Implications of their Existence and Behaviour [and Discussion]. *Philosophical Transactions of the Royal Society A: Mathematical, Physical and Engineering Sciences*, 302(1472):531–546.

Simpson, J. H., Green, J. A. M., Rippeth, T. P., Osborn, T. R., and Nimmo Smith, W. A. M. (2009). The structure of dissipation in the western Irish Sea front. *Journal of Marine Systems*, 77(4):428–440.

Simpson, J. H., Hughes, D. G., and Morris, N. C. G. (1977). The relation of seasonal stratification to tidal mixing on the continental shelf. In Angel, M. V., editor, *A Voyage of Discovery George Deacon 70th anniversary volume*, pages 327–340. Pergamon Press, London.

Simpson, J. H. and Hunter, J. R. (1974). Fronts in the Irish Sea. *Nature*, 250(5465):404–406.

Simpson, J. H. and Pingree, R. D. (1978). Shallow sea fronts produced by tidal stirring. In Bowman, M. J. and Esaias, W. E., editors, *Oceanic fronts in coastal processes*, pages 29–42. Springer-Verlag, Berlin.

Simpson, J. H., Rippeth, T. P., and Campbell, A. R. (2000). The phase lag of turbulent dissipation in tidal flow. *Interactions between Estuarise, Coastal Seas and Shelf Seas*, pages 57–67.

Simpson, J. H. and Sharples, J. (1994). Does the Earth's rotation influence the location of the shelf sea fronts? *Journal of Geophysical Research*, 99(C2):3315–3319.

Simpson, J. H. and Sharples, J. (2012). *Introduction to the Physical and Biological Oceanography of Shelf Seas*. Cambridge University Press, Cambridge.

Simpson, J. H., Tett, P. B., Argote-Espinoza, M. L., Edwards, A., Jones, K. J., and Savidge, G. (1982). Mixing and phytoplankton growth around an island in a stratified sea. *Continental Shelf Research*, 1(1):15–31.

Simpson, J. H. and Tinker, J. (2009). A test of the influence of tidal stream polarity on the structure of turbulent dissipation. *Continental Shelf Research*, 29(1):320–332.

Skyllingstad, E. D., Smyth, W. D., and Crawford, G. B. (2000). Resonant

Wind-Driven Mixing in the Ocean Boundary Layer. *Journal of Physical Oceanography*, 30(8):1866–1890.

Smith, J. A. (1992). Observed growth of Langmuir circulation. *Journal of Geophysical Research: Oceans*, 97(C4):5651–5664.

Soloviev, A. and Lukas, R. (2003). Observation of wave-enhanced turbulence in the near-surface layer of the ocean during TOGA COARE. *Deep-Sea Research Part I: Oceanographic Research Papers*, 50(3):371–395.

Sommer, U. and Lengfellner, K. (2008). Climate change and the timing, magnitude, and composition of the phytoplankton spring bloom. *Global Change Biology*, 14(6):1199–1208.

Soulsby, R. L. (1983). The bottom boundary layer of shelf seas. In Johns, B., editor, *Physical Oceanography of Coastal and Shelf Seas*, pages 189–266. Elsevier Oceanography Series, Amsterdam.

Stigebrandt, A. (1988). A note on the locus of a shelf front. *Tellus A*, pages 439–442.

Stigebrandt, A. and Aure, J. (1989). Vertical mixing in basin waters of fjords. *Journal of Physical Oceanography*, 19:917–926.

Stillinger, D. C., Helland, K. N., and Van Atta, W. C. (1983). Experiments on the transition of homogeneous turbulence to internal waves in a stratified fluid. *Journal of Fluid Mechanics*, 131:91–122.

Stips, A. (2005). Dissipation Measurement: theory. In Baumert, H. Z., Simpson, J. H., and Sundermann, J., editors, *Marine Turbulence: Theories, Observations and Models*, chapter 14, pages 115–126. Cambridge University Press, Cambridge.

Stips, A., Burchard, H., Bolding, K., Prandke, H., Simon, A., and W??est, A. (2005). Measurement and simulation of viscous dissipation in the wave affected surface layer. *Deep-Sea Research Part II: Topical Studies in Oceanography*, 52(9-10 SPEC. ISS.):1133–1155.

Stokes, C. H. (2015). *Coastal impacts in the lee of a wave energy site: waves, beach morphology and water-users (Wave Hub, Cornwall, UK)*. PhD thesis, University of Plymouth.

Sverdrup, H. (1953). On conditions for the vernal blooming of phytoplankton. *Journal du Conseil*, 18(3):287–295.

Taylor, J. R. and Sarkar, S. (2008). Stratification Effects in a Bottom Ekman Layer. *Journal of Physical Oceanography*, 38(11):2535–2555.

Tennekes, H. and Lumley, J. L. (1972). *First Course in Turbulence*. MIT Press, Cambridge.

Terray, E. a., Donelan, M. a., Agrawal, Y. C., Drennan, W. M., Kahma, K. K., Williams, a. J., Hwang, P. a., and Kitaigorodskii, S. a. (1996). Estimates of kinetic energy dissipation under breaking waves. *Journal Of Physical Oceanography*, 26(5):792–807.

Tett, P. B. (1981). Modelling phytoplankton production at shelf-sea fronts. *Philosophical Transactions of the Royal Society London A*, 302(May 2014):605–615.

Thiel, M., Hinojosa, I. A., Joschko, T., and Gutow, L. (2011). Spatio-temporal distribution of floating objects in the German Bight (North Sea). *Journal of Sea Research*, 65(3):368–379.

Thomas, H., Bozec, Y., Elkalay, K., and Baar, H. J. W. D. (2004). Enhanced Open Ocean Storage of CO2 from Shelf Sea Pumping. *Science*, 304(5673):1–5.

Thorpe, S. A. (2005). *The turbulent ocean*. Cambridge University Press, Cambridge.

Tilburg, C. E. (2003). Across-Shelf Transport on a Continental Shelf: Do Across-Shelf Winds Matter? *Journal of Physical Oceanography*, 33(12):2675–2688.

Townsend, D. W., Cammen, L. M., Holligan, P. M., Campbell, D. E., and Pettigrew, N. R. (1994). Causes and consequences of variability in the timing of phytoplankton blooms. *Deep-Sea Research Part I*, 41(5/6):747–765.

Trowbridge, J. H. and Lentz, S. J. (1991). Asymmetric Behavior of an Oceanic Boundary Layer above a Sloping Bottom.

Tsunogai, S., Watanabe, S., and Sato, T. (1999). Is there a 'continental shelf pump' for the absorption of atmospheric CO2? *Tellus, Series B: Chemical and Physical Meteorology*, 51(3):701–712.

Umlauf, L. and Burchard, H. (2005). Second-order turbulence closure models

for geophysical boundary layers. A review of recent work. *Continental Shelf Research*, 25(7-8 SPEC. ISS.):795–827.

Umlauf, L., Burchard, H., and Bolding, K. (2005). General Ocean Turbulence Model. Source code documentation. Technical report, Baltic Sea Research Institute Warnemunde, Warnemunde Germany.

Umlauf, L., Burchard, H., and Hutter, K. (2003). Extending the k-ω turbulence model towards oceanic applications. *Ocean Modelling*, 5(3):195–218.

Uncles, R. J. (2010). Physical properties and processes in the Bristol Channel and Severn Estuary. *Marine Pollution Bulletin*, 61(1-3):5–20.

van Aken, H. M., van Heijst, G. J. F., and Maas, L. R. M. (1987). Observations of fronts in the North Sea. *Journal of Marine Research*, 45(3):579–600.

Van Der Lee, E. M. and Umlauf, L. (2011). Internal wave mixing in the Baltic Sea: Near-inertial waves in the absence of tides. *Journal of Geophysical Research: Oceans*, 116(10):1–16.

van Haren, H. (2000). Properties of vertical current shear across stratification in the North Sea. *Journal of Marine Research*, 58(3):465–491.

van Haren, H. (2009). High-frequency vertical current observations in stratified seas. *Continental Shelf Research*, 29(9):1251–1263.

van Haren, H., Maas, L. R. M., Zimmerman, J. T. F., Ridderinkhof, H., and Malschaert, H. (1999). Strong inertial currents and marginal internal wave stability in the central North Sea. *Geophysical Research Letters*, 26(19):2993–2996.

Visser, A. (2011). Small, wet & rational: Individual based zooplankton ecology. Technical report, DTU, Lyngby.

Vlasenko, V., Stashchuk, N., Inall, M., and Hopkins, J. (2014). Tidal energy conversion in a global hot spot: On the 3-D dynamics of baroclinic tides at the Celtic Sea shelf break. *Journal of Geophysical Research: Oceans*, 119(6):3249–3265.

Wang, D. P., Chen, D., and Sherwin, T. J. (1990). Coupling between mixing and advection in a shallow sea front. *Continental Shelf Research*, 10(2):123–136.

Wang, J., Greenan B. J.W., Lu, Y., Oakey, N. S., and Shaw, W. J. (2014). Layered

mixing on the New England Shelf in summer. *Journal of Geophysical Research C: Oceans*, 119(9):5776–5796.

Weatherly, G. L. and Martin, P. J. (1978). On the Structure and Dynamics of the Oceanic Bottom Boundary Layer.

Witt, M. J., Sheehan, E. V., Bearhop, S., Broderick, a. C., Conley, D. C., Cotterell, S. P., Crow, E., Grecian, W. J., Halsband, C., Hodgson, D. J., Hosegood, P. J., Inger, R., Miller, P. I., Sims, D., Thompson, R. C., Vanstaen, K., Votier, S. C., Attrill, M. J., and Godley, B. J. (2012). Assessing wave energy effects on biodiversity: the Wave Hub experience. *Philosophical Transactions of the Royal Society A: Mathematical, Physical and Engineering Sciences*, 370(1959):502–529.

Wollast, R. (1998). Evaluation and comparison of the global carbon cycle in the coastal zone and the open ocean. In Brink, K. H. and Robinson, A. R., editors, *The Sea*. Wiley, New York.

Yamazaki, H. and Osborn, T. R. (1990). Dissipation Estimates for Stratified Turbulence. *Journal of Geophysical Research*, 95:9739–9744.

Young, E. F., Brown, J., Aldridge, J. N., Horsburgh, K. J., and Fernand, L. (2004). Development and application of a three-dimensional baroclinic model to the study of the seasonal circulation in the Celtic Sea. *Continental Shelf Research*, 24(1):13–36.

Young, E. F. and Holt, J. T. (2007). Prediction and analysis of long-term variability of temperature and salinity in the Irish Sea. *Journal of Geophysical Research*, 112(January):C01008.

Zhang, J., Guo, X., Zhao, L., Miyazawa, Y., and Sun, Q. (2017). Water Exchange across Isobaths over the Continental Shelf of the East China Sea. *Journal of Physical Oceanography*, 47(5):1043–1060.

Zhang, Q. and Wu, J. (2018). On the phase lag of turbulent dissipation in rotating tidal flows. *Continental Shelf Research*, 156(February):23–32.

APPENDIX A

Appendix

A.0.1 The Details on the Operation and Processing of Microstructure Shear Sensor

Table A.1: *MSSpro module list in order of operation to obtain physical shear from MSS raw shear.*

Order	Module	Selected Variables	Options	Description
1	dev_chk	press; temp; NTC; she1; she2; acc	STD-dev: 2.7; Interval: 40 lines;	Removes outliers that exceed the given standard deviation threshold (STD-dev) for all selected variables
2	move_av	press	Interval: 2230 lines	Smooths data using a moving average
3	move_av	press	Interval: 987 lines	[As above]
4	extract	press	Range[begin,end]: 5,600 lines	Extracts the required lines of data in profile between upper and lower limits
5	addtime	N/A	Interval: 0.9765 ms	Adds time variable and performs time adjustment depending on the sampling rate (Interval)
6	shear_c	press; time; she1; she2	Mean density: 1028 kg m^{-3}	Calculates the horizontal shear (du/dz) from the pressure, time and the raw shear data
7	com_sens	acc; vel	N/A	Calculates pseudo-shear (shear produced by mechanical vibrations from the profiler)
8	delsens	she1; she2	N/A	Removes data variables that are no longer required in further processing.
9	detrendn	shear1; shear2; pshear	Interval: 1024 lines	Removes any long-term trend present in the shear data. Any trend present in the profile is likely due to sensor drift since no large-scale correlations should exist in the shear
10	butworth	shear1; shear2; pshear	Type: 0; Order: 3; Cut-off: 100; Sampling freq: 1024;	A digital band pass Butterworth filter is applied to smooth shear data. Filter is applied twice; filtered forwards and then is reversed to maintain zero phase distortion
11	butworth	shear2	Type: 0; Order: 3; Cut-off: 100; Sampling freq: 1024;	[As above]
11	butworth	pshear	Type: 0; Order: 3; Cut-off: 100; Sampling freq: 1024;	[As above]

Table A.2: *MSSpro module list in order of operation to obtain turbulent dissipation and associated variables from physical shear.*

Order	Module	Selected Variables	Options	Description
1	response	temp	sensor time constant: 160; datascans: 20	Corrects variable for the 'time response' of the given sensor and calculates for the mid-point temperature from discrete time intervals. An additional low-pass filter is also applied.
2	dis_nas	shear1, shear2, pshear, press, tempcor,	Interval: 1024; Overlap: 512; Cut wave number[min,max]: 4,20	Calculates the TKE dissipation using an iterative fit to the Nasmyth turbulence spectrum
3	press_av	eps	Interval: 1 dBar	Averages variables over given depth interval
4	smooth	epsilon1, epsilon2	Max deviation factor: 5	Calculates the average of the two shear sensors and checks for spikes. A spike is identified by the difference in two shear prove values greater than a user-specified threshold value
5	log_10	epsilon1, epsilon2 epsilon, peps	N/A	calculates the base-10 log for input variables
6	press_av	temp	Interval: 0.1 dBar	Averages variables over given depth interval
7	dev_chk	press_av	STD-dev: 2; Interval: 15	Removes outliers that exceed the given standard deviation threshold (STD-dev)
8	salinity	press, tempcor, cond	N/A	Calculates the salinity from the conductivity sensor using the UNESCO PSS-78 algorithm
9	dev_chk	salinity	STD-dev: 1.5; Interval: 15	[As above]
10	sigma_t	tempcor, sal	N/A	Calculates the density anomaly using sealevel pressure
11	thorpe	sig_t, press	N/A	Calculates the Thorpe scale (r.m.s of the vertical displacement) using a bubble sort algorithm to reorder the vertical profile to be gravitationally stable
12	press av	thorpe	Interval: 1 dBar	Averages variables over given depth interval
13	merge	[all variables]	N/A	Merge selected channels

Continued...				
Order	**Module**	**Selected Variable**	**Options**	**Description**
14	bvfd	press, dens	N/A	Calculates the squared buoyancy frequency
15	copysens	N^2	Copy variables to output file	
16	com_sens	N^2	N/A	Calculates buoyancy frequency (N) from N^2
17	to_power	N	power: 0.25	Raises values to the given power
18	delsens	N2	N/A	Removes data variables that are no longer required in further processing.
19	move_av	press	Interval: 1000 lines	Smooths data using a moving average
20	move_av	ntc	Interval: 20 lines	[As above]
21	gradients	ntc; press	N/A	Calculates gradients [dt/dz] from the microstructure temperature sensor (ntc)
22	move_av	dt/dz	Interval: 23 lines	[As above]
23	detrendp	dt/dz	Interval: 1 dbar	Removes any long-term trend present in the shear data. Any trend present in the profile is likely due to sensor drift since no large-scale correlations should exist in the shear
24	press_av	dtdz	Interval: 1 dBar	[As above]
25	to_power	X	Power: 2	[As above]
26	mult	X	Constant: 8.4e-7	Multiplies variable by a constant
27	cox	ntc	Pressure interval: 1 dBar	Calculates the Cox-number
28	merge	[all variables]	N/A	[As above]
29	log_10	X; Cox;	N/A	[As above]